

## Abstract

Title of Dissertation: ASSESSMENT OF PROPERTIES OF  
TRANSIENT LIQUID PHASE SINTERED  
(TLPS) INTERCONNECTS BY SIMULATION  
AND EXPERIMENTS

Hannes Greve, Doctor of Philosophy, 2017

Dissertation directed by: Professor Patrick McCluskey, Department of  
Mechanical Engineering

Growing power densities of electronic products and application of electronic systems in high temperature environment increase the temperature requirements on electronic packaging systems. Conventional interconnect technology was designed for devices based on silicon semiconductor technology limited to 175 °C and below. The introduction of wide bandgap semiconductor materials such as silicon carbide and gallium nitride expands the potential application temperature range to 500 °C beyond the range of conventional electronic packaging solutions.

Transient Liquid Phase Sintering (TLPS) is a promising high temperature, high strength, low cost interconnect technology solution. TLPS is a liquid-assisted sintering process during which a low melting temperature constituent melts, surrounds, and diffuses with a high melting temperature constituent. A shift towards higher melting temperatures occurs as the low melting temperature phase is transformed into high melting temperature intermetallic compounds (IMCs). In this work, three TLPS sinter paste systems based on the copper-tin (Cu-Sn), nickel-tin (Ni-Sn), and copper-nickel-tin (Cu-Ni-Sn) material systems are designed. A novel process for their application as electronic interconnects is developed. Processing and thermal aging studies are performed to determine times to process completion characterized by high-temperature capability of the joints. Microstructural convergence durations are studied for each of the material systems. A

modeling approach is developed to model realistic joint geometries with varying types, sizes, and distributions of metal particles and voids in intermetallic matrices. These are used to predict the constitutive (elastic-plastic) stress-strain responses and thermal properties of these systems by simulation. The constitutive models derived by this approach are compared to constitutive properties determined experimentally by Iosipescu shear samples with TLPS joints. The thermal properties of TLPS joints are determined experimentally by transient thermal response analyses. Failure mechanisms driven by thermal and thermo-mechanical stressors are predicted and verified, and mitigation techniques are developed.

ASSESSMENT OF PROPERTIES OF TRANSIENT LIQUID PHASE SINTERED  
(TLPS) INTERCONNECTS BY SIMULATION AND EXPERIMENTS

by

Hannes Martin Hinrich Greve

Dissertation submitted to the Faculty of the Graduate School of the  
University of Maryland, College Park, in partial fulfillment  
of the requirements for the degree of  
Doctor of Philosophy  
2017

Advisory Committee:  
Professor Patrick McCluskey, Chair  
Professor Hugh Bruck  
Professor Abhijit Dasgupta  
Professor Isabel Lloyd  
Dr. Michael Osterman

© Copyright by  
Hannes Martin Hinrich Greve  
2017

## Dedication

To my parents Dorothea and Hinrich and my sister Katha for their love and support. I feel lucky to call you my family. Thank you for fostering my wanderlust and enthusiasm and for your support of my endeavors far away.

To my wonderful sweetheart Fiona. Home is where you are. Thank you for your silly jokes and for giggling about my horrible puns. Your laughs and love mean more to me than words can describe.

## Acknowledgments

I would like to thank my advisor Prof. Patrick McCluskey for his guidance and support during the course of my Ph.D. I appreciate his encouragement to discover my potential as a researcher and teacher. I would also like to thank Prof. Hugh Bruck, Prof. Abhijit Dasgupta, Prof. Isabel Lloyd, and Dr. Michael Osterman for serving on my dissertation committee and providing valuable guidance for my research. I am thankful to the faculty members of the Future Faculty Program for sharing their insight about the pursuit of an academic career.

I would like to thank current and former students, faculty, and staff at the Department of Mechanical Engineering and CALCE. The list of people I enjoyed having gotten to know during my time as a graduate student is too long to be completely written out on this page. I appreciate the input and critical thoughts from all members of the McCluskey research group. I want to thank Ali Moeini for the great exchange of ideas and all the effort on the publications we authored together. I want to thank David Squiller for providing an open ear when spontaneous venting about unhelpful simulation software error messages was required. I want to thank Marco Fries, Raphael Elspas, Patrick Reichert, and Savannah Benbrook for providing useful inputs to my research. I want to thank Dr. Robert Bonenberger for his support with the shear tests. A special thanks goes to Giovanni Flores for his support as a lab manager and for always providing me with a candid view on my work and life in general. I want to thank the CALCE Thursday's group of regulars for many moments of good cheer and highly appreciated diversion.

# Table of Contents

DEDICATION .....	II
ACKNOWLEDGMENTS .....	III
TABLE OF CONTENTS.....	IV
LIST OF FIGURES .....	VI
LIST OF TABLES.....	XXVI
1 INTRODUCTION .....	1
1.1 Background .....	1
1.2 High Temperature Interconnect Technologies for Electronic Systems.....	6
2 FUNDAMENTALS .....	11
2.1 Transient Liquid Phase Sintering (TLPS) .....	11
2.1.1 General Bonding Process.....	12
2.1.2 TLPS in Binary Systems with Intermetallic Compounds.....	21
2.2 The Cu-Sn TLPS System .....	27
2.3 The Ni-Sn TLPS System .....	38
2.4 The Cu-Ni-Sn TLPS System .....	43
2.5 Summary of Reaction Kinetics Data for the Cu-Sn and Ni-Sn Systems....	56
2.6 Comparison of Layer-based and Paste-based TLPS approaches .....	61
2.7 Paste-based TLPS Interconnects in Electronic Applications .....	73
2.7.1 Literature Overview.....	73
2.7.2 Gaps in Literature .....	84
3 OBJECTIVES AND STATEMENT OF WORK .....	86
4 PROCESSING OF PASTE-BASED TLPS INTERCONNECTS .....	90
4.1 Sinter Paste Manufacturing .....	91
4.1.1 Binders and Fluxes .....	91
4.1.2 Paste Manufacturing.....	94
4.1.3 Substrate and Device Preparation.....	96
4.2 Paste Deposition.....	97
4.2.1 Single Step Deposition Paste.....	97
4.2.2 Two Step Deposition Pastes .....	99
4.3 Sintering Process .....	106
4.3.1 Sinter Fixture .....	111
5 MICROSTRUCTURAL EVOLUTION OF TLPS INTERCONNECTS IN HIGH TEMPERATURE ENVIRONMENTS .....	116
5.1 Phase Evolution of Cu-Sn TLPS Joints.....	116
5.1.1 Microstructural Evolution.....	122
5.1.2 Voiding .....	126
5.1.3 Phase Evolution .....	129
5.2 Void Growth and Grain Structure Evolution of Cu-Sn TLPS Joints .....	138
5.2.1 $\text{Cu}_6\text{Sn}_5$ Microstructure.....	139
5.2.2 $\text{Cu}_3\text{Sn}$ Microstructure .....	143
5.3 High Temperature Stability of Ni-Sn and Ni-Cu-Sn TLPS Joints .....	152
6 ASSESSMENT OF TLPS INTERCONNECT PROPERTIES .....	174
6.1 Simulation Approach.....	174

6.2	Thermal Conductivity.....	182
6.2.1	Prediction.....	182
6.2.2	Verification.....	198
6.3	Elastic-Plastic Constitutive Behavior.....	218
6.3.1	Simulation.....	218
6.3.2	Experiments.....	230
6.4	Cooling-induced Crack Formation.....	247
7	SUMMARY AND CONCLUSIONS.....	260
7.1	Academic Contributions.....	264
7.2	Future Work.....	267
8	BIBLIOGRAPHY.....	271

## List of Figures

Figure 1-1: Intrinsic carrier concentration $n_i$ for various semiconductors [3] .....	2
Figure 1-2: Temperature-dependence of the theoretical breakdown voltage $V_{br}$ for various semiconductors [3].....	2
Figure 1-3: Automotive high-temperature environments [12].....	4
Figure 1-4: Typical power module structure [13].....	5
Figure 2-1: Taxonomy of sintering processes [20].....	12
Figure 2-2: Phase diagram of a binary eutectic system .....	16
Figure 2-3: Concentration profiles of $C_A$ (blue lines) for eutectic binary systems during the melting: a) original arrangement, b) melting and dissolution of atoms of $B$ in $L$ , c) diffusion of atoms of $A$ from $L$ in $B$ and transformation to $\beta$ , and d) final arrangement .....	17
Figure 2-4: Left: Influence of the contact angle $\theta$ on the wetting of the solid by the liquid: smaller contact angles facilitate the wetting. Right: Large $\theta$ leads to liquid retreating from the solid [29] .....	18
Figure 2-5: Infiltration of a compacted iron powder by 8 wt.% copper [29]. The left image was heated to 1075 °C, the right image to 1110 °C.....	19
Figure 2-6: Collection of pores at prior liquid locations after spreading of the liquid along solid particle boundaries [29].....	20
Figure 2-7: Pore formation with large low $T_m$ particles in a Cu-10%Sn TLP body. The pores are located at sites where former large Sn particles melted [29] .....	20
Figure 2-8: Phase diagram of a binary eutectic system with one intermetallic compound ( $B_nA_m$ ) and no solubility of $A$ in $B$ and vice versa.....	22

Figure 2-9: Concentration profiles of $C_A$ (blue lines) for the system shown in Figure 2-8 during TLPS: a) melting, b) widening of the liquid phase, c) growth of IMCs and consumption of $L$ , and d) final composition. For thin layers of $A$ , $L$ gets consumed and $T_m$ shifts (left). For thick layers $L$ cannot be fully consumed (right).....	22
Figure 2-10: Phase diagram of a binary eutectic system with two intermetallic compounds ( $B_nA_m$ and $B_pA_o$ ) and no solubility of $A$ in $B$ and vice versa.....	24
Figure 2-11: Concentration profiles of $C_A$ (blue lines) for the system shown in Figure 2-10 during TLPS: a) melting, b) widening of the liquid phase, c) initial growth of primary IMC and consumption of $L$ , d) initial growth of secondary IMC, e) consumption of $L$ , f) consumption of primary IMC, g) final microstructure .....	25
Figure 2-12: The Cu-Sn phase diagram [34] .....	28
Figure 2-13: $Cu_6Sn_5$ layer thickness vs. time after aging at 200 °C. Dotted data is extrapolated from kinetics models above $T_{m,Sn}$ .....	32
Figure 2-14: $Cu_6Sn_5$ layer thickness vs. time after aging at 250 °C. Dotted data is extrapolated from kinetics models above $T_{m,Sn}$ .....	33
Figure 2-15: $Cu_3Sn$ layer thickness vs. time after aging at 200 °C. Dotted data is extrapolated from kinetics models above $T_{m,Sn}$ .....	34
Figure 2-16: $Cu_3Sn$ layer thickness vs. time after aging at 250 °C. Dotted data is extrapolated from kinetics models below $T_{m,Sn}$ .....	34
Figure 2-17: Microstructural evolution during TLPS of a Cu-Sn joint with high Sn-content. Pockets of unconsumed $L$ remain because of the lack of Cu. The joint does not possess high temperature capability.....	36

Figure 2-18: Microstructural evolution during TLPS of a Cu-Sn joint with medium Sn-content. After process completion most of L has been consumed. The microstructure is characterized by  $\eta$  IMCs linking  $\epsilon$  IMCs and small pockets of L. The melting temperature of this joint is  $T_{m,Cu_6Sn_5}$ ..... 37

Figure 2-19: Microstructural evolution during TLPS of a Cu-Sn joint with low Sn-content. After process completion all of L has been consumed. The microstructure is characterized by  $\epsilon$  IMCs linking residual Cu. The melting temperature of this joint is  $T_{m,Cu_3Sn}$ ..... 38

Figure 2-20 The Ni-Sn phase diagram [44] ..... 39

Figure 2-21:  $Ni_3Sn_4$  layer thickness vs. time after aging at 250 °C. See [45] for original data ..... 41

Figure 2-22:  $Ni_3Sn_4$  layer thickness vs. time after aging at 200 °C ..... 42

Figure 2-23:  $(Cu,Ni)_6Sn_5$  IMC thickness growth on the Ni- and Cu-side during aging at 150, 180, and 200 °C, reproduced from [74] ..... 49

Figure 2-24: IMC growth on the Ni- and Cu-side during aging at 250 °C on the Cu- and Ni-side of a ternary and at the Cu-Sn interface of a binary diffusion couple, reproduced from [75] ..... 52

Figure 2-25: Microstructural evolution during TLPS of a Cu-Ni-Sn joint with medium Sn-content. After process completion most of L has been consumed. The microstructure is characterized by  $(Cu,Ni)_6Sn_5$  IMCs linking Ni-particles, some  $Cu_3Sn$  IMCs and pockets of L. The melting temperature of this joint is  $T_{m,(Cu,Ni)_6Sn_5}$  ..... 55

Figure 2-26: Temperature dependence of the diffusion coefficient for the growth of the  $Cu_6Sn_5$ ,  $Cu_3Sn$ , and  $Ni_3Sn_4$  IMCs. Solid lines and dashed lines indicate values below and

above the melting temperature of Sn respectively. The dotted green line is a result from studies with non-parabolic growth parameters ( $n \neq 0.5$ ) ..... 59

Figure 2-27: Principle of transient liquid phase sintering by the layer-based approach. The low melting point layer is consumed by reaction with the metallization layers ..... 62

Figure 2-28: Options for the application of the low melting temperature layer: a) Sandwiching of a preform between device and substrate metallization, b) application of a low- $T_m$  metallization on one metallization side via sputtering or plating, and c) application of a low- $T_m$  metallization on both metallization sides via sputtering or plating ..... 63

Figure 2-29: Void formation by insufficiently thick low melting temperature phase layer thickness in layer-based TLPS: a) roughness of the substrate metallization before sintering, b) partial wetting of the device metallization during sintering, and c) formation of voids in the gaps that were not filled by liquid..... 65

Figure 2-30: Roughness compensation by use of TLPS sinter pastes: A Ni-die was joined to a Ni-plated DBC substrate by the use of Ni-Sn sinter pastes. The roughness of the substrate is compensated by varying sinter paste thickness after stencil printing. The Ni die is continuously in contact with the TLPS joint..... 67

Figure 2-31: Required vol.-percentages of low and high melting temperature phases (LT and HT respectively) for complete TLPS bonding. .... 70

Figure 2-32: Minimum required high melting temperature layer thickness for complete consumption of a 25  $\mu\text{m}$  thick low melting temperature layer. .... 71

Figure 2-33: SEM image of a cross-section of TLPS interconnect formed between a Ni-substrate and a Si-diode via sinter pastes consisting of Ni- and Sn3.5Ag solder particles72

Figure 3-1: Flow chart of the research effort in this work: Raw materials (blue), intermediate steps (red), analytical methods (brown), independent study elements (purple), and derived conclusive results (green).....	89
Figure 4-1: Important process steps for the formation of paste-based TLPS interconnects .....	90
Figure 4-2: Categorization of flux systems by their stability against evaporation and metal oxide reduction capabilities their intended use application .....	92
Figure 4-3: Flow chart of the sinter paste manufacturing process .....	95
Figure 4-4: TLPS process steps – Stencil printing & Dispensing .....	100
Figure 4-5: Example structure of a device attached with TLP sinter paste systems to a substrate .....	100
Figure 4-6: Stencil printing of the high temperature paste (left) and top view on the resulting structure.....	102
Figure 4-7: Dispensing of the low temperature paste around the stencil printed high temperature layer .....	102
Figure 4-8: Placement of the device on the stencil printed high temperature paste .....	102
Figure 4-9: TLPS process steps – Printing, Drying, and Dispensing .....	103
Figure 4-10: Example structure of a device attached with TLP sinter paste systems to a substrate .....	103
Figure 4-11: Stencil printing of the high temperature paste .....	105
Figure 4-12: Drying of the high temperature paste.....	105

Figure 4-13: Stencil printing of the low temperature paste around the stencil printed high temperature layer. The stencil for the low temperature paste must be of the same thickness as the dried high temperature layer (above), or thicker (below).....	105
Figure 4-14: Placement of the device after stencil printing of the low temperature paste for the two cases described in Figure 4-13 .....	106
Figure 4-15: Spreading of the joint in vertical direction: a) Original paste arrangement, b) melting of the low $T_m$ alloys (grey) and infiltration of the mesh of high $T_m$ particles (blue); Some pockets of high viscous binder remain between the mesh (green), c) initial vertical spreading due to further infiltration and exertion pressure on the central flux region, and d) additional spreading due to flux evaporation: Voids (yellow) and solid residues (brown) remain .....	108
Figure 4-16: Application of homogeneous pressure on the samples before sintering: a) positioning of samples on the top surface of the sinter fixture, b) positioning of polyimide spacers for pressure homogenization on top of devices, and c) application of weights on the polyimide spacers.....	110
Figure 4-17: Temperature profiles for the sintering process. The 2 minute dwell time profile is similar to conventional reflow soldering profiles. The 30 minute dwell time is the expected profile to achieve full IMC formation .....	111
Figure 4-18: Overview of the sinter fixture assembly .....	112
Figure 4-19: Elements of the Hot-/Coldplate.....	113
Figure 4-20: Arrangement of holes and cooling structures within the hot-/coldplate ....	113
Figure 4-21: Schematic of the sinter fixture water cooling system .....	114

Figure 4-22: Comparison of suggested SAC reflow soldering profile (blue) and the measured sinter fixture temperature (yellow)..... 115

Figure 5-1: Schematic cross-section of a Cu-Sn TLPS aging study sample before sintering ..... 117

Figure 5-2: Flowchart of the workflow during phase analysis ..... 119

Figure 5-3: Transformation of greyscale image (left) and computation of greyscale distribution (right)..... 120

Figure 5-4: Greyscale distribution (left) and selection of maxima (right)..... 121

Figure 5-5: Example of the phase analysis of a cross-section of a Cu-Sn TLPS joint with Cu-particles (Phase 1 - black),  $\text{Cu}_3\text{Sn}$  IMCs (Phase 2 – dark grey),  $\text{Cu}_6\text{Sn}_5$  IMCs (Phase 3 – grey), and Sn (Phase 4 - white)..... 122

Figure 5-6: Cross-section of a Cu-Sn joint sintered for 2min@300 °C. Joint edges a) and c) and joint center b) shown separately. Considerable amounts of unconsumed Sn are still present in the joint.  $\text{Cu}_6\text{Sn}_5$  IMCs have started growing around the spherical Cu-particles. Voids are distributed homogeneously..... 123

Figure 5-7: Cross-section of a Cu-Sn joint sintered for 30min@300 °C. Joint edges a) and c) and joint center b) shown separately. The majority of Sn was converted to  $\text{Cu}_6\text{Sn}_5$ . Local pockets of Sn remain. Thin layers of  $\text{Cu}_3\text{Sn}$  IMCs are present at the interfaces between  $\text{Cu}_6\text{Sn}_5$  and Cu. The smallest Cu-particles were completely converted to IMCs ..... 124

Figure 5-8: Cross-section of a Cu-Sn joint after aging for 24h@250 °C. Joint edges a) and c) and joint center b) shown separately. Limited residual Cu is present at the joint edges which consist predominately of  $\text{Cu}_6\text{Sn}_5$ . The joint center has a higher percentage of  $\text{Cu}_3\text{Sn}$ . Voiding is more pronounced at the joint center..... 125

Figure 5-9: Cross-section of a Cu-Sn joint after aging for 100h@250 °C. Joint edges a) and c) and joint center b) shown separately. Sn is almost completely consumed. The joint edges consist predominately of Cu <sub>6</sub> Sn <sub>5</sub> and most Cu has been consumed in these regions. The joint center consists predominately of Cu <sub>3</sub> Sn. Voids are concentrated in the Cu <sub>3</sub> Sn-rich regions.....	126
Figure 5-10: Development of the joint voiding during sintering aging .....	127
Figure 5-11: Dependence of the development of the voiding behavior on the joint section .....	129
Figure 5-12: Evolution of Cu for the full joint .....	130
Figure 5-13: Evolution of Sn for the full joint.....	130
Figure 5-14: Evolution of Cu <sub>6</sub> Sn <sub>5</sub> for the full joint.....	131
Figure 5-15: Evolution of Cu <sub>3</sub> Sn for the full joint.....	132
Figure 5-16: Evolution of phases in the full joint.....	133
Figure 5-17: Evolution of Cu at the joint center and edges .....	134
Figure 5-18: Evolution of Sn at the joint center and edges.....	134
Figure 5-19: Evolution of Cu <sub>6</sub> Sn <sub>5</sub> at the joint center and edges .....	135
Figure 5-20: Evolution of Cu <sub>3</sub> Sn at the joint center and edges.....	136
Figure 5-21: Evolution of phases in the joint center.....	137
Figure 5-22: Evolution of phases in the joint edges .....	138
Figure 5-23: Surface morphology of Cu <sub>6</sub> Sn <sub>5</sub> grains after 30 minutes of sintering at 300 °C. The grain size is on the scale of 10 μm. Intergranular spaces are filled with residual unconsumed Sn .....	139

Figure 5-24: Surface morphology of  $\text{Cu}_6\text{Sn}_5$  grains of a joint aged for 24 hours at 250 °C after 30 minutes of sintering at 300 °C. The grain size is on the scale of 10  $\mu\text{m}$ . No residual Sn is present in the intergranular spaces ..... 140

Figure 5-25: Growth of  $\text{Cu}_6\text{Sn}_5$  IMCs and associated consumption of Sn and growth of void during particle-based TLPS of the Cu-Sn system: a) Nucleation of  $\text{Cu}_6\text{Sn}_5$  grains on the surface of the Cu-particle, b) growth of  $\text{Cu}_6\text{Sn}_5$  IMCs and consumption of Sn, c) continued growth of voids and receding of Sn into the spaces between the  $\text{Cu}_6\text{Sn}_5$  grains, and d) final structure after full consumption of Sn ..... 141

Figure 5-26: Residual intergranular Sn phase after sintering for 30 minutes at 300 °C and subsequent aging at 250 °C for 24 hours. In contrast to the image shown in Figure 5-24, the higher Sn-concentration in the proximity of the void leads to slower Sn-consumption and presence of residual Sn ..... 142

Figure 5-27: Limited residual Sn in some grain boundaries (right) between  $\text{Cu}_6\text{Sn}_5$  grains after sintering for 30 minutes at 300 °C and subsequent aging at 250 °C for 100 hours. The majority of the grain boundaries were not occupied by Sn after this aging duration (right) ..... 143

Figure 5-28: Surface morphology of the  $\text{Cu}_3\text{Sn}$  grains of a joint sintered for 30 minutes at 300 °C and subsequently aged at 250 °C for 24 hours. The grain size is on the scale of few  $\mu\text{m}$  ..... 144

Figure 5-29: Evolution of grain structure during the transformation from large-grained  $\text{Cu}_6\text{Sn}_5$  IMC to small-grained  $\text{Cu}_3\text{Sn}$  IMC (joint aged for 24 hours at 250 °C) ..... 144

Figure 5-30: Evolution of grain structure during the transformation from large-grained  $\text{Cu}_6\text{Sn}_5$  IMC to small-grained  $\text{Cu}_3\text{Sn}$  IMC (joint aged for 24 hours at 250 °C) ..... 145

Figure 5-31: Evolution of grain structure during the transformation from large-grained Cu <sub>6</sub> Sn <sub>5</sub> IMC to small-grained Cu <sub>3</sub> Sn IMC (joint aged for 100 hours at 250 °C) .....	145
Figure 5-32: EDX line-scan analysis of the transition zone from Cu <sub>6</sub> Sn <sub>5</sub> to Cu <sub>3</sub> Sn (left and center) and EDX area scan (right). The transition from large grains to small grains coincides with the transition from Cu <sub>6</sub> Sn <sub>5</sub> to Cu <sub>3</sub> Sn. The figure shows a high magnification view of Figure 5-31.....	146
Figure 5-33: EDX area scan analysis of the transition zone from Cu <sub>6</sub> Sn <sub>5</sub> to Cu <sub>3</sub> Sn. The transition from large grains to small grains coincides with the transition from Cu <sub>6</sub> Sn <sub>5</sub> to Cu <sub>3</sub> Sn .....	146
Figure 5-34: Growth of gap between Cu <sub>3</sub> Sn grains. No sign of fracture was detected. This indicates that the growth occurs during grain transformation .....	147
Figure 5-35: Contrast between the microvoiding behaviors of Cu <sub>3</sub> Sn IMCs in the bulk joint (bottom) around Cu-particles and Cu <sub>3</sub> Sn IMCs formed at the interface to Cu-coupons and Cu-substrates (top).....	148
Figure 5-36: SEM image of a cross-section of a Cu-particle before sintering (top). Regions of different crystal direction can be discerned, indicated by dotted yellow lines (bottom) .....	149
Figure 5-37: SEM image of a cross-section of a Cu-particle before sintering. Regions of different crystal direction can be discerned, indicated by dotted yellow lines (left) .....	150
Figure 5-38: Schematic cross-section of a Ni-Sn TLPS aging study sample before sintering .....	153
Figure 5-39: Cross-section of a Ni-Sn joint sintered for 2min at 300 °C. Joint edges a) and c) and joint center b) shown separately. Considerable amounts of unconsumed Sn are still	

present at the joint edges. Limited  $\text{Ni}_3\text{Sn}_4$  IMCs have started growing around the spherical Ni-particles. Few voids are present..... 156

Figure 5-40: Cross-section of the center region of a Ni-Sn joint sintered for 2min at 300 °C. No continuous high- $T_m$  phases ( $\text{Ni}_3\text{Sn}_4$  and Ni) are present between the Ni-substrate and Ni-coupon..... 156

Figure 5-41: Cross-section of a Ni-Sn joint aged for 30min at 300 °C. Joint edges a) and c) and joint center b) shown separately. Unconsumed Sn remains at the joint edges. The joint center consists predominately of Ni and  $\text{Ni}_3\text{Sn}_4$ ..... 157

Figure 5-42: Cross-section of the center region of a Ni-Sn joint sintered for 30min at 300 °C. The joint consists predominately of continuous high- $T_m$  phases ( $\text{Ni}_3\text{Sn}_4$  and Ni) ... 157

Figure 5-43: Cross-section of a Ni-Sn joint aged for 24h at 250 °C. Joint edges a) and c) and joint center b) shown separately. Two layers of unreacted Sn are present between the bulk joint and the Ni-coupons and Ni-substrates ..... 159

Figure 5-44: Cross-section of the center regions of two Ni-Sn joints aged for 24h at 250 °C. Most joints showed a delamination of the Ni-coupon and/or Ni-substrate from the bulk of the TLPS joint with layers of Sn in between (left). One joint did not show a continuous Sn-layer, but a chain regions of residual Sn (right) ..... 159

Figure 5-45: Cross-section of a Ni-Sn joint sintered for 100h at 250 °C. Joint edges a) and c) and joint center b) shown separately. Regions of prior Sn concentrations (between the Ni-coupons and Ni-substrates and the bulk TLPS joint, see Figure 5-43) are now characterized by void formation ..... 160

Figure 5-46: Cross-section of the center region of a Ni-Sn joint aged for 100h at 250 °C. A continuous void layer is present between the Ni-coupon (topside) and the bulk TLPS joint (center) .....	161
Figure 5-47: Reduction of Sn meniscus volume during aging. Infiltration of the joint region by Sn during aging is indicated by the green arrows .....	162
Figure 5-48: Thickness evolution of Ni-Sn TLPS joints during processing and aging ..	164
Figure 5-49: Setup for the assessment of the joint softening temperature: (a) shear fixture and sample, (b) locating the sample in the shear fixture, (c) thermal insulation material, and (d) setup overview.....	165
Figure 5-50: Softening temperature of Pb5.0Sn2.5Ag, Cu-Ni-Sn, and Ni-Sn joints.....	166
Figure 5-51: Illustration of the lateral growth process of large Ni <sub>3</sub> Sn <sub>4</sub> grains, redrawn from [45]. A rotation of the triple point towards the small grain occurs and the large grain grows at the expense of the small grain.....	167
Figure 5-52: Delamination of Ni <sub>3</sub> Sn <sub>4</sub> grains, compare [45] .....	168
Figure 5-53: Delamination of the Ni-coupon from the bulk of the Ni-Sn TLPS joint ...	169
Figure 5-54: Optical microscope image of a side view of a Ni-Sn joint sintered for 30 minutes at 300 °C.....	170
Figure 5-55: Thickness of unaged (30min@300 °C) and aged (100h@250 °C) samples .....	170
Figure 5-56: Thickness evolution of Ni-Sn TLPS joints with and without menisci.....	171
Figure 5-57: ESEM images of Ni-Sn TLPS joints after aging for 100 hours at 250 °C. No crack initiation or joint delamination occurred.....	172

Figure 5-58: Optical microscope images of cross-sections of Cu-Ni-Sn TLPS joints after (a) 2 minutes of sintering at 300 °C, (b) 30 minutes of sintering at 300 °C, and (c) 30 minutes of sintering at 300 °C followed by 24 hours of aging at 250 °C.....	173
Figure 6-1: Process flow of the TLPS joints properties simulation approach .....	175
Figure 6-2: Process flow of the Particle Distribution Generator .....	176
Figure 6-3: Input parameters and example arrangement of Objects within a Joint Space after completing a Particle Distribution Generator run.....	177
Figure 6-4: Process flow of the 3D CAD model creation.....	178
Figure 6-5: 3D model in SolidWorks. The geometry information from Figure 6-3 was used. White spheres in Figure 6-3 are here shown as grey-shaded voided regions. IMC regions are not shown. ....	179
Figure 6-6: Process flow of a thermal simulation in ANSYS Workbench.....	180
Figure 6-7: Cross-sectional view of a meshed TLPS interconnect in ANSYS Workbench and resulting thermal simulation.....	181
Figure 6-8: Cross-sectional view of a meshed TLPS interconnect in ANSYS Workbench and resulting heat flow distribution .....	181
Figure 6-9: Thermal conductivities for a 20 vol.-% metal particle loading.....	184
Figure 6-10: Thermal conductivity relative to that of joints with 70 μm radius particles. ....	185
Figure 6-11: Heat flow paths for a joint with high $\kappa_{IMC}$ (left) and low $\kappa_{IMC}$ (right) and identical $\kappa_{Particle}$ . In joints with a lower ratio of $\kappa_{IMC}/\kappa_{Particle}$ , heat flow paths are more concentrated in and between metal particles. ....	187

Figure 6-12: Influence of particle size on the heat flow paths within the TLPS joints. Large metal particles (a) provide uninterrupted vertical heat flow between the heat source and the heat sink. Within a critical size range (b) particles do neither bridge the entire joint thickness nor provide vertically stacked heat paths. At smaller sizes (c) low resistance heat conduction paths are provided by vertically stacked particles.....	188
Figure 6-13: Percentage of metal particles in the joint in vol.-% .....	190
Figure 6-14: Thermal conductivities for the maximally metal particle loaded sinter joints .....	190
Figure 6-15: Comparison of the thermal conductivity of joints willed with 20 vol.-% (solid lines) and max. vol.-% (dashed lines) metal particles .....	191
Figure 6-16: Thermal conductivities of the void-free sinter joints loaded with particles of mixed size .....	193
Figure 6-17: Thermal conductivities relative to that of joints with 42 vol.-% metal loading .....	193
Figure 6-18: Thermal conductivity of partially voided joints for the (Cu <sub>3</sub> Sn+Cu) system .....	194
Figure 6-19: Thermal conductivity of partially voided joints for the (Cu <sub>6</sub> Sn <sub>5</sub> +Cu) system .....	195
Figure 6-20: Thermal conductivity of partially voided joints for the (Ni <sub>3</sub> Sn <sub>4</sub> +Ni) system .....	195
Figure 6-21: Side view on structure formed by metal particles with radii of 50, 30, and 10 μm .....	196

Figure 6-22: Thermal conductivity of the joint with a metal loading as shown in Figure 6-21 .....	196
Figure 6-23: Schematic of a cross-section through the thermal stack used to analyze the thermal properties of the TLPS joint .....	199
Figure 6-24: Top view on a sample used for the transient thermal analyses. The diode is indicated by the dotted red line and the meniscus region is indicated by the dotted orange line.....	200
Figure 6-25: Top view on the test structure. The sample with the diode sintered on the DBC is placed on top of the heatsink with a grease layer sandwiched in between. Four screws are exerting pressure on the DBC. Two of these are ensuring contact between the Cu-ribbons and the diode .....	201
Figure 6-26: Calibration curve of one sample used in the test .....	201
Figure 6-27: Thermal impedance curve: Transient thermal response curves of a Cu-Sn TLPS sample after sintering (blue line) and after aging for 100 hours at 250 °C (red line) .....	202
Figure 6-28: The Foster (top) and Cauer (bottom) canonic forms of thermal networks	205
Figure 6-29: Physical equivalent of the Cauer canonic form: Every $R_i$ - $C_i$ pair corresponds one element of thermal resistance and thermal capacities in the thermal stack.....	205
Figure 6-30: Example structure function of a Cu-Sn TLPS sample .....	206
Figure 6-31: Temperature distribution in a simulated Cu-Sn TLPS sample in FloTherm. The geometry shows high resemblance with the test samples, compare Figure 6-25 ....	207
Figure 6-32: View on the die region of the simulation shown in Figure 6-31. The geometry includes menisci, Cu-ribbon, polyimide-spacers and tightening screw elements .....	207

Figure 6-33: Fitting of the simulated structure function (red line) to the structure function from T3Ster experiments (blue line).....	208
Figure 6-34: Structure functions of the unaged Cu-Sn TLPS samples.....	210
Figure 6-35: Structure functions of the Cu-Sn TLPS samples aged for 100 hours at 250 °C .....	211
Figure 6-36: Degradation of the die attach layer is the main source of difference between the structure functions of aged and unaged samples.....	212
Figure 6-37: Structure functions of unaged (green) and aged (red) Cu-Sn TLPS samples .....	213
Figure 6-38: Cross-section of an unaged Cu-Sn TLPS sample .....	213
Figure 6-39: Cross-section of a Cu-Sn TLPS sample without aging.....	214
Figure 6-40: Cross-section of a Cu-Sn TLPS sample after aging.....	215
Figure 6-41: Cross-section of a Cu-Sn TLPS sample after aging, two failure modes can be identified: (1) horizontal crack formation and (2) die detachment .....	216
Figure 6-42: Detachment of the Cu-Sn TLPS joint from the diode die after aging.....	217
Figure 6-43: Standard Iosipescu shear test sample: Solder joint between Cu-coupons (left) and coupon dimensions (right).....	219
Figure 6-44: Flow chart of the constitutive properties modeling process .....	221
Figure 6-45: Example geometry for the analysis of constitutive properties: Sample dimension and shear force application (left) and metal particle distribution (right) .....	222
Figure 6-46: Displacement contour (top) plots in x-direction for shear (left) and tensile (right) load and associated absolute displacements at the load locations (bottom). The tensile load has lower variance .....	223

Figure 6-47: Applied stress and corresponding average strain for the shear strain condition .....	223
Figure 6-48: Applied stress and corresponding average strain for the tensile strain condition .....	224
Figure 6-49: Stress-strain curve computed from the stress and strain curves for the shear load condition, see Figure 6-47.....	225
Figure 6-50: Stress-strain curve computed from the stress and strain curves for the tensile load condition, see Figure 6-48.....	225
Figure 6-51: Deformation behavior of a Cu-Cu <sub>6</sub> Sn <sub>5</sub> TLPS compound: Bilinear hardening behavior with high stiffness below yielding and low stiffness after yielding.....	226
Figure 6-52: Example for two full tensile load cycle: (1) Loading to a maximum load, (2) Unloading to zero stress level, (3) loading to a minimum load, and (4) Unloading to zero stress level. The second cycle is identical with the first cycle and includes time steps 5 - 8 .....	227
Figure 6-53: Stress-strain curves for the 1 <sup>st</sup> (left) and 2 <sup>nd</sup> (right) load cycles shown in Figure 6-52. Kinematic hardening behavior was followed .....	228
Figure 6-54: Kinematic hardening during the 1 <sup>st</sup> full load cycle: Original yield surface (dotted blue), yield surface after increasing the load to +125 MPa (red), and after decreasing the load to -125 MPa (green). Note that the load is uniaxial along the vertical direction of this figure.....	228
Figure 6-55: Standard Iosipescu shear test sample: Solder joint between Cu-coupons (left) and coupon dimensions (right).....	230
Figure 6-56: Elastic modulus of select electronic materials .....	231

Figure 6-57: Yield strength of select electronic materials .....	232
Figure 6-58: Half-model of a Iosepescu sample with TLPS joint and Mo-coupons with laminated Cu metallization. Overall structure (left), load condition (center), and mesh (right) .....	233
Figure 6-59: Semi-transparent view on a Cu-Cu <sub>6</sub> Sn <sub>5</sub> unit cell .....	234
Figure 6-60: Elastic (left) and plastic (right) strain near the joint region for the laminated Cu-Mo-Cu coupon shown in Figure 6-58.....	234
Figure 6-61: Elastic (left) and plastic (right) strain near the joint region for a sample with Mo-only coupons .....	235
Figure 6-62: Metallization layers of the Mo-coupons for the Cu-Sn Iosipescu samples	236
Figure 6-63: Sketch of the EDM-cut Mo-bar with dimensions (left) and picture of the Cu-plated bar (right) .....	236
Figure 6-64: Cross-section of a plated Mo-Coupon. Considerable roughness is visible on the top surface .....	237
Figure 6-65: Surface morphology of the plated Mo-coupons.....	237
Figure 6-66: EDS analysis of the coupon metallization .....	238
Figure 6-67: Isometric view on the Iosipescu sinter fixture individually (right) and on the sinter fixture (left).....	239
Figure 6-68: Top view on the Iosipescu sinter fixture.....	239
Figure 6-69: Process flow for the positioning of the Iosipescu coupons in the fixture ..	239
Figure 6-70: Top view on a Cu-Sn TLPS Iosipescu sample.....	240
Figure 6-71: Side view on the Cu-Sn TLPS Iosipescu sample show in Figure 6-70.....	241
Figure 6-72: SEM view of a Cu-Sn Iosipescu shear test sample.....	242

Figure 6-73: Optical microscopy image of a Cu-Sn Iosipescu shear test sample. Considerable voiding is visible on the sample frontside .....	242
Figure 6-74: Adhesion of the TLPS joint to the metallization: Locally broken Ni layer indicates flaws in the metallization layer due to coupon roughness.....	243
Figure 6-75: Shear stress-strain curve for a Cu-Sn TLPS sample cyclically displaced by $\pm 10 \mu\text{m}$ .....	244
Figure 6-76: Delamination of the metallization after cycling of a Cu-Sn TLPS sample to 80% load drop.....	246
Figure 6-77: Development of the load drop vs. number of cycles.....	247
Figure 6-78: Crack formation in a diode-on-DBC assembly after processing .....	248
Figure 6-79: Examples of crack formation in die-on-DBC systems: The crack propagates between the void, through the IMC region and Ni plating, and stops at the DBC Cu layer .....	248
Figure 6-80: Structure for the assessment of the thermo-mechanical assembly behavior .....	249
Figure 6-81: Simulation model mesh for the cooling-induced cracking study.....	250
Figure 6-82: Stress vs. plastic strain for Ni and Cu at 20 °C (above) and Cu at multiple temperatures .....	251
Figure 6-83: Dependence of the maximum principal stresses of die and IMCs on the void size. In contrast to the die maximum principal stress, the IMC shows a strong dependence on void size .....	252

Figure 6-84: Cross-section through a TLPS joint with large (30 $\mu\text{m}$ radius) voids. Two distinct types of stress concentration exist: (1) between voids and Cu or Si, and (2) between adjacent voids in close proximity .....	253
Figure 6-85: Cross-section through a TLPS joint with small (12 $\mu\text{m}$ radius) voids. The higher number of voids in the joint increases the probability of voids in close proximity .....	253
Figure 6-86: Maximum principal stress distribution at the DBC Cu-to-TLPS joint interfaces for large (30 $\mu\text{m}$ radius) voids.....	254
Figure 6-87: Maximum principal stress distribution at the DBC Cu-to-TLPS joint interfaces for small (12 $\mu\text{m}$ radius) voids .....	254
Figure 6-88: Maximum principal stresses in the IMC, diode, IMC-to-Diode and IMC-to-DBC Cu interfaces for the Ni+Ni <sub>3</sub> Sn <sub>4</sub> system with large and small voids .....	255
Figure 6-89: Maximum principal stresses in the IMC, diode, IMC-to-Diode and IMC-to-DBC Cu interfaces for the Cu+Cu <sub>6</sub> Sn <sub>5</sub> system with large and small voids.....	256
Figure 6-90: Maximum principal stresses in the IMC, diode, IMC-to-Diode and IMC-to-DBC Cu interfaces for the Cu+Cu <sub>3</sub> system with large and small voids .....	256
Figure 6-91: (a) The stress-strain curves of pillars until the onset of first strain bursts and (b) a plot showing the relation between top fracture stress and taper angle of pillars [129] .....	257
Figure 6-92: Concentration of current and heat flux by vertical cracking: The introduction of vertical cracks at the TLPS-to-DBC Cu interface should not decrease the thermal or electrical conductivity of the assembly significantly.....	258

## List of Tables

Table 1-1: Physical Properties of Si, SiC, and GaN [2].....	1
Table 1-2: Melting temperatures and characteristics of select solders and sintered silver.	8
Table 2-1: $C_A$ and $T_m$ for incomplete transformation of L to secondary IMC because of insufficient B in the original structure .....	26
Table 2-2: Dependence of the IMC type formation between Sn-Ag alloys and Ni substrates on the level of Cu doping in the alloy, adapted from [59].....	45
Table 2-3: Volumes [ $\text{\AA}^3/\text{cell}$ ], heat of formation [meV/atom], and cohesive energies [eV/atom] for $\text{Cu}_6\text{Sn}_5$ , $\text{Cu}_5\text{Ni}_1\text{Sn}_5$ , and $\text{Cu}_4\text{Ni}_2\text{Sn}_5$ , compare [73].....	48
Table 2-4: Compositional analyses of the $(\text{Cu,Ni})_6\text{Sn}_5$ IMCs at the Cu- and Ni-side after aging for 36 days at multiple temperature levels [74]. Concentrations in at.% .....	50
Table 2-5: Ni-concentration in the $(\text{Cu,Ni})_6\text{Sn}_5$ IMCs at the Cu- and Ni-side after multiple process times at 250 °C [75]. Concentrations in at.% .....	51
Table 2-6: Governing equations and associated parameters for the IMC growth kinetic models shown in Figure 2-26.....	61
Table 2-7: Calculated minimum time for complete TLPS process completion for multiple joint thicknesses for sintering temperature of 300 °C and 200 °C. Calculations are based on data summarized in Table 2-6.....	68
Table 2-8: Non-infiltrated area in percent of the Cu-mesh. Reproduced from [102].....	77
Table 5-1: Composition of substrate, coupon, sinter paste, and solder paste material ...	117
Table 5-2: Test conditions and related application conditions .....	118
Table 5-3: Composition of substrate, coupon, sinter paste, and solder paste material ...	153
Table 5-4: Test conditions and related application conditions .....	155

Table 6-1: Thermal conductivities of materials used in the simulations [122].....	183
Table 6-2: Thermal conductivities for 20 vol.-% metal particle loading.....	185
Table 6-3: Ratio of the thermal conductivities of the IMCs to the metal particles for the assessed material systems. ....	186
Table 6-4: Thermal conductivities for maximally metal particle loaded sinter joints ....	191
Table 6-5: Vol.-% of the mixed particles for the void-free test condition.....	192
Table 6-6: Vol.-% of the mixed particles for the void-free test condition.....	192
Table 6-7: Thermal conductivities of the void-free sinter joints loaded with particles of mixed size .....	196
Table 6-8: Joint thickness, best-fit thermal conductivity, and computed joint resistance of the unaged Cu-Sn TLPS sinter joints.....	209
Table 6-9: Mechanical properties of select electronic materials [122] [124] [125] [126] [127] [128] .....	231
Table 6-10: Elastic modulus, coefficient of thermal expansion (CTE), and thermal conductivity of the materials used in this study.....	250
Table 6-11: Maximum stresses in the assembly after cooling for large and small voids (30 $\mu\text{m}$ and 12 $\mu\text{m}$ respectively) .....	251

# 1 Introduction

## 1.1 Background

Continuously increasing power densities of electronic products lead to higher application temperatures. Whereas electronic products have traditionally been limited to temperatures of 175 °C and lower, the introduction of wide bandgap semiconductors, such as Silicon Carbide (SiC) and Gallium Nitride (GaN), extends the range of potential application temperatures to 500 °C and more [1]. The bandgap of Si is considerably smaller than that of SiC and GaN, see Table 1-1. As the semiconductor temperature increases, more electrons overcome the bandgap between the valence band and the conduction gap. This increases the intrinsic carrier concentration in the conduction gap, see Figure 1-1. When enough carriers are generated, the conductivity of semiconductor increases and it changes from the insulating to the conducting state. A normally-off transistor under this condition is in the on-state, even without a gate bias.

**Table 1-1: Physical Properties of Si, SiC, and GaN [2]**

	Si	6H-SiC	3H-SiC	GaN
Bandgap (eV)	1.12	2.9	3.2	3.39
Crit. elec. field (Vcm <sup>-1</sup> )	3x10 <sup>5</sup>	2.5x10 <sup>6</sup>	3x10 <sup>6</sup>	5x10 <sup>6</sup>
Thermal cond. (Wcm <sup>-1</sup> K <sup>-1</sup> )	1.3	5	5	1.3

If a high voltage bias is applied between drain/collector and source/emitter, the semiconductor switch can become conductive, even when the gate bias is set to the off-state. The voltage when this occurs is referred to as the breakdown voltage  $V_{br}$ . Figure 1-2

shows the temperature-dependence of  $V_{br}$  for several semiconductor materials. Theoretically  $V_{br}$  for SiC and GaN is many orders of magnitude higher compared to that of Si. Yet due to the high maturity of the Si manufacturing process, SiC and especially GaN devices are still further away from their theoretical limit than Si devices. Nevertheless, SiC and GaN devices are already capable of operating at higher junction temperatures and higher voltages than their Si counterparts.

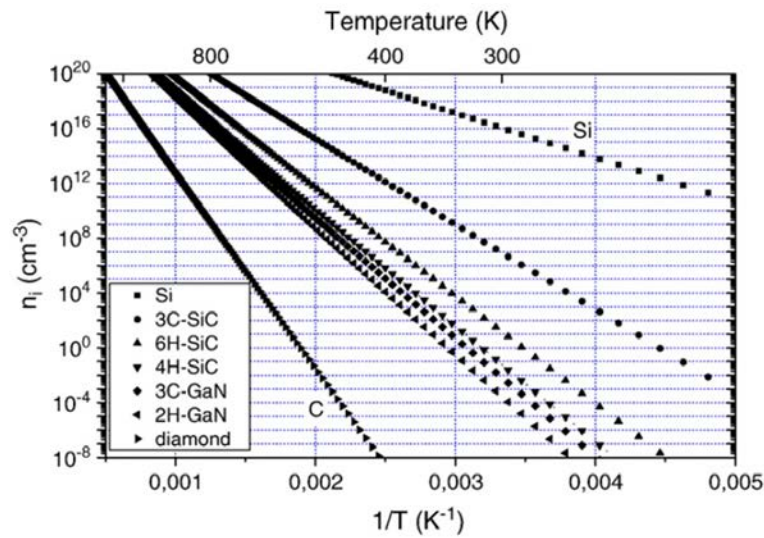


Figure 1-1: Intrinsic carrier concentration  $n_i$  for various semiconductors [3]

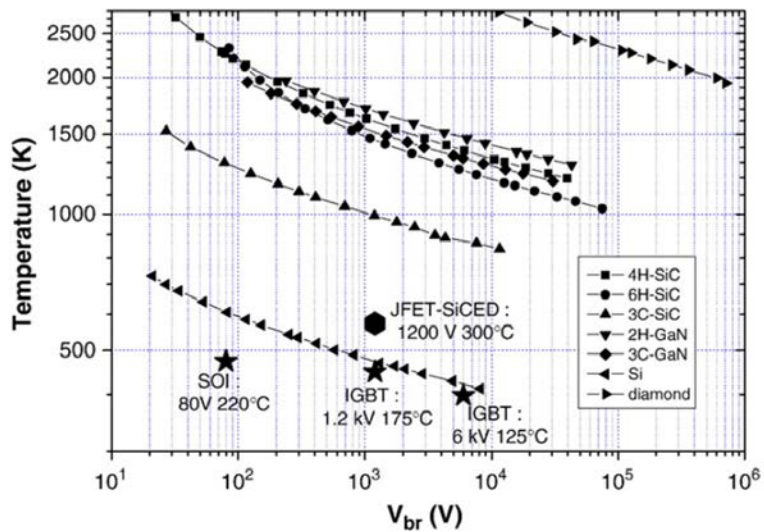
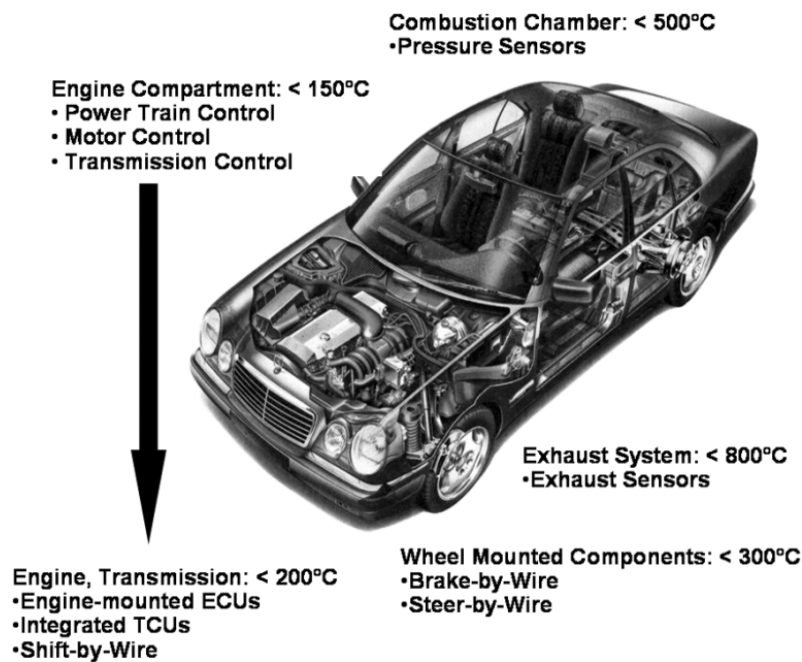


Figure 1-2: Temperature-dependence of the theoretical breakdown voltage  $V_{br}$  for various semiconductors [3]

SiC rectifiers and MOSFETs are commercially available and are now offered by multiple manufacturers including market leaders like Cree [4] and Infineon [5]. A variety of packaged devices and bare dies is available and SiC diodes have been included in commercial power modules. Furthermore, GaN devices have recently become available. EPC [6] provides GaN FETs with  $V_{DS}$  up to 450V. microGAN [7] offers normally-on and normally-off GaN FETs with  $V_{DS}$  up to 600V and GaN diodes for operation up to 600V. The high temperature capability of wide-bandgap semiconductor electronic systems has been demonstrated successfully. An 18kW SiC power module designed for HEVs for application temperatures up to 200°C has been developed [8]. A three-phase AC-DC-AC SiC converter for temperatures up to 250°C has been designed [9]. A 100V, 25W DC-DC converter based on 1.2kV/2.5A SiC JFETs and 600V/4A SiC SBDs was successfully tested at temperatures up to 450 °C [10]. Continued miniaturization of power electronic systems in conjunction with increasing voltage and current levels have led to growing power densities of power devices and power modules. The associated high heat densities lead to increased junction temperatures and system intrinsic thermal stresses. Novel packaging and interconnect technologies will be required for reliable operation of electronic systems under such load conditions.

Simultaneously, power electronics systems are increasingly operated in harsh environments, such as automotive, deep well drilling, military, or aerospace. These applications induce considerable extrinsic stresses on the power electronic devices and packages. Examples of high temperature automotive applications are inverters and power modules in electric and hybrid electric vehicles, electronic control units (ECUs) as well as sensor systems and electronics in the engine compartment, the braking systems, or the

exhaust system with temperatures up to 800 °C, compare Figure 1-3. The integration of sensor systems and data acquisition electronics in oil well drilling equipment and the increased use of electronic components in down-hole gas compressors are driving the need for high-temperature interconnect materials for the oil and gas industry. Those compressors are operated at temperatures up to 225 °C. The temperature requirements for geothermal wells typically lie in the range of up to 250 °C, but can reach 600 °C [11]. The exploration of Venus and Jupiter, with surface temperatures of up to 480°C and 400 °C respectively are examples of the high-temperature requirements that must be met by electronic systems in space exploration applications.



**Figure 1-3: Automotive high-temperature environments [12]**

The packaging and interconnect technologies for high temperature applications remain crucial issues for the reliable design of WBG power electronic systems. Power electronic packaging technologies have been optimized for Si devices and their relatively low application temperatures. New packaging concepts are required to reliably operate WBG devices at elevated temperature levels. Die attach failure is a major challenge in the design

of reliable power electronic systems [13]. In power electronics, die attach serves three functions: Mechanically affixing the chip to the substrate; providing an interface with low thermal resistance for efficient heat transfer from chip to heat spreader, and, specific to power electronic applications, providing an interface with low electrical resistance and high current-carrying capability. Figure 1-4 depicts a typical power module structure with solder for the attachment of the die to a Direct Bond Copper (DBC) substrate, which itself is then attached to a copper base that acts as the heat spreader. Considerable thermo-mechanical stresses develop within these attach layers during operation due to differences in the coefficient of thermal expansion (CTE) between the die and the substrate as well as between the substrate and the heat spreader.

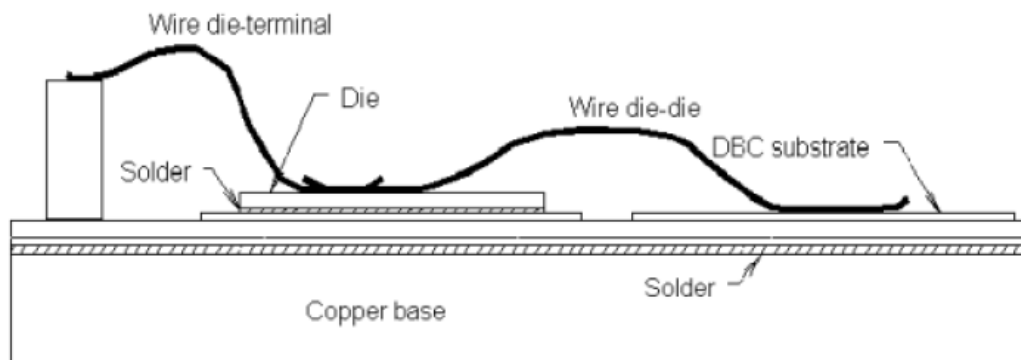


**Figure 1-4: Typical power module structure [13]**

Harsh environments coupled with growing power densities lead to higher joint temperatures, which softens the attach material, making it more susceptible to fatigue. This reduces the system time-to-failure, or, in extreme cases, can cause melting of the attach material. Furthermore, the thermo-mechanical stresses grow with increasing temperatures. The operation of WBG devices at elevated temperature levels requires the development of new attach materials and power module packaging solutions. In the following, challenges with conventional die attach technologies as well as potential high temperature alternatives are presented.

## 1.2 High Temperature Interconnect Technologies for Electronic Systems

Conventional attach solutions in power electronics were developed for application temperatures of 100°C - 150°C. The dominant die attach technologies for power electronics are solders with melting temperatures ( $T_m$ ) in the range of 200°C - 300°C, and silver filled adhesives. Several high melting point solder alloys exist, but only a limited number have seen actual market infiltration or have been assessed in literature. An overview of several high  $T_m$  solder alloys as well as sintered silver and joints is provided in Table 1-2.

Sn-Sb alloys have relatively low  $T_m$ , show poor workability because of bad wetting behavior, and have high voiding levels. Although Sb is less toxic than lead, the toxicity of Sn-Sb alloys is of concern. The applicability of bismuth and Bi-Ag alloys for systems with high power dissipation is limited by their low thermal conductivity and to systems with low power levels because of their low electrical conductivity [14]. They furthermore show limited ductility, have poor bonding strength, and are susceptible to brittle fracture [11]. The elongation to fracture can be improved by increasing the Ag-content at considerably increased material costs [15]. Common to all Bi-alloys is their limited processability because of bad wetting capabilities [14].

High-lead alloys have  $T_m$  close to 300°C. Typical high-lead alloys include Pb10Sn, Pb5Sn, Pb2Sn, or Pb1.5Ag1Sn with liquidus temperatures in the range of 301 - 322 °C [16]. They have been applied for many years and a considerable knowledge base on their processing exists, which rendered them prevalent high temperature solders. Yet, as with Sn37Pb solders, toxicity and regulatory restrictions have reduced their availability and application. They are soft materials and can withstand high levels of deformation, but show extensive creep at elevated temperatures.

Gold-based alloys like Au<sub>20</sub>Sn, Au<sub>12</sub>Ge, and Au<sub>3.2</sub>Si possess high strength and do not necessitate the use of flux during soldering. They require high process temperatures and, due to the high raw material prices, can not be used economically in consumer products and are primarily applied in aerospace and military products. Au-Sn has excellent fatigue and creep resistance [14]. The high strength and stiffness of Au-Sn solders can induce thermo-mechanical stresses in the die which can lead to die cracking. Au-Ge solders are hard to manufacture because Ge cannot be electrodeposited, which is the common method for the production of solder alloys [17].

Zn-Al alloys are hard and brittle and possess a very high  $T_m$  of 381 °C.  $T_m$  can be reduced to the range of 300-340 °C by addition of alloying elements like Cu, Mg, or Ge [16]. The applicability of Zn-based alloys as high temperature solders is limited by their corrosiveness and poor process capability [14] [17].

As solders must be processed significantly above their  $T_m$  (20°C - 50°C), high process temperatures are necessary for good joint quality. Elevated temperatures during processing can introduce high stresses on other package components, significantly reducing their remaining life time. Metal-particle filled adhesives and sintering technologies can be used to form joints at temperatures below the intended application temperature. Most silver-filled adhesives are not designed for extended high temperature operation and quickly degrade chemically under such conditions. They are relatively expensive compared to non-gold solder alloys due to their high silver content.

**Table 1-2: Melting temperatures and characteristics of select solders and sintered silver**

<b>Material</b>	<b>T<sub>m</sub></b>	<b>Issues</b>
SnSb Alloys	235°C- 240°C	- Low T <sub>m</sub> - Poor wetting - High voiding - Toxic
Bi-Ag Alloys	262°C	- Small elongation, brittle - Limited wetting capabilities - Low thermal conductivity
Au20Sn	280°C	- High process temperature - High cost
Pb5.0Sn2.5Ag	296°C	- High process temperature - Regulatory restrictions
Au12Ge	361°C	- High cost
Au3.2Si	363°C	- High process temperature
Zn6Al	381°C	- Complicated processing
Zn5.8Ge	390°C	- Corrosive - Poor wettability - High process temperature
Sintered Silver	962°C	- Relatively high cost - Considerable pressure required for solid state sintering - Toxicity of nano-Ag particles unknown - Requires noble metallization for ideal adhesion

Joining of metallized substrate surfaces and power devices by a pressure and temperature assisted solid-solid diffusion process of silver micro- and nano-particles has been proposed as a high temperature die attach solution. This technology is commonly referred to silver sintering. The reduction of surface energy by particle coalescence is the driving force behind the process and pressure and temperature act as accelerators. Initially, micrometer-sized particles were used, but substantial pressures of 40 MPa were required for successful sintering of high-density joints [18]. Later, nanometer-sized silver particles with higher surface energy were used to form similar joints at pressures in the low MPa range [19]. The sintering process can be performed at relatively low process temperatures but forms joints with a high melting temperature (< 300°C and 962°C respectively). Though the properties

of bulk silver cannot be reached, the joints show excellent thermal and electrical conductivities and their life time under thermal and power cycling conditions can significantly exceed those of conventional solders. Silver sintering has considerable associated costs due to its complex processing with a synchronous application of pressure and temperature and silver as the joint materials. The porous structure of sintered silver joints leads to significant steady state creep at elevated temperatures, which may lead to reduced fatigue life under high thermo-mechanical loads.

An alternative high-temperature attach technology is Transient Liquid Phase Sintering (TLPS). It is a liquid-assisted sintering process during which a low melting temperature constituent melts, surrounds, and diffuses with a high melting temperature constituent. Intermetallic compounds (IMCs) with a melting temperature in between those of the constituents are formed. The low temperature phase is consumed. Upon completion, the melting temperature of the joint has shifted towards the higher IMC temperature. Joints can be formed at low temperatures, but be used at high temperature levels. An in-depth description and analysis of the process can be found in the section 2.1. TLPS interconnects possess high strength at elevated temperatures, the constituents are lead-free and not subject to regulation, metallizations commonly used in electronic products can be joined, and low-cost alternatives can be utilized.

A paste-based TLPS process is developed in this work. The developed TLPS sinter pastes can be used as a substitute for high temperature solders, sintered silver, and silver-filled adhesives and epoxies conventionally used in these applications. Chapter 2 describes the fundamentals of the TLPS process and highlights differences between layer-based approaches and the paste-based TLPS approach pursued in this work. A literature review

of TLPS in electronic applications is provided. Objectives and Goals are provided in Chapter 3. Chapter 4 explains the paste manufacturing process, contrasts different paste application procedures, and compares their advantages and disadvantages. Chapter 5 details the high temperature stability and microstructural evolution behavior of joints formed from TLPS sinter pastes. Changes in voiding behavior, phase composition, and grain structure are discussed. The properties of paste-based TLPS joints are assessed in Chapter 6. Paste-based TLPS joints possess highly heterogeneous microstructures, and a simulations method was developed that has the capability to capture this complexity and include it in simulation models. The simulation method is introduced and the constitutive and thermal properties are assessed. Shear test experiments with Iosipescu samples are performed to experimentally determine the constitutive properties of these joints. Transient thermal analyses are performed to experimentally determine the thermal properties of paste-based TLPS interconnects. TLPS-specific failure mechanisms are predicted, verified, and mitigation methods are developed.

## 2 Fundamentals

### 2.1 Transient Liquid Phase Sintering (TLPS)

Sintering is a process during which particles are bonded into a coherent, predominately solid structure, without melting of all or any of the system constituents via mass transport and the formation of interparticle bonds formed by atomic motion at the sintering temperature [20] [21]. When heated to approximately half the absolute melting temperature, packed particle powders will bond together. Application of pressure facilitates the bonding process and body compaction. The bonding leads to structures and bodies with improved strength. The driving force behind sintering is the reduction of system energy (e.g. reduction of surface tension by particle agglomeration and surface area minimization). Figure 2-1 shows the taxonomy of sintering processes. This work focuses on Transient Liquid Phase Sintering (TLPS). It involves a transient liquid phase that solidifies isothermally by diffusional homogenization [21]. The liquid phase coexists between solid particles and facilitates their bonding. The liquid has a high solubility in the solid and, as the sintering process completes, is consumed and disappears. If solid solution of liquid in the solid is the primary mechanism driving liquid phase consumption, the melting point of the body is that of the alloyed solid. If a reaction and formation of new intermetallic compounds occurs between the liquid and solid phases during sintering, the driving force behind the consumption of the liquid phase is the formation of these intermetallic compounds. This is the case for the TLPS material systems assessed in this work (e.g. the Cu-Sn, Ni-Sn, and Cu-Ni-Sn systems). The melting point of these systems is that of the intermetallics connecting the alloyed solid phase particles. Prerequisites for successful

TLPS are mutual intersolubility (solid solution) or reactivity (IMC formation) between the components and wettability of the solid phase by the liquid phase.

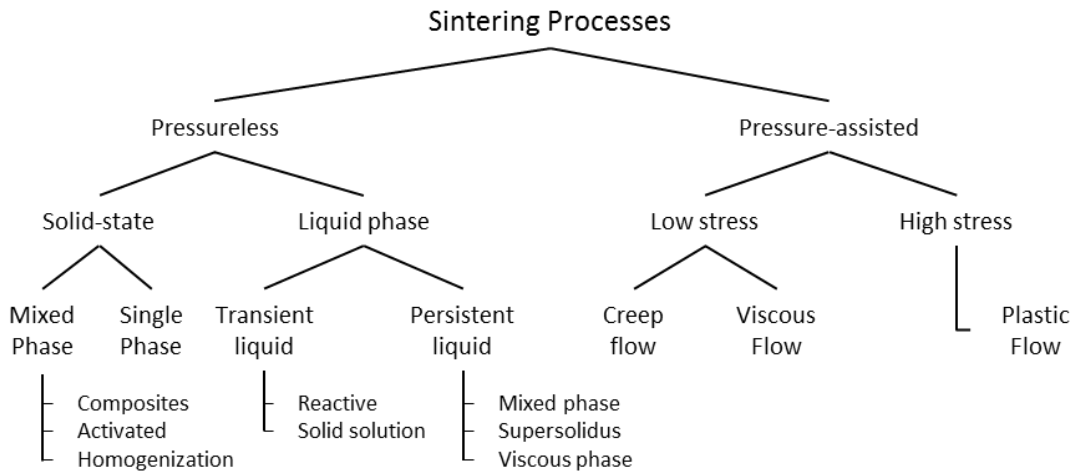


**Figure 2-1: Taxonomy of sintering processes [20]**

### 2.1.1 General Bonding Process

Important process steps during TLPS are: 1) swelling by interdiffusion prior to melt formation (Kirkendall porosity), 2) melt formation, 3) spreading of the melt and generation of pores at prior solid particle sites, 4) melt penetration along solid-solid contact, 5) diffusional homogenization, 6) loss of melt, and 7) formation of a rigid solid structure [21]. In the following, these steps are analyzed for the paste-based TLPS binary material systems assessed in this work.

#### 2.1.1.1 *Kirkendall Porosity - Swelling by interdiffusion without melt formation*

When two metals, *A* and *B*, with mutual solubility are in contact, diffusion of atoms of *A* into *B* and of atoms of *B* into *A* occurs. The associated mutual diffusion rates can be highly dissimilar. As a result, the flux of material in one direction can be highly dissimilar to that in the opposite direction. The first results on this effect were reported by Kirkendall [22] [23] when he found differences in the interdiffusion of Cu and  $\alpha$ -brass. The interface of the

material couple was marked with molybdenum wires. After annealing, the marker wires had shifted relative to the ends of the diffusion couple. This is known as the Kirkendall effect. If the fluxes in opposite directions are dissimilar, a net flux exists, which has to be identical to a flux of vacancies in the opposite direction [24]. As a result vacancies are created in the material with the higher outgoing flux and destroyed in the material with the higher incoming flux. The side of the diffusion couple where vacancies are created experiences a loss of mass, the other side will gain mass. This puts the diffusion zone in a state of stress, with the side that lost mass under tension, and the side that gained mass under compression. In Kirkendall's experiments this state of stress was the reason for the movement of the markers towards the brass side out of which more Zn atoms had diffused into Cu than Cu atoms had diffused into Zn.

The flow of vacancies and their accumulation in combination with the system under tensile stress can lead to the formation of voids over time [24]. These voids are referred to as Kirkendall voids. Associated with the growth of voids is a relaxation of the tensile stresses by straining and a volume growth. This can lead to swelling of the bodies during the initial steps of TLPS. The extent of Kirkendall void formation depends on the TLPS material system and, because diffusion is the underlying mechanism, on the time and temperature. Because of the widespread application of Sn-based solders and Cu and Ni as substrate metallization, extensive research has been performed for the material systems assessed in this study (Cu-Sn, Ni-Sn, and Cu-Ni-Sn). Labie et al. have investigated the Kirkendall void formation of diffusion couples of Sn on thin flip-chip scale Cu and Ni metallizations [25]. The metal stacks were reflowed for 40s at 260 °C and aged at 100, 125, 150, and 175 °C for 100, 500, and 1000h. No Kirkendall voids were found after reflow, but voids started to

form after extended aging durations. For the Cu-Sn system, the voids form at the Cu-to-Cu<sub>3</sub>Sn interface. For the Ni-Sn system, microcracks start forming within the Ni<sub>3</sub>Sn<sub>4</sub> IMC after aging. Similarly Tang et al. have found that only limited amounts of Kirkendall voids form after aging of thin layer Cu-Sn diffusion couples for times lower than 30 minutes and temperatures up to 200 °C [26]. Kumar et al. on the other hand found that Kirkendall voids only formed in Cu-Sn diffusion couples for 99.9 wt.% Cu substrates after aging at 200 °C for 10 days, but not for high-purity 99.999 wt.% Cu substrates. This was also confirmed by Yang et al., who did not find Kirkendall voids after reflow at 260 °C and subsequent aging of Sn on a high-purity Cu substrate (99.99%) [27]. In contrast, they found the formation of Kirkendall voids after aging of a structure with electroplated Cu between the high-purity Cu substrate and the Sn.

Common to all work on Kirkendall voiding for the above systems is that these voids only appear for extended periods of time (> 1h) at elevated temperatures (> 125 °C). In this work, the heating rates during processing are high, compare section 4.3. As a result, melting occurs is so fast that the solid Sn-powders and Ni- or Cu-powders are in contact only for a brief period of time (< 10 minutes between 100 °C and 250 °C). As a result, no significant formation of Kirkendall voids will occur during the heating stage of the TLPS process, and the swelling by interdiffusion prior to melt formation will be minimal.

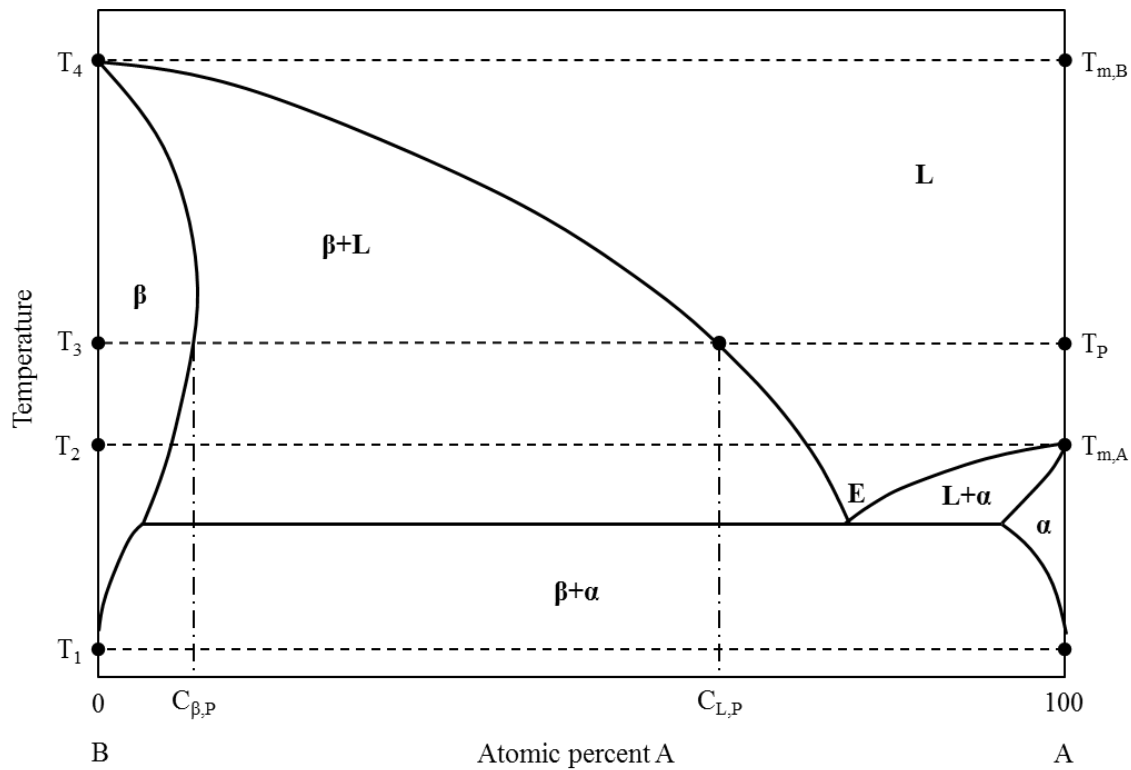
On the other hand Kirkendall voids might be formed during the high-temperature dwell period during processing or a subsequent aging process. A study assessing the microstructural evolution including the assessment of Kirkendall void formation due to high temperature aging will be performed in Chapter 5.

### 2.1.1.2 Melt formation

A good understanding of the melting behavior of binary systems is essential to understanding of the TLPS process as a whole. In the following, the melting of mutually soluble systems will be discussed, initially, for fully soluble binary systems, and subsequently for eutectic binary systems. This is a prerequisite to the discussion of concentration profile analyses and phase formation in later sections.

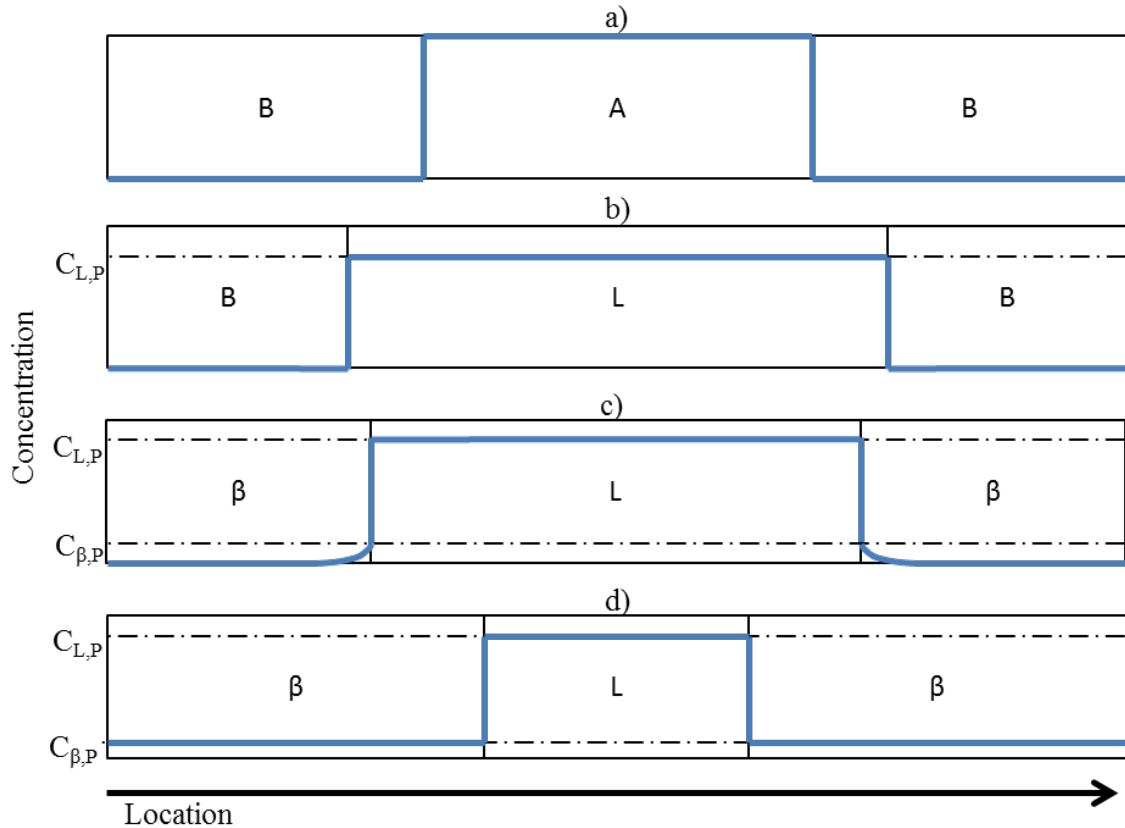
Let  $A$  be a constituent with a low melting temperature  $T_{m,A}$ , and let  $B$  be a constituent with a high melting temperature  $T_{m,B}$ . Let the surfaces of  $A$  and  $B$  furthermore be in close contact with one another to provide ideal wetting and diffusion paths. At this point of the discussion let changes in temperature occur instantaneously.

Figure 2-2 shows the phase diagram of a binary eutectic system. Upon heating to  $T_{m,A}$ ,  $A$  melts and forms a liquid phase  $L$ . Atoms of  $B$  start to dissolve into  $L$ . This process occurs within seconds due to the infinite concentration gradient at the interface between the solid and the liquid and the high diffusivity into the liquid [28]. If the temperature is increased to the process temperature  $T_p$ , additional atoms of  $B$  dissolve into  $L$ . This continues until the concentration of  $B$  in  $L$  reaches  $C_{L,P}$ . The dissolution of solid  $B$  in liquid  $L$  leads to a reduction of the solid volume and an increase in the liquid volume. After  $C_{L,P}$  has been reached, atoms of  $A$  from the liquid  $L$  diffuse into  $B$ , which leads to the formation of  $B$  to the solid solution phase  $\beta$ , and atoms of  $B$  from the liquid  $L$  diffuse into  $A$ , which leads to the formation of the solid solution phase  $\alpha$ . In systems with intermetallic compounds, this process is preceded by the formation of intermetallic compounds, see section 2.1.2.



**Figure 2-2: Phase diagram of a binary eutectic system**

Figure 2-3 shows the concentration profile (blue line) for a binary eutectic material system with a layer of A sandwiched in between two layers of B. Upon heating to  $T_p$ , A melts and transforms into L. The dissolution of atoms of B into L leads to a widening of the liquid layer thickness. Subsequently, a solid solution phase  $\beta$  forms as atoms of A from the liquid L diffuse into B. This process requires considerably more time than the dissolution processes during the widening of the liquid zone.



**Figure 2-3: Concentration profiles of  $C_A$  (blue lines) for eutectic binary systems during the melting: a) original arrangement, b) melting and dissolution of atoms of  $B$  in  $L$ , c) diffusion of atoms of  $A$  from  $L$  in  $B$  and transformation to  $\beta$ , and d) final arrangement**

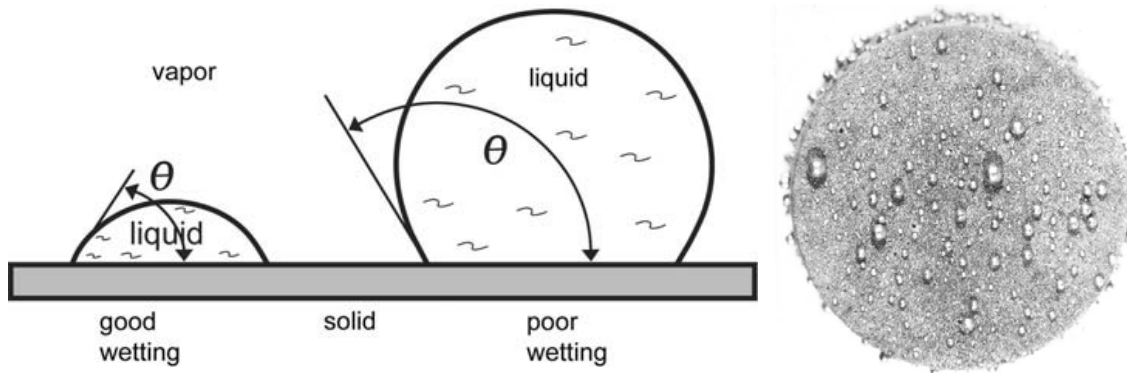
### 2.1.1.3 Spreading of the melt and generation of pores at prior solid particle sites

When using particle mixes to form TLPS joints, upon melting of the low melting temperature constituent  $A$ , the microstructure consists of three phases: solid particles of constituent  $B$ , a liquid phase where particles of  $A$  melted, and a third phase that consists of vapor and flux residue in the case of flux-based pastes. The latter phase is from hereon referred to simply as vapor phase. The liquid phase starts spreading on the solid particle surfaces. Three interfaces are now present in the body: a solid-vapor (SV) interface, a solid-liquid (SL) interface, and a liquid-vapor (LV) interface. The degree of spreading depends

on the contact angle  $\theta$  [29]. The relationship between  $\theta$  and the interfacial energies  $\gamma_{SV}$ ,  $\gamma_{SL}$ , and  $\gamma_{LV}$  is given by:

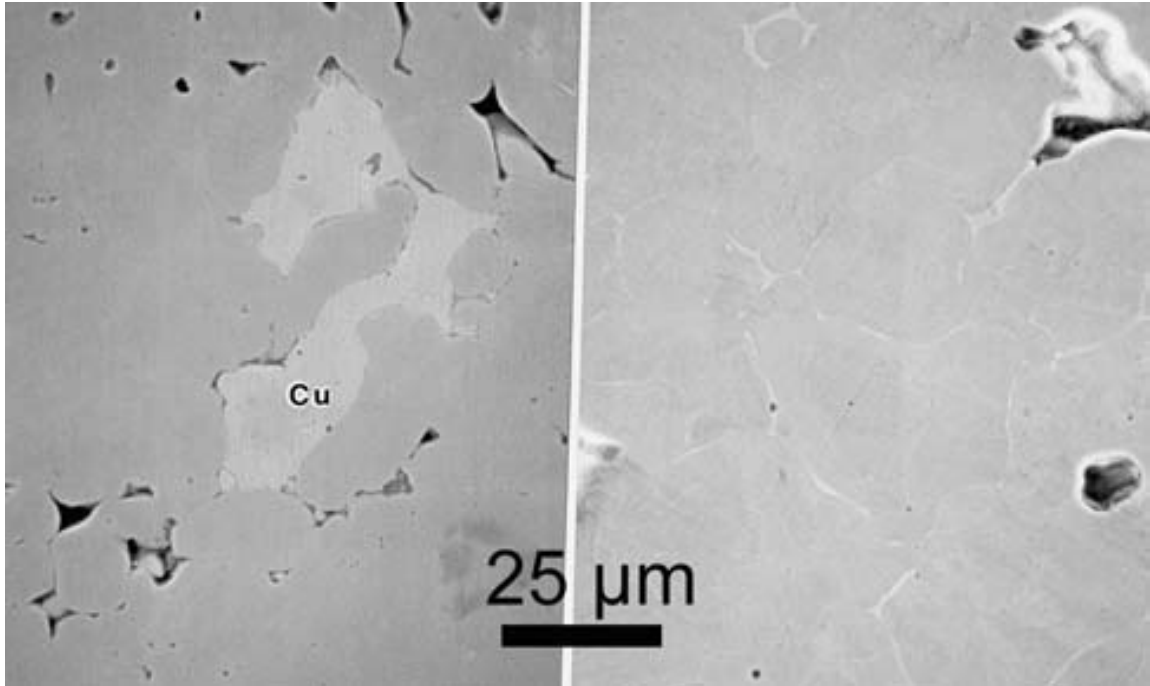
$$\gamma_{SV} = \gamma_{SL} + \gamma_{LV} \cos \theta \quad (1)$$

Figure 2-4 (left) illustrates the influence of the contact angle on the wetting of a solid body by a liquid. Smaller contact angles improve the wetting behavior. For large wetting angles, dewetting can occur. Figure 2-4 (right) shows a SEM image of the surface of a LPS sample from which a non-wetting liquid (with high contact angle) has escaped the bulk sample towards the surface.



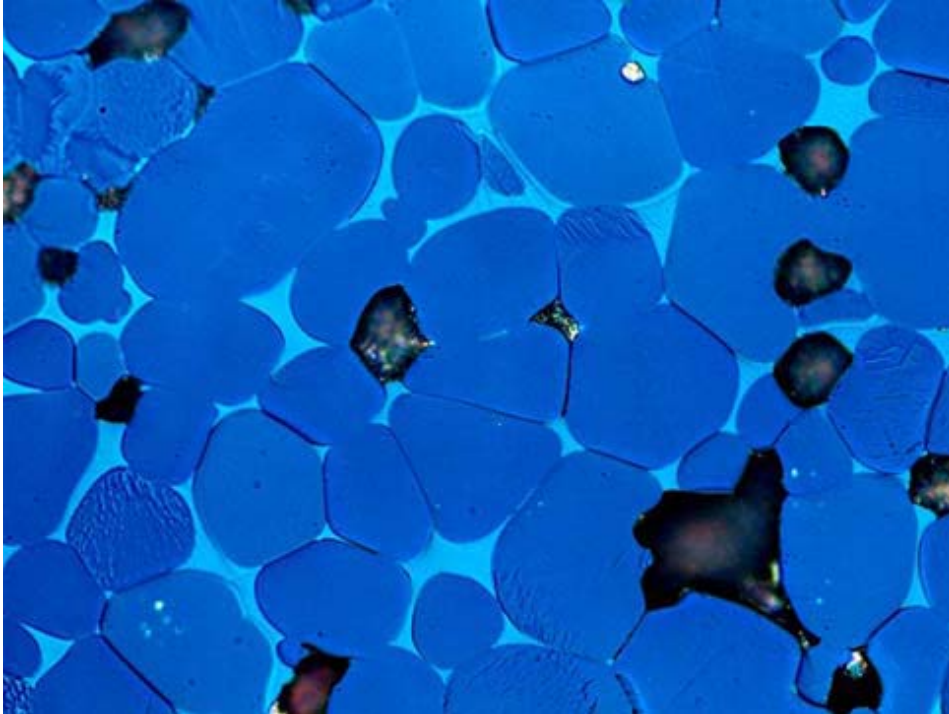
**Figure 2-4: Left: Influence of the contact angle  $\theta$  on the wetting of the solid by the liquid: smaller contact angles facilitate the wetting. Right: Large  $\theta$  leads to liquid retreating from the solid [29]**

Figure 2-5 demonstrates a case of low contact angle wetting behavior for a Fe-Cu LPS system. The left image shows the compacted microstructure after heating to just below the melting temperature of Cu,  $T_{m,Cu}$ . High levels of densification are achieved with small spaces between the grain boundaries. Upon heating above the  $T_{m,Cu}$  the liquid phase forms and infiltrates the grain boundaries. Further compaction is achieved by capillary forces.



**Figure 2-5: Infiltration of a compacted iron powder by 8 wt.% copper [29]. The left image was heated to 1075 °C, the right image to 1110 °C**

Figure 2-6 shows a cross-section of the microstructure of a LPS sample. After melting of the liquid, it is attracted from large pores towards smaller pores by capillary forces. The pore structure is defined by spaces in between the large solid particles. This behavior is typical for high  $T_m$  particles of large size and low  $T_m$  particles of small size. For large low  $T_m$  constituent particles, the location of pores is determined by the low  $T_m$  constituents. Figure 2-7 shows a cross-section of a Cu-10%Sn transient liquid phase sintered body. The size of the former Cu-particles (high  $T_m$  constituent) is small compared to that of the former Sn-particles (low  $T_m$  constituent). The Sn melts, infiltrates the small pores between Cu-particles, and leaves behind voided pore regions.



**Figure 2-6: Collection of pores at prior liquid locations after spreading of the liquid along solid particle boundaries [29]**

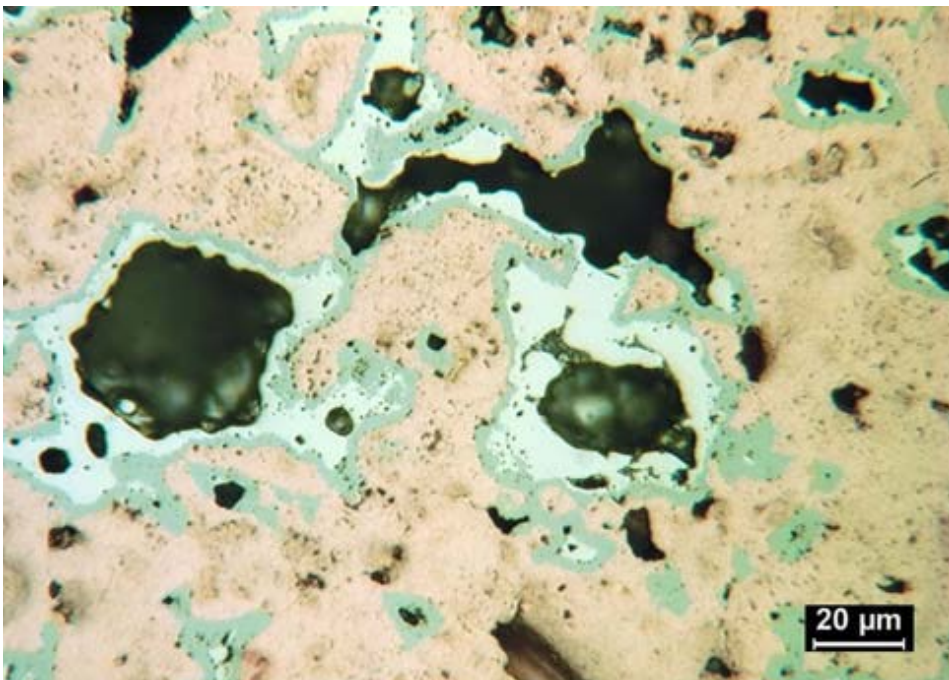


**Figure 2-7: Pore formation with large low  $T_m$  particles in a Cu-10%Sn TLP body. The pores are located at sites where former large Sn particles melted [29]**

### 2.1.2 TLPS in Binary Systems with Intermetallic Compounds

The microstructural development of TLPS joints varies widely with the characteristics of the phase diagram of the material system. The material systems assessed in this work (Cu-Sn, Ni-Sn, and Cu-Ni-Sn) are eutectic systems with multiple intermetallic phases. In this section the microstructural behavior during sintering of binary eutectic systems with one or more intermetallic phases. In sections 2.2, 2.3, and 2.4 the discussion will be extended to the actual material systems, which are eutectic systems with multiple intermetallic phases.

#### 2.1.2.1 Binary Eutectic System with one IMC

Figure 2-8 shows a phase diagram of a binary eutectic system with one intermetallic compound. The intermetallic phase has the stoichiometry  $B_nA_m$  with a concentration  $C_A = m/(m + n)$ . Figure 2-9 shows the concentration profile changes of  $C_A$  during TLPS of this system. The left and right sides of the figure show concentration profiles for a thin layer and a thick layer of  $A$  sandwiched between  $B$  respectively. The melting behavior of this system follows that described in 2.1.1.2 for the binary eutectic system. As the process temperature increases to  $T_p$ ,  $A$  melts and transforms into  $L$ . Atoms of  $B$  diffuse into  $L$  and the liquid region widens, see Figure 2-9 b). This continues until  $C_A$  in  $L$  is  $C_{L,P}$ . At the interface of  $L$  and  $B$  the intermetallic compound  $B_nA_m$  forms, Figure 2-9 c).  $C_A$  of  $B_nA_m$  lies between  $C_A$  in  $B$  or  $L$ . Atoms of  $B$  from the solid and atoms of  $A$  and  $B$  from  $L$  are consumed during the formation of this phase. The consumption of atoms of both types,  $A$  and  $B$ , from  $L$  keeps  $C_A$  in  $L$  constant at  $C_{P,L}$  and ensures conservation of mass. This process continues until either all of  $L$  is consumed, see Figure 2-9 d) (left), or until all of  $B$  is consumed, see Figure 2-9 d) (right). The system is now in a state of equilibrium.

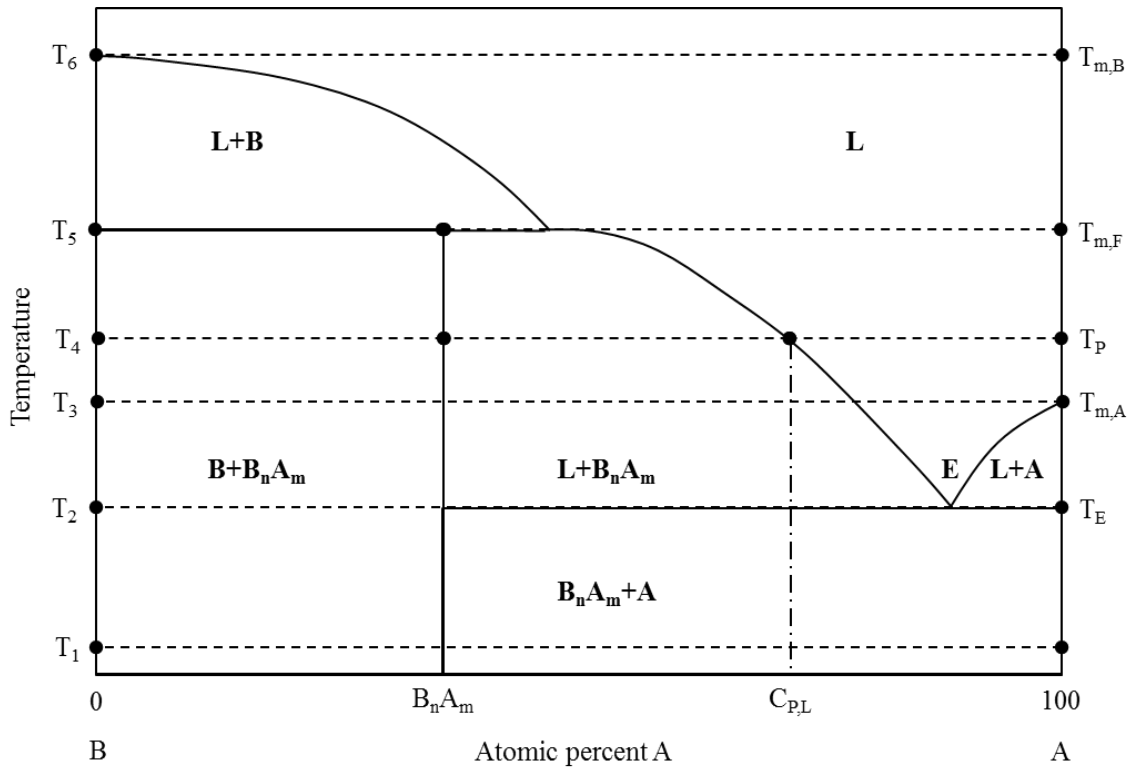


**Figure 2-8: Phase diagram of a binary eutectic system with one intermetallic compound ( $B_n A_m$ ) and no solubility of  $A$  in  $B$  and vice versa**

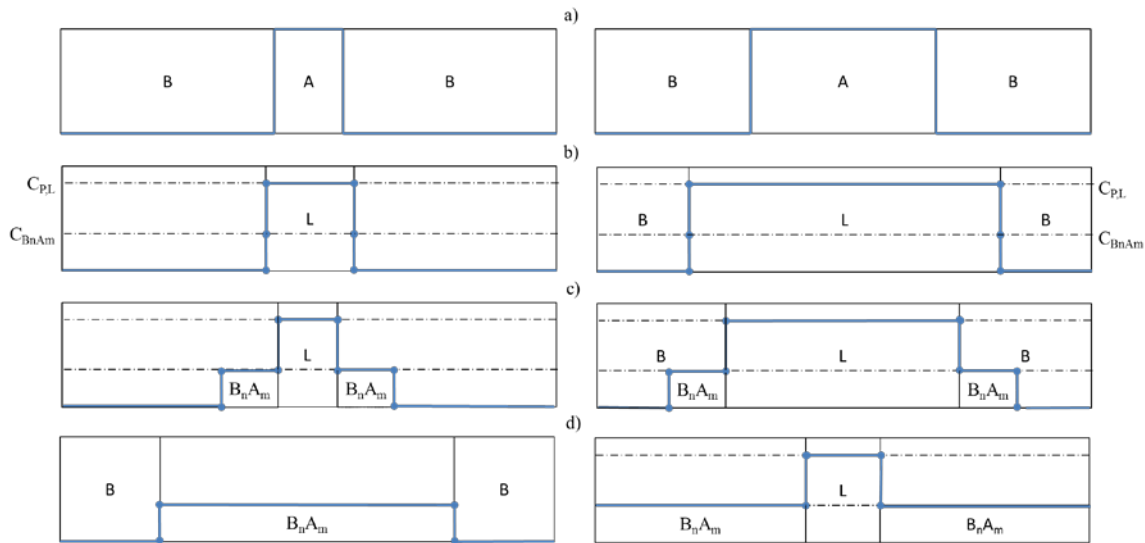


**Figure 2-9: Concentration profiles of  $C_A$  (blue lines) for the system shown in Figure 2-8 during TLPS: a) melting, b) widening of the liquid phase, c) growth of IMCs and consumption of  $L$ , and d) final composition. For thin layers of  $A$ ,  $L$  gets consumed and  $T_m$  shifts (left). For thick layers  $L$  cannot be fully consumed (right)**

$T_m$  for binary eutectic systems with intermetallics does not always shift towards higher temperatures. In case of the stable concentration profile shown in Figure 2-9 d) (left) in

which all of L was consumed, the body consists of three zones: two consisting of B and one of  $B_nA_m$  with  $T_m$ s of  $T_{m,B}$  and  $T_{m,B_nA_m}$  respectively. The latter  $T_{m,B_nA_m}$  is the lowest and the final  $T_m$  ( $T_F$ ) is identical with it as shown in Figure 2-8. In the second case, as shown in Figure 2-9 d) (right), in which all of B was consumed, the body consists of three different zones: two consisting of  $B_nA_m$  and one of L with  $T_m$ s of  $T_{m,B_nA_m}$  and the melting temperature at the eutectic point  $T_E$  respectively. The latter  $T_E$  is the lowest and  $T_F$  in this case is identical with  $T_E$ .  $T_E$  is even lower than  $T_{m,A}$ . In this case, the  $T_m$  has shifted towards lower temperatures. This illustrates the importance of designing a joint system with a high enough percentage of high melting temperature constituents. In order for a temperature shift towards higher temperatures to occur, the ratio of A/B has to be at least lower than  $C_A = m/(m + n)$ .

#### 2.1.2.2 Binary Eutectic System with two IMCs

Figure 2-10 shows a phase diagram of a binary eutectic system with two intermetallic compounds. The intermetallic phase  $B_nA_m$  has a stoichiometry with the concentration  $C_A = m/(m + n)$  and the intermetallic phase  $B_pA_o$  has a stoichiometry with the concentration  $C_A = o/(o + p)$ . In the following,  $B_nA_m$ , and  $B_pA_o$  will be referred to as the primary and secondary IMC according to the chronological order of their formation.

Figure 2-11 shows the concentration profile changes of  $C_A$  during TLPS of this system. The melting behavior of this system follows that described in 2.1.1.2 for the binary eutectic system. As the process temperature is set to  $T_p$ , A melts and transforms into L while atoms of B diffuse into L and the liquid region widens, see Figure 2-11 b). This continues until  $C_A$  in L is  $C_{L,P}$ . At the interface of L and B the primary IMC  $B_nA_m$  forms, Figure 2-11 c). While this IMC grows, atoms of B from the solid and atoms of A and B from L are

consumed. The consumption of atoms of both types,  $A$  and  $B$ , from  $L$  keeps  $C_A$  in  $L$  constant at  $C_{P,L}$  and ensures conservation of mass.

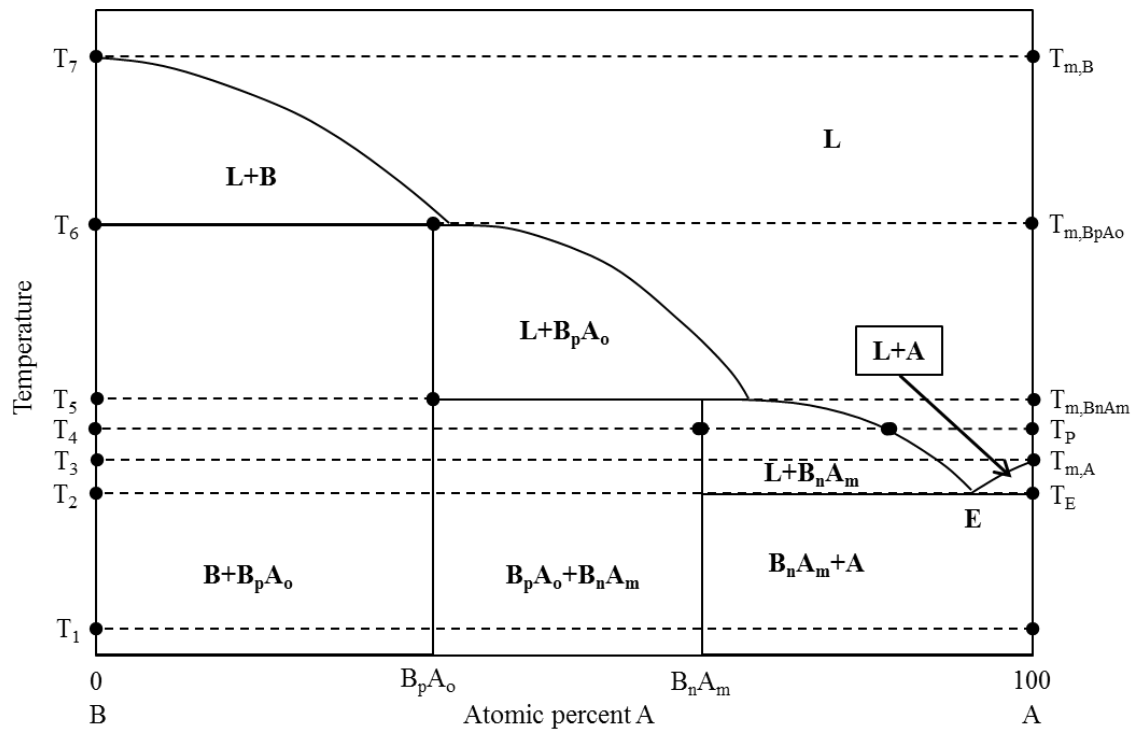


**Figure 2-10: Phase diagram of a binary eutectic system with two intermetallic compounds ( $B_nA_m$  and  $B_pA_o$ ) and no solubility of  $A$  in  $B$  and vice versa**

Parallel to the growth of the  $B_nA_m$  primary IMC layer at the solid-liquid interface, a  $B_pA_o$  secondary IMC layer starts growing at the interface between  $B_nA_m$  and the solid  $B$ , Figure 2-11 d). From this point on the primary IMC layer grows by consumption of atoms of  $A$  and  $B$  from  $L$  and the secondary IMC. The secondary IMC layer grows from the consumption of atoms of  $A$  and  $B$  from the primary IMC and solid  $B$ . The consumption of atoms of both types,  $A$  and  $B$ , from  $L$ ,  $B$ ,  $B_nA_m$ , and  $B_pA_o$  occurs so that  $C_A$  is constant in  $L$ ,  $B_nA_m$ , and  $B_pA_o$  with  $C_{L,P}$ ,  $m/(m+n)$ , and  $o/(o+p)$ , respectively and while conserving mass. The relative growth speed of the primary and secondary IMC is determined by the diffusivities of atoms of  $A$  and  $B$  through  $L$ ,  $B_nA_m$ ,  $B_pA_o$ , and  $B$ .

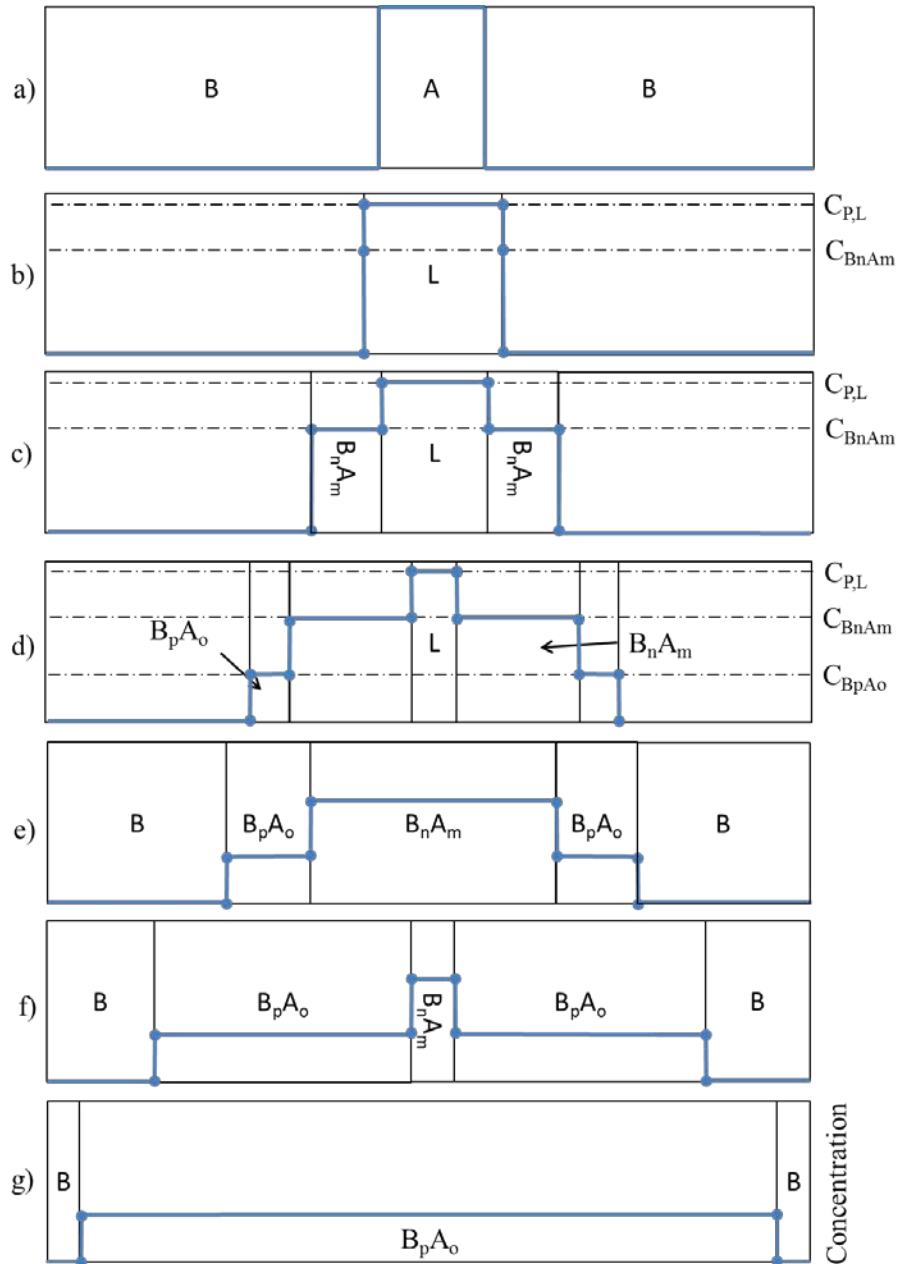


**Figure 2-11: Concentration profiles of  $C_A$  (blue lines) for the system shown in Figure 2-10 during TLPS: a) melting, b) widening of the liquid phase, c) initial growth of primary IMC and consumption of  $L$ , d) initial growth of secondary IMC, e) consumption of  $L$ , f) consumption of primary IMC, g) final microstructure**

The growth of the primary IMC continues until  $L$  is consumed, Figure 2-11 e). From this point on, the thickness of the primary IMC layer reduces as it is consumed by the growth of the secondary IMC layer, Figure 2-11 f). This continues until the entire primary IMC layer is consumed, Figure 2-11 g). The body now consists of two layers of  $B$  with an

interlayer of the secondary IMC,  $B_pA_o$ . The final melting temperature of this structure,  $T_{m,F}$ , is that of the secondary IMC,  $T_{m,BpAo}$ .

A prerequisite for the full transformation of the L to the secondary IMC is the availability of sufficient amounts of  $B$  in the original structure. Table 2-1 shows two potential microstructures which can form due to lack of atoms of  $B$  in the original structure. The structure shown in Table 2-1 (left) has a thick layer of  $A$  before increasing of the temperature. The difference to the process shown in Figure 2-11 is that the growth of the secondary IMC ends because of lack of atoms of  $B$  from  $B$  before the primary IMC is fully consumed. The phase with the lowest  $T_m$  in this case is the primary IMC  $B_nA_m$  with  $T_{m,BnAm}$ .

Another structure with an even thicker layer of low melting temperature constituent  $A$  is shown in Table 2-1 (right). In this case all atoms of type  $B$  are consumed into stable phases (IMCs and  $L$ ) before the liquid phase  $L$  is consumed. In this case, as in the case shown in Figure 2-9 (right), the remelting temperature of the structure after sintering is the solidus temperature of the  $L$  phase,  $T_E$ , which is below the original melting temperature  $T_{m,A}$ .

**Table 2-1:  $C_A$  and  $T_m$  for incomplete transformation of L to secondary IMC because of insufficient B in the original structure**

Before Sintering	B	A	B	B	A	B			
After Sintering	$B_pA_o$	$B_nA_m$		$B_pA_o$	$B_pA_o$	$B_nA_m$	L	$B_nA_m$	$B_pA_o$
$T_m$	$T_{m,BnAm}$				$T_{m,L} = T_E$				

## 2.2 The Cu-Sn TLPS System

Figure 2-12 shows the Cu-Sn phase diagram. The melting temperatures of Sn ( $T_{m,Sn}$ ) and Cu ( $T_{m,Cu}$ ) are 232 °C and 1085 °C respectively. It has a eutectic point at a  $T_{m,E}$  of 227 °C at 5.3 at.% Cu. The solubility of Sn in Cu and vice versa are small (e.g. 3.3at% Sn in solid Cu at 300 °C, which translates into 6.0wt% or 7.6vol.%). Similarly the solubility of Cu in the liquid phase  $L$  at potential processing temperatures is limited (e.g. 5.3at% Cu in  $L$  at 300 °C, which translates into 2.9wt% or 2.2vol.%). The growth of Cu-Sn intermetallics during sintering can occur while Sn is in the liquid state or in the solid state or a combination thereof. In this work, the microstructure of Cu-Sn joints was assessed with as-formed samples after reflow (predominately liquid-solid diffusion) and with samples after reflowing with additional high temperature annealing steps (potentially liquid-solid and solid-solid diffusion).

The IMCs formed during the solid-solid diffusion of Sn and Cu below the  $T_{m,Sn}$  of 232 °C [25] [26] are identical with those formed at temperatures above  $T_{m,Sn}$  but below 340 °C [30] [31] [32] [33]. The primary IMC formed at the interface between Sn and Cu is the  $Cu_6Sn_5$ , or  $\eta$ -phase. The secondary IMC formed at the interface between  $Cu_6Sn_5$  and Cu is the  $Cu_3Sn$ , or  $\epsilon$ -phase. The IMC phase that would grow at the next lowest temperatures is the  $Cu_{41}Sn_{11}$ , or  $\delta$ -phase, which requires temperatures  $>350$  °C to form. Process temperatures above this range are considered too high for most electronic applications and were not in the scope of this work.

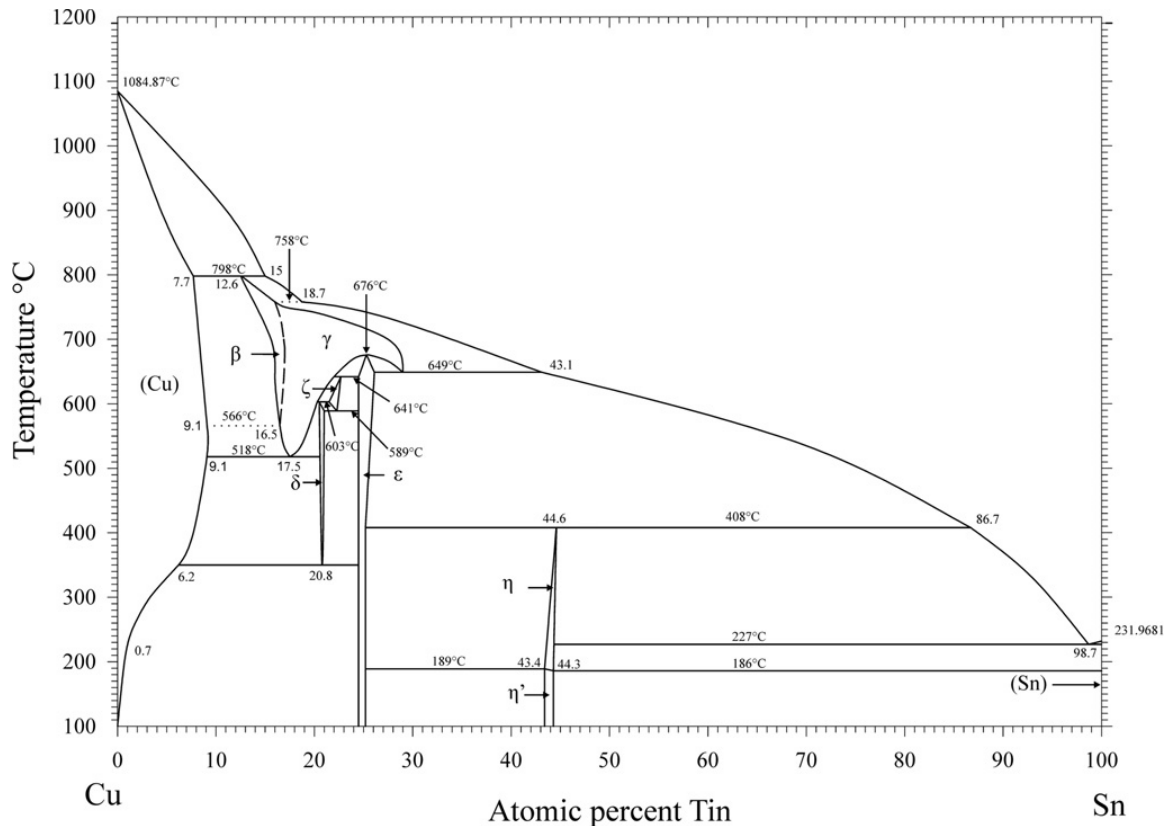


**Figure 2-12: The Cu-Sn phase diagram [34]**

$\text{Cu}_6\text{Sn}_5$  exists in two different structural forms [35]. The first type is the room temperature stable  $\eta'$  phase with monoclinic crystal structure. The other  $\eta$  type phase with hexagonal crystal structure forms at high temperatures. The equilibrium temperature for the  $\eta$ - $\eta'$  transformation is 186 °C. At process temperatures above  $T_{m,\text{Sn}}$  the  $\text{Cu}_6\text{Sn}_5$  IMC grows as  $\eta$ . Upon cooling below this temperature, the phase transformation process occurs. If the temperature is low (e.g. room temperature), this process takes considerable time. Yet, if the temperature is close to but below the transformation temperature, the transformation can occur within minutes [35]. During phase transformation from the  $\eta'$  to the  $\eta$  phase, the density of the intermetallic phase increases, or in other words, the volume reduces by 2.15%. This induces stresses in the IMC and can lead to crack formation during temperature swings above and below the transition temperature [36]. No phase

transformation exists for the  $\epsilon$  phase for temperatures higher than 600 °C. The melting temperatures of the  $\eta$  and  $\epsilon$  phase are 408 °C and 676 °C respectively.

Even though the phases that form during processing of Cu-Sn joints are identical for the entire temperature range up to 340 °C, the microstructure of the  $\eta$  phase formed at the Cu-to-liquid interfaces is different between processing above or below  $T_{m,Sn}$  (232 °C). Hayashi et al. and Kao found that the microstructure of the  $Cu_6Sn_5$  IMCs grown between Cu substrates and a pure Sn bath is characterized by long protrusions into the Sn region [31] [32]. In contrast, the microstructure of  $Cu_6Sn_5$  IMCs grown between Cu substrates and “Sn + Cu” baths (liquid reservoirs of Sn that had been enriched with twice the amount corresponding to the Cu solubility limit at the test temperature) led to a microstructure that is similar to the scallop-edge microstructure of reaction couples of Cu with solid Sn. An explanation for the difference in morphology during dipping of Cu substrates in the pure Sn baths and that of samples dipped into the Cu-saturated Sn baths might be the dissolution of Cu from the substrates onto the pure Sn bath, which would not occur for the Cu-saturated bath. As discussed in 2.1.1.2 the dissolution rate is very fast. The rapid dissolution might lead to a high concentration profile gradients inside the liquid, especially considering that different Cu grain orientations in the substrate might possess different dissolution rates [35]. The  $\eta$  phase nucleates within early seconds of the reaction and IMCs grow rapidly [37]. In contrast, the  $\epsilon$  phase is not formed instantaneously as the process begins. Its growth is homogeneous, which indicates that it is diffusion and reaction rate controlled.

In contrast to the protrusions and the needle-like growth of  $Cu_6Sn_5$  IMCs in the solid-liquid diffusion as described above, the growth of  $Cu_6Sn_5$  IMCs at temperatures below  $T_{m,Sn}$  is characterized by continuous, slightly scallop-shaped growth front development [25] [26]

[38] [39]. The smoother microstructure compared to the liquid-solid IMC growth can be explained by reaction and diffusion kinetics being the limiting factor for solid-solid diffusion. The concentration gradients within the Cu, Sn, Cu<sub>3</sub>Sn, and Cu<sub>6</sub>Sn<sub>5</sub> zones are small, which results in homogeneous diffusion and layer growth.

Limited literature exists on the growth kinetics of diffusion couples of pure tin and pure copper at elevated temperatures. Vianco et al. assessed the growth of copper dipped in liquid Sn at annealing temperatures between 70 °C and 170 °C for durations of up to 400 days, but no growth constants were calculated, and only one dataset above 135 °C was assessed [38] [40]. Bader et al. [30] and Tang et al. [26] studied the formation of Cu-Sn IMCs above  $T_{m,Sn}$ , but their Sn layers were limited to thicknesses smaller than 2.6 μm and 1 μm respectively, far below the diffusion lengths encountered in this work. Labie et al. limited the thickness of their Cu layer to less than 5 μm, which leads to similar issues related to the growth kinetic models required here [25]. Onishi et al. determined the growth constants of Cu<sub>6</sub>Sn<sub>5</sub> and Cu<sub>3</sub>Sn for temperatures range between 190 °C and 220 °C and between 190 °C and 404 °C respectively [41]. They showed that the Cu<sub>3</sub>Sn growth behavior is constant over the entire temperature range for Cu-Sn and Cu/Cu<sub>6</sub>Sn<sub>5</sub> diffusion couples and that only slight differences exist between the growth constants for Cu/Cu<sub>6</sub>Sn<sub>5</sub> and α/Cu<sub>6</sub>Sn<sub>5</sub> diffusion couples. The growth exponent was 0.5 for Cu<sub>6</sub>Sn<sub>5</sub> and Cu<sub>3</sub>Sn, which indicates volume diffusion as the primary diffusion process. Yet there is no consistency between the activation energies they derived, and the growth constants they list. Furthermore, they only display IMC thickness information for one temperature, 220 °C, which renders it impossible to derive the activation energies independently.

Paul et al. studied the diffusion parameters and growth mechanisms of the Cu-Sn system with Cu/Cu<sub>6</sub>Sn<sub>5</sub> and Cu<sub>3</sub>Sn/Sn below and above  $T_{m,Sn}$  respectively [42]. Bulk single-phase Cu<sub>6</sub>Sn<sub>5</sub> and Cu<sub>3</sub>Sn IMC specimens were made by liquid atomization, rapid solidification and hot isostatic pressing. Cu<sub>3</sub>Sn IMCs were grown with Cu/Cu<sub>6</sub>Sn<sub>5</sub> diffusion couples at temperatures between 225 °C and 350 °C. Below that temperature range, bonding of Cu to Cu<sub>6</sub>Sn<sub>5</sub> could not be achieved. Cu<sub>6</sub>Sn<sub>5</sub> IMCs were grown with Cu<sub>3</sub>Sn/Sn diffusion couples at temperatures between 150 °C and 200 °C. Temperature-dependent growth constants were determined. A Cu-Sn diffusion couple was used to verify consistency between this approach and conventional Cu-Sn diffusion couples. Takenaka et al. studied the growth of Cu-Sn IMCs at 160 °C, 180 °C, and 200 °C, and derived growth constants for Cu<sub>6</sub>Sn<sub>5</sub> and Cu<sub>3</sub>Sn for these temperatures [39]. They showed that the growth exponent increases from 0.37 to 0.43 to 0.50 with increasing temperature limits, which indicates that at 160 °C and 180 °C grain boundary diffusion contributes significantly to the IMC growth and that at 200 °C volume diffusion is the rate-controlling process. Gagliano et al. assessed the growth of Cu<sub>6</sub>Sn<sub>5</sub> and Cu<sub>3</sub>Sn layers above  $T_{m,Sn}$  with Cu-Sn diffusion couples at temperatures between 250 °C and 325 °C [43]. They found that the growth exponent for Cu<sub>3</sub>Sn IMCs is 0.5 as in the other studies, but that the growth of Cu<sub>6</sub>Sn<sub>5</sub> IMCs was best described with a growth exponent of 0.30. This can be explained by the scallop structure formed by Cu<sub>6</sub>Sn<sub>5</sub> during growth at the liquid-solid Sn-Cu<sub>6</sub>Sn<sub>5</sub> interface. Copper diffuses along grain boundaries between neighboring scallops. As the Cu<sub>6</sub>Sn<sub>5</sub> layer increases in thickness, the number of fast diffusion paths reduces, decelerating the growth process. Hayashi et al. [31] and Kao [32] studied the differences between the growth of Cu-Sn IMCs for saturated and unsaturated tin baths but also did not include growth parameters or provide combined

growth kinetics for Cu-Sn IMCs for 240 °C and 275 °C or separate analyses for Cu<sub>6</sub>Sn<sub>5</sub> and Cu<sub>3</sub>Sn at 250 °C. Li et al. studied the growth of IMCs during the TLPS of a Cu-Sn-Cu sandwich structure [33].

Considerable variation exists between the growth parameters of different publications. Figure 2-13 shows the growth of the Cu<sub>6</sub>Sn<sub>5</sub> layer thickness over time at an aging temperature of 200 °C with solid-solid diffusion. The results obtained by Paul et al [42] and Onishi et al. [41] are close for the one temperature Onishi et al. reported (200 °C), which indicates consistency. The layer growth found by Takenaka et al. [39] is slower. This could be explained by the lack of adhesion at the beginning of their aging experiments and the considerable voiding that appeared in the Cu<sub>6</sub>Sn<sub>5</sub> layer. The result from Gagliano et al. [43] is extrapolated from their kinetics model obtained from liquid-solid diffusion.

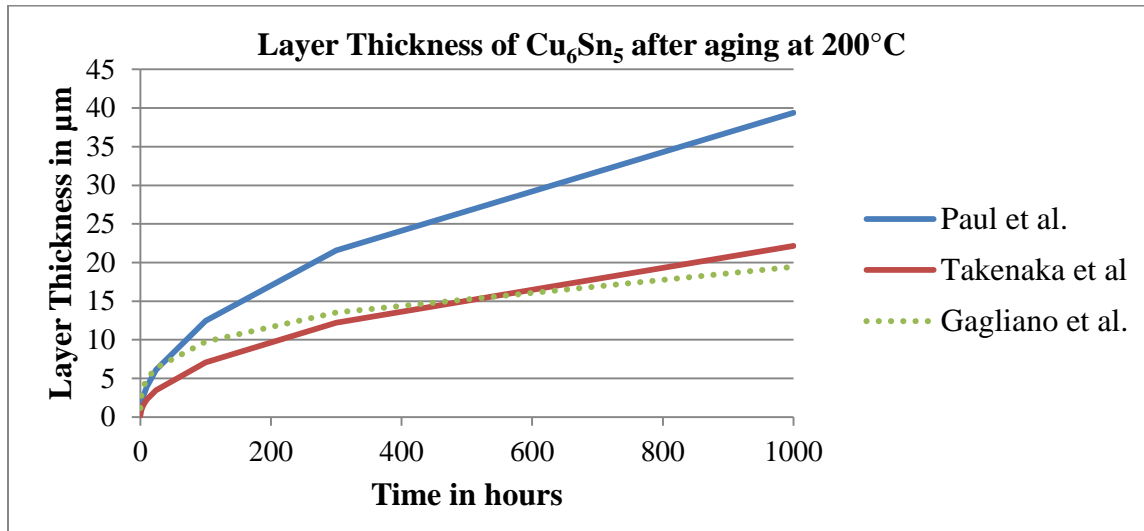


**Figure 2-13: Cu<sub>6</sub>Sn<sub>5</sub> layer thickness vs. time after aging at 200 °C. Dotted data is extrapolated from kinetics models above T<sub>m,Sn</sub>**

Figure 2-14 shows the growth of the Cu<sub>6</sub>Sn<sub>5</sub> layer thickness over time at an aging temperature of 250 °C with liquid-solid diffusion. The results obtained by Hayashi et al. [31] and Li et al. [33] are close, which is true for the entire temperature range assessed by both. The results obtained by Galiano et al. [43] are considerably lower and show only

limited growth. The results from Paul et al. [42] and Onishi et al. [41] are extrapolated from their kinetics model obtained from solid-solid diffusion. When discarding the result by Galiano et al., these extrapolated values are considerably lower than the results obtained by solid-liquid diffusion at this temperature level.

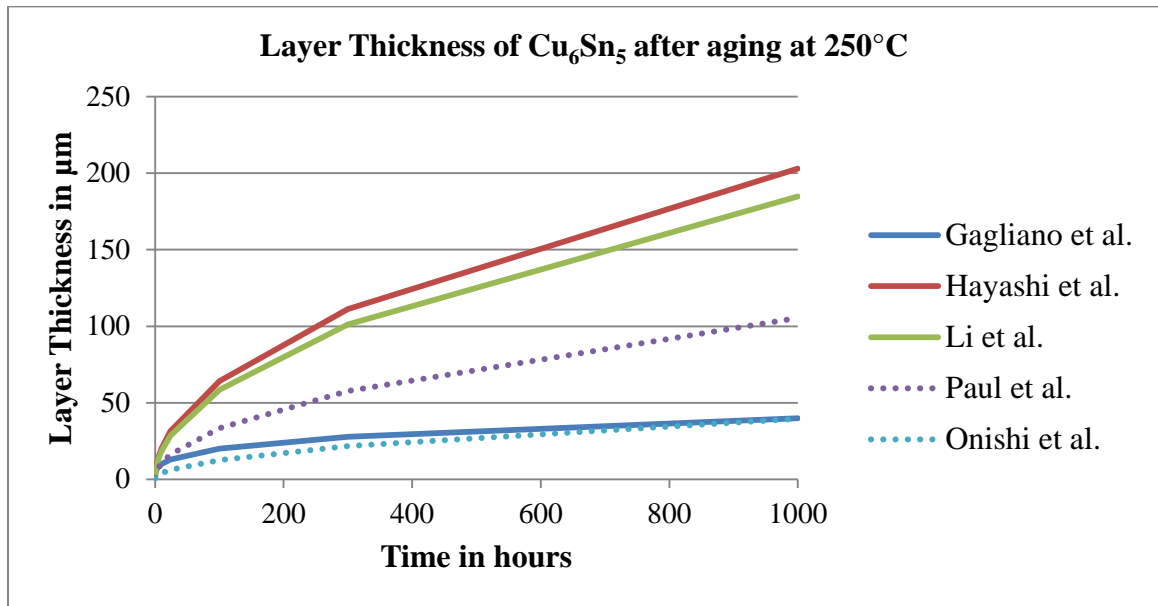
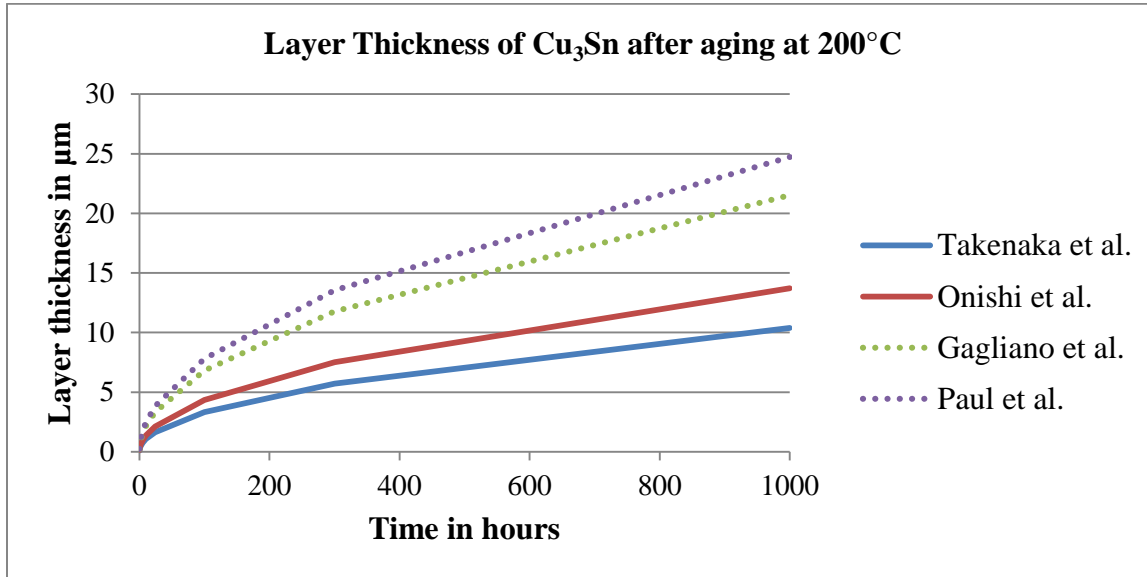


**Figure 2-14:  $\text{Cu}_6\text{Sn}_5$  layer thickness vs. time after aging at 250 °C. Dotted data is extrapolated from kinetics models above  $T_{m,\text{Sn}}$**

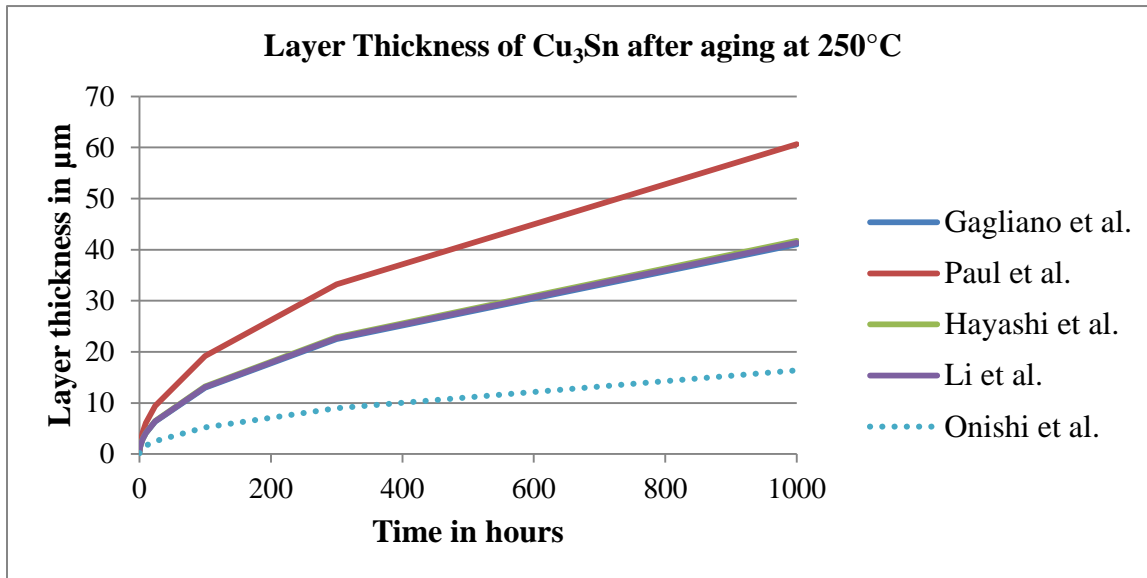
Figure 2-15 shows the growth of the  $\text{Cu}_3\text{Sn}$  layer thickness over time at an aging temperature of 200 °C with solid-solid diffusion. The results obtained by Takenaka et al. [39] and Onishi et al. [41] are close, which is true for the entire temperature range assessed by both. The results from Gagliano et al. [43] and Paul et al. [42] are extrapolated from their kinetics model obtained from liquid-solid diffusion. These extrapolated values are considerably higher than the results obtained by solid-solid diffusion at this temperature level.

Figure 2-16 shows the growth of the  $\text{Cu}_3\text{Sn}$  layer thickness over time at an aging temperature of 250 °C with solid-liquid diffusion. The results obtained by Gagliano et al. [43], Hayashi et al. [31], and Li et al. [33] are almost identical. The results from Paul et al.

[42] are significantly higher. The results from Onishi et al. [41] are extrapolated from their kinetics model obtained from solid-solid diffusion. They are considerably lower than the non-extrapolated results.



**Figure 2-15: Cu<sub>3</sub>Sn layer thickness vs. time after aging at 200 °C. Dotted data is extrapolated from kinetics models above T<sub>m,Sn</sub>**



**Figure 2-16: Cu<sub>3</sub>Sn layer thickness vs. time after aging at 250 °C. Dotted data is extrapolated from kinetics models below T<sub>m,Sn</sub>**

The inconsistencies of these results render a quantitative prediction of microstructural evolution in TLPS sinter joints challenging. Because of the voiding behavior in the Cu<sub>6</sub>Sn<sub>5</sub>

layer by Takenaka et al., their results in the 200 °C model were not considered in this work. The results of Gagliano et al. [43] are so far off from the otherwise consistent results of the 250 °C  $\text{Cu}_6\text{Sn}_5$  growth study that they were not considered in this work. In contrast, their  $\text{Cu}_3\text{Sn}$  layers did not show this voiding behavior. Hayashi et al. [31] do not provide temperature-dependent parameters, but limit them to specific temperatures, which limits the applicability of their results to temperatures of interest in this work up to 325 °C. The same is true for the work by Takenaka et al. [39]. Furthermore, it is evident from the figures above that results obtained from solid-solid diffusion situations should not be used to predict the microstructural evolution behavior under solid-liquid conditions and vice versa. As a consequence, in this work the results of Paul et al. [42] were used to assess the solid-solid growth behavior of  $\text{Cu}_6\text{Sn}_5$  phases, the results of Li et al. [33] were used to assess the solid-liquid growth behavior of  $\text{Cu}_6\text{Sn}_5$  phases, the results of Takenaka et al. [39] were used to assess the solid-solid growth behavior of  $\text{Cu}_3\text{Sn}$  phases, and the results of Gagliano et al. [43], Paul et al. [42], and Li et al. [33] were used to assess the solid-liquid growth behavior of  $\text{Cu}_3\text{Sn}$  phases.

The intermetallic compound formation discussed in 2.1.2 was focused on the general case of a low- $T_m$  and a high- $T_m$  constituent in contact. In the case of Cu-Sn sinter pastes, those constituents are Sn and Cu respectively. Furthermore, in a particle arrangement found after printing of sinter pastes, the processes described above occur in parallel in multiple locations, namely all interfaces of the Sn, L, Cu,  $\eta$  and  $\epsilon$  phases. This is schematically shown in Figure 2-17. In the following discussion it is assumed that before raising the temperature above  $T_{m,\text{Sn}}$ , all Cu particles are ideally surrounded and connected through solid Sn, Figure 2-17 a). Upon heating above  $T_{m,\text{Sn}}$ , Sn melts and transforms to the liquid

phase L, see Figure 2-17 b). Cu from the copper particles is dissolved into L. The volume of the Cu particles reduces. The original particle size before dissolution is indicated by dashed circles. After the dissolution process is completed,  $\eta$ -IMCs start to grow at the L-to-Cu interface, see Figure 2-17 c). As the process continues, the  $\eta$ -IMCs become thicker. Furthermore,  $\epsilon$ -IMCs start to grow at the  $\eta$ -to-Cu interface, see Figure 2-17 d). Both IMCs grow simultaneously, see Figure 2-17 d). This continues until either all of Sn or all of Cu is consumed. In this case, insufficient amounts of Cu were present in the original arrangement. Residual pockets of the low- $T_m$  phase L are present in the joint and limit its high-temperature capability, see Figure 2-17 e).

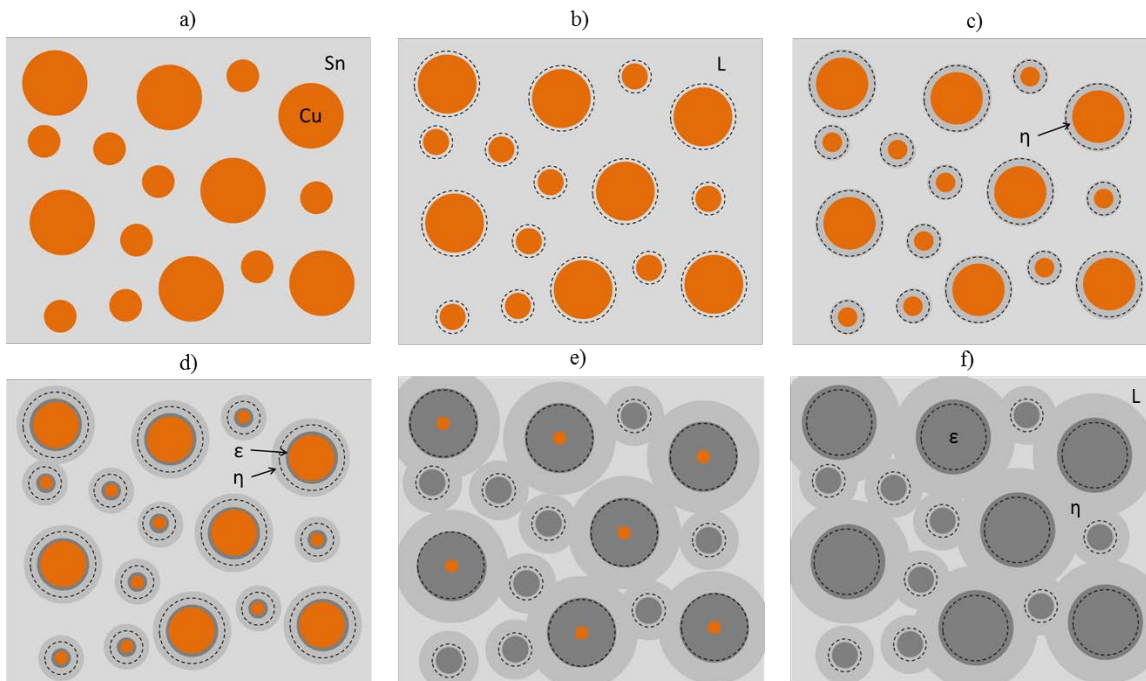


**Figure 2-17: Microstructural evolution during TLPS of a Cu-Sn joint with high Sn-content. Pockets of unconsumed L remain because of the lack of Cu. The joint does not possess high temperature capability**

Figure 2-18 shows a similar particle arrangement as Figure 2-17. In this case more Cu particles are present in the sinter paste mix. The process steps are identical: Melting of Sn, formation of L, and dissolution of Cu (Figure 2-18 a-b), followed by formation and growth

of  $\eta$  and  $\epsilon$  IMCs (Figure 2-18 c-e) until full consumption of Cu (Figure 2-18 f). Because of the higher Cu-concentration in the original arrangement, more Sn is transformed to IMCs before the process reaches its steady-state condition. As a consequence, the final joint microstructure in this case is characterized by  $\eta$  IMCs linking  $\epsilon$  IMCs and few isolated pockets of L. In this case the melting temperature of the joint is equal to that of the  $\eta$  IMCs:  $T_{m,Cu6Sn5}$ . Small pockets of L do not influence the  $T_m$  of the joint, but can lead to reduced strength at temperatures above  $T_{m,L}$ , which can be detrimental to joint integrity. Even though the joint does not melt as a whole, its structural integrity is impaired.

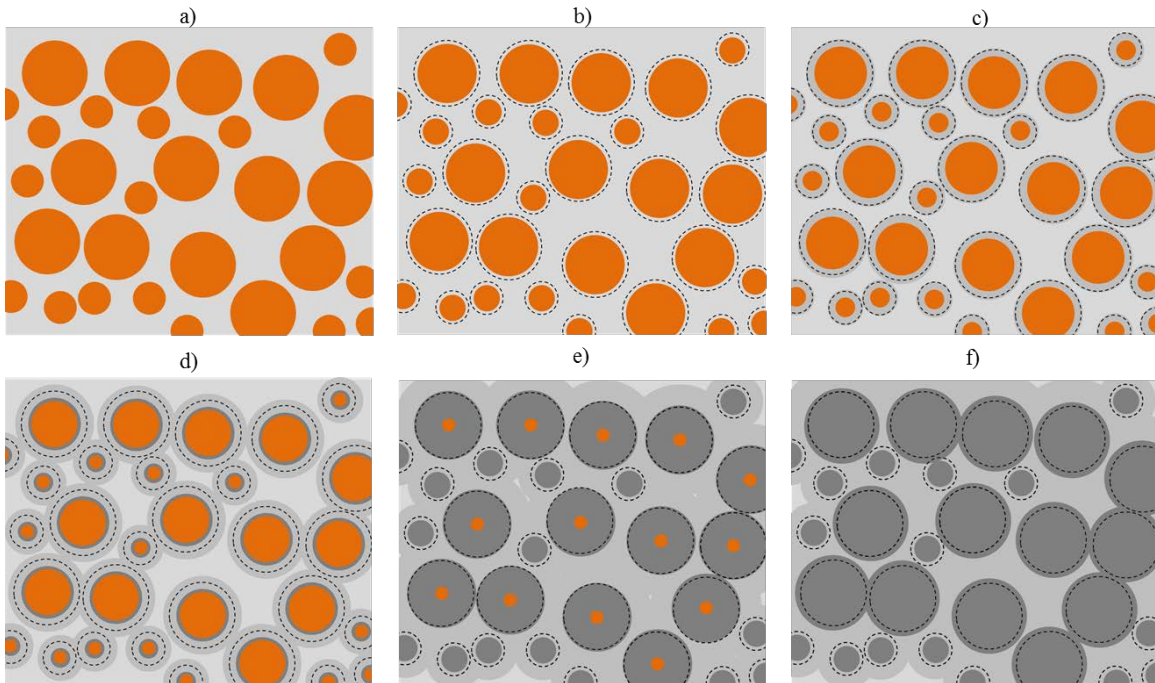


**Figure 2-18: Microstructural evolution during TLPS of a Cu-Sn joint with medium Sn-content. After process completion most of L has been consumed. The microstructure is characterized by  $\eta$  IMCs linking  $\epsilon$  IMCs and small pockets of L. The melting temperature of this joint is  $T_{m,Cu6Sn5}$**

To achieve higher joint  $T_m$ , even higher concentrations of Cu in the original arrangement are required. This is shown in Figure 2-19 a). Here the density of the Cu particles is very high. The microstructure after sintering is shown in Figure 2-19 b). The Sn atoms from L are consumed before all of the Cu is consumed. The microstructure is characterized by  $\epsilon$ -

IMCs bridging residual Cu. A pocket of  $\eta$ -IMCs exists because of a local lack of Cu in the original arrangement. With additional processing time this IMC will be transformed to  $\epsilon$ -IMC and surrounding residual Cu will be consumed.

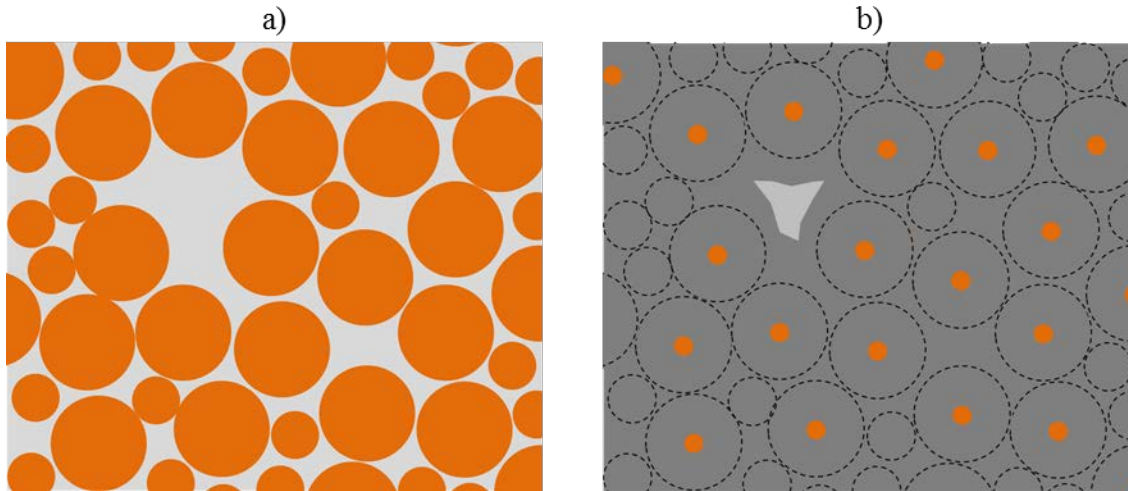


**Figure 2-19: Microstructural evolution during TLPS of a Cu-Sn joint with low Sn-content. After process completion all of L has been consumed. The microstructure is characterized by  $\epsilon$  IMCs linking residual Cu. The melting temperature of this joint is  $T_{m,Cu3Sn}$**

### 2.3 The Ni-Sn TLPS System

The prevailing application of Ni in attach applications is as a diffusion barrier layer between the solder and an underlying metallization [35]. The reaction rate of Ni and Sn is slower compared to that of Cu and Sn. As a consequence, the IMC layers formed under identical process conditions are thinner for the Ni-Sn system than for the Cu-Sn system. Figure 2-20 shows the Ni-Sn phase diagram. The melting temperatures of Sn ( $T_{m,Sn}$ ) and Ni ( $T_{m,Cu}$ ) are 232 °C and 1455 °C respectively. Three different stable Ni-Sn intermetallic stoichiometries exist:  $Ni_3Sn_4$ ,  $Ni_3Sn_2$ , and  $Ni_3Sn$ . It has been found that  $Ni_3Sn_4$  in combination with metastable phases is formed preferentially during soldering applications [35].  $Ni_3Sn_4$  has a melting temperature of 798 °C. The Ni-Sn system has a eutectic point at a  $T_{m,E}$  of 231 °C. The solubility of Sn in Ni and vice versa is small (e.g. 2.2at% Sn in solid

Ni at 300 °C, which translates into 4.4wt% or 5.5vol.%). The solubility of Ni in the liquid phase L at potential processing temperatures is negligible (e.g. < 0.2a% Ni in L at 300 °C).

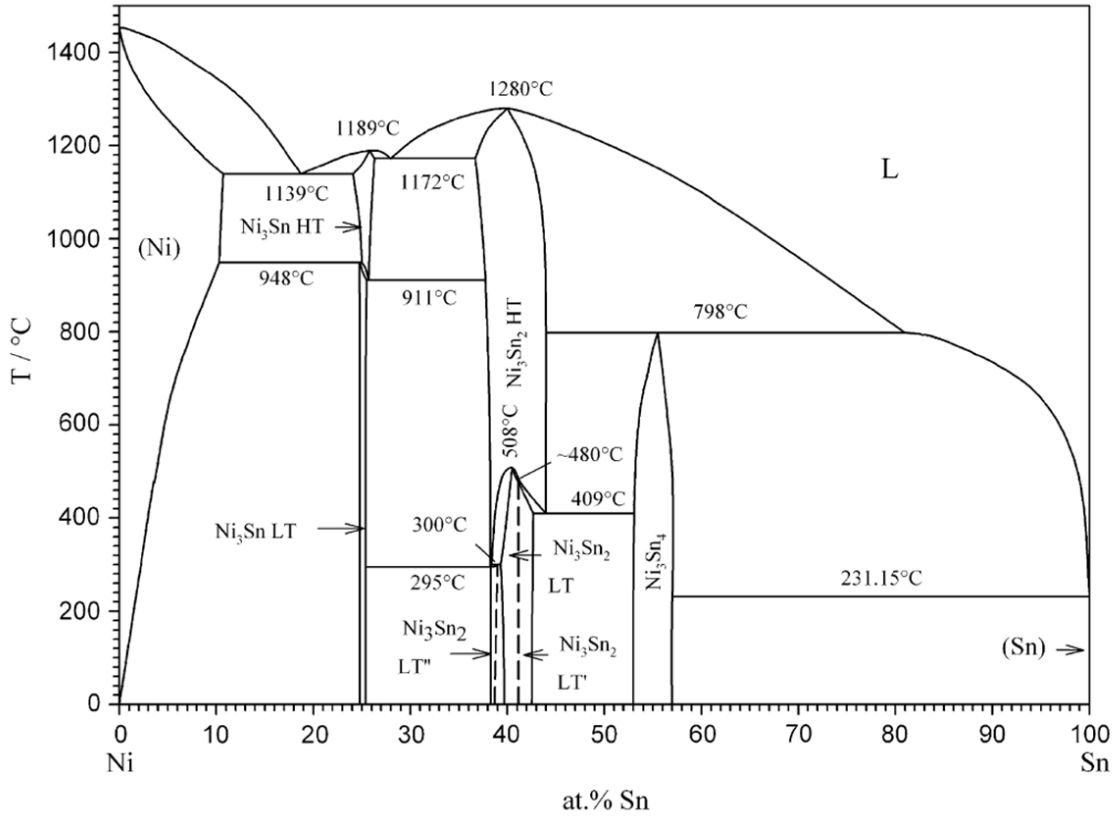


**Figure 2-20 The Ni-Sn phase diagram [44]**

Gur and Bamberger [45] have shown that though only one IMC stoichiometry ( $\text{Ni}_3\text{Sn}_4$ ) grows during the reaction of liquid Sn with solid Ni, two types of grains grow: (1) coarse grains at the Sn-Ni interface and (2) fine grains at the interface between the coarse grains and the underlying Ni substrate. As the sintering process proceeds, grain-to-grain mass transfer occurs between adjacent coarse grains, with grains of smaller lateral size reducing their solid-liquid interfacial curvature. As a consequence the grain boundaries migrate towards the interface of coarse and fine grains and a groove of liquid Sn grows in between them. The groove grows in between the coarse and fine grains until complete separation of the coarse grain from the fine layer occurs. They referred to this phenomenon as the

*Crumbling Effect* [45]. Görlich et al. similarly found that in contrast to the Cu-Sn IMC reactions, during  $\text{Ni}_3\text{Sn}_4$  IMC growth between solid Ni and liquid Sn new particles continuously nucleate at the reaction interface and pre-existing particles are pushed towards the liquid Sn [46]. This leads to the formation of a sponge-like microstructure with coarse  $\text{Ni}_3\text{Sn}_4$  grains in close proximity to the bulk Sn and fine  $\text{Ni}_3\text{Sn}_4$  grains near the Ni substrate. The microstructure is characterized by a  $\text{Ni}_3\text{Sn}_4$  IMC sponge with pockets of Sn in the pores. With extended sintering time the sponge densifies and the amount of Sn in the pores decreases [46]. As with the Cu-Sn IMCs, the growth of the  $\text{Ni}_3\text{Sn}_4$  IMC in the solid state is characterized by homogeneous growth of a continuous intermetallic layer at the interface of Ni and Sn [47] [48] [49].

The literature base of the growth kinetics of diffusion couples of pure tin and pure nickel is even more limited than for the Cu-Sn system. The majority of research effort is focused on studying  $\text{Ni}_3\text{Sn}_4$  IMC growth of Sn-based solders on plated Ni metallization layers below the melting temperature of the solders. For multiple reasons this data should not be used: (1) The addition of small amounts of alloying elements changes the solubility limit of Ni in the liquid as well as the diffusivity of Ni into  $L$ . (2) metallized Ni layers have different microstructures (e.g. grain size) and can contain high levels of impurities. The most common Ni-based metallization layer contains high levels of Phosphorus, completely changing the reaction layers and IMC growth behavior [35]. (3) The addition of alloying elements can alter the IMC phase that is energetically advantageous to form. For example alloying Sn with Zn leads to the formation of Cu-Zn IMCs on Cu substrates instead of Cu-Sn IMCs [50] [51]. One example for Sn-based solders on Ni substrates is the alloying with Cu. This can change the preferred IMC layer from the  $\text{Ni}_3\text{Sn}_4$  to the  $\text{Cu}_6\text{Sn}_5$  stoichiometry

[35]. Details of this will be introduced in section 2.4. As a consequence, only literature investigating the reaction of high-purity Ni with high-purity Sn was included in the following discussion on  $\text{Ni}_3\text{Sn}_4$  IMC growth kinetics.

Labie et al. [25] limited the thickness of their Ni layers to 2  $\mu\text{m}$ , far below the diffusion lengths encountered in this work. The same is true for the work of Bader et al. [30], who used coupons with Ni thicknesses of 4.1  $\mu\text{m}$  and 4.4  $\mu\text{m}$ . Görlich et al. [46] assessed the reaction kinetics for thick layers of Sn and Ni. Yet they limited their investigation to only one temperature condition of 250 °C which does not provide information on the temperature-dependence of the kinetics. Gur et al. performed the only other research of the liquid-solid diffusion kinetics of pure Sn and pure Ni [45]. They assessed the  $\text{Ni}_3\text{Sn}_4$  growth rate at temperatures between 235 °C and 600 °C. Figure 2-21 shows the expected growth of the  $\text{Ni}_3\text{Sn}_4$  layer thickness for 250 °C following data from their work.

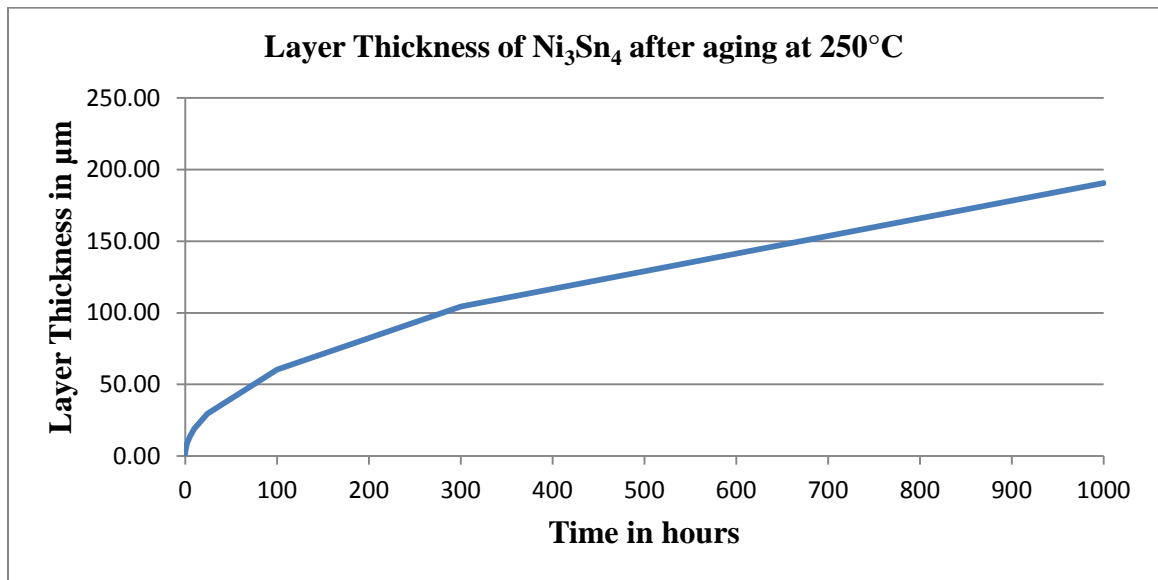


**Figure 2-21:  $\text{Ni}_3\text{Sn}_4$  layer thickness vs. time after aging at 250 °C. See [45] for original data**

More work has been published for solid-solid annealing of pure Ni-Sn diffusion couples at temperature below  $T_{\text{m,Sn}}$ . Tomlinson and Rhodes studied the growth of Ni-Sn IMCs on

annealed sheets of high purity Ni plated with bright tin at temperatures between 180 °C and 220 °C [47]. They found that the growth of Ni<sub>3</sub>Sn<sub>4</sub> follows a parabolic growth law. Blair et al. studied the growth of Ni<sub>3</sub>Sn<sub>4</sub> layers at temperatures between 75 °C and 160 °C and came to the same conclusion [48]. Mita et al. used sandwiched foils of high purity Ni sandwiched between high purity foils of Sn to study the growth behavior of Ni-Sn IMCs at temperatures between 160 °C and 200 °C [49]. In their study the growth kinetics did not follow a parabolic law, but had a growth exponent between 0.46 and 0.41 at temperatures of 180 °C and 200 °C respectively. They concluded from this that at these temperatures grain boundary diffusion contributes to the total diffusion. Figure 2-22 plots the results of the growth kinetics models from [47] [48] [49] for the thermal annealing condition of 200 °C. The result of Blair et al. was extrapolated from their results at lower temperatures because their studies were limited to the range below 160 °C. It can be seen that it yields considerably higher IMC growth rates than the other two studies which is most likely due to that extrapolation.

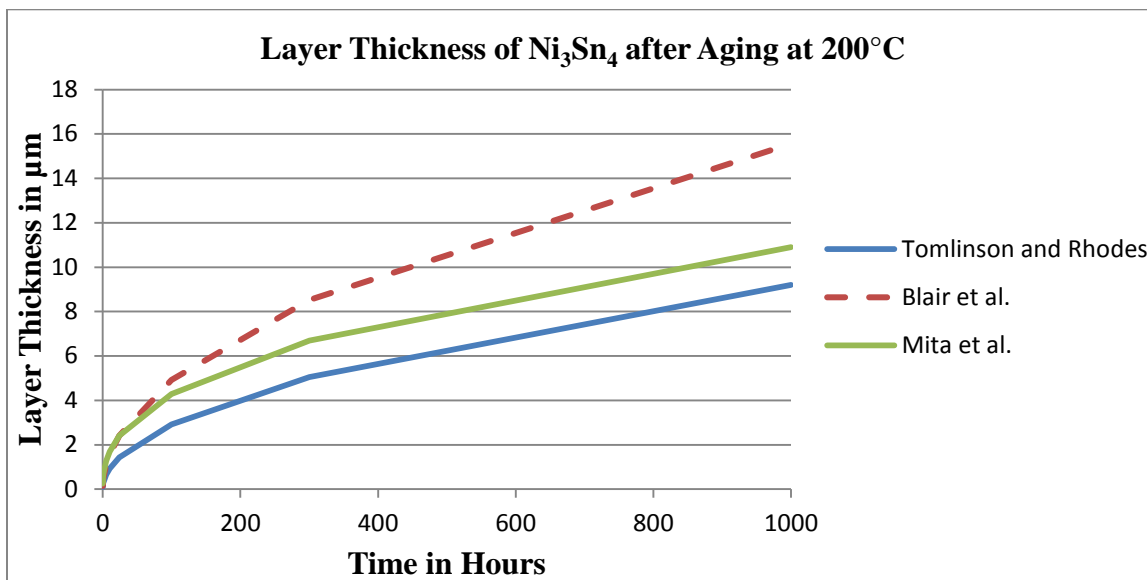


Figure 2-22: Ni<sub>3</sub>Sn<sub>4</sub> layer thickness vs. time after aging at 200 °C

Mita et al. [49] provide only two dataset at two temperature close temperature levels (180 °C and 200 °C) which makes calculations of activation energy prone to high uncertainty. For this reasons it was decided not to use their results for assessment of IMC growth close to the melting temperature of Sn. As a conclusion the work of Gur et al. [45] was used for analyzing the growth behavior of Ni<sub>3</sub>Sn<sub>4</sub> IMCs above the melting temperature of Sn and the works of Tomlinson and Rhodes [47] for temperatures below the melting temperature of Sn.

#### 2.4 The Cu-Ni-Sn TLPS System

The tertiary Cu-Ni-Sn systems is much more complex than the binary Cu-Sn or Ni-Sn systems. Very limited literature exists on Cu-Ni-Sn phase diagrams. Gupta has provided a review of phase diagrams of the Cu-Ni-Sn system in [52]. Lin et al. have analyzed phase equilibria and solidification properties of Sn-Cu-Ni alloys and proposed a liquidus projection of this system [53]. Sadi and Servant have studied the phase transformation and phase diagrams in the Cu-Ni-Sn and provided a ternary isothermal section at 400 °C which shows that the liquid phases only exist for high contents of Sn at this temperature [54]. Unfortunately no solidus temperature projections have been performed for the Cu-Ni-Sn system. Cu-Ni-Sn IMCs can exist with different concentrations of Cu- and Ni-atoms, and the melting temperature of the resulting TLPS joints depends on these concentrations. As no literature exists on the solidus temperature of these joints, their softening temperature will be assessed in this work to ensure high temperature capability.

The addition of Cu or Ni in Sn-based alloys has a significant impact on the types and associated growth kinetics of IMCs formed on Ni and Cu substrates respectively. Even trace amounts of Ni in Sn alloys (< 0.5 wt.%) reduce the growth of Cu<sub>3</sub>Sn IMCs on Cu

substrates during liquid-solid [55] [56] and solid-solid diffusion [57] [58]. The reduced growth of  $\text{Cu}_3\text{Sn}$  minimizes the formation of Kirkendall voids in the joints [59]. The primary IMC grown at the Cu-to-solder interface has the  $\text{Cu}_6\text{Sn}_5$  stoichiometry, but some of the Cu positions within the IMC is occupied Ni, forming a  $(\text{Cu}_{1-x}\text{Ni}_x)_6\text{Sn}_5$  IMC. The growth rate of this  $(\text{Cu}_{1-x}\text{Ni}_x)_6\text{Sn}_5$  IMC is up to ten times faster than that of a pure  $\text{Cu}_6\text{Sn}_5$  IMC and even the addition of 0.1 wt.% accelerated the growth approximately fivefold [56]. The reason for the faster growth of  $(\text{Cu}_{1-x}\text{Ni}_x)_6\text{Sn}_5$  IMCs is the decreased equilibrium solubility of Cu with the addition of Ni to the liquid as explained by Ho et al. [59]. Even though the dissolution flux of Cu into molten solder is not altered by the addition of Ni, its reduced solubility in the melt is compensated by the more rapid formation of IMCs. The reactions of Cu-Ni alloys and Sn have been assessed experimentally by Vuorinen et al. in [60] and thermodynamically by Yu et al. in [61]. They found that with increasing Ni-content, the growth of  $\text{Cu}_3\text{Sn}$  IMCs is suppressed and that if enough Ni is present for the dissolution in the liquid, the growth of  $(\text{Cu},\text{Ni})_6\text{Sn}_5$  is preferred compared to  $(\text{Ni},\text{Cu})_3\text{Sn}_4$ . They also showed that this is the case not only for liquid Sn, but also for Sn3.5Ag [61].

The microstructures of the  $(\text{Cu}_{1-x}\text{Ni}_x)_6\text{Sn}_5$  and  $\text{Cu}_6\text{Sn}_5$  IMC differ: The addition of Ni in the Sn-alloy leads to a sponge-like microstructure [56] similar to the microstructure found for liquid-solid Ni-Sn diffusion couples [45] [46], which might explain the accelerated growth. As grains are continuously detached from the Cu-Sn-alloy interfaces, the diffusion path for Cu atoms into the liquid is shortened, expediting the quick growth of new IMCs. Subsequent aging below the melting lead to a reduction of the pockets of Sn-alloy in the

pores of the  $(\text{Cu}_{1-x}\text{Ni}_x)_6\text{Sn}_5$  IMC sponge. The growth of these new IMC occurs with lower concentrations of Ni atoms than the growth of the IMCs sponge [56].

**Table 2-2: Dependence of the IMC type formation between Sn-Ag alloys and Ni substrates on the level of Cu doping in the alloy, adapted from [59]**

Cu (wt.%)	Ag (wt.%)	Sn (wt.%)	IMC(s)	References
0.0	3.5 – 3.9	Balance	$\text{Ni}_3\text{Sn}_4$	[62] [63]
0.1	0	Balance	$\text{Ni}_3\text{Sn}_4$	[64]
0.2	0 - 3.9	Balance	$(\text{Ni,Cu})_3\text{Sn}_4$	[65] [62] [66] [67]
0.3	0	Balance	$(\text{Ni,Cu})_3\text{Sn}_4$	[64]
0.4	3.9	Balance	$(\text{Ni,Cu})_3\text{Sn}_4/$ $(\text{Cu,Ni})_6\text{Sn}_5$	[68]
0.5	1.0 – 4.0	Balance	$(\text{Cu,Ni})_6\text{Sn}_5$	[68]
			$(\text{Ni,Cu})_3\text{Sn}_4/$ $(\text{Cu,Ni})_6\text{Sn}_5$	[62] [67]
0.6	0 – 3.9	Balance	$(\text{Cu,Ni})_6\text{Sn}_5$	[65] [62] [67] [68]
0.7	0 – 3.8	Balance	$(\text{Cu,Ni})_6\text{Sn}_5$	[62] [64] [66] [69] [70]

The stoichiometry of IMCs formed at the interface between Ni substrates and Cu-doped Sn-based alloys during liquid-solid diffusion depends on the Cu-concentration in the alloy. The IMC layer grown by pure Sn on Ni is  $\text{Ni}_3\text{Sn}_4$ , see above. With the addition of Cu to the Sn-alloy the primary IMC type first changes from  $\text{Ni}_3\text{Sn}_4$  to  $(\text{Ni,Cu})_3\text{Sn}_4$  (identical stoichiometry) and later to  $(\text{Cu,Ni})_6\text{Sn}_5$ , depending on the Cu concentration, see Table 2-2. The required Cu-concentrations are very small: 0.2 wt.% Ni for the transition from  $\text{Ni}_3\text{Sn}_4$  to  $(\text{Ni,Cu})_3\text{Sn}_4$ , and 0.6 wt.% for the transition to  $(\text{Cu,Ni})_6\text{Sn}_5$ . At Cu levels of 0.4 wt.% individual particles of  $(\text{Cu,Ni})_6\text{Sn}_5$  begin forming over the  $(\text{Ni,Cu})_3\text{Sn}_4$  layer and at concentrations of 0.5 wt.% a continuous layer of  $(\text{Cu,Ni})_6\text{Sn}_5$  begins forming over the  $(\text{Ni,Cu})_3\text{Sn}_4$  layer.

As described in section 2.2, the Cu-Sn system shows a phase transformation for the  $\text{Cu}_6\text{Sn}_5$  IMC stoichiometry:  $\eta$  and  $\eta'$ . The equilibrium temperature for the  $\eta - \eta'$  transformation is 186 °C, which is a crucial range for high temperature electronic applications. The associated density change can induce stresses and may lead to crack initiation and propagation. Nogita et al. have shown that cracking is likely to occur in the  $\text{Cu}_6\text{Sn}_5$  IMC layer formed at the interface between Sn0.7Cu solders and Cu substrates after reflowing, but that the formation of these cracks can be inhibited by trace amounts of Ni added to the solder [36]. Two solder compositions were assessed: (1) Sn-0.7wt%Cu and (2) Sn-0.7wt%Cu-0.05wt%Ni. Two types of samples were manufactured with these alloys: (1) BGA solder balls which were reflowed twice with a reflow cycle with a peak temperature of approximately 250 °C and approximately 30sec above the solder melting temperature, and (2) dipped Cu plates that were dipped into molten solder at a temperature of 250 °C for 10sec. The samples were subsequently annealed at 120 °C for 1000 hours. They found that for the Sn-0.7wt%Cu alloy many cracks were present in the interfacial IMCs for both the reflowed and dipped samples, but none or very few for the IMCs formed from the Sn-0.7wt%Cu-0.05wt%Ni alloy. In addition to the reduction in crack quantity the length of the cracks also decreased for the Ni-doped alloy. An analysis of the chemical composition of the IMCs showed that the Sn-0.7wt%Cu-0.05wt%Ni contained about 5at% Ni. X-ray diffraction analysis showed that the  $\text{Cu}_6\text{Sn}_5$  IMCs formed from the Sn-0.7wt%Cu existed only in the monoclinic  $\eta'$  phase after annealing, while all the  $(\text{Cu,Ni})_6\text{Sn}_5$  IMCs formed from the Sn-0.7wt%Cu-0.05wt%Ni possess a hexagonal ( $\eta$ ) structure. In [71] Nogita further analyzed the behavior of the IMCs found in the experiments in [36] by performing Differential Scanning Calorimetry (DSC) tests on  $(\text{Cu,Ni})_6\text{Sn}_5$  IMCs by heating and

cooling between 110 °C and 210 °C with ramp rates of 1 °C/min and compared the results to those obtained by Ghosh and Asta [72]. It was found that the  $\text{Cu}_6\text{Sn}_5$  IMCs show a phase transformation during heating and cooling, whereas the  $(\text{Cu,Ni})_6\text{Sn}_5$  IMCs do not.

An explanation for the phase stabilization of  $\text{Cu}_6\text{Sn}_5$  IMCs by alloying with Ni is given by Yu et al. in [73]. They used first-principles calculations to determine the stable structure of  $\text{Cu}_{6-x}\text{Ni}_x\text{Sn}_5$  IMCs and determined the structural properties for  $x = 0, 1, 2$ . They used ab initio calculations to calculate lattice parameters and cell volumes for  $\text{Cu}_6\text{Sn}_5$  IMCs doped with Ni atoms. Even though the atomic radius of Ni is close to that of Cu, the volume of the IMC decreased with Ni atoms occupying Cu locations, which indicates that the increase of bond energy is the cause of the volume reduction. Their results indicate that the distance between the Ni and the nearest neighbor Cu is larger than the original Cu-Cu bond, but that the bond lengths of the modified Cu-Sn and Cu-Cu bonds are slightly decreased. Table 2-3 provides an overview of the cell volume, the heat of formation, and the cohesive energies for the three assessed IMCs:  $\text{Cu}_6\text{Sn}_5$ ,  $\text{Cu}_5\text{Ni}_1\text{Sn}_5$ , and  $\text{Cu}_4\text{Ni}_2\text{Sn}_5$ . For the latter two IMC types, two possible atom arrangements were assessed each. The cell volume is highest for  $\text{Cu}_6\text{Sn}_5$  ( $185.55 \text{ \AA}^3/\text{cell}$ ), considerably smaller for the  $\text{Cu}_5\text{Ni}_1\text{Sn}_5$  structures ( $182.95$  and  $182.94 \text{ \AA}^3/\text{cell}$ ), and smallest for the  $\text{Cu}_4\text{Ni}_2\text{Sn}_5$  structures ( $180.29$  and  $179.94 \text{ \AA}^3/\text{cell}$ ). The heat of formation is more negative for the ternary Cu-Ni-Sn IMCs than for the binary  $\text{Cu}_6\text{Sn}_5$  IMC, which means that they are thermodynamically more stable. The heat of formation is most negative for the  $\text{Cu}_4\text{Ni}_2\text{Sn}_5$  IMC with a Ni atom at the 8f (Cu2) site, which indicates that it is the thermodynamically most stable structure [73]. The calculated cohesive energies show a similar trend. The cohesive energy is the energy required to break the interatomic bonds and transform the atom into an isolated species. It is a measure of

the stability of a crystal structure. The cohesive energies are more negative for the Cu-Ni-Sn IMCs compared to that of the  $\text{Cu}_6\text{Sn}_5$  IMC. As a consequence, the ternary Cu-Ni-Sn crystals are more stable than the binary Cu-Sn crystal. Like the heat of formation, the cohesive energy is most negative for the  $\text{Cu}_4\text{Ni}_2\text{Sn}_5$  IMC with a Ni atom at the 8f (Cu2) site. It can be seen that the cell volume and cohesive energy correlate highly with the number of Ni atoms and less with their location. The heat of formation on the other hand correlates well with both the number of Ni atoms and their location.

**Table 2-3: Volumes [ $\text{\AA}^3/\text{cell}$ ], heat of formation [meV/atom], and cohesive energies [eV/atom] for  $\text{Cu}_6\text{Sn}_5$ ,  $\text{Cu}_5\text{Ni}_1\text{Sn}_5$ , and  $\text{Cu}_4\text{Ni}_2\text{Sn}_5$ , compare [73]**

Structure	Site	Volume	Heat of Formation	Cohesive Energies
$\text{Cu}_6\text{Sn}_5$	-	185.55	-272.8	-4.977
$\text{Cu}_5\text{Ni}_1\text{Sn}_5$	4a (Cu3)	182.95	-518.5	-5.424
$\text{Cu}_5\text{Ni}_1\text{Sn}_5$	4e (Cu4)	182.94	-538.0	-5.444
$\text{Cu}_4\text{Ni}_2\text{Sn}_5$	8f (Cu1)	180.29	-556.9	-6.654
$\text{Cu}_4\text{Ni}_2\text{Sn}_5$	8f (Cu2)	179.94	-612.8	-6.710

Limited literature on the growth kinetics of Cu-Ni-Sn IMCs is available. Hong et al. studied the cross-interaction in ternary Ni-Sn-Cu diffusion couples [74]. Their diffusion couples consisted of electroplated layers of Sn and Ni on a Cu substrate with two different Ni plating thicknesses. The Sn plating thickness was 65  $\mu\text{m}$ , those of the Ni metallizations were 15  $\mu\text{m}$  and 2  $\mu\text{m}$ , and the Cu substrates were 300  $\mu\text{m}$  thick. The samples were aged at 150, 180, and 200  $^\circ\text{C}$  (in the solid-diffusion state below the melting temperature of Sn) for up to 49 days. Figure 2-23 shows the dependence of the growth of the  $(\text{Cu,Ni})_6\text{Sn}_5$  IMCs at the Ni and Cu side on the aging temperature. At temperatures of 150  $^\circ\text{C}$  and 180  $^\circ\text{C}$  the growth of the IMCs at the Cu side is faster than at the Ni side at all times. The growth is characterized by parabolic growth behavior. This changes for the aging condition of 200  $^\circ\text{C}$ : Here the growth at the Ni side deviates from parabolic growth behavior and the

IMCs at the Ni grow faster than at the Cu side for long aging times whereas for short aging times the IMCs at the Cu side grow faster. Furthermore, the growth of IMCs at the Cu side initially shows parabolic growth behavior, but is later retarded by the rapid growth of IMCs on the Ni side. A compositional analysis of the IMCs showed that the Ni concentration depends both on the substrate side (Cu or Ni) and the aging temperature. Table 2-4 summarizes the Ni and Cu concentration in the  $(\text{Cu,Ni})_6\text{Sn}_5$  IMCs at the Cu- and Ni-side after aging for 36 days at 150, 180, and 200 °C. It can be seen that the Ni-concentration in the IMCs increases with the aging temperature. On the Ni-side the Ni-concentration is highest near the Ni and lowest near the Sn. At the Cu-side the Ni-concentration is highest near the Sn. The concentration of Ni near the Cu on the Cu-side was below the detection capabilities of the EDX equipment used.

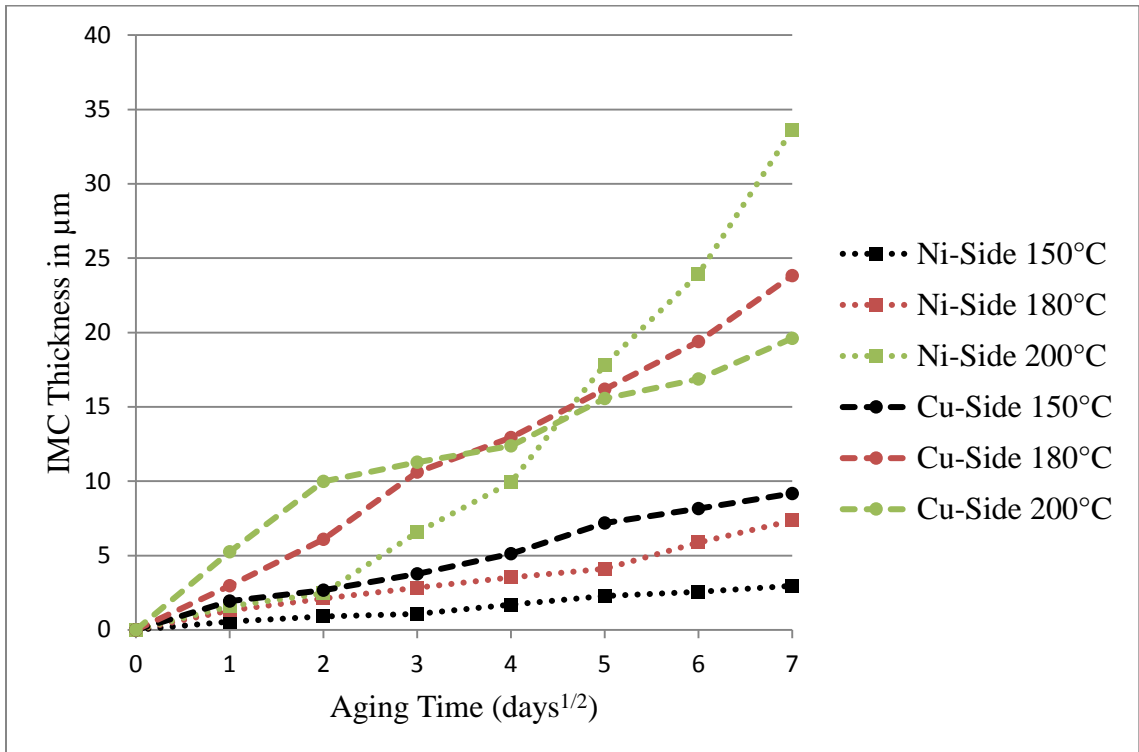


**Figure 2-23:  $(\text{Cu,Ni})_6\text{Sn}_5$  IMC thickness growth on the Ni- and Cu-side during aging at 150, 180, and 200 °C, reproduced from [74]**

**Table 2-4: Compositional analyses of the (Cu,Ni)<sub>6</sub>Sn<sub>5</sub> IMCs at the Cu- and Ni-side after aging for 36 days at multiple temperature levels [74]. Concentrations in at.%**

Temp.	Ni-Side						Cu-Side	
	Near Ni		Center		Near Sn		Near Sn	
	Ni	Cu	Ni	Cu	Ni	Cu	Ni	Cu
150 °C	-	-	4.2	49.8	-	-	2.5	54.8
180 °C	12.8	43.9	5.8	48.5	4.4	51.1	3.3	53.6
200 °C	15.4	42.7	13.5	43.6	7.8	47.9	4.3	52.3

It was furthermore found that even for short aging times below 16 hours a low temperatures of 150 °C, sufficient Cu atoms had diffused from the Cu side to the Ni side to initiate the formation of (Cu<sub>1-x</sub>Ni<sub>x</sub>)<sub>6</sub>Sn<sub>5</sub> IMCs. An analysis of the consumption of the Ni layer showed that after aging for 36 days at 200 °C only 2.1 μm of Ni had been consumed from the Ni-side, but a total growth of 23.9 μm of IMCs had grown. This shows that the primary growth of IMCs is yielded by consumption of Cu atoms at the both the Cu- and Ni side. They also compared the IMC growth kinetics on the Cu side to a binary Cu-Sn diffusion couple without a Ni layer. The growth of Cu<sub>3</sub>Sn IMCs was decelerated by the addition of the Ni layer on the diffusion couple. The growth of (Cu,Ni)<sub>6</sub>Sn<sub>5</sub> IMCs in the ternary diffusion couple was faster than that of the Cu<sub>6</sub>Sn<sub>5</sub> IMCs at the binary diffusion couple at 150 °C and 180 °C, but slower at 200 °C. This is in agreement with the growth kinetic behavior shown in Figure 2-23, which showed that the growth of (Cu,Ni)<sub>6</sub>Sn<sub>5</sub> IMCs at the Cu-side is decelerated at 200 °C.

Wang and Liu studied the IMC growth behavior of ternary Cu-Sn-Ni sandwich structures at 250 °C above the melting temperature of Sn and compared the result to those obtained by binary Cu-Sn diffusion couples under the same process condition [75]. The morphology of the IMCs at the Cu-Sn interface is initially (t < 10sec) scallop-shaped and the IMCs contain low levels of Ni (< 0.1 at.%). After longer process times (t > 1min) the IMC

morphology changed to a column-shaped type and the Ni-content increased. Table 2-5 shows the dependence of the Ni-concentration on the  $(\text{Cu,Ni})_6\text{Sn}_5$  IMCs at the Cu- and Ni-side on the process time. It can be seen that the concentration of Ni in the IMCs at the Cu-side increases with process duration. The IMCs at the Ni-Sn interface are also of the ternary  $(\text{Cu,Ni})_6\text{Sn}_5$  type. They started growing at process durations below 10sec. with extended process time, gradients of the Ni-concentration in the IMCs on the Ni-side developed. The Ni-content at the IMC-Sn interface decreases with processing time and the Ni-content at the IMC-Ni interface increases with processing time. The authors hypothesized this behavior can be attributed to the diffusion of Ni from the Ni foil through the IMCs. The Ni atoms require time for the diffusion in the newly formed Cu-rich  $(\text{Cu,Ni})_6\text{Sn}_5$  IMCs. Initially the morphology of the interfacial IMCs at the Ni-side is needle-like, but transforms to a column-like shape for longer process durations. It was furthermore observed that a sponge-like microstructure existed with scattered IMCs between liquid Sn on top of a continuous IMC layer.

**Table 2-5: Ni-concentration in the  $(\text{Cu,Ni})_6\text{Sn}_5$  IMCs at the Cu- and Ni-side after multiple process times at 250 °C [75]. Concentrations in at.%**

Process Time (Min)	Cu-Side	Ni-Side	
	Average	Near Sn	Near Ni
~0.5	0.1	8.2	8.2
1 – 5	2.1	6.7	9.6
10 – 30	2.6	3.9	11.3
60 – 120	3.2	4.6	15.4

Figure 2-24 shows the dependence of the IMC thickness on the processing time at 250 °C for a ternary Cu-Sn-Ni and a binary Cu-Sn diffusion couple. The growth at the Cu-side of the ternary diffusion couple and at the interface of the binary Cu-Sn couple both show a parabolic growth behavior. The growth of the IMCs at the Cu-side is slower than that of

the Cu-Sn diffusion couple. The authors additionally noted that the growth of the  $\text{Cu}_3\text{Sn}$  layer at the interface is approximately 4 times faster in the binary Cu-Sn diffusion couple compared to the growth of the  $\text{Cu}_3\text{Sn}$  layer at the Cu-side of the ternary diffusion couple after 1h of reflow. In contrast, the growth of the IMC layer at the Ni-side of the ternary diffusion couple shows a linear growth behavior for extended process times. As a result, the thickness of the IMC layer increases much faster for longer process times than the IMC layer at the Cu-side or the IMC layer for the binary diffusion couple. The authors further showed that the growth of the IMC layer at the Ni-side is achieved through a consumption of Cu atoms from the Cu-side of the diffusion couple. The reason for the rapid, non-parabolic growth of the IMCs on the Ni-side might be the loose sponge-like structure. Cu-atoms dissolved in the liquid Sn are highly mobile and fast diffusion of Cu atoms from the Cu-side to the Ni-side is possible. Additionally, IMCs grow within the sponge-structure while simultaneously IMC grains disconnect from the continuous solid IMC layer by the same mechanism that has been described above (see section 2.3).

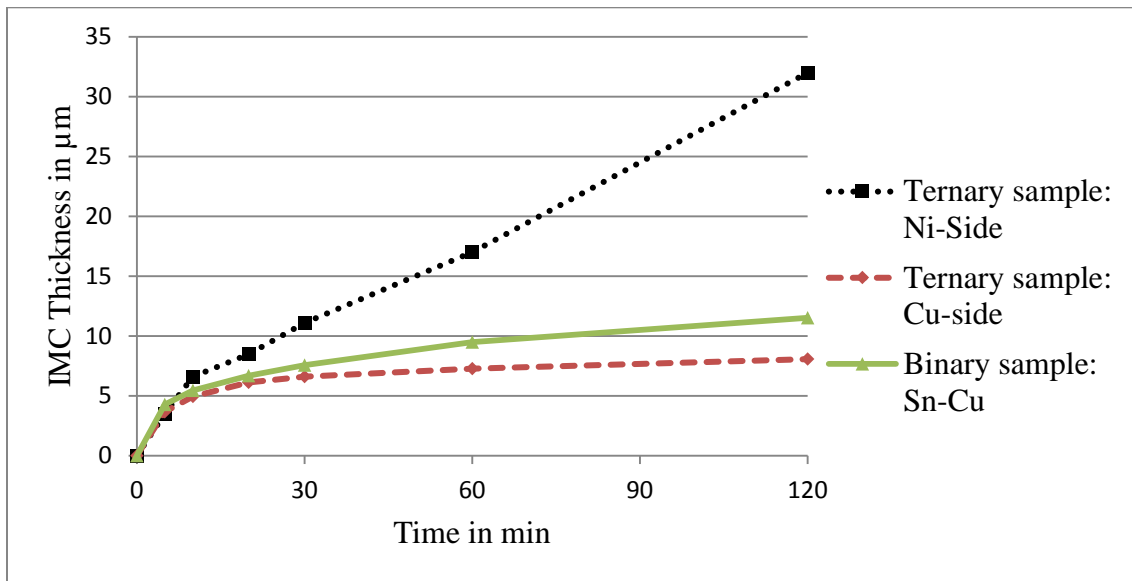


**Figure 2-24: IMC growth on the Ni- and Cu-side during aging at 250 °C on the Cu- and Ni-side of a ternary and at the Cu-Sn interface of a binary diffusion couple, reproduced from [75]**

In summary, the ternary Cu-Ni-Sn system shows considerably different IMC nucleation and growth behavior and different growth kinetics than both the Cu-Sn and Ni-Sn systems. The main characteristics of the Cu-Ni-Sn system and the difference to the other systems studied in this work are listed below:

- The primary IMC growing in the Cu-Ni-Sn system is the  $(\text{Cu,Ni})_6\text{Sn}_5$  IMC. This is true for the Cu-side and the Ni-side
- On the Cu-side a secondary  $(\text{Cu,Ni})_3\text{Sn}$  IMC is growing. The concentration of Ni in this is very small. Yet the growth of this IMC is inhibited by Ni compared to the Cu-Sn system
- No secondary IMC is growing on the Ni-side
- Considerably more Cu than Ni is present in the  $(\text{Cu,Ni})_6\text{Sn}_5$  IMC. This is true for the Cu-side and the Ni-side
- The concentration of Ni in the  $(\text{Cu,Ni})_6\text{Sn}_5$  IMC on the Ni-side is higher than on the Cu-side
- Below 180 °C the  $(\text{Cu,Ni})_6\text{Sn}_5$  IMCs on the Cu-side grow faster than the IMCs on the Ni-side. The opposite is the case at temperatures above 200 °C because under this condition the IMC growth on the Ni-side is not limited by parabolic growth in contrast to the Cu-side
- The microstructure of the  $(\text{Cu,Ni})_6\text{Sn}_5$  IMCs grown above  $T_{m,\text{Sn}}$  on the Ni-side is similar to the sponge-like microstructure found in the  $\text{Ni}_3\text{Sn}_4$  IMCs growing, and not similar to the continuous microstructure of the  $(\text{Cu,Ni})_6\text{Sn}_5$  IMCs on the Cu-side

- The sponge-like microstructure of the  $(\text{Cu,Ni})_6\text{Sn}_5$  IMCs on the Ni-side leads to a linear growth behavior of the IMCs considerably faster than the parabolic growth behavior of  $\text{Cu}_6\text{Sn}_5$  found in Cu-Sn diffusion couples

The expected IMC growth behavior of paste-based Cu-Ni-Sn TLPS joints is shown schematically in Figure 2-25. The original arrangement consists of particles of Cu (orange) and Ni (blue) embedded in a matrix of solid Sn (bright grey), see Figure 2-25 a). Upon melting of the Sn, Cu and Ni are dissolved in the melt, forming the liquid phase L, see Figure 2-25 b). Because the solubility of Cu in liquid Sn is considerably smaller than that for Ni at the same temperature levels, only the volume reduction of the Cu particles is indicated here. After the dissolution is completed,  $(\text{Cu,Ni})_6\text{Sn}_5$  IMCs start growing on the surfaces of the Cu and Ni particles, see grey areas in Figure 2-25 c). The majority of the solid consumed is Cu from the Cu particles which undergo a considerable reduction in volume. The volume reduction is less pronounced for the Ni particles. Dotted lines illustrate the original particle sizes. The growth of IMCs is faster at the Ni-particles compared to the Cu-particles, compare Figure 2-24. In reality the growth of IMCs on the Ni particles is characterized by formation of sponge-like structures. This was not included in Figure 2-25 to better illustrate the fundamentals of the process kinematics. With continued processing Cu and Ni continues to be consumed with small Cu particles reaching the point of total consumption first, see Figure 2-25 d). Limited growth of  $\text{Cu}_3\text{Sn}$  phases (dark grey) occurs and IMCs of this type remain at locations of former Cu particles, see Figure 2-25 e). Simultaneously Ni from the Ni particles is consumed and  $(\text{Cu,Ni})_6\text{Sn}_5$  IMCs continue to grow. After ending of the process this leads to a microstructure shown in Figure

2-25 f). The final microstructure is characterized by a matrix of  $(\text{Cu,Ni})_6\text{Sn}_5$  IMCs connecting Ni particles, Sn-rich liquid phases, and  $\text{Cu}_3\text{Sn}$  IMCs.

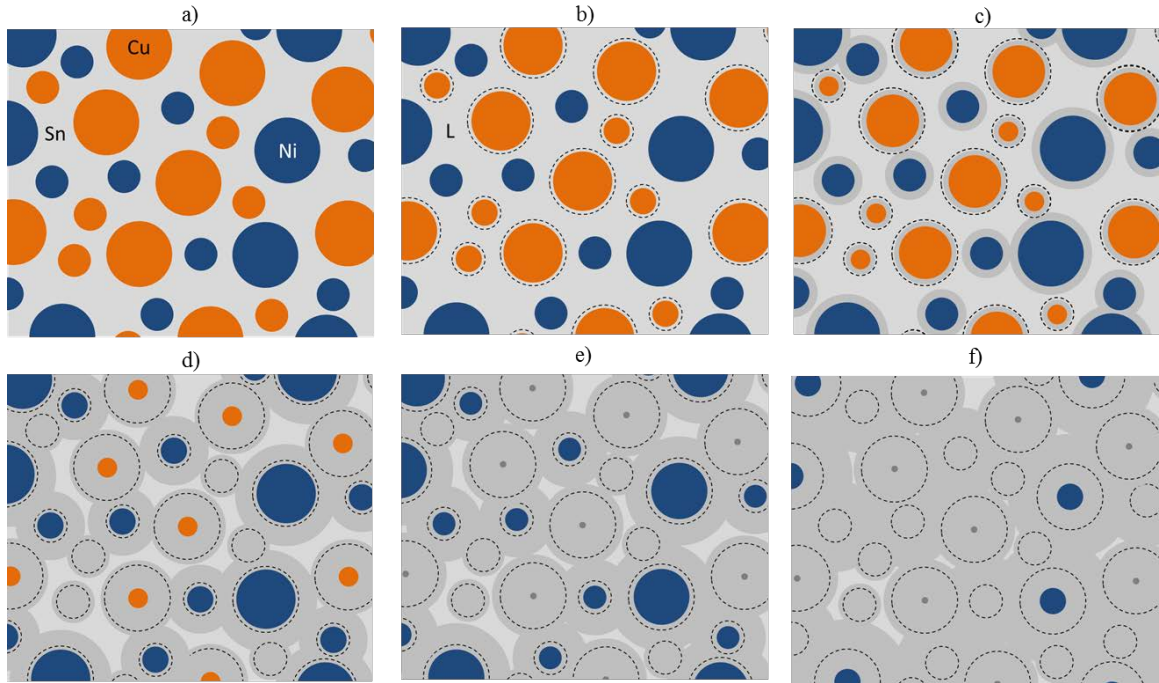


**Figure 2-25: Microstructural evolution during TLPS of a Cu-Ni-Sn joint with medium Sn-content. After process completion most of L has been consumed. The microstructure is characterized by  $(\text{Cu,Ni})_6\text{Sn}_5$  IMCs linking Ni-particles, some  $\text{Cu}_3\text{Sn}$  IMCs and pockets of L. The melting temperature of this joint is  $T_{m,(\text{Cu,Ni})_6\text{Sn}_5}$**

The melting temperature of the joint is the melting temperature of  $(\text{Cu,Ni})_6\text{Sn}_5$ ,  $T_{m,(\text{Cu,Ni})_6\text{Sn}_5}$ . The percentages of Cu and Ni in  $(\text{Cu,Ni})_6\text{Sn}_5$  can vary not just between joints of different composition, but also within one joint due to residual concentration gradients. The thermodynamic properties of  $T_{m,(\text{Cu,Ni})_6\text{Sn}_5}$  depend on these percentages (e.g. the liquidus temperature [76] [77]). Unfortunately limited literature exists on the solidus temperature of  $(\text{Cu,Ni})_6\text{Sn}_5$  and its dependence on the concentration of Cu and Ni. Greve et al. tested the softening of paste-based Cu-Ni-Sn TLPS interconnects by shear tests under high temperature conditions [78]. They showed that the shear strength of joints with similar percentages of Cu and Ni dropped below 10 MPa in the range of 400 - 450 °C. The feasibility of this approach as an indicator for testing of the solidus temperature was

verified by shear tests of high-temperature solders with known melting temperature. From these results it is expected that  $T_{m,(Cu,Ni)_6Sn_5}$  is higher than 400 °C, which is consistent with the melting temperature of  $Cu_6Sn_5$  ( $T_{m,Cu_6Sn_5} = 415$  °C) for the binary Cu-Sn system, see section 2.2.

## 2.5 Summary of Reaction Kinetics Data for the Cu-Sn and Ni-Sn Systems

This section summarizes the results of the literature review on the IMC growth kinetics from sections 2.2 and 2.3. Further details on the research on IMC growth behavior in the Cu-Sn and Ni-Sn material system can be found in those sections respectively. The growth kinetic models described below and the summary of the model parameters and constants will help optimize the sintering process, predict microstructural evolution and process completion times and analyze joint microstructures. The growth behavior of IMCs can generally be described by:

$$l_{IMC} = (Dt)^n \quad \text{Equation 2-1}$$

with  $l_{IMC}$ : Thickness of the IMC layer [m]  
 D: Diffusion Coefficient [ $m^{1/n}/s$ ]  
 t: Time [s]  
 n: Growth Exponent

If volume diffusion is the dominating diffusion mechanism, then  $n = 0.5$  and the growth of the IMCs follows Fick's second law of diffusion with a parabolic growth behavior and Equation 2-1 simplifies to:

$$l_{IMC} = \sqrt{Dt} \quad \text{Equation 2-2}$$

As described in sections 2.2 and 2.3, most studies found that the growth of Cu-Sn and Ni-Sn IMCs shows parabolic growth behavior. In this case the unit of the Diffusion Coefficient simplifies to  $m^2/s$ .

The temperature-dependence of the Diffusion Coefficient for IMC growth has been found to correlate well with the Arrhenius equation:

$$D = D_0 e^{-Q/(RT)} \quad \text{Equation 2-3}$$

- with
- D: Diffusion Coefficient [ $m^{1/n}/s$ ]
  - $D_0$ : Diffusion Coefficient at infinite temperature [ $m^{1/n}/s$ ]
  - Q: Activation Energy [J/mol]
  - R: Gas constant: 8.314 J/(K mol)
  - T: Temperature [K]

As described above for the case of parabolic growth the units for the Diffusion Coefficients simplify to  $m^2/s$ . The Growth Exponent can show a dependence on temperature (e.g. when different diffusion mechanisms compete):

$$n = k_n \frac{1000}{T} + c_n \quad \text{Equation 2-4}$$

- with
- n: Growth Exponent
  - $k_n, c_n$ : Constants
  - T: Temperature [K]

In this case the calculation of the Diffusion Coefficient becomes more complex:

$$D = K^{1/n} \quad \text{Equation 2-5}$$

with D: Diffusion Coefficient [ $m^{1/n}/s$ ]  
 K: Proportionality Coefficient [ $m/s^n$ ]

and

$$K = m_n \frac{1000}{T} + d_n \quad \text{Equation 2-6}$$

with K: Proportionality Coefficient [ $m/s^n$ ]  
 $m_n, d_n$ : Constants  
 T: Temperature [K]

Figure 2-26 summarizes and plots the Diffusion Coefficients of available literature versus  $1/T$ . The range to the left of the vertical dotted line indicates temperatures above the melting temperature of Sn  $T_{m,Sn}$  (232 °C) and the range to the right indicates temperatures below that temperature. Dashed lines are results from test run above  $T_{m,Sn}$ , solid lines are results from test performed below  $T_{m,Sn}$ . The dotted line correlates to tests on  $Cu_3Sn$  below  $T_{m,Sn}$  that showed a temperature-dependence of the Growth Exponent  $n$ . As a consequence, the unit of the Diffusion Coefficient for this curve is  $m^{1/n}/s$  rather than  $m^2/s$ . This furthermore leads to a shape deviating from a straight line in this plot. The blue, green, and red lines correspond to the Diffusion Coefficients for the growth of  $Cu_6Sn_5$ ,  $Cu_3Sn$ , and  $Ni_3Sn_4$ , respectively. The data is plotted only for the studied temperature ranges and no extrapolation was performed. The information is based on research published in [33] [39] [42] [43] [45] and [47] as described in sections 2.2 and 2.3.

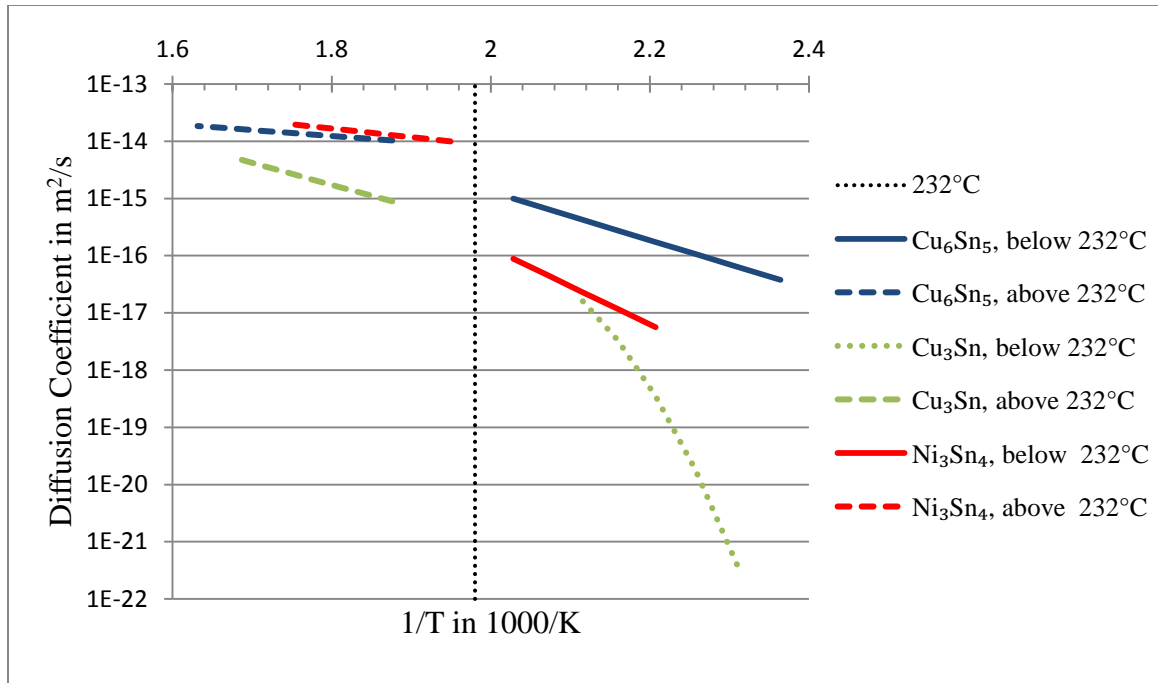


**Figure 2-26: Temperature dependence of the diffusion coefficient for the growth of the Cu<sub>6</sub>Sn<sub>5</sub>, Cu<sub>3</sub>Sn, and Ni<sub>3</sub>Sn<sub>4</sub> IMCs. Solid lines and dashed lines indicate values below and above the melting temperature of Sn respectively. The dotted green line is a result from studies with non-parabolic growth parameters ( $n \neq 0.5$ )**

If extrapolated to approximately  $T_{m,Sn}$ , the Diffusion Coefficients of Cu<sub>6</sub>Sn<sub>5</sub> are similar and would intersect near that temperature and show quasi-continuous consistent behavior. The same is true for the case of Cu<sub>3</sub>Sn. If the curves for Cu<sub>3</sub>Sn were extrapolated towards  $T_{m,Sn}$ , they would intersect close to that temperature, showing quasi-continuous and consistent behavior.

A different behavior can be observed for the case of Ni<sub>3</sub>Sn<sub>4</sub>. If extrapolated close to  $T_{m,Sn}$ , a jump of the Diffusion coefficient from growth by solid-solid diffusion (below  $T_{m,Sn}$ ) to growth by solid-liquid (above  $T_{m,Sn}$ ) by almost two orders of magnitude exists. The explanation for this is the different microstructure resulting from IMC growth of Ni<sub>3</sub>Sn<sub>4</sub> between Ni and solid Sn compared to Ni and liquid Sn as described in section 2.3. In the solid state, the growth of the Ni<sub>3</sub>Sn<sub>4</sub> IMC is continuous and homogeneously, whereas in the liquid state the sponge-like microstructure with pores of liquid Sn forms, which is

highly heterogeneous.  $\text{Ni}_3\text{Sn}_4$  grains dislocate from the IMC surface and move into the liquid, leading to rapid spreading of the IMC. The liquid pores provide a fast diffusion path for Sn atoms towards the Ni, reinitiating nucleation and growth of  $\text{Ni}_3\text{Sn}_4$  IMC grains. Table 2-6 summarizes the governing equations, parameters, and constants of the growth kinetic models plotted in Figure 2-26.

The IMC growth kinetics can be summarized as follows:  $\text{Cu}_3\text{Sn}$  has the slowest IMC growth rates under all temperature conditions. The growth of  $\text{Cu}_6\text{Sn}_5$  is the fastest of all growth rates below  $T_{m,\text{Sn}}$ . The growth of  $\text{Ni}_3\text{Sn}_4$  is slow below  $T_{m,\text{Sn}}$ , but above that temperature threshold these IMCs show the fastest growth of all binary IMC systems. This has important implications. The growth of the  $\text{Ni}_3\text{Sn}_4$  IMCs in this case is slightly faster than that of  $\text{Cu}_6\text{Sn}_5$  IMCs. If the TLPS processing has not completed the IMC growth for  $\text{Ni}_3\text{Sn}_4$  IMCs, extensive annealing time above  $T_{m,\text{Sn}}$  is required for complete convergence to a TLPS joint consisting of Ni-particles and  $\text{Ni}_3\text{Sn}_4$  IMCs. This effect is less pronounced for the IMCs of the Cu-Sn system. No quantitative temperature-dependent growth kinetic models exist for the ternary Cu-Ni-Sn system. But the literature review in section 2.4 shows that the growth of  $\text{Cu}_3\text{Sn}$  IMCs is further slowed down by the presence. The growth of  $(\text{Cu},\text{Ni})_6\text{Sn}_5$  IMCs above  $T_{m,\text{Sn}}$  at the Ni-side is faster than that of  $\text{Cu}_6\text{Sn}_5$  IMCs in the Cu-Sn system while the growth rate of  $(\text{Cu},\text{Ni})_6\text{Sn}_5$  IMCs at the Cu-side is approximately as fast as that of  $\text{Cu}_6\text{Sn}_5$  IMCs in the Cu-Sn system. Consequently the predicted process completion times for the systems assessed in this study are in descending order<sup>1</sup>:  $\text{Cu}_3\text{Sn}$  IMCs in the Cu-Sn system,  $\text{Cu}_6\text{Sn}_5$  in the Cu-Sn system,  $\text{Ni}_3\text{Sn}_4$  IMCs in the Ni-Sn system, and  $(\text{Cu},\text{Ni})_6\text{Sn}_5$  IMCs in the Cu-Ni-Sn system.

---

<sup>1</sup> Under otherwise identical parameters, e.g. particle size and distribution, sintering temperature etc.

**Table 2-6: Governing equations and associated parameters for the IMC growth kinetic models shown in Figure 2-26**

IMC Type	Governing Equations	$D_0$	$n$	$k_n$	$c_n$	Q in kJ/mol	$m_n$	$d_n$
$\text{Cu}_6\text{Sn}_5$ <232 °C	Equation 2-3	3.80e-7	0.5	-	-	81.00	-	-
$\text{Cu}_6\text{Sn}_5$ >232 °C	Equation 2-3	8.85e-13	0.5	-	-	19.72	-	-
$\text{Cu}_3\text{Sn}$ <232 °C	Equation 2-4 Equation 2-5 Equation 2-6	-	-	-0.67	1.91	-	6.16e-8	-1.25e-7
$\text{Cu}_3\text{Sn}$ >232 °C	Equation 2-3	1.36e-8	0.5	-	-	73.33	-	-
$\text{Ni}_3\text{Sn}_4$ <232 °C	Equation 2-3	3.22e-3	0.5	-	-	128.00	-	-
$\text{Ni}_3\text{Sn}_4$ >232 °C	Equation 2-3	8.47e-12	0.5	-	-	28.78	-	-

## 2.6 Comparison of Layer-based and Paste-based TLPS approaches

A multitude of Layer-based TLPS interconnect approaches have been introduced in literature. The amount of published work is too numerous to be completely reviewed in this work. The majority of the work is based on the joint fabrication by sandwiched layers of Au-Sn [79] [80] [81], Au-In [82] [83] [84] [85], Ag-Sn [86] [87], Ag-In [88] [89] [88] [90], Cu-Sn [91] [92] [93] [94], Cu-In [95], and Ni-Sn [96] [97]. Common to this approach is a layer of low melting temperature constituents (*A*) which is sandwiched between layers of high melting temperature constituents (*B*). Upon melting of *A* the growth of *A-B* IMCs is initiated and the sintering proceeds as described above. The principle of the process is shown in Figure 2-27. The layer thicknesses in this figure are not to scale.

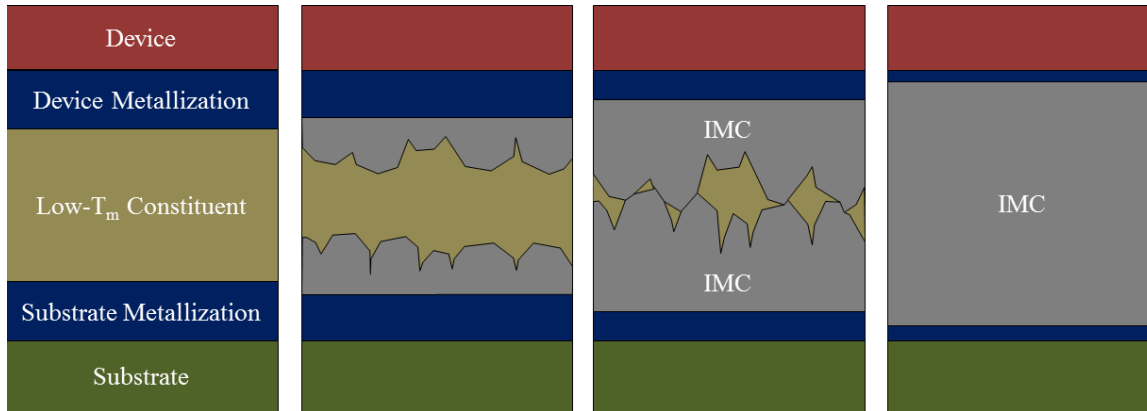


**Figure 2-27: Principle of transient liquid phase sintering by the layer-based approach. The low melting point layer is consumed by reaction with the metallization layers**

Multiple options for the application of the low melting temperature layer exist, compare Figure 2-28. The first option is the use of a preform, compare Figure 2-28 a). In this case no modification to the metallized surfaces of the substrate and the device is required. The preform is applied right before the sintering process is initiated. The advantage of this process is that the thickness of the low melting temperature layer is easily adaptable by the use of thicker preforms. Compared to the other two options thicker bond layers are practically achievable. Disadvantageous is that this approach requires good wetting capability of the low melting temperature material on the metallization surfaces of substrate and device. Furthermore high precision is required during positioning of the preform and the device to minimize misalignment in the joint region. Additionally soft preforms can easily be bent during handling which can lead to issues concerning their planarity.

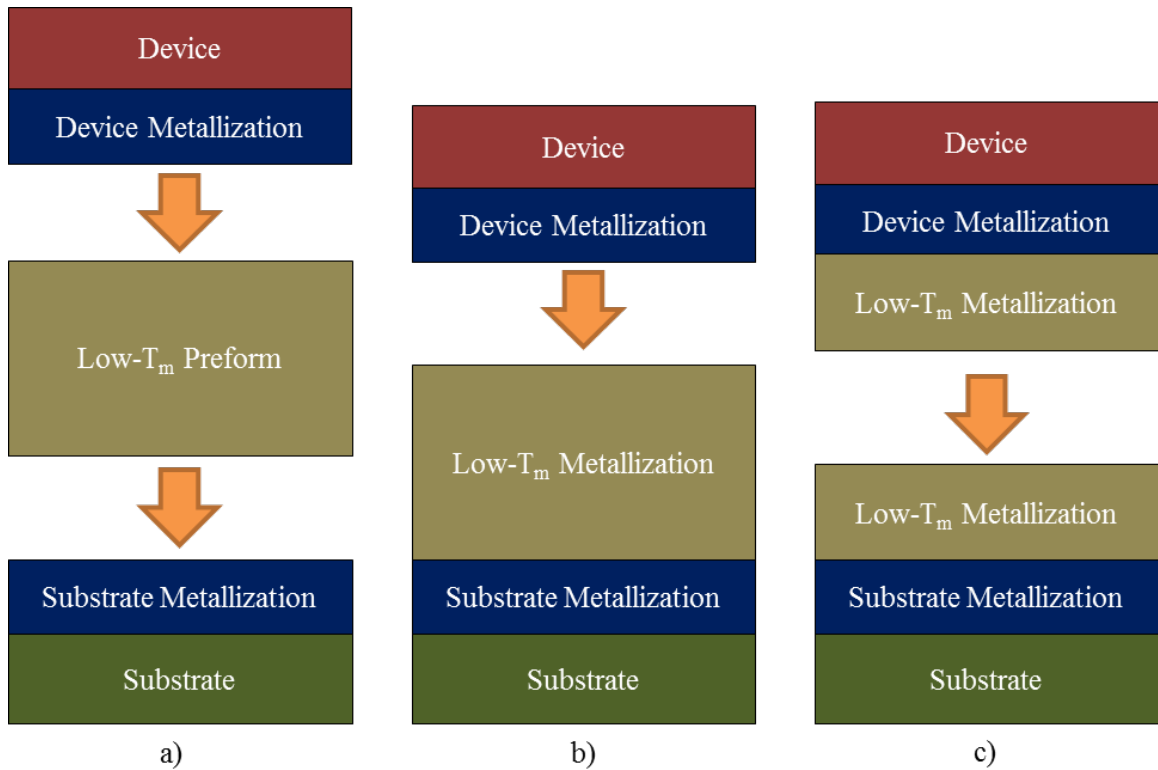


**Figure 2-28: Options for the application of the low melting temperature layer: a) Sandwicing of a preform between device and substrate metallization, b) application of a low- $T_m$  metallization on one metallization side via sputtering or plating, and c) application of a low- $T_m$  metallization on both metallization sides via sputtering or plating**

The second option is the adding of a low melting temperature metallization layer on top of either the substrate or the device metallization, see Figure 2-28 b). This metallization can either be applied by sputtering, physical vapor deposition (PVD), chemical vapor deposition (CVD), electroless plating, or electroplating. Sputtering forms metallization layers with the best adhesion properties, but layer thicknesses are limited to few micrometers for feasible sputtering durations. Electroplating can be used to deposit thicker layers, but is time-consuming for thick layers (e.g. > 20  $\mu\text{m}$ ), Furthermore electroplating of diced devices is impractical and devices with low melting temperature metallizations of considerable thickness are commercially not available, which explains why this approach has mainly been used to metallize the substrate side. Advantageous to this approach is that

standard devices can be used without prior modification. Furthermore no wetting issues exist at the metallized joint side because of the intimate contact after deposition. Additionally no alignment issues exist because the entire joint area is metallized with low melting temperature materials. Disadvantages are the limited achievable joint thicknesses and the associated tolerance requirements to surface roughness and planarity. Furthermore, the plating (or deposition) process can consume excessive time.

The third option is the adding of a low melting temperature metallization layer on top of the substrate and the device metallization, see Figure 2-28 c). The plating options are identical with those mentioned above. The plating of layers with thicknesses of multiple micrometers on the device side is only possible for full wafers, not for diced devices. Not all devices might be available in this form, and they might be harmed by the electroplating process. The advantage of this approach compared to the plating of only the substrate side is the doubled effective joint thickness, which can be used to reduce the plating duration or increase the total joint thickness.

All layer-based Transient Liquid Phase Sintering approaches have multiple disadvantages concerning the process requirements for high temperature interconnects manufacturing. The thickness of conventional solder interconnects is in the range of 10 - 150  $\mu\text{m}$ , with high temperature die attaches thicknesses of approximately 50  $\mu\text{m}$ . In theory thinner bond lines can be achieved, but practically the minimum bond line thickness is limited by multiple factors concerning the roughness of the joint surfaces: (1) Roughness of substrate and device surfaces from original material or preceding process steps. (2) Roughness of the preform or electroplated low melting temperature layers: These metal layers inherently show certain degrees of roughness that add to the roughness of the substrate and device

surfaces. During melting, the low melting temperature phase must wet all surfaces of the high melting temperature metallizations. If the roughness between the joint surfaces is too high, areas that are not in contact remain unwetted during processing. The gaps between material peaks protruding into the melt region cannot be filled sufficiently with liquid and voids remain after process completion. Figure 2-29 shows the mechanism of void formation for this case. The deposited low melting temperature phase (brown) follows the surface profile of the underlying substrate metallization, see Figure 2-29 a). After placing the device on the metallized substrate, the process temperature is increased above the melting temperature of the low melting temperature phase. It melts and partially wets the surface of the device metallization at locations of roughness peaks, see Figure 2-29 b).

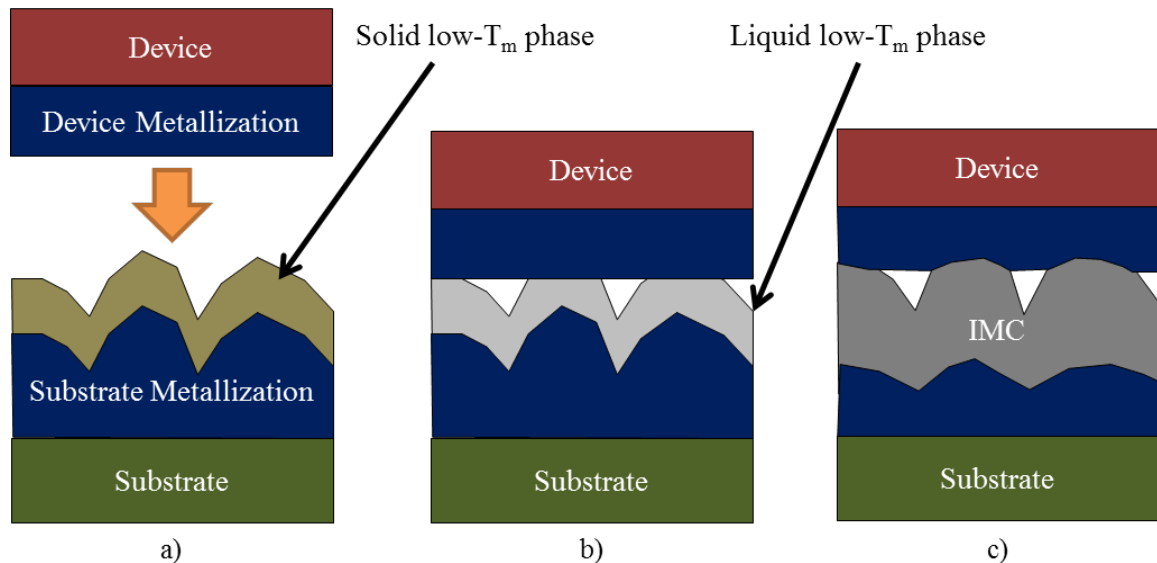


**Figure 2-29: Void formation by insufficiently thick low melting temperature phase layer thickness in layer-based TLPS: a) roughness of the substrate metallization before sintering, b) partial wetting of the device metallization during sintering, and c) formation of voids in the gaps that were not filled by liquid**

Areas of roughness recesses will not contact the surface of the device metallization if the thickness of the low melting temperature layer is too thin. Intermetallic phases form and voids remain between the IMCs and the device metallization, see Figure 2-29 c). This

behavior becomes more pronounced as the thickness of the deposited low melting temperature phase approaches the roughness of the substrate metallization. Furthermore tight tolerance limits are required for bending of substrates and devices before and during processing, which can be impossible to satisfy for complex substrates with heterogeneous structures based on technologies such as PCB, DBC/DBA, or AMB. This creates a lower limit to the low melting temperature phase layer minimum thickness.

Soto et al. have demonstrated reliability issues associated with the formation of these voids for layer-based TLPS interconnects [81]. In their work they joined a SiC diode and an AlN DBC substrate by consumption of a layer of eutectic Au-Sn solder sandwiched between Au metallization layers. The backside metallization of the 4 x 4mm<sup>2</sup> SiC diode consisted of 0.1 μm of Ti and a final metallization layer of 4 μm Au. Both layers were deposited by an evaporation process. The DBC substrate featured a 5 μm thick Electroless Nickel Immersion Gold (ENIG) diffusion barrier layer upon which in sequence a 4 μm thick Au layer, an 8 μm eutectic Au-Sn layer, and a 400Å thick Au flash layer as oxidation prevention layer were applied. All DBC metallization layers besides the original Cu and ENIG layers were deposited by a Jet Vapor Deposition (JVD) system. The sintering process was performed under four bonding conditions: 315 °C for 5min, 315 °C for 10min, 340 °C for 1min, and 340 °C for 5min. Subsequently samples were aged at 250 °C for 1000, 2000, 3000, and 4000 hours. It was found that the deposited eutectic Au-Sn layer conformed the roughness of the underlying ENIG metallization. This caused the formation of a repetitive pattern of gaps between the SiC and the joint material, similar to the one shown in Figure 2-29. Upon aging this initiated the formation of cracks between these gaps,

which is a crucial reliability issue reducing the adhesions strength, joint cohesion, and reliability of the TLPS joint.

In contrast to the layer-based TLPS approaches, paste-based TLPS approaches are able to compensate for peaks and recesses due to surface roughness of the joint surfaces. Figure 2-30 shows this for the example of a joint formed between a Ni die and a Ni-plated DBC substrate. The sinter pastes were mixed from particles of Ni and Sn embedded in a binder.

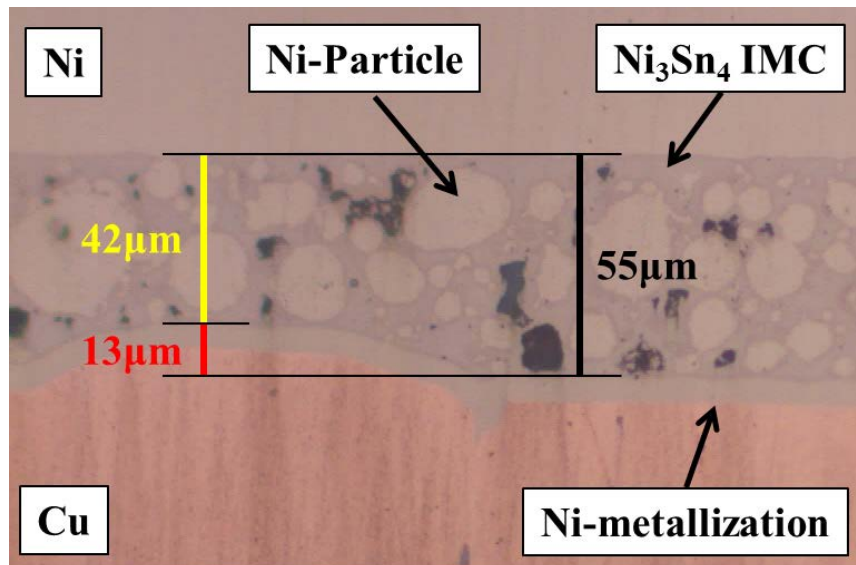


**Figure 2-30: Roughness compensation by use of TLPS sinter pastes: A Ni-die was joined to a Ni-plated DBC substrate by the use of Ni-Sn sinter pastes. The roughness of the substrate is compensated by varying sinter paste thickness after stencil printing. The Ni die is continuously in contact with the TLPS joint**

The sinter pastes were applied by stencil printing. The roughness of the DBC metallization is approximately 13 μm in this cross-section. It can be seen that the sinter paste is able to compensate for the height variation of the substrate metallization. The thickness of the sinter layer is adapted so that the surface of the printed layer has high levels of planarity. As a consequence, the surfaces of the substrate and the die are in intimate contact with the sinter paste and show excellent wetting during and adhesion after the sintering process.

The fact that reliable joining of TLPS joint necessitates a minimum thickness of the liquid layer that is thick enough to compensate for the roughness of the substrate and device metallization layers creates a set of issues related to processing of layer-based TLPS joints. As mentioned above, the sputtering or plating of thick film layers thick layers ( $> 5 \mu\text{m}$ ) requires long process times, with high associated costs.

Additionally the sintering of thick layers requires extensive processing times at elevated temperatures for full process convergence and complete formation of high melting temperature phases. Long processing at high temperature can degrade elements of the electronic package and reduce system reliability, and again, has high associated costs. The formation of IMCs in the Cu-Sn, Ni-Sn, and Cu-Ni-Sn systems, as well as the associated process kinetics, have been discussed in detail in sections 2.2 to 2.5. Table 2-7 summarizes the required times for process completion assuming theoretical full process convergence (no residual low melting temperature phases present in joint).

**Table 2-7: Calculated minimum time for complete TLPS process completion for multiple joint thicknesses for sintering temperature of 300 °C and 200 °C. Calculations are based on data summarized in Table 2-6.**

IMC growth Thickness [ $\mu\text{m}$ ]	Min. Sintering time at 300 °C [min]			Min. Sintering time at 200 °C [min]		
	Cu <sub>6</sub> Sn <sub>5</sub>	Cu <sub>3</sub> Sn	Ni <sub>3</sub> Sn <sub>4</sub>	Cu <sub>6</sub> Sn <sub>5</sub>	Cu <sub>3</sub> Sn	Ni <sub>3</sub> Sn <sub>4</sub>
5	30	146	21	967	21468	17694
10	118	585	83	3868	85874	70775
25	739	3655	517	24172	536712	442346
50	2955	14619	2068	96688	2146850	1769382
100	11821	58475	8273	386752	8587399	7077529

Conventional die attach solder joints have a thickness of approximately 50  $\mu\text{m}$ . When high melting temperature material for TLPS is present only on the substrate side, this would require an IMC growth of 50  $\mu\text{m}$  for layer based TLPS. This would require a time to

process completion at a sintering temperature of 300 °C of 2955, 14619, and 2068 minutes (approximately 2.1, 10.2 and 1.4 days) for full joint transformation to  $\text{Cu}_6\text{Sn}_5$ ,  $\text{Cu}_3\text{Sn}$ , and  $\text{Ni}_3\text{Sn}_4$ , respectively. For a layer arrangement with high melting temperature material on the substrate and device side with a joint thickness of 50  $\mu\text{m}$ , the required IMC growth thickness reduces to 25  $\mu\text{m}$  as IMC growth occurs simultaneous from both joint surfaces. This would reduce the required process duration at 300 °C to 739, 3655, and 517 minutes or approximately 0.5, 2.5, and 0.4 days. These process durations are not economically or technically feasible for the manufacturing of electronic systems. If the total joint thickness was reduced to 20  $\mu\text{m}$  and high temperature material was present on device and substrate side, the time to process completion would reduce to 118, 585, and 83 minutes, which are approximately 2.0, 9.7, and 1.4 hours for  $\text{Cu}_6\text{Sn}_5$ ,  $\text{Cu}_3\text{Sn}$ , and  $\text{Ni}_3\text{Sn}_4$ , respectively. This means the process is technical but not economically feasible for the  $\text{Cu}_6\text{Sn}_5$ , and  $\text{Ni}_3\text{Sn}_4$  systems. Joint thicknesses below that range run the risk of inadequate wetting and adhesions and associated high voiding levels as shown in [81].

Another issue with layer-based TLPS approaches is the requirement of consumable high melting temperature material on the device and substrate side. The ratio of high and low melting temperature constituents depends on the material system used. Figure 2-31 gives an overview of the minimum and maximum volume percentages of high and low melting temperature materials respectively for potential high temperature TLPS systems. The volume percentages were calculated from the stoichiometry of the dominant IMC (e.g.  $\text{Cu}_3\text{Sn} \rightarrow$  Atomic percentages Cu/Sn:  $3/1 = 75/25$ ) converted to the volume ratio by weighting the atomic percentages with their atomic weights and the density. The volume percentage of the high melting temperature constituent is the minimum percentage required

for full consumption of the low melting temperature phase. The systems with In as low temperature constituent require relatively low percentages of high melting temperature material, but their application is limited by the high material costs. The noble metals Ag and Au are widely applied metallization types in the electronic industry because of their resilience to the formation of oxide layers. Yet their application in TLPS interconnects is not just limited by their high cost, but also the high volume percentage required for successful TLPS bonding, see Figure 2-31. The percentage of Cu required for the full formation of  $\text{Cu}_6\text{Sn}_5$  IMCs is relatively low, but the formation of the  $\text{Cu}_3\text{Sn}$  IMC requires much higher levels of Cu. Ni is a good candidate system from the layer thickness point of view. Yet the wetting properties of Ni are worse than for the other metals in consideration.

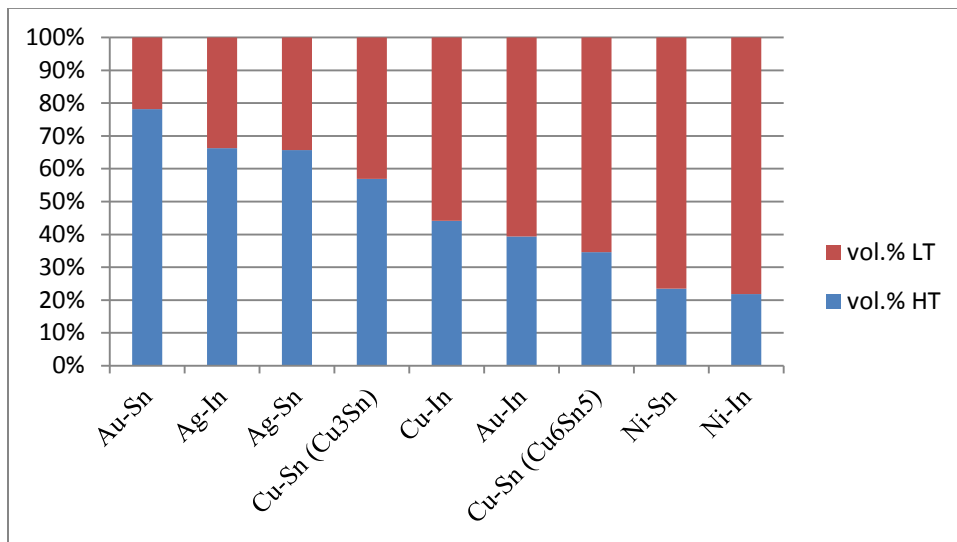


**Figure 2-31: Required vol.-percentages of low and high melting temperature phases (LT and HT respectively) for complete TLPS bonding.**

Figure 2-32 summarizes the required high melting temperature constituent layer thickness for complete TLPS of a 25  $\mu\text{m}$  thick low melting temperature layer. This describes the case of a joint thickness of 50  $\mu\text{m}$  with consumable high melting temperature material on the device and substrate side. The material systems are identical with those shown in Figure 2-31. The layer thickness was calculated from the volume percentages ratios assuming that

the volume is proportional to the layer thickness, which means that the area of the layers is identical, which is the case in layer-based approaches. Only the Ni-Sn and Ni-In systems can practically be used to form layer-based TLPS in this case. All other material systems require layer thicknesses  $>10\ \mu\text{m}$ , which, as mentioned above, is not feasible considering the duration of the plating/sputtering process for these layer thicknesses. Metallization layer thicknesses of commercially available power electronic device are usually in the range of 1 - 2  $\mu\text{m}$  (e.g. Wolfspeed CPW5-1700-Z050B Silicon Carbide Schottky Diode has a Ni/Ag cathode metallization with a total thickness of 1.8  $\mu\text{m}$  [98]), orders of magnitude below the required layer thicknesses.

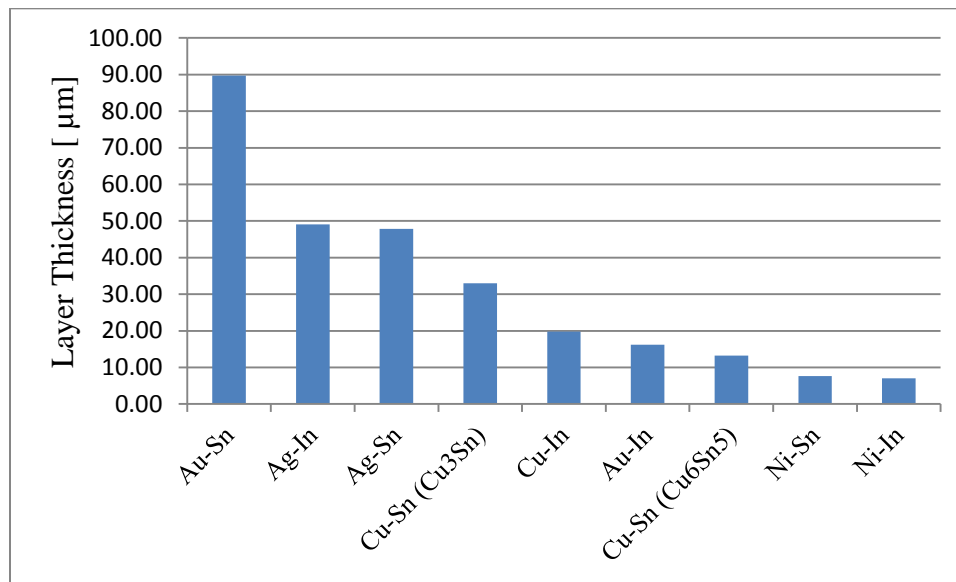


**Figure 2-32: Minimum required high melting temperature layer thickness for complete consumption of a 25  $\mu\text{m}$  thick low melting temperature layer.**

In contrast to layer-based TLPS approaches, paste-based TLPS approaches do not suffer from such limitations. Figure 2-33 shows a SEM image of a cross-section of a TLPS interconnect formed between a Ni-substrate and a Si-diode with Ag-metallization. The sinter paste constituents were Ni-spheres and Sn<sub>3.5</sub>Ag spheres in resin-based flux binders. The joint was formed by sintering for 30 minutes above melting temperatures with a peak

temperature of 300 °C. The joint thickness is approximately 100 μm. As shown in Table 2-7, the formation of 100 μm of pure Ni<sub>3</sub>Sn<sub>4</sub> IMCs from TLPS layers at 300 °C requires a calculated time to process completion of 8273 minutes, approximately 276 times longer than the processing time for this joint. Yet it can be seen that the Ni-particles are embedded in an almost continuous matrix of Ni<sub>3</sub>Sn<sub>4</sub> IMCs. The reason for this is that in the paste-based approach the required IMC growth thickness is approximately ½ the distance between neighboring particles. As the cross-section in Figure 2-33 shows, the half-distance between particles is on the order of 5 - 10 μm, which leads to considerably shorter required sintering durations.

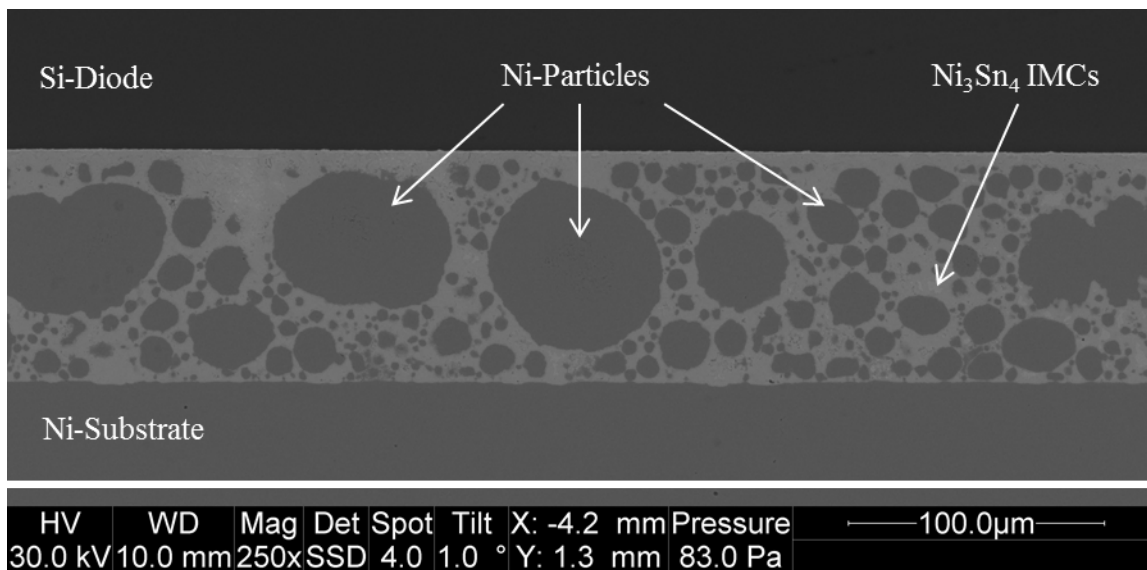


**Figure 2-33: SEM image of a cross-section of TLPS interconnect formed between a Ni-substrate and a Si-diode via sinter pastes consisting of Ni- and Sn3.5Ag solder particles**

It can be seen in Figure 2-33 that the Ni-Substrate has hardly been consumed. The distance between the substrate and adjacent Ni-particles is similar to the spacing between particles. This indicates that the IMCs in the joint are formed predominately by consumption of high melting temperature constituent materials from particles, not the substrate. As a consequence, in contrast to layer-based approaches, no additional high melting temperature

metallization needs to be applied on the substrate or device side. This can also be seen in Figure 2-30. The  $\text{Ni}_3\text{Sn}_4$  IMCs have grown throughout the entire joint up to the Ag-metallization of the diode, which has partially transformed to  $\text{Ag}_3\text{Sn}$  IMCs. In consequence, the paste-based approach decouples the time to joint completion from the joint thickness and eliminates the need for costly thick metallization layer on the device or substrate side. Potential disadvantages of the paste-based approach are the larger area of metal surfaces that is susceptible to oxidation during the heating phase of the sintering process. The oxidation of these surfaces can be avoided by the use of a reducing flux binder that reduces metal oxides and improves the wettability of the metal particle surfaces. Yet the complex organic compounds present in these flux binders evaporate during the process and, if the formed gases are trapped inside the joint, pose a risk for void formation. Details on relevant process parameters and process challenges for the manufacturing of paste-based TLPS interconnects can be found in section 4.

## 2.7 Paste-based TLPS Interconnects in Electronic Applications

### 2.7.1 Literature Overview

In contrast to layer-based TLPS approaches, only limited literature has been published on paste-based TLPS. Sharif et al. performed TLPS between Cu substrates with Ag-Sn sinter pastes [99]. The percentage of the Ag relative to the total metal content was varied between 50 and 100 weight-%. Two types of sample were prepared: (1) Pastes were formed by a mix of Ag and Sn particles with particle sizes  $<5 \mu\text{m}$  and no-clean flux. Pastes were stencil printed on a Cu substrate with side length of 5mm x 5mm and a Cu die with side length of 2.5mm x 2.5mm was placed on the printed layer. Subsequently they were sintered at 250 °C for 10 minutes with an applied pressure of 1.2 MPa. The resulting joint thickness ranged

between 30 - 50  $\mu\text{m}$ . These samples were used for shear strength tests at room temperature and at elevated temperature conditions by placing them on a hotplate set to 250  $^{\circ}\text{C}$ . (2) The other type of sample was prepared by dry mixing of Ag and Sn particles and subsequent uniaxial pressing into pellets. These samples were sintered without pressure in air atmosphere at 250  $^{\circ}\text{C}$  for 10 minutes, too. These samples were used for Vickers hardness, process completion, and electrical resistance tests. A minimum amount of 75% Ag by weight was required for the complete consumption of Sn. The sintered samples showed an increase in microhardness with an increase of Ag up to 75% by weight and a decrease beyond that concentration. The electrical resistivity decreased continuously with increasing Ag-content. The shear strength decreased with increasing Ag content both at room temperature and elevated temperature conditions. The difference between room temperature and high temperature shear strength was most pronounced for high Ag contents, which is counterintuitive considering their results from the process completion analysis. They showed that higher Sn-concentrations lead to the formation of a less voided Ag/Cu interface which might explain the improved strength of these joints.

Fujino et al. joined Si-dies to Cu-substrates with Sn-Ag sinter pastes [100]. Their sinter paste consisted of Ag- and Sn-powders with grain sizes of approximately 0.2-0.3  $\mu\text{m}$  and 3  $\mu\text{m}$ , respectively, embedded in terpeneol. Three types of sinter paste were used: Ag-30Sn, Ag-40Sn, and Ag-50Sn sinter pastes with 30, 40, and 50 wt.% Sn, respectively. The pastes were printed with a thickness of 90  $\mu\text{m}$  on Cu-substrates with side lengths of 10mm. Au/Ni/Ti-sputtered Si-dies with side lengths of 3.5mm were subsequently placed on the printed layers. Sintering was performed by preheating the samples at 125  $^{\circ}\text{C}$  for 10min and subsequent heating to 260  $^{\circ}\text{C}$ , 280  $^{\circ}\text{C}$ , and 300  $^{\circ}\text{C}$  at 30-40  $^{\circ}\text{C}/\text{s}$  under simultaneous

application of 5 MPa of pressure. Heat and pressure were held at those levels for 1min. They showed that the voiding levels reduced with increasing Sn-content and increased process temperature. Cu-Sn IMCs formed at the interface between the Ag-Sn sinter joints and the Cu-substrates. Die shear tests showed that the Ag-30Sn samples possess good shear strength up to 250 °C, but that only limited sintering occurred at the edge of the Si-dies. They concluded that the formation of Cu-Sn IMCs near the Cu-substrates causes considerable consumption of Sn, which leads to insufficient presence of Sn at the joint edges during processing.

Ehrhardt et al. have demonstrated Cu-Sn sinter pastes for power electronic applications [101]. Initially flux-based sinter pastes consisting of commercial Sn95.5Ag4Cu0.5 (SAC405) solder and Cu powder with Cu percentages between 10% and 40% by weight were used to join Cu-coupons and Cu-substrates. They showed that Cu-ratios required for full joint transformation (> 35 weight%) prevented the densification of their joint and lead to the formation of a skeleton structure of Cu-particles connected by solder with large amount of voiding. This minimized wetting of the surfaces of the Cu die and Cu substrate and reduced the overall joint integrity, strength, and reliability. In another approach they tested a Cu-Sn sinter paste with 35 weight% Cu and 65 weight% SAC405 in a non-reducing, non-flux solvent. In this case the solder melted, but the oxides on the surfaces of the Cu-particles, die, and substrate were not reduced and only limited wetting occurred. Due to application of a pressure on the die, solder was partially pressed out of the joint region. A secondary process step above melting temperature was applied in an atmosphere with activation gas (CO, SF<sub>6</sub>, HCOOH). For short activation times (< 1 hour), the reducing gas was not able to activate all surfaces at the center of a 100 mm<sup>2</sup> die, and liquid solder

was running under the edge of the pre-processed joint, causing joint line delamination and extensive void formation. For extended process times (> 1 hour) the solder that had been squeezed out during processing successfully infiltrated the joint, leading to a continuous bondline. Shear tests performed at 1 MPa shear load with heating rates of 6 K/min showed that the bonding re-melting temperature was approximately 400 °C.

In [101] Ehrhardt et al. also suggested a TLPS concept with solder deposited outside the chip area which, upon melting, infiltrates a Cu-paste mesh below a die. They demonstrated joints formed by this concept in [102]. Here the process steps are as follows: In the initial state, a Cu-Sn paste formed from Cu- and Sn-particles and a non-reducing flux is printed on a substrate and a chip placed on top. The paste is dried and additional solder is positioned at the die edges. Afterwards the Cu-oxides are reduced at elevated temperatures in the activation gas atmosphere described above. Solder wets and infiltrates the Cu-mesh under the die and the Cu-Sn IMCs are formed. A design of experiment with variation of the following parameters was performed: Substrate metallization (Ni-Au- or Cu-finish), Chip metallization (Ni-Ag- or Cu-finish), Cu powder size (20-45 or 5-15  $\mu\text{m}$ ), Stencil thickness (50 or 150  $\mu\text{m}$ ), and arrangement of stencil printed structure (fully printed and four-times splitting). Substrate and chip metallization did not influence the infiltration behavior of the Cu-mesh significantly. The infiltration behavior improved with a reduction of the stencil thickness. The use of a splitting mask improved the wetting of the Cu-mesh, but low-melting temperature solder which will not convert to high-temperature phases filled the channels in between the separated areas. The use of finer Cu powders reduced the infiltration of the Cu-mesh. Table 2-8 gives an overview of the influence of the parameters on the voiding of the Cu-Sn sinter joint.

**Table 2-8: Non-infiltrated area in percent of the Cu-mesh. Reproduced from [102]**

<b>Process Parameter Variation</b>	<b>Non-infiltrated Area</b>
Reference	35%
Cu-surface on substrate	31%
Cu-surface on die	40%
Decrease of stencil thickness	13%
Splitting stencil mask	17%
Splitting stencil mask and decreased Cu-particle size	28%

Additionally they performed passive thermal cycling test between -55 °C and +125 °C. Multiple failure modes were detected. In the case of a Si-die on a direct bonded aluminum substrate (DBA), vertical cracks were detected propagating from the DBA through the Cu-Sn TLPS layer into the Si-die. The crack propagated deeply into the Si-die, but stopped after few micrometers in the aluminum layer of the DBA. A different failure mode was detected for Si-dies on a Cu leadframe. Here the Ti/Ni die backside metallization peeled off from the Si-die leading to complete delamination. Another failure mode appeared when a Si-die with an additional 40-50 µm Cu/Al metallization layer on top was used. In this case the top side chip metallization peeled off with Si residues attached. When this arrangement was used with the Si-die with Cu/Al buffer layer flipped (in this case the Cu/Al buffer layer was oriented towards the Cu-Sn TLPS joint), the above failure modes could be suppressed successfully.

Liu et al. have used Sn-coated micro-sizes Cu particles for Cu-to-Cu bonding [103] [104]. They fabricated the sinter paste particles by electroless plating of Cu particles with Sn. The average diameter of the Cu particle before plating was 6.2 µm and the thickness of the Sn coating approximately 0.5 µm. A sinter paste was manufactured by mixing the Sn-coated particles with 15 wt.% terpeneol. The sinter paste was applied between two discs of pure

Cu. The initial processing step was a pre-heating of the Cu-Cu joint specimens to 130 °C for 3 minutes in air at a pressure of 10 MPa to evaporate the solvent. Subsequently the specimens were heated to 300 °C at a ramp rate of 1 °C/s and bonded at that temperature level with a dwell time of 30s. This process step was performed in a formic acid gas atmosphere to reduce the oxides on the Sn coating and Cu disks. The microstructure of these joints was characterized by a Cu<sub>3</sub>Sn matrix with embedded Cu particles. The microstructure did not develop further after aging for 200h at 300 °C, which indicates that the process converged and completed fully after processing. Accordingly, no pronounced deviation between the shear test results of as-processed and aged specimens could be detected. The average shear strength of unaged joints was 24.2 MPa.

Hu et al used Sn-plated Cu-particles with a diameter of 30 μm that were plated with Sn in an electroless plating solution [105]. The thickness of the Sn-plating was approximately 2 μm. The Cu-Sn microparticles were subsequently compressed into a preform with a thickness of approximately 400 μm. The preforms were reflowed at 250 °C for 8, 16, and 40 minutes between Cu-substrates. It was shown that process times of 20 minutes are sufficient for the creation of matrix of Cu-Sn IMCs between the Cu substrates and after 40 minutes the joint consists predominately of Cu-particles embedded in a matrix of Cu<sub>3</sub>Sn IMCs. The joints possessed high shear strength up to 500 °C. The failure mode during shear testing changed from inter-IMC grain failure in the Cu<sub>6</sub>Sn<sub>5</sub> IMCs after 20 minutes of sintering to propagation along the interface between Cu-particles and Cu<sub>3</sub>Sn IMCs after 40 minutes of aging,

Corbin analyzed the TLPS process for the Sn-Sb system [106]. The sinter pastes were formed from a metal particle mix of 90 wt.% Sn and 10 wt.% Sb. The Sb particles had a

median diameter of 89  $\mu\text{m}$ . Spherical Sn particles with three median diameters of 9, 89, and 145  $\mu\text{m}$  were used. The flux consisted of mixes of DMA-HCl dissolved in water and rosin dissolved in isopropanol. Higher levels of fluxes reduced the initial melting temperature range, which can be explained by the improved reduction potential of higher concentrated fluxes. For lower flux content the solder paste melted primarily by melting of the Sb particles rather than by melting of the Sn particles (with higher and lower melting temperatures respectively). It was shown that for temperatures below the melting point of Sb, significant amounts of intermetallic phases formed at the interface between liquid Sn and solid Sb. Furthermore, the liquid Sn is alloyed with Sb, raising the melting temperature of the joint by up to 9.5  $^{\circ}\text{C}$ . Though phenomenologically this material system is interesting, the amplitude of the melting temperature shift is too small to be of interest in for high temperature applications.

Mokhtari and Nishikawa studied the transient liquid phase bonding of Sn-Bi solder with added Cu particles [107]. The eutectic Sn-Bi alloy is Sn-58Bi and possesses a melting point of 139  $^{\circ}\text{C}$ . Because of its low melting temperature, Sn-58Bi is usually used for low temperature applications. As described in section 2.2, Cu and Sn form intermetallic compounds, which can be used to form joints with high melting temperature. Bi on the other hand does not form IMCs with Cu. Upon melting, Sn-58Bi wets surfaces of Cu. Sn from the alloy is consumed and Cu-Sn IMCs are formed. A mix of Bi-rich phases and residual Sn-58Bi remains. After complete consumption of Sn from Sn-58Bi, only high melting temperature Cu-Sn IMCs and the Bi-rich phase remains. Under the assumption that in the early stages of the process only  $\text{Cu}_6\text{Sn}_5$  IMCs form, they predicted that a Cu content of approximately 30% Cu by mass was necessary to consume all Sn from the Sn-

58Bi solder. Sinter pastes consisting of Sn-Bi solder with 30 mass% Cu added were mixed and sintered by pre-heating at 100 °C for 150s and subsequent reflowing at 170, 200, and 230 °C for 1, 10, and 50min. Reflow temperatures of 170 °C did not result in a completed consumption of the Sn-phase. At 200 and 230 °C reflow periods of 50min lead to complete consumption of the Sn-rich phase. The final microstructure of these joints consisted of a matrix of a Bi-rich phase with dispersed Sn-Cu IMCs. Spalling of Cu-Sn IMCs from the Cu particles into the liquid phases was observed throughout the joint. DSC analyses of the paste pre-processing showed that two types of heat flow peaks existed, one corresponding to the Sn-Bi eutectic at 139 °C, the other type of peaks corresponding to the Sn-Cu IMCs. After 10 minutes of processing at 200 °C another type of peak appeared with a corresponding melting temperature of 201 °C. When reflowed for 50 minutes at 200 °C, the peak at 139 °C disappeared almost completely and the peak at 201 °C grew significantly. This indicates that the low melting temperature Sn-Bi phase was consumed and transformed to a phase with a high melting temperature of 201 °C. As a consequence, a melting temperature shift by approximately 62 °C could be achieved. Yet the re-melting temperature did not exceed the process temperature, and the resulting joint melting temperature was below those required in the above mentioned high temperature applications and even below those of Sn-based solder alloys such as Sn3.5Ag or SAC.

Lang et al. used Cu-Sn sinter pastes with a weight ratio of Cu/Sn = 60:40 formed by particle sizes < 1 µm to attach SiC diodes to active metal brazed copper substrates with Ni/Ag and Ni(P) metallization respectively [108]. Sintering was performed under nitrogen atmosphere at 260 °C for 20 minutes under application of a pressure of 0.3 MPa. Subsequently the packages were aged at 300 °C in air. The shear strength was measured at a temperature of

300 °C after multiple aging durations and compared to shear test performed with packages with Au-12Ge solder as die attach material. It was found that the shear strength of the Au-12Ge solder joints after processing was high ( $> 80$  MPa), but rapidly degraded after aging with a reduction of shear strength to below 20 MPa for aging durations  $> 500$  hours. In contrast, the shear strength of the Cu-Sn TLPS joints increased over time from below 40 MPa to above 50 MPa for aging durations longer than 200 hours. The consumption of the Ni metallization of the substrate was at least more than three times higher for the Au-12Ge at 300 °C as well as for SAC405 and Sn0.7Cu solders at 200 °C compared to the Cu-Sn TLPS joint, which indicates that this system has the potential to provide better longer term durability and reliability compared to these solders.

Dudek et al. simulated mechanical properties of Cu-Sn TLPS joints with regular particle arrangement [109] [110] [111]. Their simulations were based on a unit cell model consisting of 27 Cu spheres surrounded by spherical  $\text{Cu}_6\text{Sn}_5$  IMC layers in a solder matrix. The Cu spheres were arranged in a regular 3 by 3 by 3 grid. Five different test conditions with varying Cu and IMC content in the unit cell were assessed. Reducing Sn volume fractions correlate with TLPS process progression. The three highest Sn load conditions simulated structures without bridging between the Cu particles. The other two conditions correlated to a process progression state with limited and full IMC cross-bridging with limited Sn content and zero Sn content respectively. The boundary condition to the unit cells formed by this structure was subjected to 1% of tensile strain at room temperature. For the test conditions without IMC bridging, the stress peaked at the contact areas between the particles in the solder. The extent of stress concentration increased with reduced Sn content. After IMC bridging occurred, the stresses were concentrated at the interfacial

edges between the contacting IMC layers and the residual solder. The maximum creep strain condition was found to occur when the IMCs were not yet bridging. On the other hand the reaction force of the unit cell to the tensile load increased continuously with decreasing solder content [109]. For completely IMC filled cell structures the stiffness increased by a factor of seventeen compared to that of a unit cell with pure solder. It was furthermore found that for a constant solder content of 20vol%, the yield strength of the TLPS joint is not significantly influenced by small amounts of residual Cu in the joint, while for higher Cu contents (e.g. 20vol%) the yield strength of the TLPS joint decreases. This can be explained by the lower yield strength of Cu compared to  $\text{Cu}_6\text{Sn}_5$ . They applied the generalized stress-strain models to simulate the thermo-mechanical response to a structure consisting of a Si-die attached to a Direct Bond Copper (DBC) substrate with a TLPS joint. They found that this structure shows a much increased susceptibility to interface delamination compared to solder interconnects [109] as well as sintered silver interconnects [110]. In another publication they compared the simulated and experimental thermo-mechanical deformation behavior of a type CR1206 chip resistor attached to a Printed Circuit Board (PCB) [111]. A cross-sectioned arrangement of this structure was subjected to a temperature profile and the displacement measured with an optical correlation technique. The shear displacement between the resistor and the PCB was approximately three times higher for SAC solder joints compared to TLPS joints. Thermal cycling test with thermal cycles with low dwell temperatures of  $-40\text{ }^\circ\text{C}$  and high dwell temperature of 150, 200, and  $240\text{ }^\circ\text{C}$  were performed. The specimens were assessed after a period of 500 cycles. None of the samples cycled between  $-40$  and  $250\text{ }^\circ\text{C}$  survived the initial 500 cycles. For lower cycling amplitudes more samples survived the same period of

time. Brittle fracture of the IMC was found to be the dominant failure mode. The failure locations were at the interface of the resistor metallization to the TLPS joint or in the high stress IMC bridging regions.

Ji et al. used Ni-Sn sinter pastes to bond Si-dies to Ni-substrates [112]. The sinter paste consisted of Sn-particles and Ni-particles with particle sizes of approximately 40  $\mu\text{m}$  and 10  $\mu\text{m}$ , respectively. The pastes were formed by mixing the particles in an unspecified flux. The percentage of Ni in the sinter paste was varied between 0% and 30% by weight. The dies had side lengths of 5mm and possessed an 8  $\mu\text{m}$  thick deposited layer of Ni. The Ni-substrates had a side length of 10mm. Temperature-assisted ultrasonic bonding was used as joining process. The process parameters were 35kHz, 0.4 MPa, 10s, and 500W for the frequency, pressure, time, and power, respectively. The samples were simultaneously heated to 250 °C with heating and cooling rates before and after bonding of 35 °C/min and 16 °C/min, respectively. The sinter pastes with Ni-contents below 24wt.% Ni did not possess high melting temperatures. A Ni-content of 30wt.% limited the process capability because of the poor wettability. The 24wt.% Ni sinter pastes were identified as best solution for ultrasonic-assisted bonding. After aging at 300 °C for 72 hours, joints with 10wt.% Ni showed increased formation of  $\text{Ni}_3\text{Sn}_4$  IMCs, which lead to improved shear strength. Conversely, the shear strength of joints formed from 24wt.% and 30wt% Ni sinter pastes reduced after aging. The reaction mechanism of Ni-Sn IMC formation changed from a diffusion-controlled reaction to an ultrasonic-diffusion-controlled reaction with the application of ultrasonic excitation.

Noguchi et al studied the influence of tertiary metal particles on the stiffness of Ni-Sn sinter pastes [113]. Spark Plasma Sintering (SPS) was used to manufacture bulk TLPS samples

at a temperature of 300 °C for 60 minutes with simultaneous application of 2.7 MPa of pressure in vacuum. Subsequently, dog-bone structures were cut out of the bulk samples by electrical discharge machining (EDM). The length, width, and thickness of the dog-bone structures were 26mm, 9mm, and 2mm, respectively. Two types of sinter pastes were used: (1) a binary Ni-Sn sinter paste with a composition of 40-60 by wt.%, and (2) a tertiary Ni-(Ag-Al)-Sn sinter paste with a composition of 32-20-48 wt.%. The diameter of the Ni-particles and Sn-particles was  $< 44 \mu\text{m}$ . The Ag-Al particles consisted of an Al-core particle with diameters of 40-50  $\mu\text{m}$  and an Ag shell thickness of approximately 0.4  $\mu\text{m}$ . It was found that the average Young's Modulus of the binary sinter pastes was 87GPa compared to 39GPa for the tertiary sinter pastes. This demonstrates that the addition of third elements into sinter pastes can reduce the stiffness of the resulting joints below the stiffness of conventional solder alloys and sintered silver joints.

### 2.7.2 Gaps in Literature

Prior to this research, no research had been published on Ni-Sn TLPS sinter pastes. No research has been published on Cu-Ni-Sn interconnects. Limited literature exists on the aging behavior of paste-based TLPS interconnects. Prior to this research, no work had been published on the aging behavior of Ni-Sn or Cu-Ni-Sn sinter pastes. Limited research has been published on constitutive properties of joints formed from TLPS sinter pastes. Simulations have only been performed for Cu-Sn sinter paste joints with particles in regular arrangements. The constitutive properties of Cu-Sn sinter paste joints have not yet been assessed experimentally. Experiments assessing the constitutive properties of TLPS sinter paste joints have only been performed on Ni-Sn sinter pastes and only elastic properties have been determined. No simulation data of constitutive properties of Ni-Sn sinter paste

joints has been published. TLPS interconnects are characterized by particles randomly arranged within an intermetallic matrix system. No such simulations and experimental verifications have been performed. The thermal properties of TLPS sinter paste joints have not yet been assessed either by simulation or by experiments.

As of the writing of this document there is high interest in the field of high temperature attach materials for electronics and TLPS in particular. Consequently, multiple research efforts were performed in parallel to the work presented here. All of the research presented herein and the associated publications either predate other research efforts and publications or have been performed simultaneously to those efforts.

### 3 Objectives and Statement of Work

In this research, copper-tin (Cu-Sn), nickel-tin (Ni-Sn), and copper-nickel-tin (Cu-Ni-Sn) transient liquid phase sintering (TLPS) paste systems for high temperature applications are assessed. Sinter pastes for each material system (Cu-Sn, Ni-Sn, and Cu-Ni-Sn) will be developed and one optimized paste will be chosen each for in-depth process, constitutive and thermal properties, and microstructural assessments. Five major studies will be performed:

- 1) A process development study which will be used to identify potential material systems and to develop best practice methods for the manufacturing of sinter pastes. This will include the determination of optimal particle size ranges and of percentages of high melting temperature and low melting temperature constituents. Additionally, multiple paste deposition processes will be introduced to develop a substitute technology for conventional high temperature attach technologies. Process conditions (e.g. heating, dwell and cooling rates and times, pressure) will be optimized to ensure controlled processing and consistent results.
- 2) An aging study will be used to analyze the joint microstructure after processing and after extended annealing times under thermal aging conditions. Cross-sectioned samples will be analyzed by Optical Microscopy and Scanning Electron Microscopy (SEM). Elemental analyses will be performed by Energy-dispersive X-ray Spectroscopy (EDS/EDX). This will yield valuable insight into the formation and development of joint microstructure (e.g. void size and distribution, growth of intermetallic compounds, amount of residual metal particles in the joint, size, distribution, and orientation of grains) in processing and application conditions.

This will determine if and when steady-state conditions are approached and annealing processes are completed. It will furthermore show if the material systems converge to high application temperature capability and document the time to high temperature capability.

- 3) The results from the microstructural analyses will be used as input data for the creation of representative joint geometries with a high level of detail concerning joint features and microstructure in a newly developed software. Three-dimensional joint models will be derived from the geometry information and further assessed in simulation environments. Homogenized bulk material constitutive and thermal properties will be derived and used to simulate the thermo-mechanical behavior of large-scale systems (i.e. Iosipescu shear test samples and power module structures).
- 4) An Iosipescu shear test study will be performed to experimentally investigate the constitutive properties of the TLPS joints. The results of this study will be used to verify, validate, and, if appropriate, calibrate the constitutive properties derived through simulation.
- 5) The T3Ster thermal test system will be used to determine the transient thermal responses of thermal stacks with TLPS sinter paste joints. Thermal structure functions will be derived experimentally and compared to structure functions determined by transient simulations of the thermal stack. The thermal properties of TLPS sinter joints will be derived by iterative calibration of the simulated structure function to experimental data.

In combination, the aging study, the assessment of microstructure-dependent constitutive properties via simulation, the assessment of the micro-structure dependent thermal

properties via simulations, the constitutive properties measured by shear test experiments, and the thermal properties determined through coupled experimental-simulation approaches will for the first time demonstrate an integrated constitutive and thermal properties assessment approach for paste-based TLPS materials. The heterogeneous microstructure and high strength and stiffness of this class of materials requires the development of new assessment methods (i.e. simulation of constitutive properties) and the adaptation of conventional test approaches (i.e. use of more complex and difficult to manufacture high-strength Iosipescu coupons). The TLPS-specific processing requires the use of non-bulk joint samples for thermal properties analysis. The outlined approach is performed for three specific material systems (Cu-Sn, Ni-Sn, and Cu-Ni-Sn), but is versatile and can be adapted to other material types of interest in related and future work. Constitutive and thermal properties of paste-based TLPS interconnects will be assessed experimentally for the first time. This will in the future enable failure mode prediction and reliability assessments of interconnects consisting of this class of material. An overview of the approach can be found in Figure 3-1.

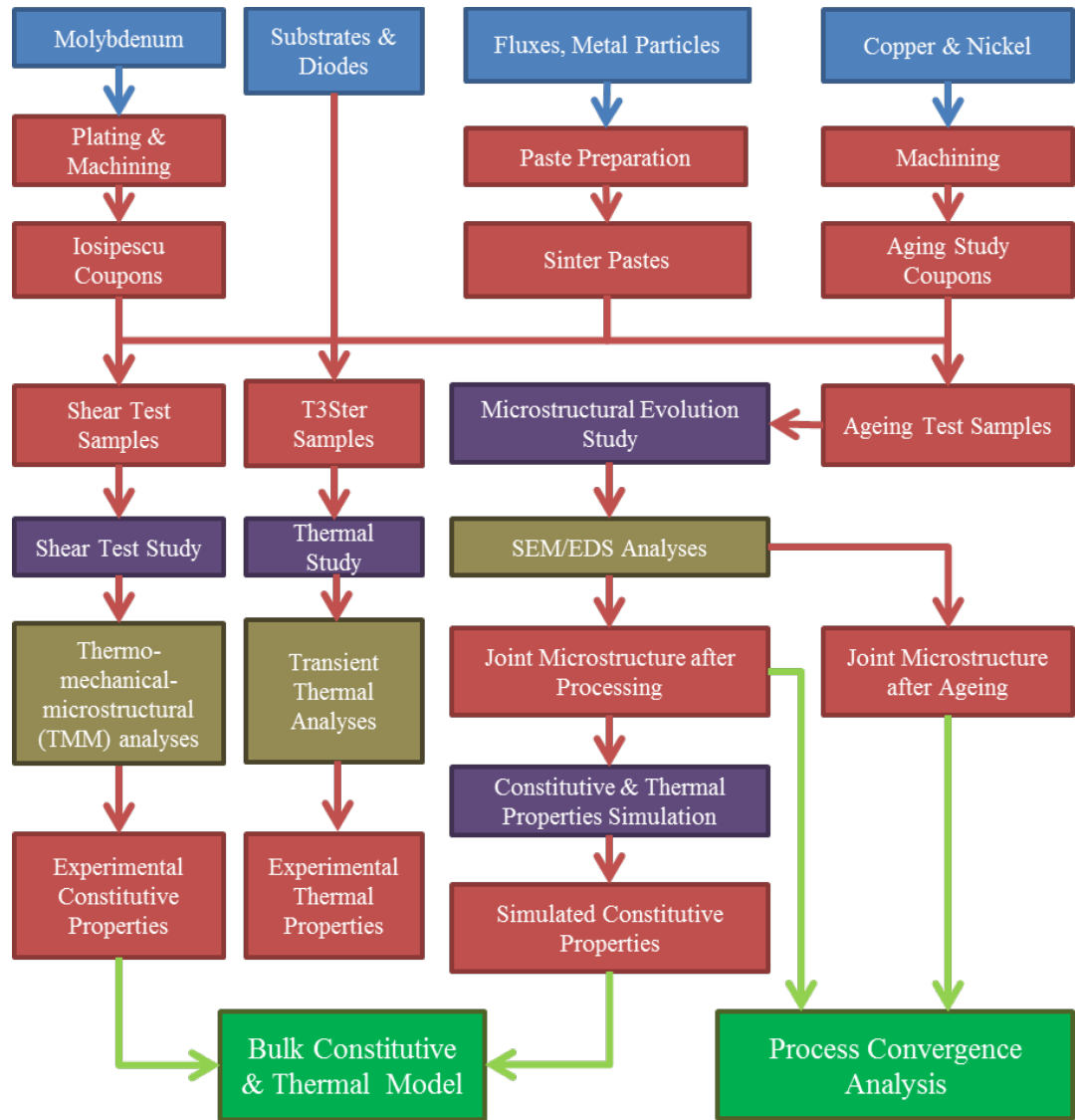


**Figure 3-1: Flow chart of the research effort in this work: Raw materials (blue), intermediate steps (red), analytical methods (brown), independent study elements (purple), and derived conclusive results (green)**

## 4 Processing of Paste-based TLPS Interconnects

The sintering of TLPS sinter pastes is a complex process. The fundamental material reactions of TLPS systems have been discussed in detail in sections 2.1 to 2.4. Besides the reaction between the metallic paste constituents, many side reactions occur during the sintering process. The requirements for these processes to occur without detrimental effects to the joint quality will be explained below.

Multiple process steps are required before the sintering process can be initiated. Figure 4-1 provides an overview of important process steps for the formation of paste-based TLPS interconnects. The details of the individual steps will be discussed below.

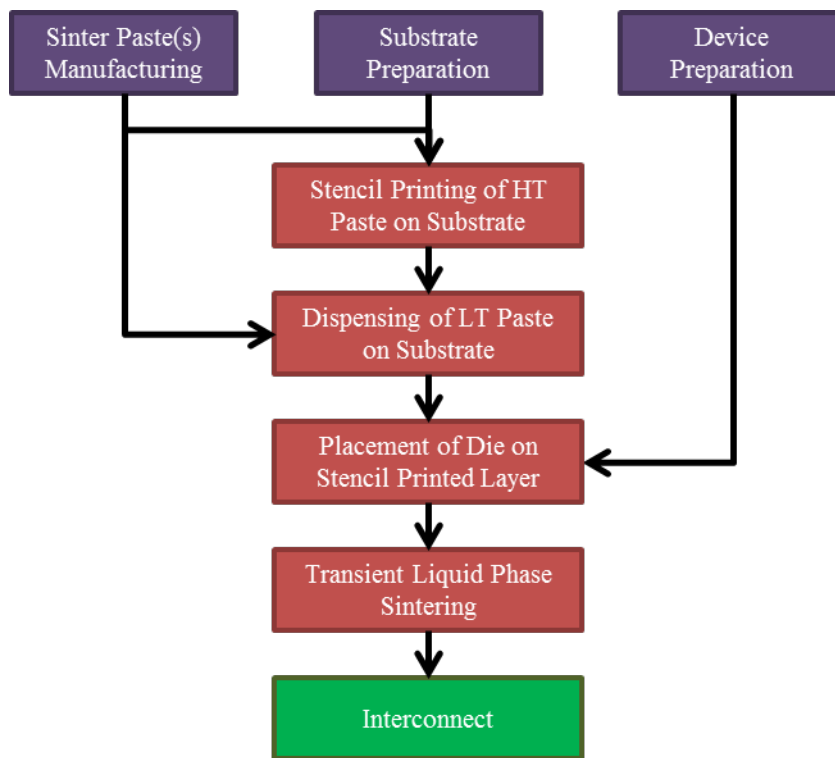


**Figure 4-1: Important process steps for the formation of paste-based TLPS interconnects**

## 4.1 Sinter Paste Manufacturing

In the following, details on the manufacturing of paste constituents such as binders and fluxes, on the mixing of the sinter pastes, and on the preparation of the substrates and devices will be described.

### 4.1.1 Binders and Fluxes

Pure powders possess very limited stencil printing capabilities. The lack of cohesion between particles renders dense packing after completion of stencil printing almost impossible. Powders possess no tackiness and do not stick to the substrate surface. As a consequence, binders are needed that ensure cohesion of the sinter pastes during printing and good adhesions between the sinter paste particles as well as between the printed sinter paste layer and its substrate. Additionally the tackiness of the binder can be used to tweak the viscosity of the paste, which influences the roughness of the printed layer after stencil printing.

The sinter paste binder properties also influence the capability of the sintering process itself. In this work, multiple different types of binders have been used and their impact on the sinter process assessed. All binders need to possess adequate viscosity to provide enough tackiness for the stencil printing to succeed. Another aspect of potential binder candidates is their stability against evaporation. If the only task of the binder is to provide good printability, it should evaporate quickly after printing to not impede the wetting phase of the TLPS process. One example for this kind of binder is Isopropyl Alcohol (IPA). On the other hand, it can be beneficial to create a protective layer around metal particles until wetting begins, for example to minimize oxidation of the metal sphere surface. If the latter is the case, the binder has to be stable against evaporation up to the melting temperature of

the low melting temperature constituent. These fluxes need to have the capability to reduce metal oxides. Examples for this type of binder are typical commercially available solder fluxes. Figure 4-2 gives an overview of the categorization of fluxes by the above criteria.

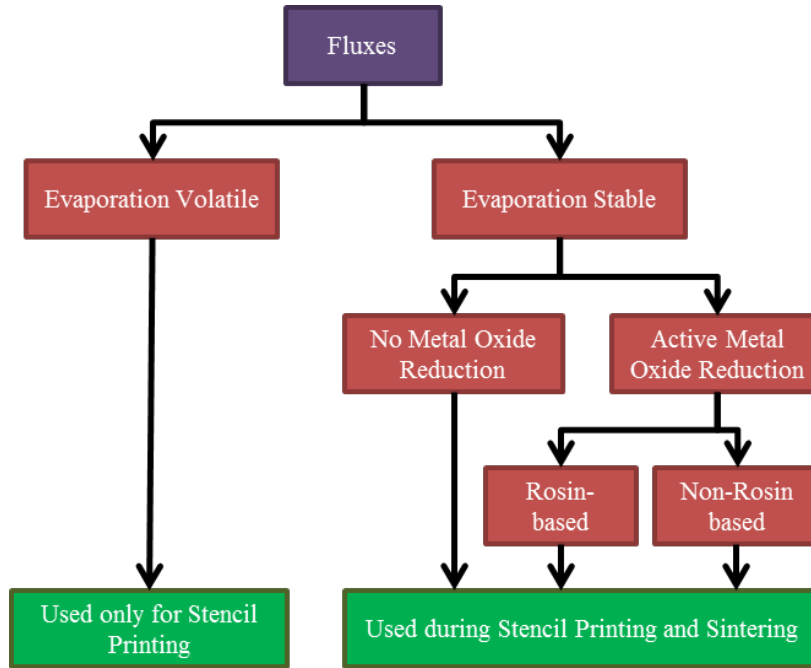


**Figure 4-2: Categorization of flux systems by their stability against evaporation and metal oxide reduction capabilities their intended use application**

The advantage of binders that are volatile to evaporation and are only used during the stencil printing process is that they do not present obstacles to the infiltration of inter-particle space during the spreading of the melt and the formation of intermetallic phases. Disadvantageous are their low viscosities, which reduce the paste adhesion and tackiness and complicate the stencil printing process. The advantages of evaporation stable binders are the wide range of viscosity, activation temperatures, decomposition stability, and chemical activity. They can protect the metal surfaces from additional oxidation during the heating phase and act as reducing agents for the metal oxide layers on the surface of the metal particles. Furthermore the printability of pastes formed by these binders is good. The non-volatile binders allow rearrangement of metal particles by application of pressure to a

certain degree because the binders act as lubricants between the particles. This becomes important when pressure is applied on the device during sintering because the paste can be compressed and/or squeezed out of the joint region leading to tilting of the device or inhomogeneous particle distribution in the printed sinter paste layer.

Another important characteristic of fluxes is their chemical activity to reduce metal oxides. The metals used in this work are Cu, Ni, and Sn. They are non-noble and susceptible to oxidation. During storage and heating to the sintering temperature, oxide layers form on the surface of the metal particles. These oxides can have high melting temperatures higher than the sintering temperature (e.g. SnO<sub>2</sub> with a melting temperature of 1630 °C). During processing, these oxides will not melt and their wettability will be reduced significantly. To ensure successful sintering the metal oxides must be reduced before and during processing. Many binders contain acids that act as reducing agents during sintering. These acids can include but are not limited to acetic acid, formic acid, citric acid, glutaric acid, or a variety of acids contained in resins. If no reducing agents are provided by the flux, the metal particles must be free of oxidation before sintering and must be sintered in inert atmosphere, or, if metal oxides are present, must be sintered in a reducing atmosphere environment.

The evaporation behavior of fluxes during the sintering process has a considerable influence on the voiding behavior and quality of the sintered joint. If the flux system is activated too late, the metal oxides cannot be reduced and the metal particles will show reduced melting and wetting capabilities, leading to partially unreacted joint regions. If the activation temperature range is narrow, the evaporation occurs at high reaction rates, which can lead to turbulent joint behavior and extrusion of metal particles from the joint region,

causing high voiding levels. If flux constituents start decomposing at temperatures significantly above the melting temperature of the low temperature constituent, but below the processing temperature, volume expansion by flux evaporation can occur within the joint. This can lead to either joint spreading if the reaction time is short and predominately liquid phases exist between the metal particles, or crack formation in the solid IMCs if pressure builds up in voids that form within IMC regions. Lastly fluxes with high amounts of solid constituents can act as flow barriers for the infiltration and spreading of the melt in the space between metal particles.

#### 4.1.2 Paste Manufacturing

Sinter pastes are manufactured by mixing pre-mixed metal powders with binders. Figure 4-3 shows the flow chart of the sinter paste manufacturing process. The ratio of metal powders mixed depends on the application character of the sinter paste. If single step deposition pastes are used (see section 4.2.1) the percentage of low melting temperature particles must not exceed the thresholds for full joint conversion (see sections 2.2 to 2.4). If two step deposition pastes are used (see section 4.2.2) the percentage of high melting temperature constituents must exceed those levels because additional low temperature constituents will infiltrate empty spaces between the high melting temperature particles. In the two step case, the low temperature pastes (LT) consist completely of low melting temperature particles mixed in flux binders. The high temperature pastes (HT) consist either completely of high melting temperature (high- $T_m$ ) particles or a mix of predominately high- $T_m$  particles with some low melting temperature (low- $T_m$ ) particles dispersed. Higher ratios of high- $T_m$  particles reduce the required process time and metal particle density. Higher ratios of low- $T_m$  particles improve the infiltration behavior of the

LT pastes during sintering by providing paths of low flow resistance, which can mitigate the potential issue of the joint center showing reduced wetting of metal surfaces and increased voiding.  $T_m$  particle percentages of  $<20\%$  were found to be necessary to ensure homogeneous infiltration of the joint region. Low- $T_m$  and high- $T_m$  metal powders are mixed in the dry state until they are homogeneously distributed.

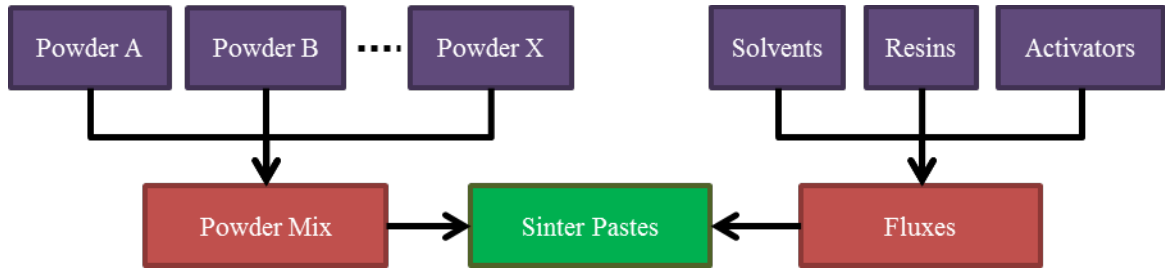


**Figure 4-3: Flow chart of the sinter paste manufacturing process**

Most commercially available fluxes are designed for reflow soldering applications during which the solder melts completely. As a consequence, they show limited capability for application in sinter pastes, which are characterized by partial melting of their constituents. They are optimized for reduction of one specific type of oxide (e.g.  $\text{SnO}_2$ ), but sinter pastes possess multiple types of metal particles with different oxides (e.g. Cu-Sn sinter pastes with  $\text{SnO}_2$  and  $\text{Cu}_2\text{O}$  and Sn and Cu particles respectively). Thus besides the use of commercially available fluxes, fluxes were also developed and manufactured as part of this study. To guarantee the quick reduction of Cu-, Ni-, and Sn-oxides during sintering, the fluxes were formed by dissolution of resins and organic acids in organic solvents. Besides the pure organic acids, the resins consist of an abundance of organic acids such as abietic-type acids and pimaric-type acids. Initially, chunks and flakes of resins reduced in size until a homogeneous resin powder is formed. Afterwards solvents such as Dipropylene Glycol, 2-Butanone or 2-Phenoxyethanol are added to the resin powder in a petri dish. The mix is heated to a temperature that enables the full dissolution of solid resin powder in the solvent,

but does not lead to evaporation of the solvent or the resin. The temperature limits depend on the boiling temperature of the solvents. After full dissolution is achieved, the acid activators (such as Succinic Acid, Glutaric Acid, Malonic Acid, or Citric Acid) are added in powder form to the heated solution. Subsequent dissolution of the acids leads to a homogeneous material with honey-like viscosity. Upon cooling to room temperature the viscosity increases. No dissolution of solid materials was detected after cooling of the flux to room temperature.

The final step in the preparation of the sinter paste is the mixing of the pre-mixed metal powders with the flux. This is done in a petri dish at room temperature. The mix is mechanically agitated by continuous stirring for a minimum of 5 minutes. Optical microscopy is used to verify homogeneous particle distribution and completed de-agglomeration of particles. If not applied right after the paste quality control is completed, the pastes are filled into syringe barrels. An air-tight fitting plunger is inserted into the barrel and pressed towards the sinter pastes until shortly before the material starts to flow out of the barrel tip. A barrel cap is placed on the syringe barrel to prevent outflow of the paste and to isolate the sinter paste from the environment. If necessary, the syringes are stored in a chemistry fridge to prevent sinter paste degradation during long term storage.

#### 4.1.3 Substrate and Device Preparation

Substrate in this context refers to the material that the sinter pastes are deposited on. Device in this context refers to the object that is placed on top of the sinter pastes after their printing. Iosipescu coupons (compare section 6.2) do not count as either substrates or devices. Their preparation procedure will be described at the end of this section.

If the device is an electronic component such as a power diode, it is inspected optically for damage of the Si chip and the metallization layer as well as for stains, oxidation, and corrosion of the metallization. Subsequently the device is dipped in a liquid flux for 10 seconds, afterwards for 10 seconds in deionized water, for 10 seconds in IPA, and finally dried. If the device is a Cu- or Ni-chip, the preparation procedure is identical with that of the substrates.

Substrates in this context are Cu- and Ni-plates or Direct Bond Copper (DBC) substrates without additional metallization layers. The substrates are first inspected optically for surface damages, stains, oxidation, and corrosion. Subsequently they are ground with 400 grit, 600 grit and 800 grit SiC grinding paper for 1 minute respectively to eliminate potential surface defects and roughness. Before sinter pastes are applied to the substrate, they are cleaned by the same procedure as the devices: dipping for 10 seconds in a liquid flux followed by 10 seconds in deionized water, 10 seconds in IPA, and drying. Other types of power electronic substrates (Ni-plated DBCs, DBAs) and the Iosipescu coupons used in this study have thin metallization layers that would be ground off by this approach. They are subject only to the subsequent dipping in liquid flux, deionized water, and IPA, as described above.

## 4.2 Paste Deposition

### 4.2.1 Single Step Deposition Paste

Sinter pastes are formed by mixing of metal powders and organic flux binders. The binders provide viscosity, coherence and adherence to the paste. Furthermore organic compounds are included in the binders which facilitate the sinter process by prevention of metal surface

oxidation, activation and reduction of oxides and removal of stains, and improving of surface wetting behavior.

Dispensing and stencil printing are two potential paste application processes. Dispensing leads to a drop-like cross-sectional shape. Potential high temperature solder applications are primarily die attach applications with flat device surfaces. For conventional soldering, the paste constituents completely melt during processing, which gives the paste constituents a high degree of freedom concerning their ability to adapt their shape to the required joint surface geometries. In TLPS systems only parts of the paste constituents melt and the shape of the final joint geometry is highly depended on the original applied paste geometry. As a consequence, the surface of the sinter pastes after their application should match the surface geometry of the joint partners as closely as possible. For devices such as power diodes, perfectly smooth and plane surfaces present the ideal case. This can best be accomplished by the stencil printing approach.

The initial approach was a one-step approach of a sinter paste that consisted of high temperature constituents (Cu, Ni), low temperature constituents (Sn) and flux binders. The pastes were stencil printed on a Cu or Ni substrate, a Cu or Ni coupon was positioned on the stencil printed layer, and the sintering process started. Initial test revealed that joints formed by these “single step deposition pastes” showed high levels of voiding. The reason behind this is the limited densification capability of the sinter pastes. Conventional solders liquefy during soldering, the flux binders evaporate, and the volume that was occupied by the flux binders in the pasty state reduces by joint densification. The sinter pastes on the other hand do not fully liquefy. The Cu and Ni particles remain in the solid state. Only limited rearrangement can be achieved. The joints show no good capability for

densification. The volume occupied by flux binders cannot be reduced. The result is considerable voiding and reduced joint properties (Shear strength, thermal and electrical conductivity).

#### 4.2.2 Two Step Deposition Pastes

Because of the voiding behavior of the “Single Step Deposition Pastes”, other approaches for paste deposition were developed. The underlying concept is to fill the voids of the structure formed by the Cu and Ni particles with extra low temperature alloys from outside the high temperature particle region. The sinter paste system consists of two pastes: A high temperature paste (HT) consisting predominately of high melting temperature metal particles embedded in an organic flux binder, and a low temperature paste (LT) consisting predominately of low melting temperature metal particles embedded in an organic flux binder. During processing, organic flux binders are activated and used to reduce oxides on the metal particles as well as device and substrate metallization, to improve the wetting capabilities of the low melting temperature constituents, and facilitate the sintering process. After melting, the low melting temperature alloy infiltrates the mesh formed by the high melting temperature particles. The low melting temperature material fills the space between the high melting temperature particles, minimizes voiding, and maximizes thermal and electrical conductivity. High melting temperature IMCs grow where the low melting temperature constituents are present, until the latter have been fully consumed, which completes the process. The voiding levels achieved by this approach are considerably reduced compared to the “Single Step Deposition” approach. Two deposition alternatives for the “Two Step Deposition Approach” have been developed and are described in detail below.

#### 4.2.2.1 Printing and Dispensing (PD)

Figure 4-4 provides an overview of the process steps associated with the TLPs sintering process for the Printing and Dispensing (PD) process. Figure 4-5 shows an example structure that will be used to describe the high temperature paste printing, low temperature paste dispensing, and sintering process. It consists of a substrate with a metallization layer and a device with a metallization layer. These two components are connected by a TLPS joint.

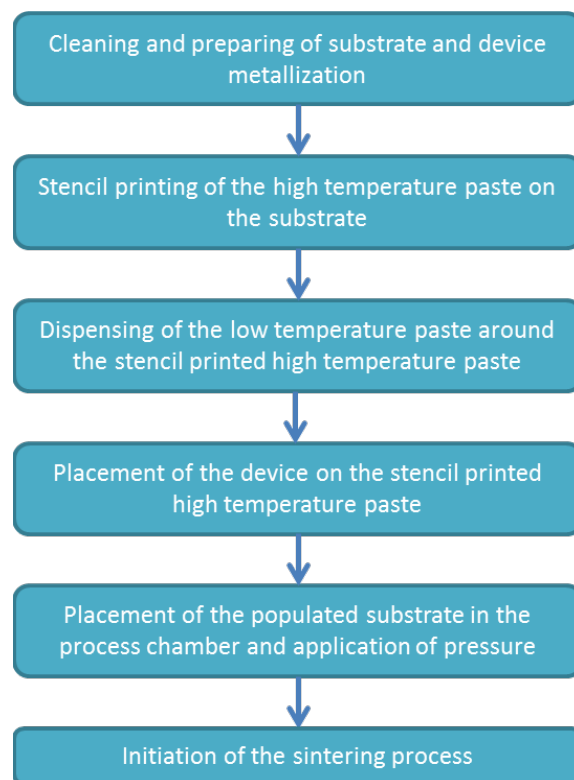


**Figure 4-4: TLPS process steps – Stencil printing & Dispensing**

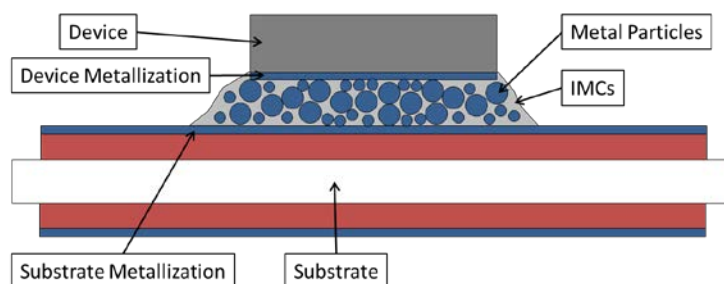


**Figure 4-5: Example structure of a device attached with TLP sinter paste systems to a substrate**

In the following, the process steps will be explained in detail:

1. Cleaning and preparing of substrate and device metallization: The metallized surfaces of the device and substrate should be free of contaminants such as grease or dust. The procedures and routines for cleaning and preparation (e.g. treatment with acetone or liquid fluxes) of metal surfaces can vary between different metallization types (e.g. Cu, Ni, Ag). Established standards or best practices should be followed.
2. Stencil printing of the high temperature paste on the substrate: The high temperature paste is stencil printed on the prepared substrate surface, see Figure 4-6.
3. Dispensing of the low temperature paste around the stencil printed high temperature paste: A ring of low temperature paste is dispensed around the printed layer, see Figure 4-7.
4. Placement of the device on the stencil printed high temperature paste: The device should be placed at the center of the stencil printed area. It should be fully in contact with the high temperature paste over all of its metallized area, see Figure 4-8.
5. Placement of the populated substrate in the process chamber and application of pressure: The populated substrates are placed in the process chamber (e.g. multi-zone reflow oven). Pressure is applied to the top of the devices. The pressure is not driving the sintering process, but ensures that the devices stay in place as the sintering occurs. The pressure should be homogenized over the device area by a sheet of high temperature rubber or graphite.

6. Initiation of the sintering process: The sintering process is initiated. The low temperature alloy melts. Shortly after the melting is completed, it will infiltrate the mesh of high temperature particles below the device and the formation of IMCs is initiated. After the process is completed, the joint should be fully transformed to the IMC or an IMC and metal particle structure.

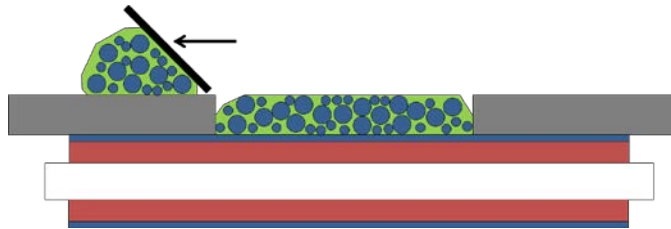


**Figure 4-6: Stencil printing of the high temperature paste (left) and top view on the resulting structure**

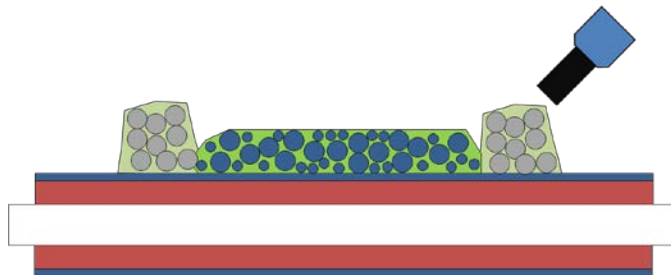


**Figure 4-7: Dispensing of the low temperature paste around the stencil printed high temperature layer**

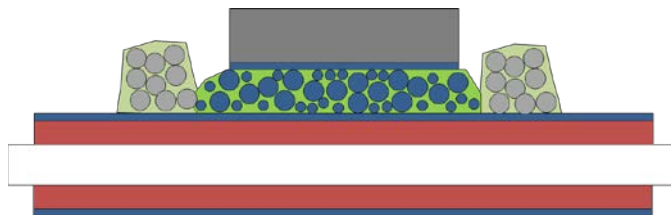
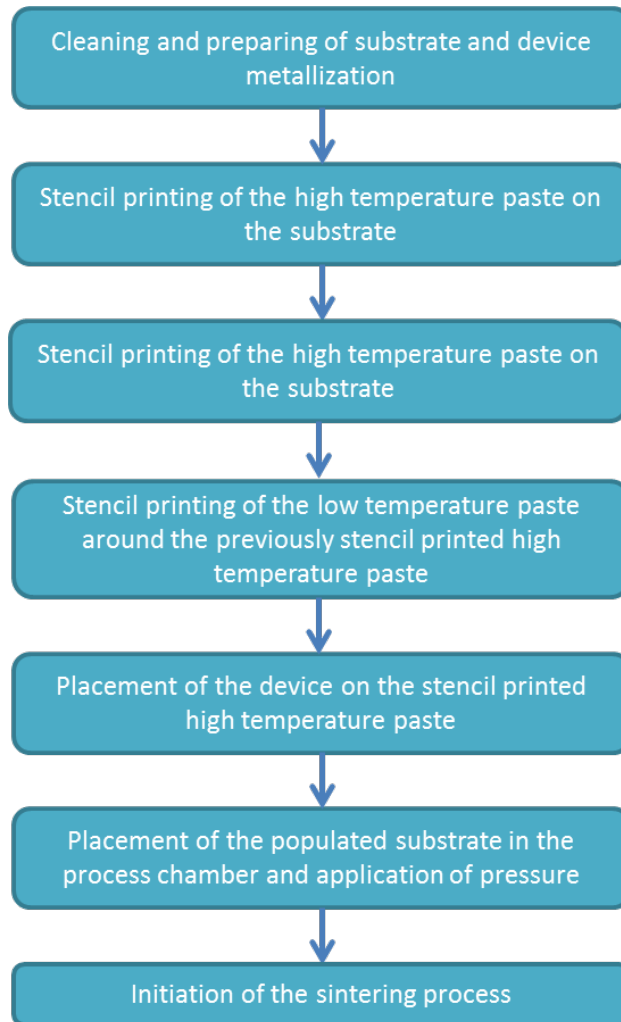


**Figure 4-8: Placement of the device on the stencil printed high temperature paste**

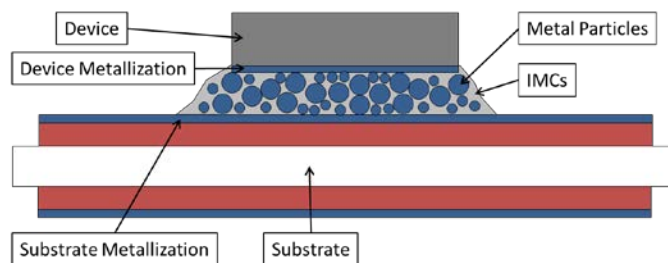
#### 4.2.2.2 Printing, Drying and Printing (PDP)

Figure 4-9 gives an overview of the process steps associated with the TLPS sintering process for the Printing, Drying, and Printing (PDP) process. Initially, the high temperature paste is printed. A drying step is initiated before the low temperature paste is applied. After the drying step, the low temperature paste is printed around and above the dried high

temperature paste. Figure 4-10 shows an example structure that will be used to describe the high temperature paste printing, low temperature paste printing, and sintering process. It consists of a substrate with a metallization layer and a device with a metallization layer. These two components are connected by a TLPS joint.



**Figure 4-9: TLPS process steps – Printing, Drying, and Dispensing**



**Figure 4-10: Example structure of a device attached with TLP sinter paste systems to a substrate**

In the following, the process steps will be explained in detail:

1. Cleaning and preparing of substrate and device metallization: The metallized surfaces of the device and substrate should be free of contaminants such as grease or dust. The procedures and routines for cleaning and preparation (e.g. treatment with acetone or liquid fluxes) of metal surfaces can vary between different metallization types (e.g. Cu, Ni, Ag). Established standards or best practices should be followed.
2. Stencil printing of the high temperature paste on the substrate: The high temperature paste is stencil printed on the prepared substrate surface, see Figure 4-11.
3. Drying of the high temperature paste: The layer of high temperature paste that has been deposited on the substrate is heated to a temperature below  $T_{m,A}$ . The flux binders partially evaporate, and change the structure from a paste to a firm, brittle porous arrangement. This leads to a structure similar to that shown in Figure 4-12.
4. Stencil printing of the low temperature paste around the stencil printed high temperature paste: A layer of low temperature paste is stencil printed around the printed and dried high temperature layer, see Figure 4-13.
5. Placement of the device on the stencil printed high temperature paste: The device is placed at the center of the stencil printed area, see Figure 4-14.
6. Placement of the populated substrate in the process chamber and application of pressure: The populated substrates are placed in the process chamber (e.g. multi-zone reflow oven). Pressure is applied to the top of the devices. The pressure is not driving the sintering process, but ensures that the devices stay in place as the

sintering occurs. The pressure should be homogenized over the device area by a sheet of high temperature rubber or graphite.

- 7. Initiation of the sintering process: The sintering process is initiated. During sintering the low temperature alloy will melt. Shortly after the melting is completed, it will infiltrate the mesh of high temperature particles below the device and the formation of IMCs is initiated. After the process is completed, the joint should be fully transformed to the IMC or an IMC and metal particle structure as described in the introduction.

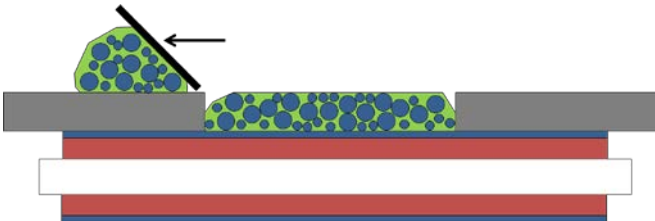


**Figure 4-11: Stencil printing of the high temperature paste**

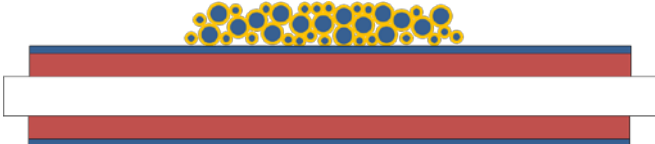


**Figure 4-12: Drying of the high temperature paste**

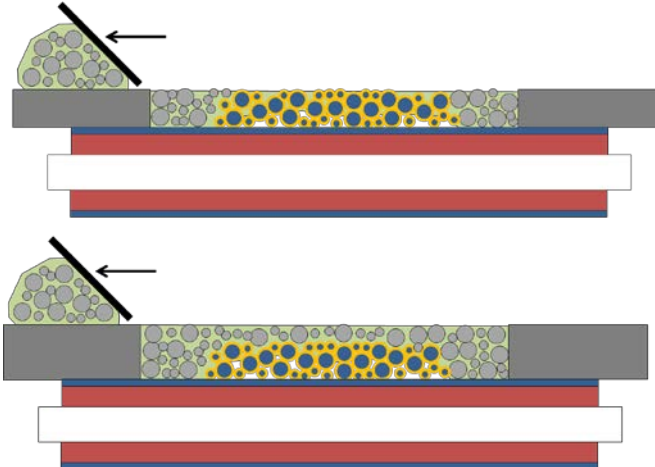


**Figure 4-13: Stencil printing of the low temperature paste around the stencil printed high temperature layer. The stencil for the low temperature paste must be of the same thickness as the dried high temperature layer (above), or thicker (below)**

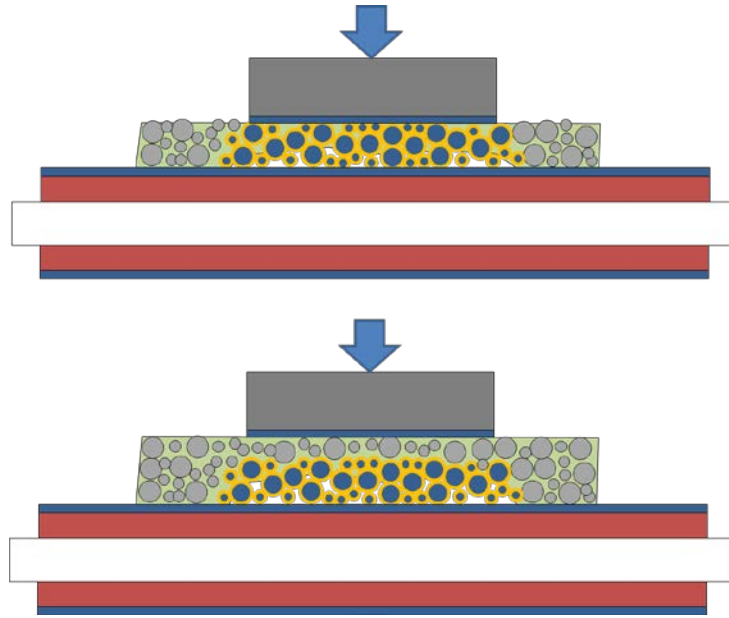


**Figure 4-14: Placement of the device after stencil printing of the low temperature paste for the two cases described in Figure 4-13**

### 4.3 Sintering Process

After depositing the paste on the substrate and the device on the paste layer as detailed in section 4.2, the samples are can be processed. The TLPS sinter pastes developed in this work were designed for maximum processing compatibility with different process environments and do not require inert or reducing gas atmospheres. A process device providing a smooth, almost homogeneously surface upon which the samples are processed was developed for this study. It is in the following referred to as the “Sinter Fixture”. A detailed description of the sinter fixture is given in section 4.3.1. The sintering atmosphere for all samples manufactured in this work was ambient.

During processing flux constituents evaporate and the low melting temperature metal melt, wet the surfaces of the high melting temperature metal, and infiltrate the high temperature particle mesh in the joint region. These processes are characterized by turbulent behavior which can cause considerable particle rearrangement and formation of voids. This can lead

to a spreading of the joint in vertical direction leading to high void percentages and low metal particle density. This process is illustrated in Figure 4-15. In the initial arrangement, the device was placed on a stencil printed layer of the high melting temperature particles (blue) embedded in a highly viscous flux binder (green), see Figure 4-15 a). Upon heating above the melting temperature of the low melting temperature particles (grey), they melt and start infiltrating the sinter paste region below the device, see Figure 4-15 b). The driving force behind the infiltration process are capillary forces acting on the liquid during its wetting of the solid metal surfaces. Some pockets of liquid flux can remain in the area already infiltrated by the liquid metal. As the sintering process proceeds, the infiltration of inter-particle space by the liquid metal continues, see Figure 4-15 c). At this point, the highly viscous flux located at the center of the joint is under compressive stress from the continued horizontal mass influx from the joint edges. This pressure is relaxed by expansion of the liquid flux in vertical direction, perpendicular to the flow direction of the liquid metal. This causes considerable spreading of the joint in vertical direction. After continued sintering, the flux located at the joint center and in pockets in the infiltrated regions decomposes into gaseous (yellow) and solid (brown) constituents, see Figure 4-15 d). This causes additional volumetric expansion, which is compensated by further spreading of the joint in vertical direction. IMCs are formed between the solid (blue) and liquid (grey) metals, which enclose the gaseous and solid residues.

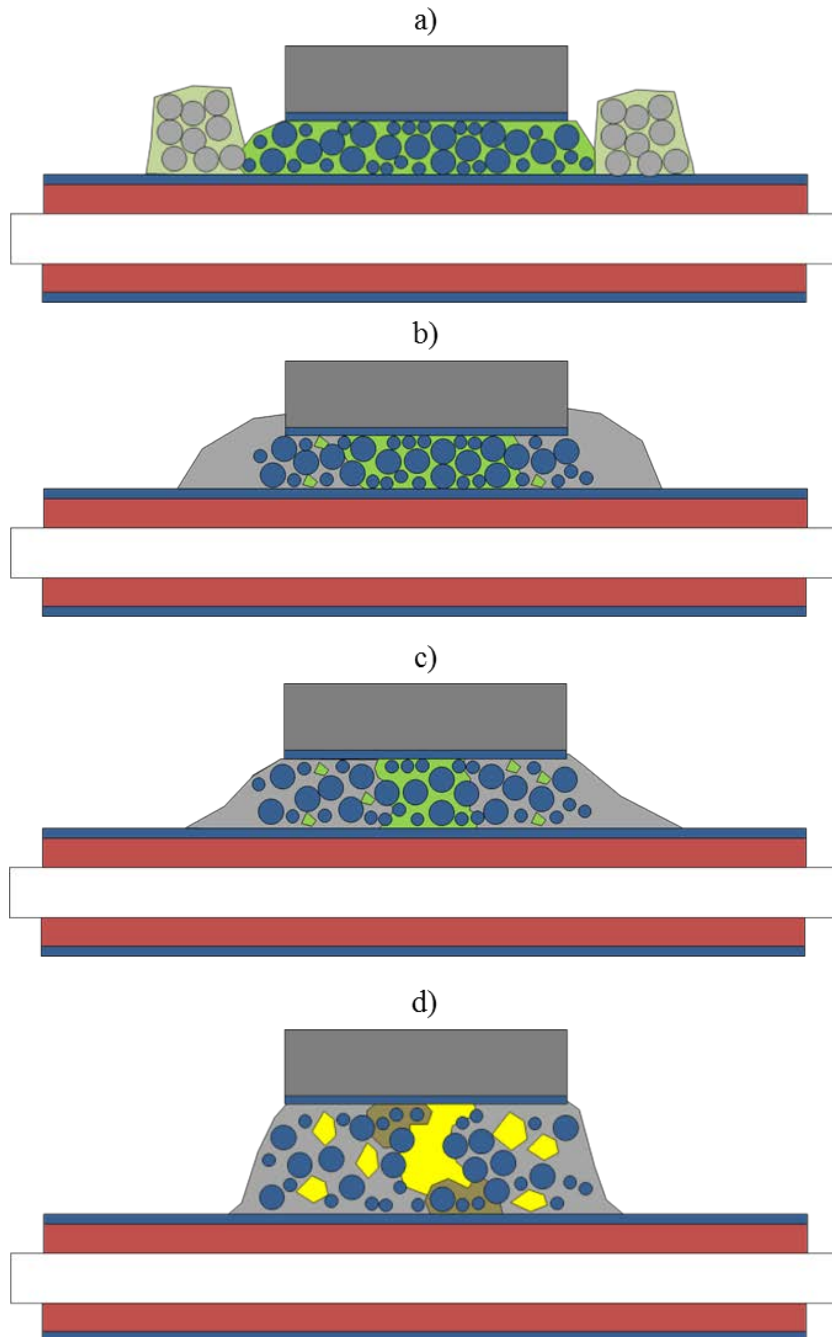


**Figure 4-15: Spreading of the joint in vertical direction: a) Original paste arrangement, b) melting of the low  $T_m$  alloys (grey) and infiltration of the mesh of high  $T_m$  particles (blue); Some pockets of high viscous binder remain between the mesh (green), c) initial vertical spreading due to further infiltration and exertion pressure on the central flux region, and d) additional spreading due to flux evaporation: Voids (yellow) and solid residues (brown) remain**

In consequence, the rearrangement of metal particles and the compensation of horizontal mass influx of the liquid metals into the solid metal particle mesh cause a pressure increase

in the central joint region, which is compensated by an expansion of the joint in vertical direction accompanied by void formation and reduction of solid metal particle density. This phenomenon can be mitigated by application of pressure on the top of the device towards the substrate direction during the sintering process. In preliminary work it was found that pressures of 75 kPa reduce the joint spreading considerably and that pressures of 0.33 MPa minimize the joint spreading. Additionally, the application of pressure prevents the tilting of the die and ensures a parallel arrangement of the device and the substrate.

Figure 4-16 schematically shows how pressure is applied homogeneously during the sintering process. Initially, the unsintered samples are placed on the top surface of the sinter fixture, see Figure 4-16 a). Afterwards polyimide spacers are placed on top of the device surface, see Figure 4-16 b). The spacer length and width follow the length and width of the devices. They are cut from a 3mm thick high temperature polyimide rubber sheet. They have a durometer hardness of 50A – 55A which reduces as the temperature increases. Subsequently, weights are placed on top of the polyimide spacers. The samples are arranged in a regular pattern (usually a 2x2 array), ensuring an even weight distribution and eliminating the threat of tilting of the weights as the polyimide spacers soften. The applied pressure is calculated by dividing the total weight force by the total device area. Identical shape, size, and position of the polyimide spacers on top of the devices ensures homogenous pressure distribution.

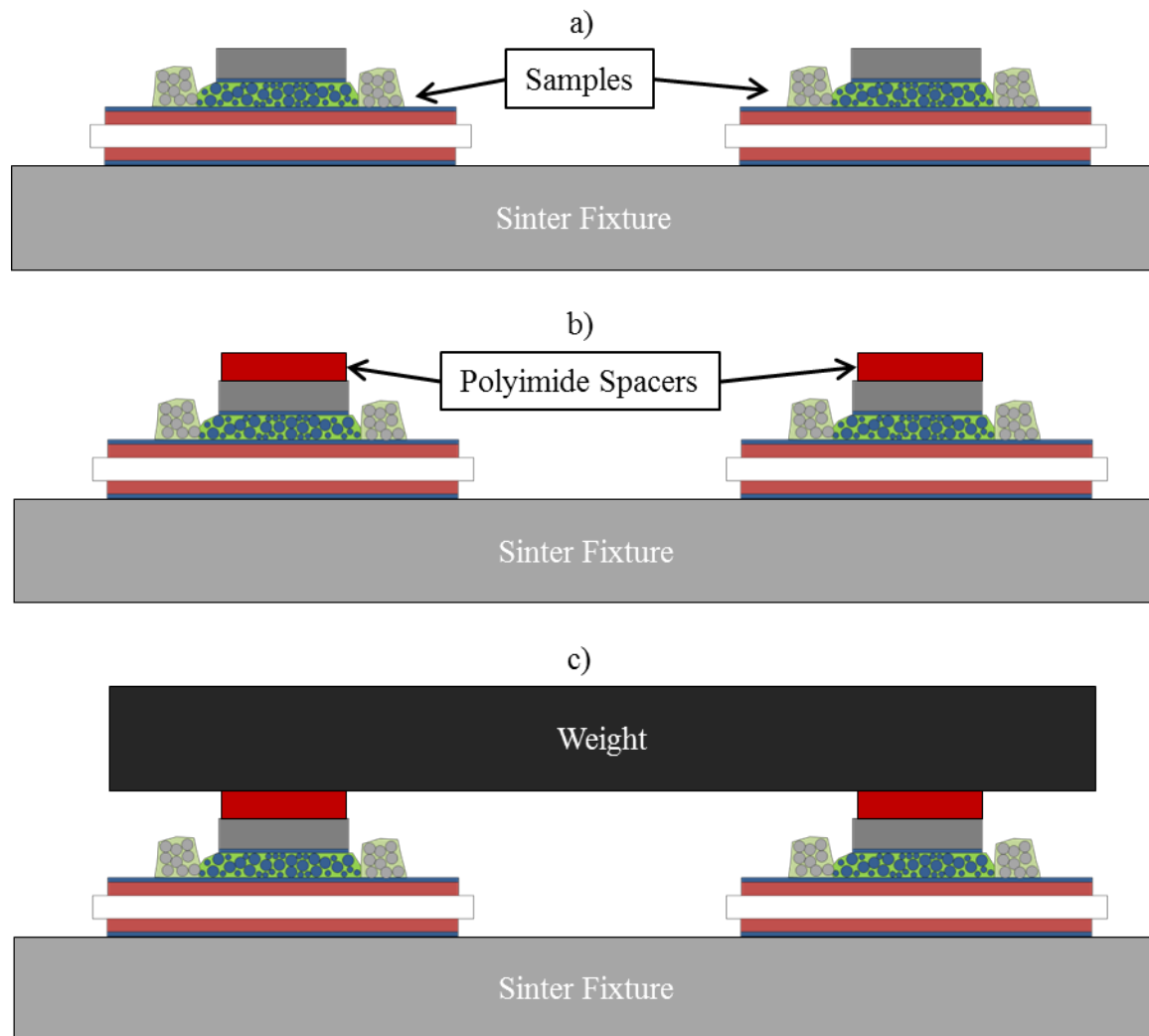


**Figure 4-16: Application of homogeneous pressure on the samples before sintering: a) positioning of samples on the top surface of the sinter fixture, b) positioning of polyimide spacers for pressure homogenization on top of devices, and c) application of weights on the polyimide spacers**

After positioning of samples, polyimide spacers, and weights, the sintering process is initiated. A pre-programmed temperature profile of the sinter fixture is loaded. The low melting temperature alloy melts, infiltrates the mesh, and IMCs grow, see above. Two optimized temperature profiles were developed that yield joints of good and consistent quality: The first profile is a temperature profile with a short dwell time at the maximum sintering temperature. The temperature is ramped to 35 °C within the first minute, followed by a dwell at 35 °C for 1 minute. These first two steps compensate for potential ambient

temperature fluctuations and ensure consistency between different sample batches. Subsequently the temperature of ramped from 35 °C to 300 °C within 4 minutes and held at this temperature for 2 minutes. Afterwards the temperature is reduced to ambient temperature within 6 minutes. This profile is similar to conventional reflow soldering profiles. The second temperature profile is very similar: The only difference is an extended dwell time at 300 °C of a total of 30 minutes. This is the expected time for almost full consumption of low melting temperature phases in the joint region. Figure 4-17 contrasts the two temperature profiles.

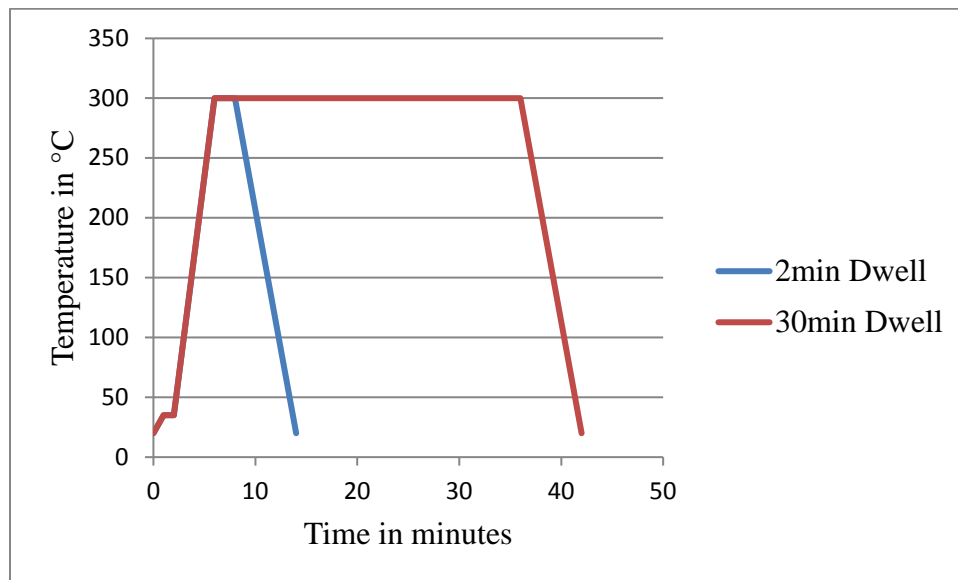


**Figure 4-17: Temperature profiles for the sintering process. The 2 minute dwell time profile is similar to conventional reflow soldering profiles. The 30 minute dwell time is the expected profile to achieve full IMC formation**

#### 4.3.1 Sinter Fixture

Figure 4-18 provides an overview of the sinter fixture assembly. The top surface of the combined Hot-/Coldplate is where the samples are located during processing. Holding brackets attach the sinter fixture to a laboratory table via nuts and bolts. Additional rigidity is provided by a steel plate under the holding brackets. Thermal insulation is achieved by a polyimide high temperature sheet between the steel plate and the table surface. Cold water

is provided through a water inlet pipe. The water pipes are thermally insulated from the water supply loop by high-temperature polyimide tubing.

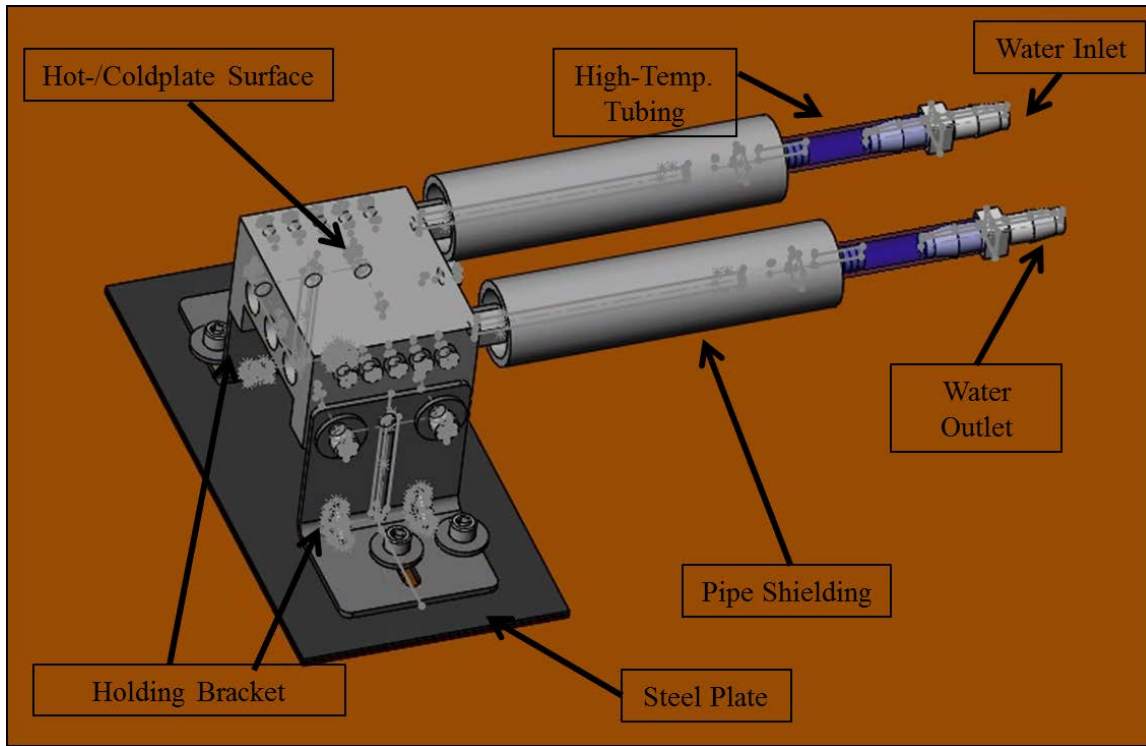


**Figure 4-18: Overview of the sinter fixture assembly**

Figure 4-19 shows the elements of the sinter fixture hot-/coldplate. The main body consists of a block of 6061 aluminum with a length of 3", and width of 2.5", and a height of 1.75". Three holes are drilled through the entire width of the body. Three steel sheath cartridge heaters with a heating power of 400W each are positioned in these holes after assembly of the sinter fixture. Six threaded holes are located at the bottom of the fixture body where the holding brackets are attached by steel screws during assembly. Figure 4-20 shows the arrangement of holes and cooling structures within the fixture main body. Five cooling channels are connecting the water inlet and water outlet channel. They are located 1/4" beneath to the top surface and perpendicular to the inlet and outlet channels. A hole for a PT100 thermal resistor is located between the heating elements and the cooling channels.

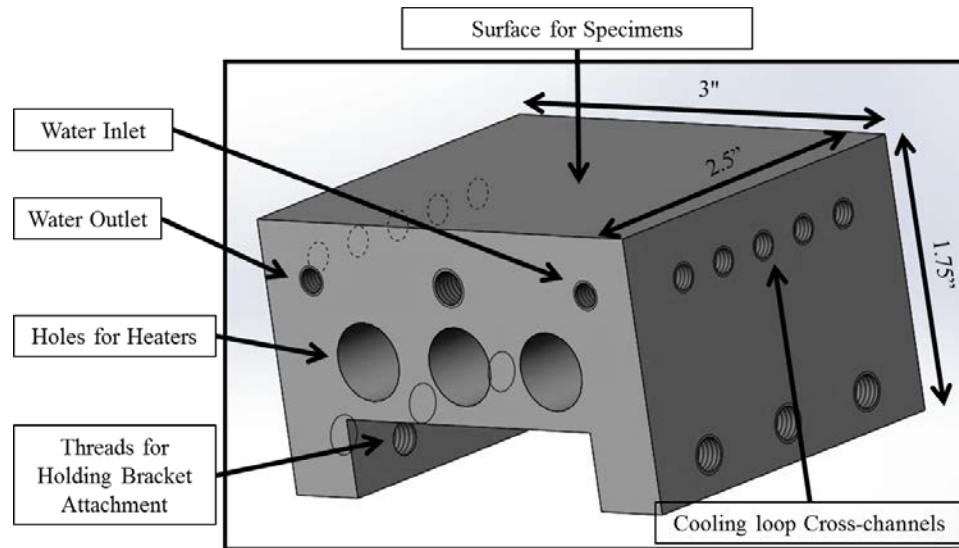


**Figure 4-19: Elements of the Hot-/Coldplate**

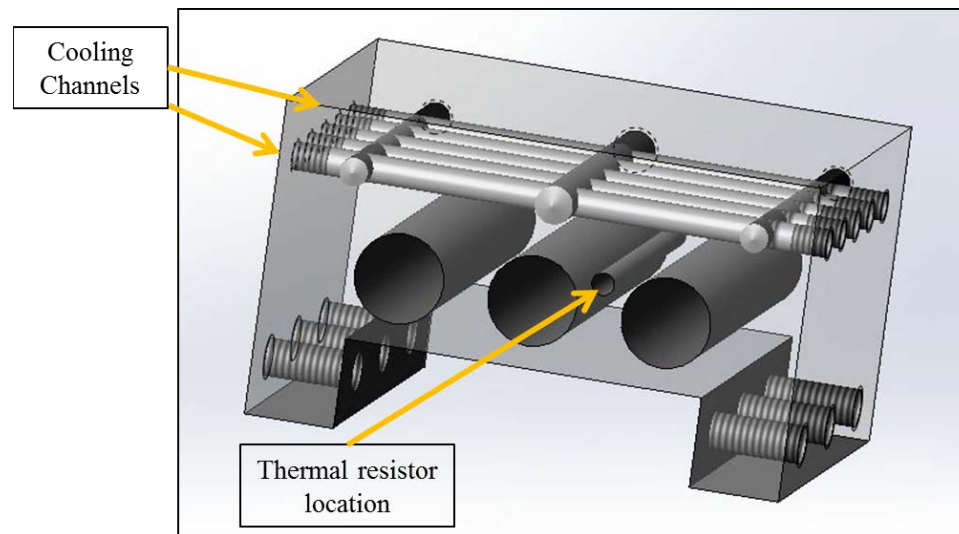


**Figure 4-20: Arrangement of holes and cooling structures within the hot-/coldplate**

The PT100 sensor is used as temperature feedback for an Omega CN7500 Ramp/Soak controller [114]. This PID controller automatically compares the set temperature profile with the actual temperature profile and regulates the duty cycle of the heating and cooling systems. The CN7500 controller is integrated with a power diode rectifier and an IGBT used for pulsing the 1.2kW heating power of the cartridge heaters. The pulse width of the ON-control signal of the IGBT is adjusted according to the heating power requirements.

The sinter fixture cooling is achieved by a pulsed water-cooling. Analogously to the heating system, the cooling is controlled by the pulse-width of the ON-signal of the cooling output of the CN7500 temperature controller. The controller signal itself is a switching 0V – 12V pulse width signal that is used to control a DC-controlled AC relay. This relay controls whether or not cooling water is pumped through the cooling channels of the sinter fixture. Figure 4-21 shows the elements of the sinter fixture cooling system. It consists of two distinct loops. The first loop is the inner loop that is controlled by a normally-ON valve. If no cooling of the sinter fixture is needed, this loop is active and the pump continuously flows water through the radiators and tank to keep the water temperature at low levels. The second loop is the loop through the sinter fixture. Its flow is controlled by a normally-OFF valve. This valve opens only if the controller provides a 12V cooling signal. Simultaneously the normally-ON valve of the inner loop will close. Water is now pumped through the cooling structures of the sinter fixture to reduce its temperature.

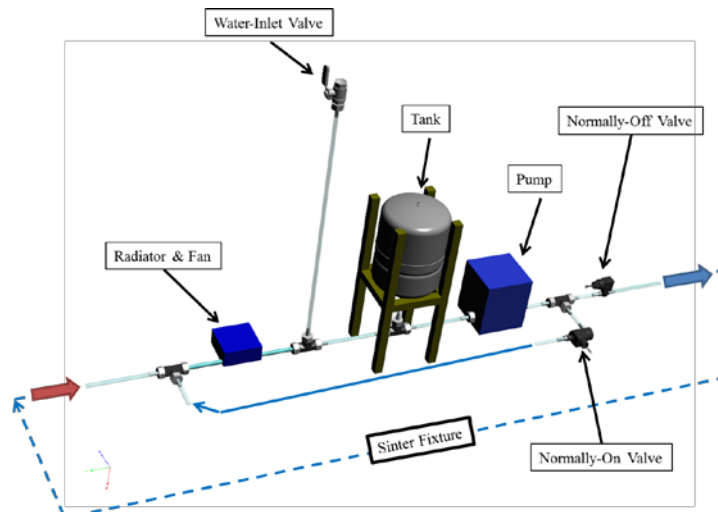


**Figure 4-21: Schematic of the sinter fixture water cooling system**

The sinter fixture can provide fast heating and cooling rates in a repeatable and controlled manner. The maximum heating rate is 75K/min and the average cooling rate from 300 °C to 40 °C is >125K/min. This capability enables fine control of the heating rates and good

process control. Furthermore the rapid cooling rates ensure that the progression of the sintering process can be analyzed at precise time intervals. If, for example, the microstructure after five minutes of sintering at 300 °C is of interest, the rapid cooling to low temperatures ensures that the microstructure is not significantly influence by extensive cooling durations. Figure 4-22 compares a recommended typical SAC solder reflow profile with that achieved by the sinter fixture system. They are very similar in their overall behavior with almost identical heating and cooling rates as well as maximum and minimum temperatures.

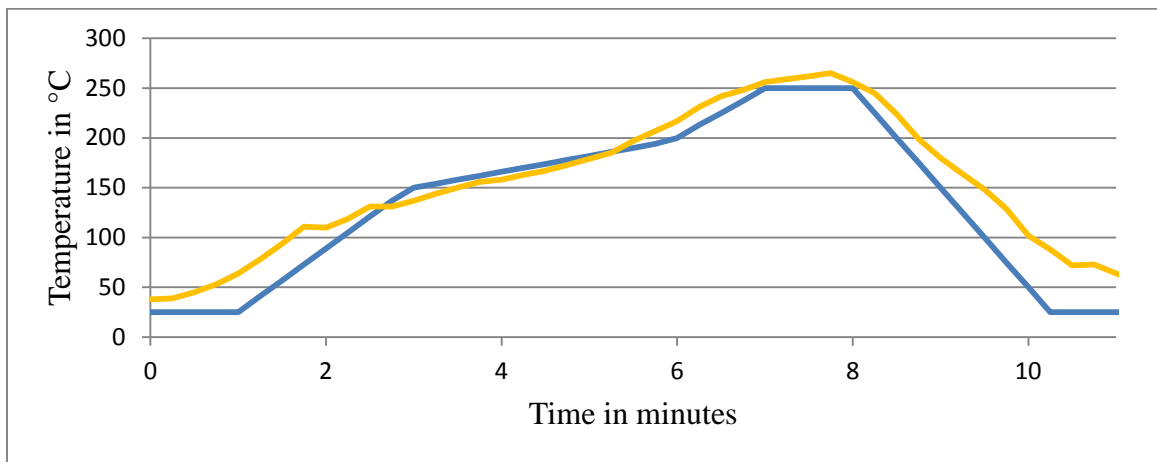


**Figure 4-22: Comparison of suggested SAC reflow soldering profile (blue) and the measured sinter fixture temperature (yellow)**

## 5 Microstructural Evolution of TLPS Interconnects in High Temperature Environments

In this chapter, the microstructural evolution of TLPS interconnects during sintering and during subsequent high temperature aging is assessed. Initially, a quantitative analysis of the evolution of phases for the Cu-Sn system is given. Afterwards, the growth of voids and the development of grain structure in Cu-Sn TLPS joints are studied. Finally, the high temperature stability of TLPS joints formed by the Ni-Sn system will be analyzed.

### 5.1 Phase Evolution of Cu-Sn TLPS Joints

The samples used in this study were manufactured by sintering Cu-Sn sinter pastes between Cu-substrates and Cu coupons, see Figure 5-1. Sinter and solder pastes were printed and dispensed by the approach introduced in section 4.2.2.1. The dimensions and composition of the materials involved are summarized in Table 5-1. The size of the Cu-coupons and Cu-substrate were 6.35mm x 6.35mm x 1mm and 20mm x 20mm x 3mm and the both consisted of annealed Cu with a purity of 99.9%. The size of the final Cu-Sn TLPS joints was 6.35mm x 6.35mm x 0.2mm. The sinter paste used in this study consisted of a mix of spherical Cu-particles with diameters between 37  $\mu\text{m}$  and 88  $\mu\text{m}$  and spherical Sn<sub>0.7</sub>Cu-particles with diameters between 25  $\mu\text{m}$  and 45  $\mu\text{m}$ . Sinter pastes were manufactured by mixing 66 weight-percent (wt.%) Cu-particles, 17wt.% Sn<sub>0.7</sub>Cu-particles and 17wt% resin-free flux (flux type R0L0) with low post-reflow solid residue. The paste constituents were mixed manually under ambient conditions until homogeneity could be confirmed by optical microscopy inspection. The Cu-coupons and Cu-substrates were ground with 600 grit SiC grinding paper to remove stains and oxide layers. Afterwards 6.5mm x 6.5mm x

0.2mm layers of sinter paste were stencil printed on top of the center of the Cu-substrates. Cu-coupons were placed on the center of the stencil printed sinter paste layer. Afterwards a ring of Sn0.7Cu solder paste with a diameter of 1mm was dispensed around the stencil printed sinter paste. The solder paste consisted of 85wt.% Sn0.7Cu particles with particle diameters between 25  $\mu\text{m}$  and 45  $\mu\text{m}$  mixed with 15wt.% resin-based flux with high activity.

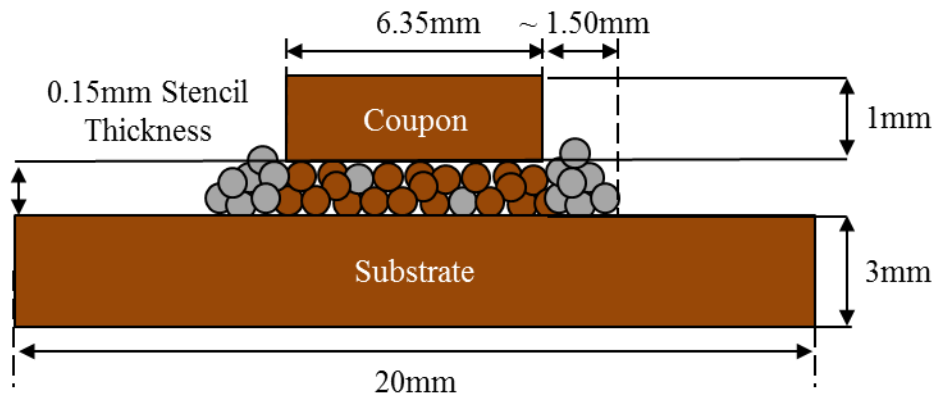


**Figure 5-1: Schematic cross-section of a Cu-Sn TLPS aging study sample before sintering**

**Table 5-1: Composition of substrate, coupon, sinter paste, and solder paste material**

Component	Length [mm]	Width [mm]	Material	Comment
Substrate	20.00	3.00	Cu	
Coupon	6.35	1.00	Cu	
Sinter Paste	6.50	0.15	80 wt.% Cu 20 wt.% Sn0.7Cu	Stencil Thickness
Solder Paste	~ 1.50	~ 0.30	Sn0.7Cu	

The samples were placed on the sinter fixture described in section 4.3.1. A pressure of 0.30 MPa was applied homogeneously to the top surfaces of the Cu-coupons. Subsequently the sinter process was started by initiation of the sinter temperature profile. Two sinter process profiles were used: (1) a heating ramp from ambient to 300 °C within 5 minutes followed by a dwell time of 2 minutes at 300 °C and subsequent cooling to room temperature within

5 minutes (from here on referred to as 2min@300 °C) and (2) a heating ramp from ambient to 300 °C within 5 minutes followed by a dwell time of 30 minutes at 300 °C and subsequent cooling to room temperature within 5 minutes (from here on referred to as 30min@300 °C). The former sinter profile is similar to conventional high temperature soldering reflow profiles and the latter was chosen because preliminary results with Cu-Sn TLPS indicated high temperature capability. Sintering was performed in ambient atmosphere: no inert or reducing gas was supplied.

After cooling to ambient temperatures, the pressure applied to the Cu-coupon top surface was relieved. Eight out of twelve samples sintered for 30 minutes were chosen randomly and placed in a convection oven to anneal without application of pressure at 250 °C for 24 hours and 100 hours (from hereon referred to as 24h@250 °C and 100h@250 °C respectively). Four samples were manufactured for each sintering and aging condition. They were mounted and cross-sectioned at the centerline of the Cu-coupons parallel to the coupon side. The cross-sectioning procedure was as follows: (1) grinding with a diamond grinding disk until a distance approximately 0.5mm away from the joint center, (2) grinding with SiC grinding papers with grit sizes of 240, 400, 600, 800, and 1200 until the joint center was reached, and (3) polishing with 1 μm diamond suspension until no scratches could be detected by optical microscope inspection. Table 5-2 summarizes the sintering and aging test conditions and related application conditions.

**Table 5-2: Test conditions and related application conditions**

<b>Test Condition</b>	<b>Related Application Condition</b>
2min@300 °C	Typical reflow
30min@300 °C	Expected high-temp. capability
(30min@300 °C) + 24h@250 °C	Few high-temp. excursions
(30min@300 °C) + 100h@250 °C	Long-term high-temp operation

To quantify the presence of different phases consistently between multiple cross-sections, a Phase Analysis Software was developed in MatLab. The software automatically reads the distribution of greyscale in an image and provides a histogram of the greyscale distribution on a user interface. The user then manually selects greyscale peaks of interest corresponding to the phases to be analyzed. Subsequently the software computes the percentages of phases present in the image and writes the results in an .xls file, which is used for further data analysis. A computed image is presented with the greyscales converted from the original continuous greyscale distribution to discrete phases (e.g. dark grey for Cu, bright grey for Cu<sub>6</sub>Sn<sub>5</sub>). The software is capable of analyzing multiple images sequentially in batches and provides high levels of consistency. Figure 5-2 shows a flowchart of the workflow during phase analyses of multiple images with the Phase Analysis Software.

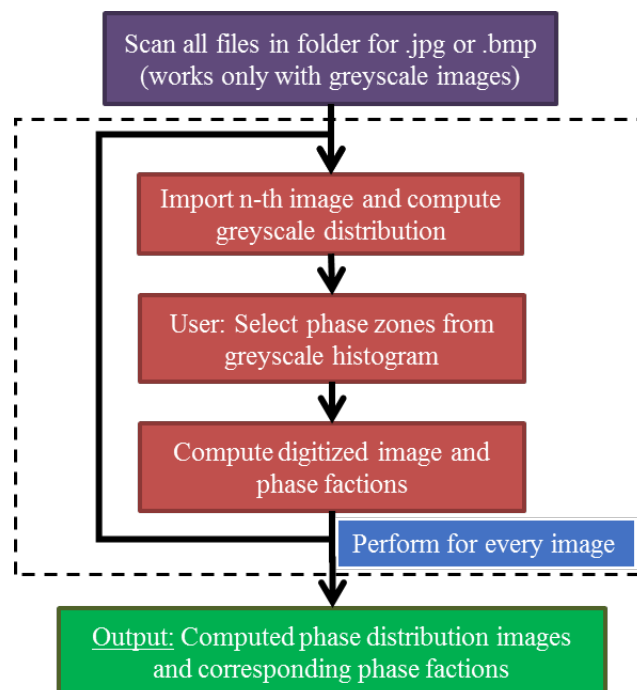


**Figure 5-2: Flowchart of the workflow during phase analysis**

In the following, one example analysis of a section of a Cu-Sn TLPS is performed with the Phase Analysis Software. A section of a SEM microscopy image of a Cu-Sn TLPS joint is shown in Figure 5-3 (left). It shows parts of three Cu-particles (black) joined by  $\text{Cu}_3\text{Sn}$  IMCs (dark grey) and  $\text{Cu}_6\text{Sn}_5$  IMCs (grey), and some Sn (white) in the upper right corner. The first step of the phase analysis is the computation of the greyscale distribution of the image. Subsequently, a graph is displayed showing the distribution of the number of pixels with a specific greyscale value (on the y-axis) over the greyscale value (on the x-axis), see Figure 5-3 (right). An x-axis value of zero corresponds to black and a value of 255 corresponds to white.

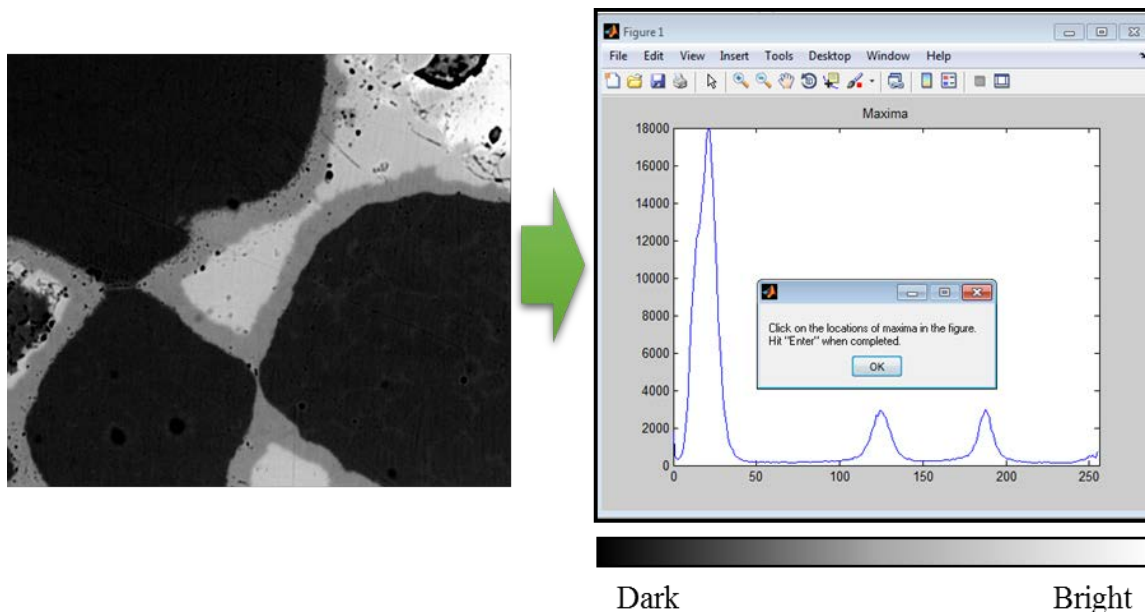


**Figure 5-3: Transformation of greyscale image (left) and computation of greyscale distribution (right)**

The second step of the phase analysis is the determination of different types of phases. On the greyscale distribution graph shown in Figure 5-4 (left), distinct phases are represented by maxima in the distribution graph. In this example, four maxima can be detected, corresponding to the four phases present. Next, the maxima must be selected, which is performed manually by the user. Figure 5-4 (right) shows an example of the indicated

locations of these maxima illustrated by green circles. Similarly, minima must be selected manually by the user.

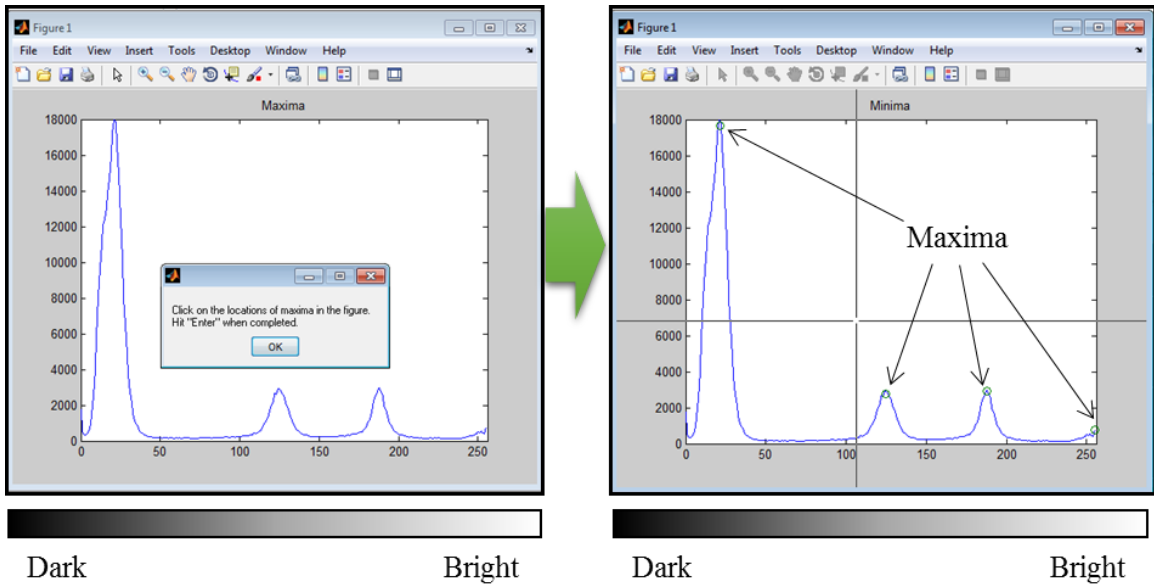


**Figure 5-4: Greyscale distribution (left) and selection of maxima (right)**

The third step of the phase analysis is the computation of phase distributions. Figure 5-5 (bottom) indicates the regions of distinct phases by the areas between the red vertical lines. In this example, Cu corresponds to the number of all pixels with a grey value between the left end of the graph and the first red line with a maximum indicated by “Phase 1”. Similarly, the  $\text{Cu}_3\text{Sn}$  phase corresponds to all pixels with a greyscale value between the first red line and the second red line, indicated by “Phase 2”. The number of pixels of the remaining phases is computed analogously. Figure 5-5 (top left) shows the original image and Figure 5-5 (top right) shows the computed simplified image. In the former image, pixels have the grey value of the original image. In the simplified image, only four distinct greyscale values are displaying the four distinct phases determined in prior analysis steps. The two images show a high degree of resemblance.

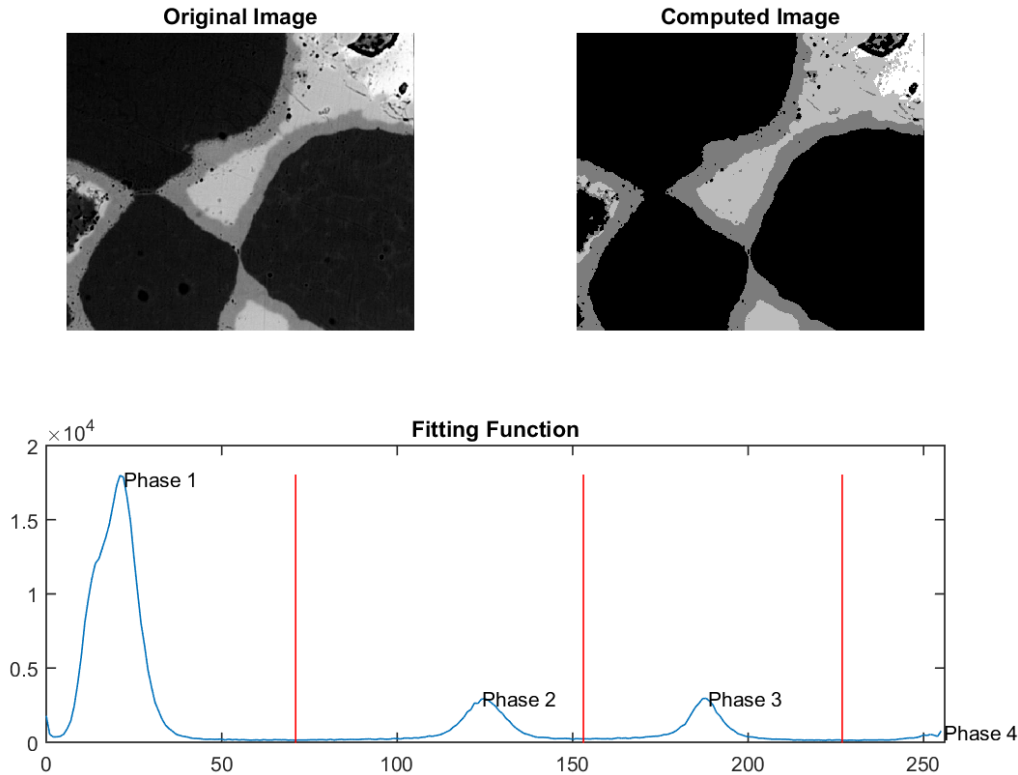


**Figure 5-5: Example of the phase analysis of a cross-section of a Cu-Sn TLPS joint with Cu-particles (Phase 1 - black),  $\text{Cu}_3\text{Sn}$  IMCs (Phase 2 – dark grey),  $\text{Cu}_6\text{Sn}_5$  IMCs (Phase 3 – grey), and Sn (Phase 4 - white)**

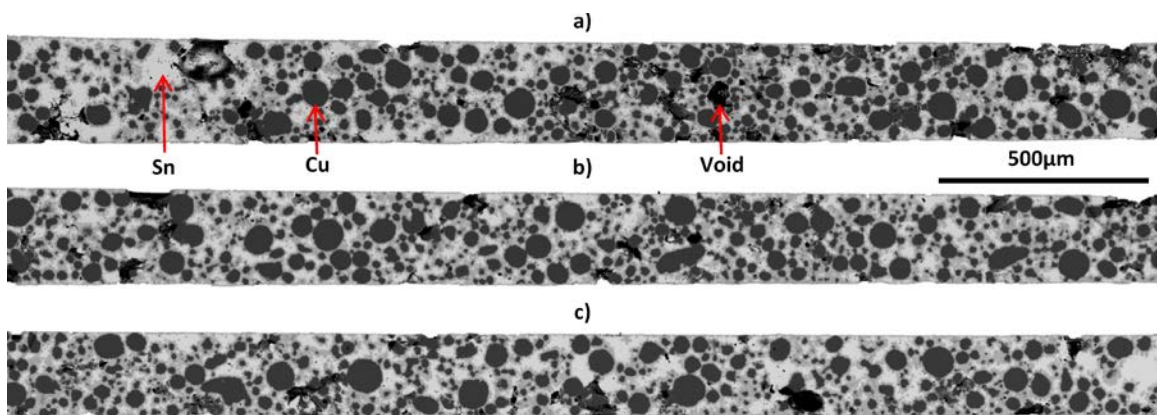
Different metallic phases can easily be analyzed by greyscale images obtained by SEM microscopy. It can be difficult to discern voided areas from dark phases in SEM images because of their similarity. For a quantification of the voiding behavior, optical microscopy images of the joints were converted to greyscale and subsequently analyzed by the Phase Analysis Software. In those images, voids can be identified as dark grey or black areas.

#### 5.1.1 Microstructural Evolution

Figure 5-6 to Figure 5-9 show cross-sections of joints after the two processing (sintering for 2 and 30 minutes at 300 °C) and two aging steps (aging for 24 and 100 hours at 250 °C) obtained from ESEM. Because of the large joint area, a complete joint image cannot be obtained by a single ESEM picture. The images shown in Figure 5-6 to Figure 5-9 were

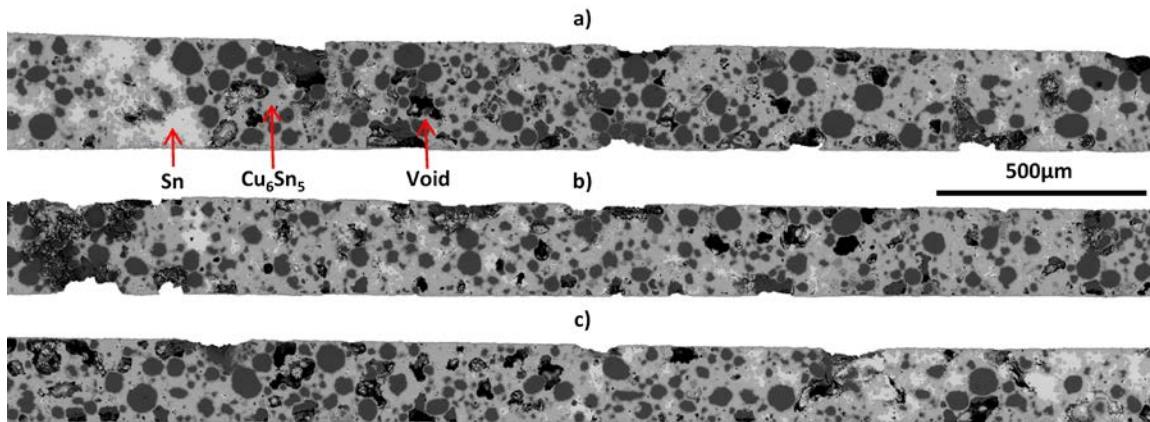
created by joining multiple individual images taken with 500x magnification for each joint. To provide a higher magnification and more detailed view, the resulting full joint images were then separated into three sections of equal size (indicated in the figures by a) and c) for the left and right sides of the cross-section, respectively, and b) for the center third of the joint).

Figure 5-6 shows a cross-section of a joint sintered for 2 minutes at 300 °C. A considerable amount of unconsumed Sn is present throughout the joint. Thin layers of  $\text{Cu}_6\text{Sn}_5$  have started to grow at the interfaces between the Cu-particles and Sn as well as at the interfaces between the Cu-substrate and Cu-coupon and Sn. No significant presence of  $\text{Cu}_3\text{Sn}$  IMCs could be detected at this stage. Spherical Cu-particles with a wide range of diameters are present. The actual average particle size can be higher than the apparent particle diameter because a cross-section does not intersect the majority of the particles close to their center. Voids are distributed homogeneously throughout the joint. The lack of a continuous presence of high  $T_m$  phases (IMCs and Cu-particles) between the top and the bottom of the joint shows that the joint as a whole does not possess high temperature capability.



**Figure 5-6: Cross-section of a Cu-Sn joint sintered for 2min@300 °C. Joint edges a) and c) and joint center b) shown separately. Considerable amounts of unconsumed Sn are still present in the joint.  $\text{Cu}_6\text{Sn}_5$  IMCs have started growing around the spherical Cu-particles. Voids are distributed homogeneously**

Figure 5-7 shows a cross-section of a joint sintered for 30 minutes at 300 °C. The majority of the Sn in the joint was converted to IMCs. Local pockets of Sn remain and the majority of those are located at the far edges of the joints (left side of Figure 5-7 a) and right side of Figure 5-7 c)). The majority of the interconnect microstructure is characterized by Cu-particles embedded in a matrix of  $\text{Cu}_6\text{Sn}_5$  IMCs. Thin layers of  $\text{Cu}_3\text{Sn}$  IMCs have grown at the interfaces between Cu and  $\text{Cu}_6\text{Sn}_5$  IMCs. The number of Cu-particles has decreased compared to the shorter process duration shown in Figure 5-6. This indicates that small Cu-particles have been completely consumed and converted to IMCs. At this point most of the joint consists of high  $T_m$  phases (predominately  $\text{Cu}_6\text{Sn}_5$  and Cu-particles with some  $\text{Cu}_3\text{Sn}$ ). This indicates that the joint possesses high temperature under this process condition. Similar to Figure 5-6, voids are distributed homogeneously.



**Figure 5-7: Cross-section of a Cu-Sn joint sintered for 30min@300 °C. Joint edges a) and c) and joint center b) shown separately. The majority of Sn was converted to  $\text{Cu}_6\text{Sn}_5$ . Local pockets of Sn remain. Thin layers of  $\text{Cu}_3\text{Sn}$  IMCs are present at the interfaces between  $\text{Cu}_6\text{Sn}_5$  and Cu. The smallest Cu-particles were completely converted to IMCs**

Figure 5-8 shows a cross-section of a joint sintered for 30 minutes at 300 °C and subsequently aged for 24 hours at 250 °C. At this point hardly any residual Sn is present in the joint region. Limited pockets of Sn can be found at the edges of the joint (left side of Figure 5-8 a) and right side of Figure 5-8 c)). Limited residual Cu is present at the joint

edges. The majority of the joint edge microstructure is characterized by these Cu-particles embedded in a matrix of  $\text{Cu}_6\text{Sn}_5$  IMCs. On the top and bottom interfaces between the bulk joint and the Cu-coupon and the Cu-substrate, a layer of  $\text{Cu}_3\text{Sn}$  IMC with a thickness of  $\sim 8 \mu\text{m}$  has grown towards the joint centerline. The microstructure at the joint center is characterized by few Cu-particles surrounded by thick layers of  $\text{Cu}_3\text{Sn}$  IMCs embedded in a matrix of  $\text{Cu}_6\text{Sn}_5$  IMCs. The percentage of  $\text{Cu}_3\text{Sn}$  in the joint center is higher than at the joint edges. The voiding percentage is higher at the joint center compared to the joint edges.

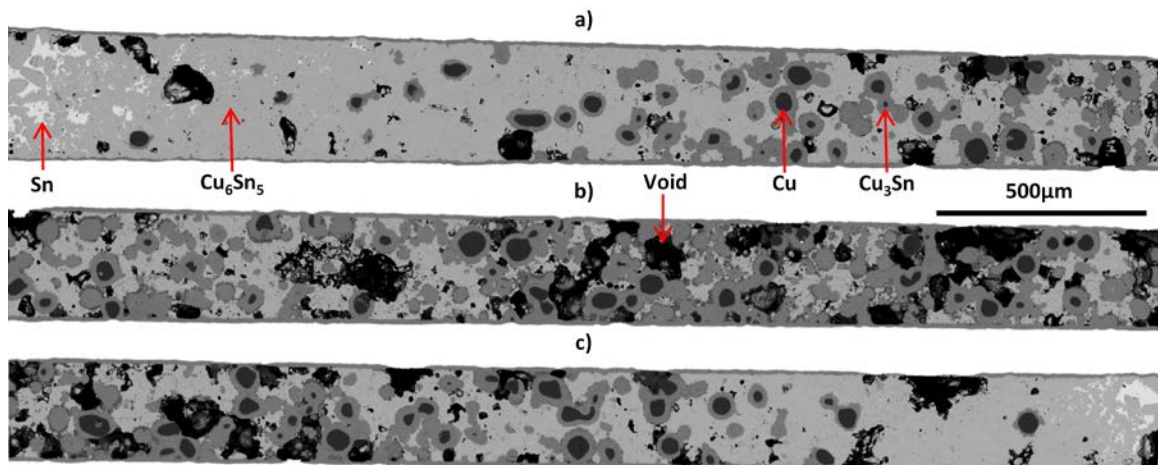


**Figure 5-8: Cross-section of a Cu-Sn joint after aging for 24h @ 250 °C. Joint edges a) and c) and joint center b) shown separately. Limited residual Cu is present at the joint edges which consist predominately of  $\text{Cu}_6\text{Sn}_5$ . The joint center has a higher percentage of  $\text{Cu}_3\text{Sn}$ . Voiding is more pronounced at the joint center**

Figure 5-9 shows a cross-section of a joint sintered for 30 minutes at 300 °C and subsequently aged for 100 hours at 250 °C. At this point Sn is almost completely consumed besides small traces at the joint edges (left side of Figure 5-9 a) and right side of Figure 5-9 c)). No residual Cu is present at the joint edges. The joint edge microstructure is characterized by a continuous layer of  $\text{Cu}_6\text{Sn}_5$  IMCs sandwiched between two layers of  $\text{Cu}_3\text{Sn}$  IMCs with a thickness of  $\sim 17 \mu\text{m}$  that have grown towards the joint centerline. This  $\text{Cu}_3\text{Sn}$  layer is about twice as thick as for the joint shown in Figure 5-8. This is in agreement

with the behavior predicted by Fick's second law of diffusion: as the aging time increases ~4 fold from 24 hours to 100 hours, the diffusion length should increase with a factor of ~2. The joint center consists predominately of  $\text{Cu}_3\text{Sn}$  IMCs with few embedded Cu-particles. Similar to Figure 5-8, the center of the joint shows higher voiding levels than the edges of the joint: the regions dominated by  $\text{Cu}_6\text{Sn}_5$  IMCs show low voiding levels whereas the regions dominated by  $\text{Cu}_3\text{Sn}$  show higher voiding levels.

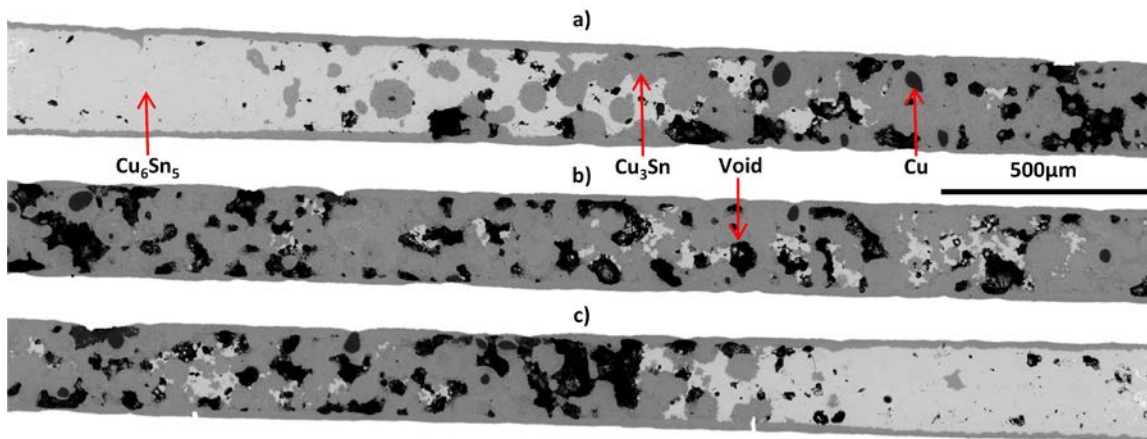


**Figure 5-9: Cross-section of a Cu-Sn joint after aging for 100h@250 °C. Joint edges a) and c) and joint center b) shown separately. Sn is almost completely consumed. The joint edges consist predominately of  $\text{Cu}_6\text{Sn}_5$  and most Cu has been consumed in these regions. The joint center consists predominately of  $\text{Cu}_3\text{Sn}$ . Voids are concentrated in the  $\text{Cu}_3\text{Sn}$ -rich regions**

### 5.1.2 Voiding

Figure 5-10 shows the development of the joint voiding during sintering and aging. After two minutes of sintering 4.88% of the cross-sectional area consists of voids. This percentage increases to 9.24% for 30 minutes of sintering. During subsequent annealing the voiding levels remain relatively constant with 10.59% after 24 hours of aging and 8.92% after 100 hours of aging. The initial increase in voiding levels from 2 minutes of sintering to 30 minutes of sintering can be explained by the reduction of volume during the formation of  $\text{Cu}_6\text{Sn}_5$  IMCs from Cu and Sn. As detailed above, a reduction in volume of

4.76% is associated with liquid-solid formation of this type of IMC. As will be shown below, the majority of  $\text{Cu}_6\text{Sn}_5$  IMCs are formed during sintering, not during aging. Therefore, the increase in void volume is most pronounced during sintering. The volume reduction due to the formation of  $\text{Cu}_3\text{Sn}$  from  $\text{Cu}_6\text{Sn}_5$  and Cu is only 1.19%, which is small compared to the initial volume reduction due to the formation of  $\text{Cu}_6\text{Sn}_5$ , and small compared to the maximum and minimum voiding levels, see Figure 5-10. The main IMC type formed during aging (after processing) is the  $\text{Cu}_3\text{Sn}$  IMC, as will be shown in the phase analysis section below. As a result, no significant increase in voiding levels was detected after the initial sintering. Additionally, a wide range of voiding levels was observed for the condition with 24 hours of aging, which could explain the slightly higher voiding levels compared to the 30 minutes of sintering and 100 hours of aging conditions.

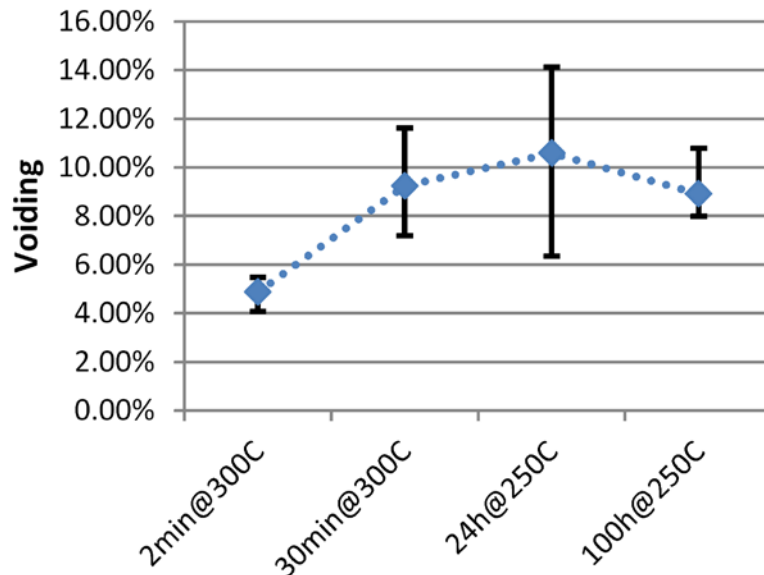


**Figure 5-10: Development of the joint voiding during sintering aging**

Figure 5-11 shows the dependence of the void formation on the location within the joint. The general voiding trend in the joint edges and center follows the behavior shown for the full joint, compare Figure 5-10. After 2 minutes of sintering the center of the joints shows higher voiding levels compared to the edges of the joints (5.61% and 3.44% respectively).

For the longer sintering condition and after subsequent aging this trend reverses and the joint center shows higher voiding levels compared to the joint edges. After 30 minutes of sintering the center and edge voiding levels are 10.39% and 8.67% respectively. After subsequent aging the voiding levels in the joint center remains continuously above 10% while in the joint edge regions it remains below 10%.

An explanation for the reversal of the voiding behavior trend between the joint center and edges can be given by analyzing the initial stages of the sintering process. After the melting of the solder paste dispensed around the joint region, it infiltrates the Cu-particle mesh in the joint region. The driving forces behind the influx of liquid towards the joint center are capillary forces. As the solder infiltrates the solid particle mesh, Cu-particles are dragged along the flow direction which leads to an increase in particle density and a reduction of voiding levels in the joint center compared to the joint edges. It is well-known that particle rearrangement on considerable scales is possible in liquid phase sintering processes, see section 2.1. This explains the lower voiding levels at the joint center after short sintering times of 2 minutes.

For longer process durations, the rearrangement process is completed and the formation of intermetallic phases is the dominant process determining voiding levels. IMCs are growing faster at the joint center (which will be shown below) than at the joint edges, which leads to a faster growth of voids after longer sintering times. The void growth can be mitigated by additional influx of liquid Sn. Yet, as IMCs form between Cu-particles, pathways for liquid Sn reduce and it becomes increasingly difficult to compensate for the IMC formation induced void growth. The reduction of Sn influx is more pronounced for the joint center region compared to the joint edge regions. This explains the low levels of voiding at the

very edges of the joints for long process durations, compare Figure 5-7 to Figure 5-9 a) and c).

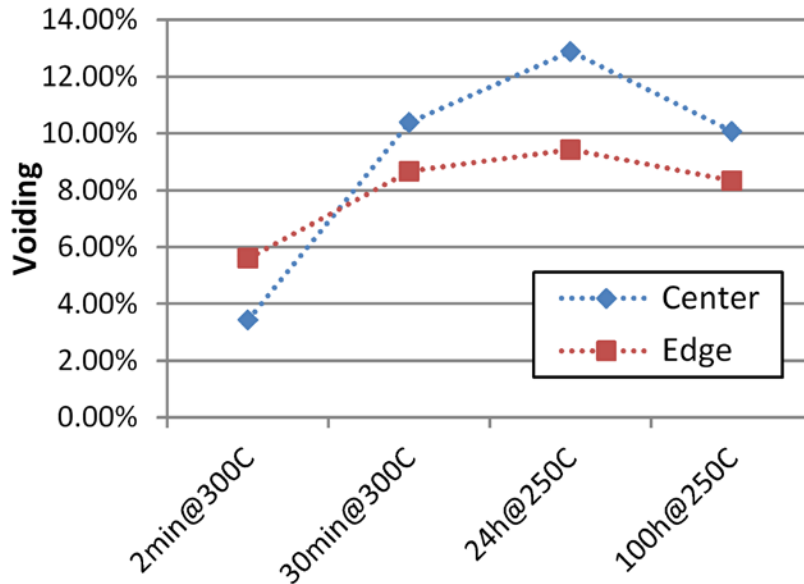


**Figure 5-11: Dependence of the development of the voiding behavior on the joint section**

### 5.1.3 Phase Evolution

Figure 5-12 shows the development of the vol.% of Cu for the full joint during sintering and subsequent annealing. The Cu concentration reduces slightly from 35.85% to 29.01% during the initial 2 and 30 minutes of sintering, respectively. It afterwards drops to 9.99% during the first 24 hours of aging after which it slowly reduces to 7.19% after 100 hours of aging. The highest variation of the Cu-concentration between different samples exists after 30 minutes of sintering.

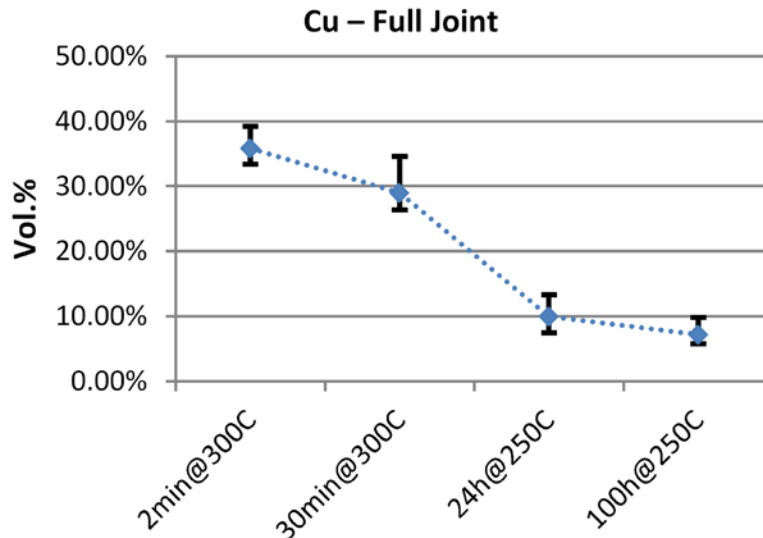


**Figure 5-12: Evolution of Cu for the full joint**

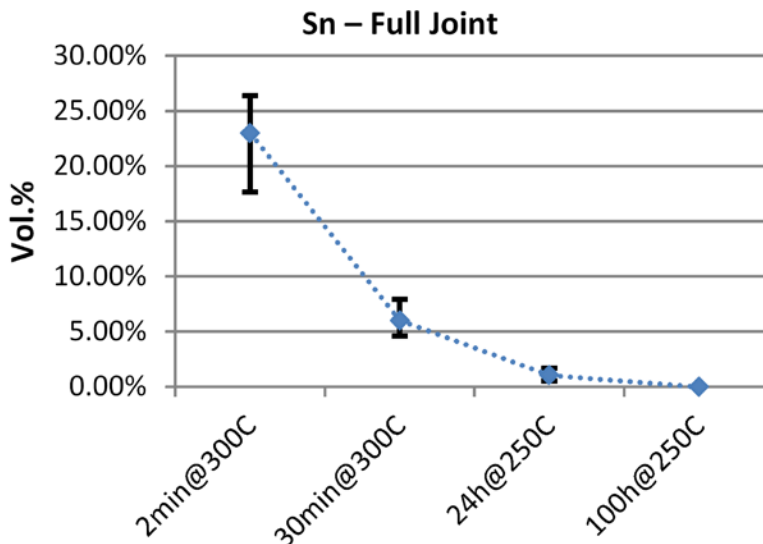


**Figure 5-13: Evolution of Sn for the full joint**

Figure 5-14 shows the development of  $\text{Cu}_6\text{Sn}_5$  IMCs in the full joint. After 2 minutes of sintering already 41.14% of the joint consists of  $\text{Cu}_6\text{Sn}_5$ . The vol.% of this phase shows only a slight increase up to aging of 24 hours but shows a rapid decline to 29.64% after 100 hours of aging. The highest variation of this phase is present after 24 hours of aging.

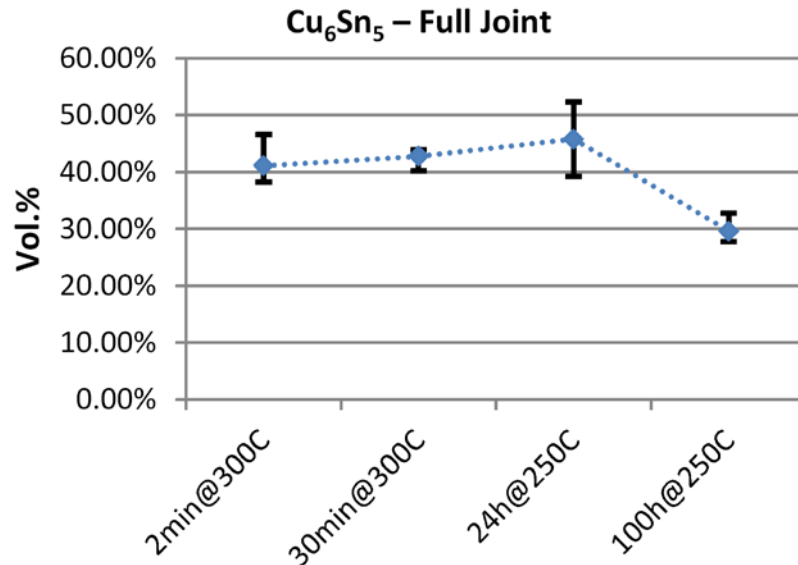


**Figure 5-14: Evolution of  $\text{Cu}_6\text{Sn}_5$  for the full joint**

Figure 5-15 shows the development of the  $\text{Cu}_3\text{Sn}$  IMC in the full joint. After 2 minutes of sintering only trace amount of  $\text{Cu}_3\text{Sn}$  are present in the joint. The concentration increases steadily during the three subsequent annealing steps to a final concentration of 62.30%. Its highest variability is coupled to that of  $\text{Cu}_6\text{Sn}_5$  after 24 hours of aging.

These statistics confirm the impression from the qualitative inspections performed above. After two minutes, significant amounts of low temperature alloy (Sn) are still present in the joint area, limiting its high temperature capability. Furthermore, the lack of Sn for additional transformation to  $\text{Cu}_6\text{Sn}_5$  explains the stagnation of voiding levels during thermal aging. After 30 minutes of sintering the majority (93.88%) of the joint phases are high temperature phases ( $\text{Cu}_6\text{Sn}_5$ ,  $\text{Cu}_3\text{Sn}$ , and Cu) and the interconnect melting temperature has shifted to higher temperatures. The  $\text{Cu}_6\text{Sn}_5$  percentage remains relatively unchanged beyond 24 hours of aging even though this IMC is initially formed rapidly. There are two explanations for this behavior: (1) the lack of Sn after 30 minutes of sintering limits the new formation of  $\text{Cu}_6\text{Sn}_5$  and (2) with increasing aging time more and more  $\text{Cu}_6\text{Sn}_5$  IMCs are converted to  $\text{Cu}_3\text{Sn}$ .

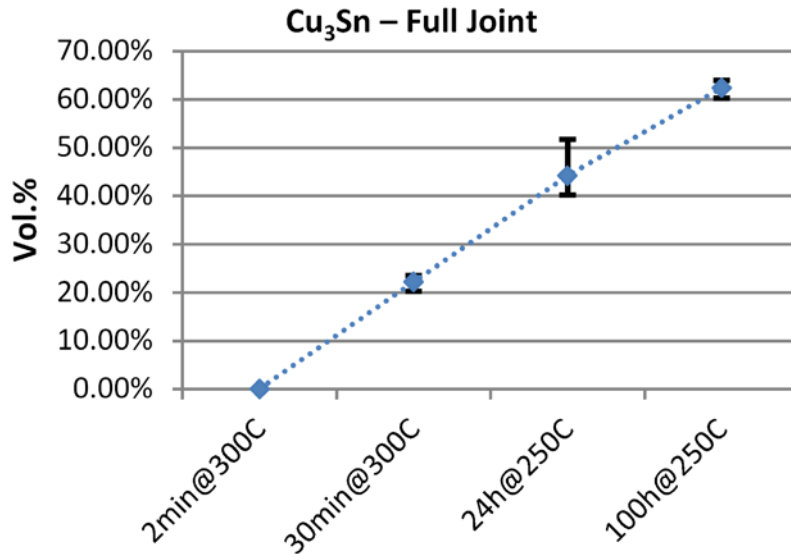


**Figure 5-15: Evolution of Cu<sub>3</sub>Sn for the full joint**

An assessment of the initial composition at the beginning of the sinter process by inspection is not possible because of the separation of the majority of Cu (stencil printed paste) and the majority of Sn (dispensed) before the initiation of the sinter process. Yet from the presence of phases after sintering and aging in combination with knowledge of phase stoichiometries and densities the vol.% of the original joint composition can be computed. The average Sn, Cu, Cu<sub>6</sub>Sn<sub>5</sub> and Cu<sub>3</sub>Sn concentrations for the two sintering and two aging conditions were used to estimate the original Sn and Cu concentration at the beginning of the sintering process (from here on referred to as *0min est.*). The computed highest, lowest, and average estimates for the vol.% Cu at the beginning of the sintering process are 55.26%, 49.22%, and 51.47% respectively. Figure 5-16 shows the evolution of phases in the full joint including the estimate for the condition at the beginning of the sintering process.

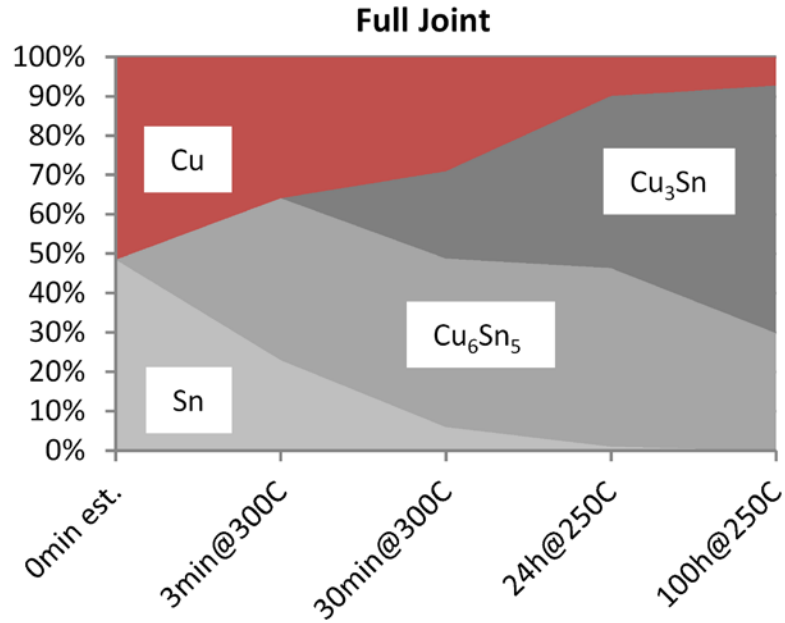
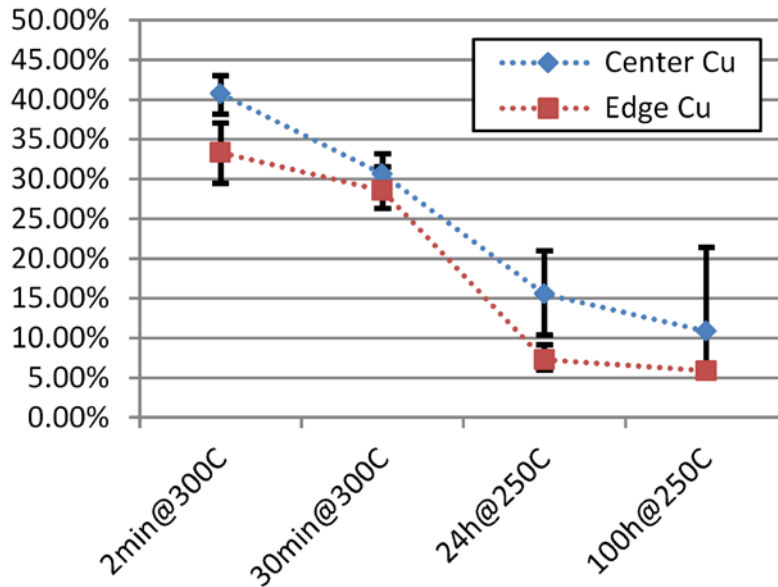


**Figure 5-16: Evolution of phases in the full joint**

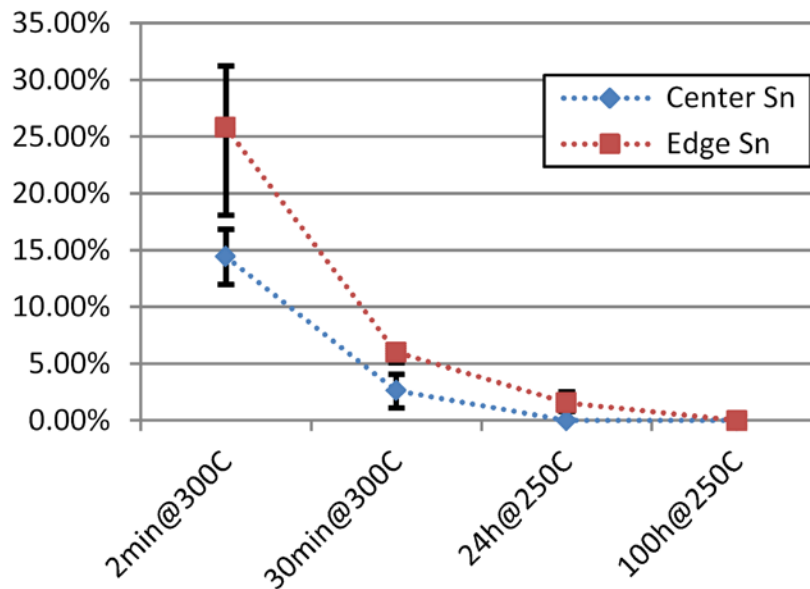
Figure 5-17 shows the development of the vol.% Cu during sintering and aging for the joint center and the joint edges. The trend is similar for both regions: a slight reduction of the Cu-content during processing (from 40.75% to 30.67% at the center and from 33.37% to 28.59% at the edges) is followed by a more pronounced decrease during the initial 24 hours of aging (to 15.57% and 7.30% respectively). At the joint edges the Cu-content is hardly reduced between 24 hours and 100 hours of aging, whereas at the joint center Cu continues to be consumed. The average amount of Cu present at the joint center exceeds the Cu at the joint edges at all times. The variation of the Cu-content decreases with time at the joint edges while it increases at the joint center.

Figure 5-18 shows the development of the Sn-content during sintering and aging. The amount of Sn is lower at the joint center than at the joint edges under all conditions. Initial concentrations are 14.45% and 25.83% respectively. Both, the absolute concentration as well as the variation of the Sn-content decrease over time throughout the joint. No Sn could

be detected at the joint center after 24 hours of aging. In contrast, full consumption of Sn at the joint edges occurred only after 100 hours of aging.



**Figure 5-17: Evolution of Cu at the joint center and edges**



**Figure 5-18: Evolution of Sn at the joint center and edges**

Figure 5-19 shows the development of the  $\text{Cu}_6\text{Sn}_5$  phase in the TLPS interconnect. The growth and consumption of this phase follow different patterns at the joint center and the joint edges. During sintering the concentration of  $\text{Cu}_6\text{Sn}_5$  is still comparable throughout

the joint. After 2 minutes of sintering the vol.% of  $\text{Cu}_6\text{Sn}_5$  is higher at the joint center compared to the joint edges (44.79% and 40.80% respectively). After 30 minutes of sintering this behavior inverts as the vol.% of  $\text{Cu}_6\text{Sn}_5$  increases at the joint edges and decreases at the joint center but is close (42.92 and 43.49% respectively). During the initial 24 hours the  $\text{Cu}_6\text{Sn}_5$  concentration increases to 51.69% at the joint edges but decreases to 16.73% at the joint center. Additionally, the variability of the  $\text{Cu}_6\text{Sn}_5$  phase is most pronounced at this point.

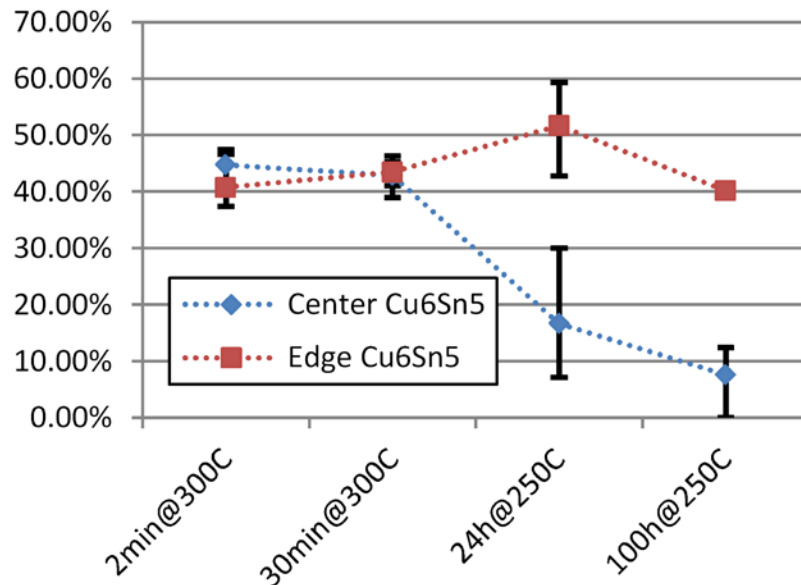


**Figure 5-19: Evolution of  $\text{Cu}_6\text{Sn}_5$  at the joint center and edges**

After 100 hours of aging, the presence of the  $\text{Cu}_6\text{Sn}_5$  is reduced throughout the whole interconnect to 7.63% at the joint center and 40.21% at the joint edges. The reason for the difference of the  $\text{Cu}_6\text{Sn}_5$  phase development between the joint center and the joint edges can be explained by the concentrations of Cu and Sn at the beginning of the sintering process: After 24 hours of aging, all Sn at the joint center is consumed and no new  $\text{Cu}_6\text{Sn}_5$  can be formed. Simultaneously residual Cu is present in this region and drives the transformation of  $\text{Cu}_6\text{Sn}_5$  to  $\text{Cu}_3\text{Sn}$ . In contrast, residual Sn is still present at the joint edges,

which drives the formation of  $\text{Cu}_6\text{Sn}_5$  IMCs, but the edges lack Cu for the transformation of  $\text{Cu}_6\text{Sn}_5$  to  $\text{Cu}_3\text{Sn}$ , which explains the high levels of  $\text{Cu}_6\text{Sn}_5$  at the joint edges throughout the process.

Figure 5-20 shows the development of the  $\text{Cu}_3\text{Sn}$  phase during sintering and aging. No  $\text{Cu}_3\text{Sn}$  could be detected throughout the joint after 2 minutes of sintering. The reaction time is too short for significant formation and growth of  $\text{Cu}_3\text{Sn}$  IMCs. The vol.% of  $\text{Cu}_3\text{Sn}$  after 30 minutes of sintering is almost identical at the joint center and the joint edges (23.77% and 21.90% respectively). This similarity correlates with the similar consumption rate of Cu throughout the whole joint during the sintering stage, compare Figure 5-17.

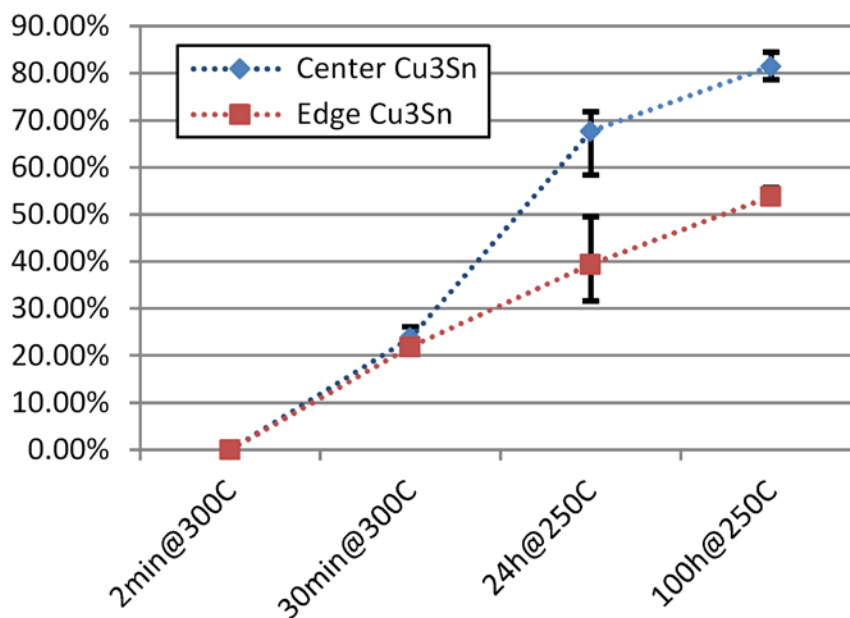


**Figure 5-20: Evolution of  $\text{Cu}_3\text{Sn}$  at the joint center and edges**

After 24 hours of aging the growth at the joint center occurs much faster than at the joint edges (67.71% compared to 39.43%). This can be explained by the lack of Cu at the joint edges after 24 hours, compare Figure 5-17, which limits the transformation of  $\text{Cu}_6\text{Sn}_5$  to  $\text{Cu}_3\text{Sn}$ . In contrast, considerable amounts of Cu are still present at the joint center, which drives the fast growth of  $\text{Cu}_3\text{Sn}$ . The growth rate of  $\text{Cu}_3\text{Sn}$  at the center slows down

between 24 hours and 100 hours because the microstructure has already stabilized and is characterized by residual Cu-particles embedded in a  $\text{Cu}_3\text{Sn}$  matrix.

Figure 5-21 and Figure 5-22 summarize the development of phases at the joint center and the joint edges respectively. The initial Cu- and Sn-concentrations have been estimated for both cases by the approach introduced above: The initial Cu-concentrations were 58.63% at the joint center and 49.24% at the joint edges with Sn as the balance. The difference of the initial Cu-concentrations is the defining element explaining the differences of the resulting voiding levels, phase growth, and final phase distribution, as explained above.

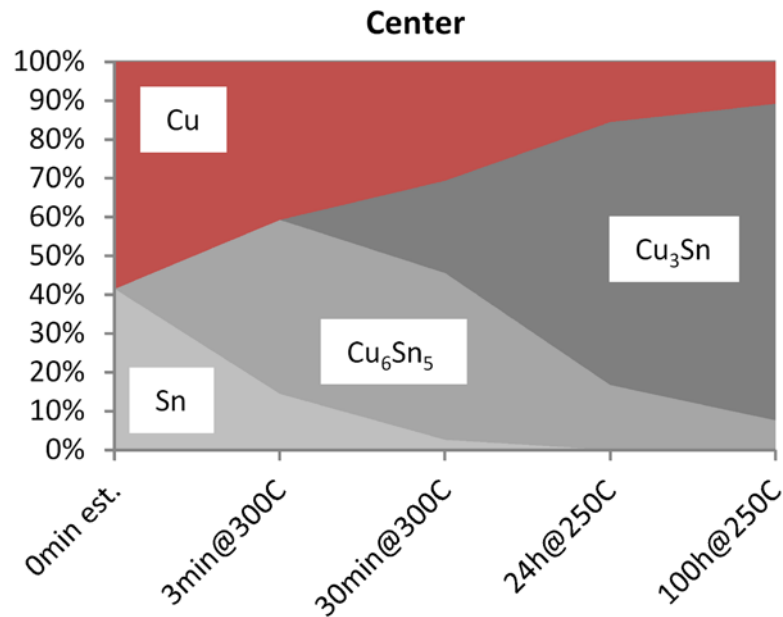


**Figure 5-21: Evolution of phases in the joint center**

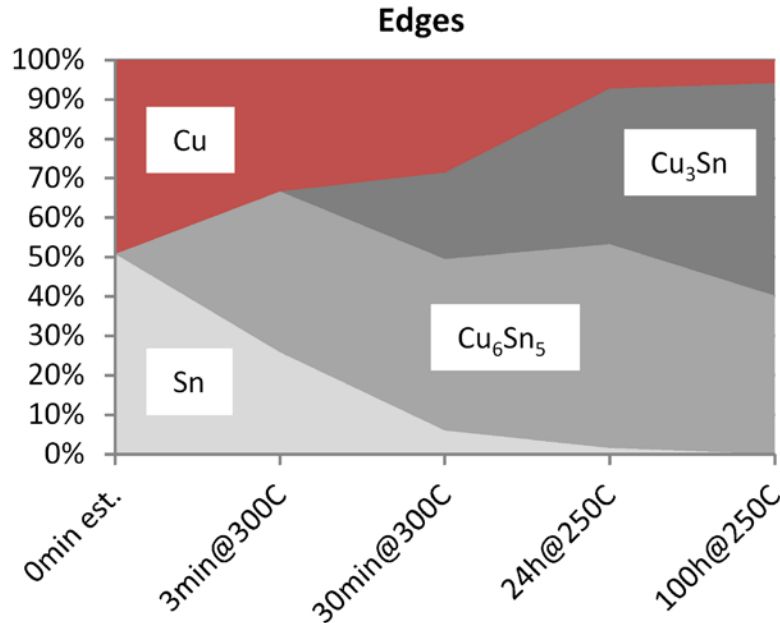


**Figure 5-22: Evolution of phases in the joint edges**

## 5.2 Void Growth and Grain Structure Evolution of Cu-Sn TLPS Joints

In the following section, the nucleation of voids, the growth of voids, and the evolution of the grain structure of IMCs in Cu-Sn TLPS joints during high temperature aging is assessed. The samples are identical with the samples analyzed in section 5.1, but because of the lack of IMC growth during early sintering stages, the samples sintered for 2 minutes were excluded from the analysis. The discussion here will be limited to the samples sintered for 30 minutes at 300 °C without aging and samples sintered for 30 minutes at 300 °C subsequently aged for 24 hours and 100 hours at 250 °C.

The evolution of the grain morphology of the Cu-Sn IMCs in these joints can be investigated without the application of etchants (as is required in solder joints) by inspection of surfaces in voided areas. Conventionally, the surface morphology of IMCs is exposed by selective etching of the solder layer. Yet, this is only feasible for exposing the Cu<sub>6</sub>Sn<sub>5</sub> layer, not the underlying Cu<sub>3</sub>Sn layer. To analyze the surface morphology of Cu<sub>3</sub>Sn IMCs in solder joints, the Cu<sub>6</sub>Sn<sub>5</sub> IMCs would have to be etched selectively, too. In

contrast, in TLPS sinter joints with significant voiding levels, the IMC surface morphologies can be analyzed by investigation of the surface areas at the back of cross-sectioned voids. Combined with multiple aging steps, this provides information about the evolution of the grain structure of IMC phases.

### 5.2.1 Cu<sub>6</sub>Sn<sub>5</sub> Microstructure

Figure 5-23 shows a cross-section of a joint after 30 minutes of sintering to 300 °C. Figure 5-23 (left) shows the entire voided area with the IMC surface morphology in focus few micrometers below the cross-section surface. A detailed view on the surface morphology is shown in Figure 5-23 (right). Two phases are present at the surface: large grains consisting of Cu<sub>6</sub>Sn<sub>5</sub> IMCs and thin layers of residual Sn. The size of the Cu<sub>6</sub>Sn<sub>5</sub> grains is approximately 10 μm. The Sn-phase is occupying the interspaces between the Cu<sub>6</sub>Sn<sub>5</sub> grains.

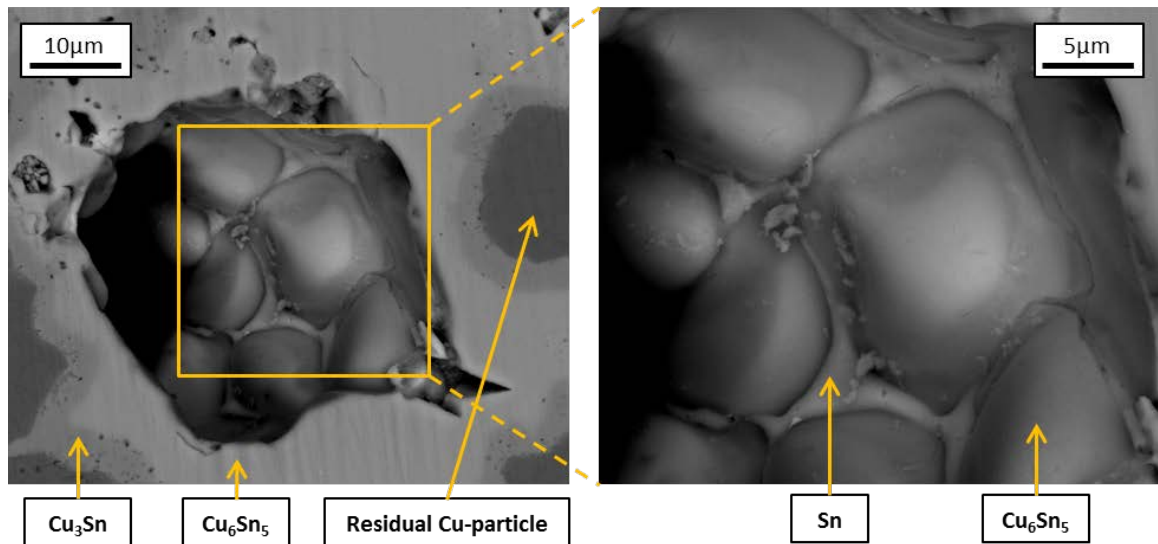


**Figure 5-23: Surface morphology of Cu<sub>6</sub>Sn<sub>5</sub> grains after 30 minutes of sintering at 300 °C. The grain size is on the scale of 10 μm. Intergranular spaces are filled with residual unconsumed Sn**

Figure 5-24 shows the surface morphology of a joint that was sintered for 30 minutes at 300 °C and subsequently aged for 24 hours at 250 °C. Only the Cu<sub>6</sub>Sn<sub>5</sub> IMC phase is

present for this condition. The size of the  $\text{Cu}_6\text{Sn}_5$  grains is similar to that of the unaged joint with approximately  $10\ \mu\text{m}$ . Thin gaps are present between the grain boundaries at locations of prior Sn phase.

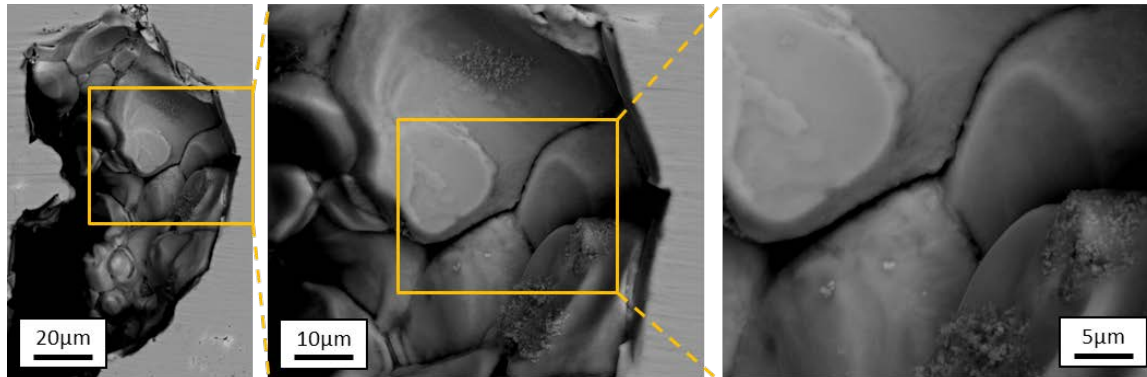


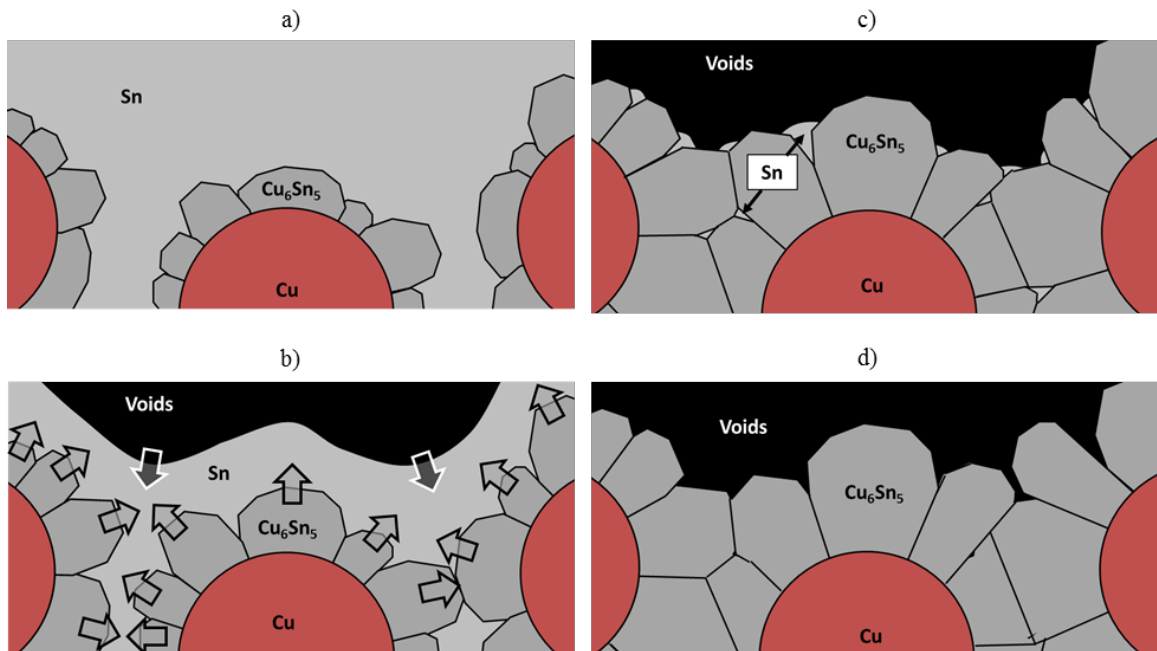
**Figure 5-24: Surface morphology of  $\text{Cu}_6\text{Sn}_5$  grains of a joint aged for 24 hours at  $250\ ^\circ\text{C}$  after 30 minutes of sintering at  $300\ ^\circ\text{C}$ . The grain size is on the scale of  $10\ \mu\text{m}$ . No residual Sn is present in the intergranular spaces**

The development of the morphologies shown in Figure 5-23 and Figure 5-24 can be explained by the growth behavior of  $\text{Cu}_6\text{Sn}_5$  IMCs at the interface between solid Cu-particles and liquid Sn. Figure 5-25 illustrates this during the sintering of Cu-Sn TLPS joints. The growth of  $\text{Cu}_3\text{Sn}$  IMCs was not included in this figure, because the growth of sub- $\text{Cu}_6\text{Sn}_5$   $\text{Cu}_3\text{Sn}$  does not influence the morphology at the top of the  $\text{Cu}_6\text{Sn}_5$  grains. Initially the Cu-particles are embedded in a matrix of liquid Sn, see Figure 5-25 a), and grains of  $\text{Cu}_6\text{Sn}_5$  IMCs nucleate at the Cu-to-Sn interface. As sintering continues, the  $\text{Cu}_6\text{Sn}_5$  grains grow and Sn and Cu are consumed simultaneously. The density of Cu and Sn in  $\text{Cu}_6\text{Sn}_5$  IMCs is higher than the density of equal ratios of Cu and Sn in their pure metal state. The density of solid Cu is  $8.96\ \text{g}/\text{cm}^3$  [115] and the densities of Sn in the solid and liquid<sup>2</sup> state are  $7.287\ \text{g}/\text{cm}^3$  [116] and  $7.032\ \text{g}/\text{cm}^3$  [117] respectively. The density of

---

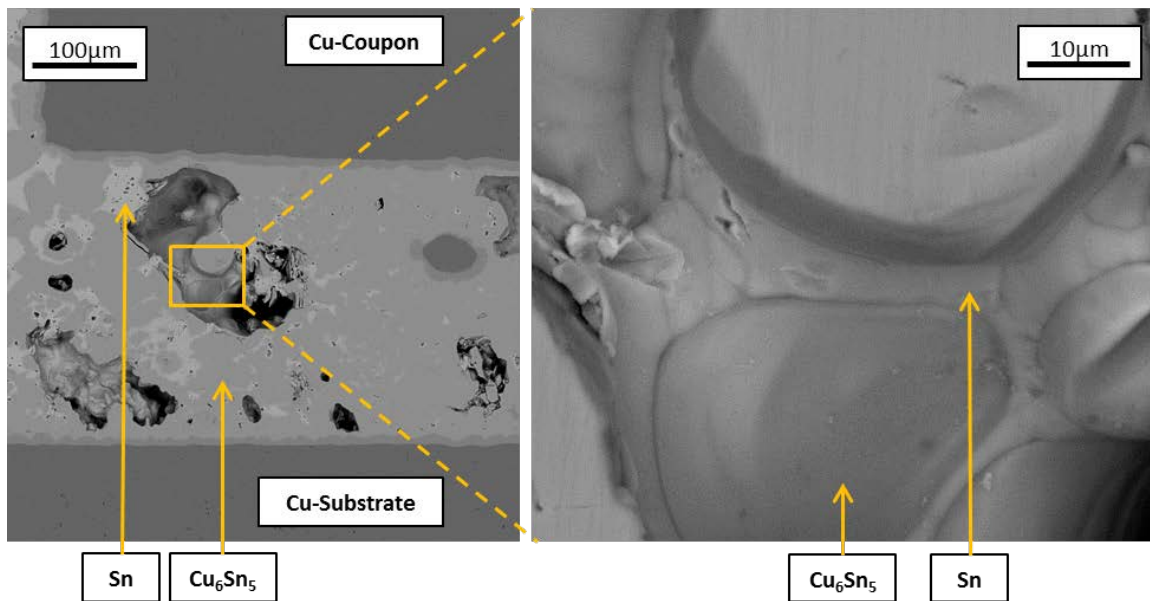
<sup>2</sup> Determined at 506.8K, close to the process temperature used in this work

$\text{Cu}_6\text{Sn}_5$  has been determined as  $8.28 \text{ g/cm}^3$  [118]. Calculating the volume of a unit cell of  $\text{Cu}_6\text{Sn}_5$  and comparing it to volume of an equal amount of Cu and Sn atoms in their pure solid metal state yields that the change in density causes a volume reduction of 2.01% compared to the original volume. The volume reduction is compensated by rearrangement of liquid Sn, which is attracted to the Cu-particles and associated  $\text{Cu}_6\text{Sn}_5$  grains by capillary forces. This rearrangement leads to the formation and growth of voids at locations of prior voids and Sn, see Figure 5-25 b). As sintering continues, Sn is continually consumed until only small quantities remain at the interspaces between  $\text{Cu}_6\text{Sn}_5$  grains because of preferential surface tension conditions, see Figure 5-25 c). This stage of joint microstructure and morphology exists after 30 minutes of sintering at  $300 \text{ }^\circ\text{C}$ , compare Figure 5-23. Eventually, all Sn is consumed and only  $\text{Cu}_6\text{Sn}_5$  is present at the void surface, see Figure 5-25 d). This is the case for joints aged for 24 hours at  $250 \text{ }^\circ\text{C}$ , see Figure 5-24.

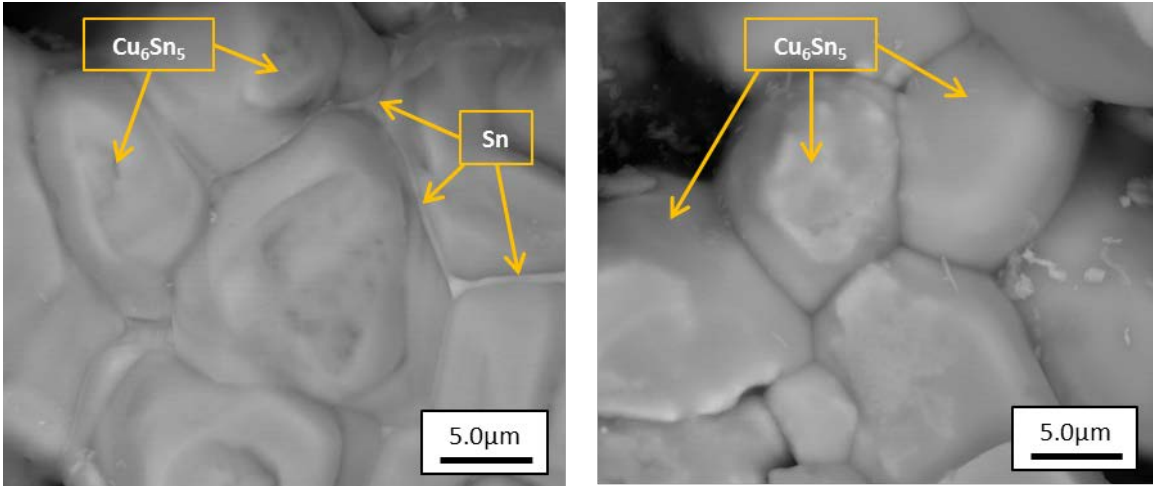


**Figure 5-25: Growth of  $\text{Cu}_6\text{Sn}_5$  IMCs and associated consumption of Sn and growth of void during particle-based TLPS of the Cu-Sn system: a) Nucleation of  $\text{Cu}_6\text{Sn}_5$  grains on the surface of the Cu-particle, b) growth of  $\text{Cu}_6\text{Sn}_5$  IMCs and consumption of Sn, c) continued growth of voids and receding of Sn into the spaces between the  $\text{Cu}_6\text{Sn}_5$  grains, and d) final structure after full consumption of Sn**

The presence of intergranular residual Sn furthermore depends on the local concentration of Sn in the region around the void. Figure 5-26 shows the morphology of a void from a joint sintered for 30 minutes at 300 °C and subsequently aged for 24 hours at 250 °C, identical process conditions as the morphology shown in Figure 2-21. In contrast to the joint region shown in Figure 2-21, residual Sn is present in the intergranular spaces between the  $\text{Cu}_6\text{Sn}_5$  grains after aging for the joint region shown in Figure 5-25. The reason is the high Sn-concentration and presence of local pores of Sn at the edge of the joint near the void in Figure 5-25. This shows that the time for complete consumption of intergranular Sn does not only depend on the process time, but also on localized variation of Sn-concentration. Some  $\text{Cu}_6\text{Sn}_5$  grain boundaries are filled with residual Sn even after aging at 250 °C for 100 hours, see Figure 5-27. After this aging duration only few  $\text{Cu}_6\text{Sn}_5$  grain boundaries showed residual traces of pure Sn.



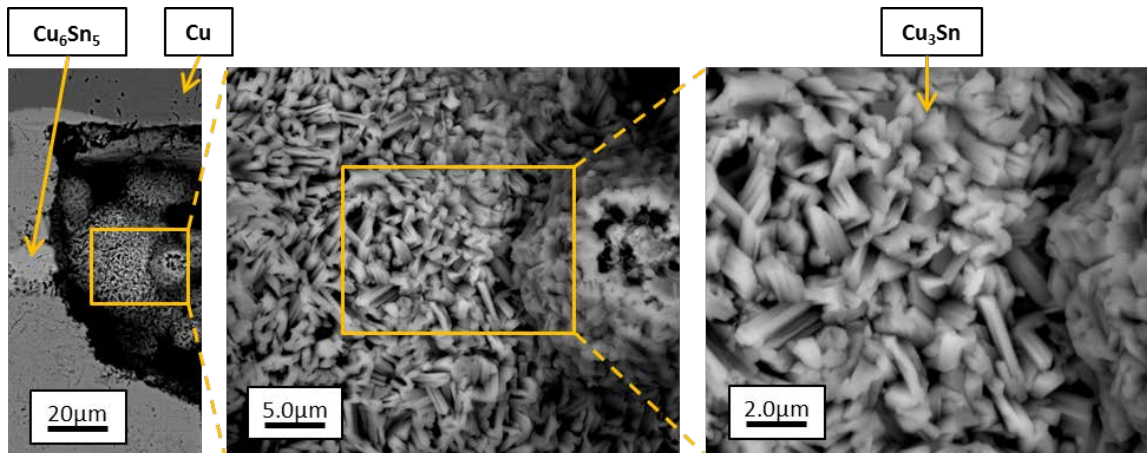
**Figure 5-26: Residual intergranular Sn phase after sintering for 30 minutes at 300 °C and subsequent aging at 250 °C for 24 hours. In contrast to the image shown in Figure 5-24, the higher Sn-concentration in the proximity of the void leads to slower Sn-consumption and presence of residual Sn**



**Figure 5-27: Limited residual Sn in some grain boundaries (right) between  $\text{Cu}_6\text{Sn}_5$  grains after sintering for 30 minutes at  $300\text{ }^\circ\text{C}$  and subsequent aging at  $250\text{ }^\circ\text{C}$  for 100 hours. The majority of the grain boundaries were not occupied by Sn after this aging duration (right)**

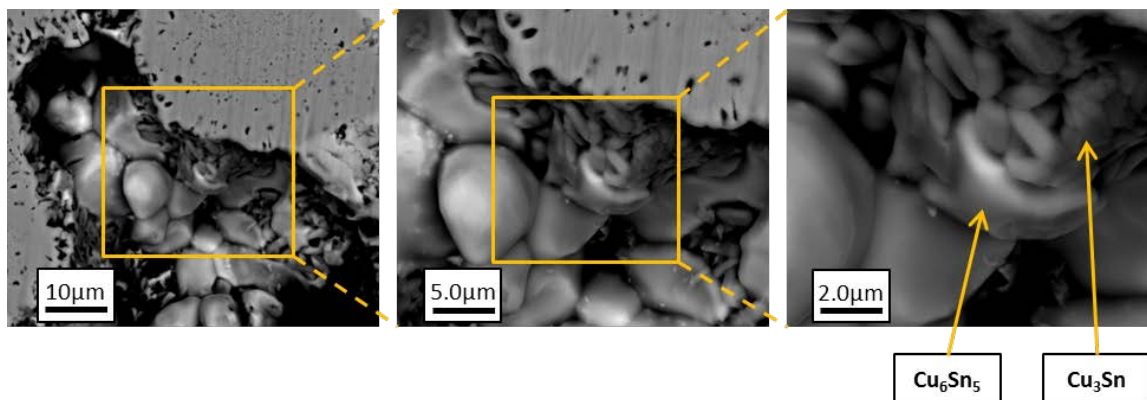
### 5.2.2 $\text{Cu}_3\text{Sn}$ Microstructure

Figure 5-28 shows the surface morphology of  $\text{Cu}_3\text{Sn}$  IMCs after sintering for 30 minutes at  $300\text{ }^\circ\text{C}$  and subsequent aging for 24 hours at  $250\text{ }^\circ\text{C}$  at different magnification levels. The  $\text{Cu}_3\text{Sn}$  crystals have lengths of few micrometers and thicknesses in the sub-micrometer range. They are considerably smaller than  $\text{Cu}_6\text{Sn}_5$  grains formed after identical aging conditions, compare Figure 5-24. The  $\text{Cu}_3\text{Sn}$  IMCs consist of a matrix of intersecting needle-like  $\text{Cu}_3\text{Sn}$  crystals interspersed by sub-micrometer sized voids. This contrasts with the  $\text{Cu}_6\text{Sn}_5$  IMCs, which consist of a continuous structure of nodule-like  $\text{Cu}_6\text{Sn}_5$  crystals with almost void-free grain boundaries. The direction of the  $\text{Cu}_3\text{Sn}$  crystals does not follow specific patterns or leads to a higher-order structure.



**Figure 5-28: Surface morphology of the  $\text{Cu}_3\text{Sn}$  grains of a joint sintered for 30 minutes at  $300\text{ }^\circ\text{C}$  and subsequently aged at  $250\text{ }^\circ\text{C}$  for 24 hours. The grain size is on the scale of few  $\mu\text{m}$**

Figure 5-29, Figure 5-30, and Figure 5-31 show the transformation of  $\text{Cu}_6\text{Sn}_5$  IMCs to  $\text{Cu}_3\text{Sn}$  IMCs after different aging durations. The transformation of the phase occurs simultaneously with a change of crystal structure. As the  $\text{Cu}_3\text{Sn}$  crystals grow out of a  $\text{Cu}_6\text{Sn}_5$  grain, their size and direction changes. This behavior is independent of aging time (24 hours of aging for Figure 5-29 and Figure 5-30 and 100 hours of aging for Figure 5-31) and location within the TLPS joint (within the bulk of the TLPS joints for Figure 5-29 and close to the Cu-substrate for Figure 5-30).



**Figure 5-29: Evolution of grain structure during the transformation from large-grained  $\text{Cu}_6\text{Sn}_5$  IMC to small-grained  $\text{Cu}_3\text{Sn}$  IMC (joint aged for 24 hours at  $250\text{ }^\circ\text{C}$ )**

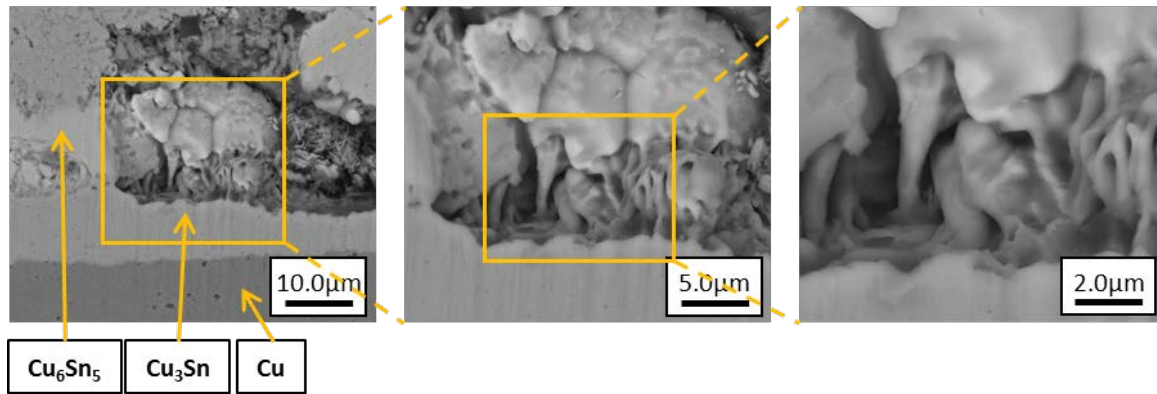


**Figure 5-30: Evolution of grain structure during the transformation from large-grained  $\text{Cu}_6\text{Sn}_5$  IMC to small-grained  $\text{Cu}_3\text{Sn}$  IMC (joint aged for 24 hours at 250 °C)**

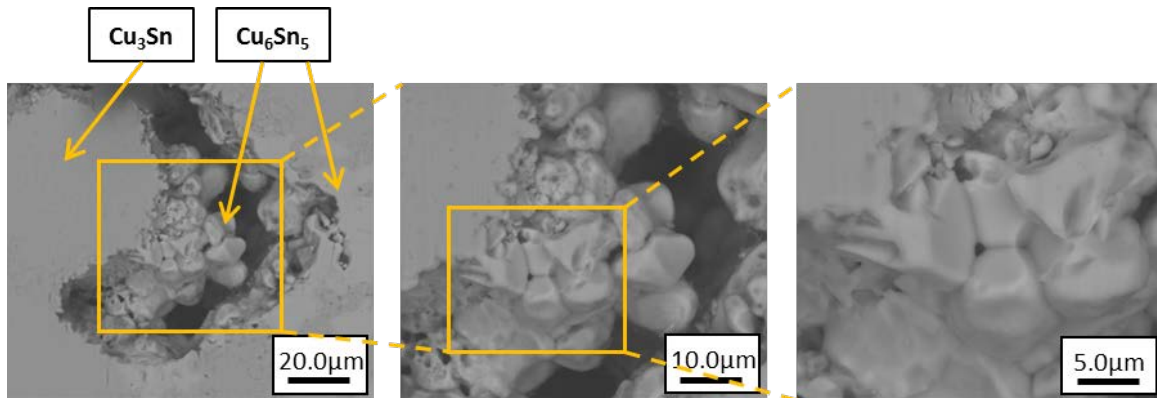


**Figure 5-31: Evolution of grain structure during the transformation from large-grained  $\text{Cu}_6\text{Sn}_5$  IMC to small-grained  $\text{Cu}_3\text{Sn}$  IMC (joint aged for 100 hours at 250 °C)**

To verify that the phase transformation and crystal transformation occur simultaneously, EDX-analyses of the phase transformation regions were performed. Figure 5-32 and Figure 5-33 show line-scans and area-scans of the material composition in the phase transition zone. Figure 5-32 (left) shows a high magnification view of the images shown in Figure 5-31 (right). The pink line in Figure 5-32 (left) shows the position of the line-scan. Figure 5-32 (center) shows an EDX compositional analysis along the line. The combination of Figure 5-32 (left) and Figure 5-32 (center) demonstrates that the IMC composition changes simultaneously with a change of crystal structure. The phase in the lower right side of Figure 5-32 (left) is the  $\text{Cu}_6\text{Sn}_5$  phase with relatively large, continuous grains with well-

defined boundaries, whereas the phase in the upper left side of Figure 5-32 (left) consist of  $\text{Cu}_3\text{Sn}$  IMCs with relatively small, more needle-like crystals.

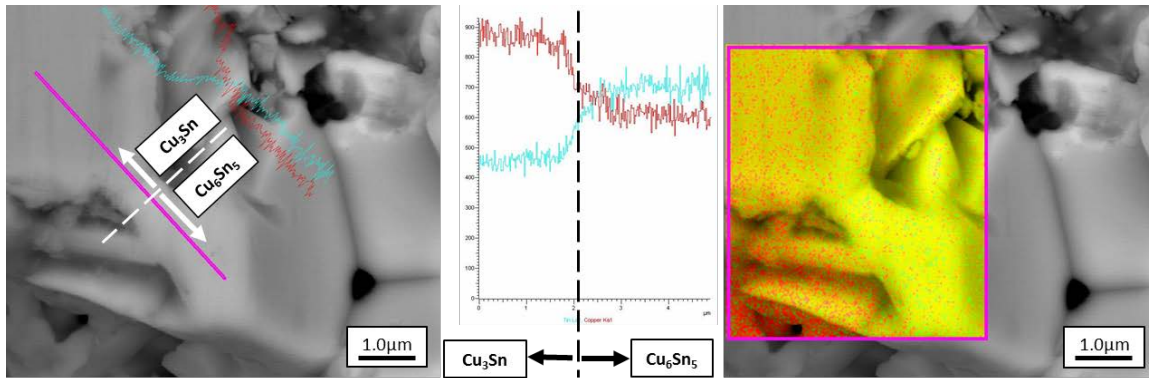


**Figure 5-32: EDX line-scan analysis of the transition zone from  $\text{Cu}_6\text{Sn}_5$  to  $\text{Cu}_3\text{Sn}$  (left and center) and EDX area scan (right). The transition from large grains to small grains coincides with the transition from  $\text{Cu}_6\text{Sn}_5$  to  $\text{Cu}_3\text{Sn}$ . The figure shows a high magnification view of Figure 5-31**

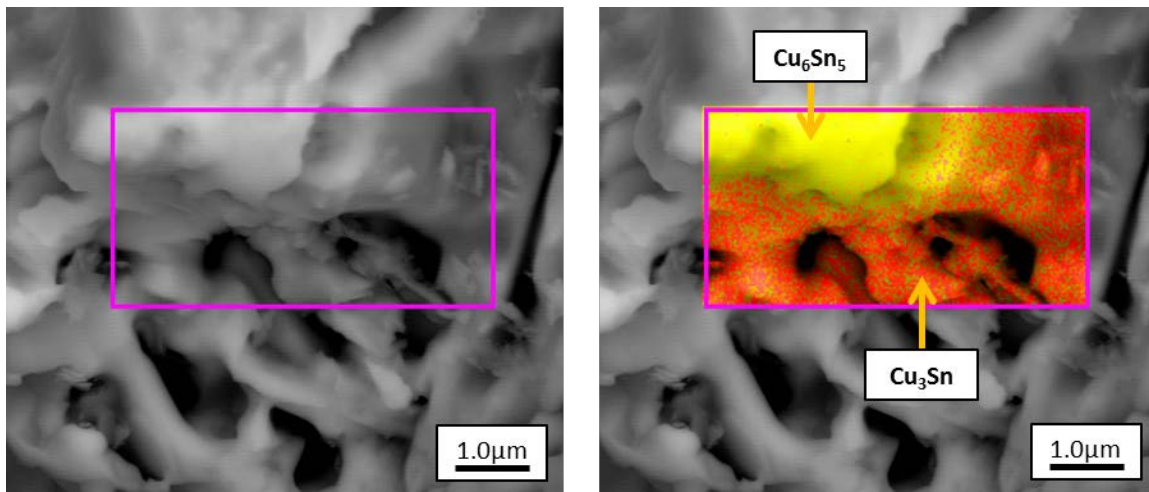


**Figure 5-33: EDX area scan analysis of the transition zone from  $\text{Cu}_6\text{Sn}_5$  to  $\text{Cu}_3\text{Sn}$ . The transition from large grains to small grains coincides with the transition from  $\text{Cu}_6\text{Sn}_5$  to  $\text{Cu}_3\text{Sn}$**

Figure 5-32 (right) and Figure 5-33 show area-scans of the  $\text{Cu}_6\text{Sn}_5$ -to- $\text{Cu}_3\text{Sn}$  transition regions. Regions with higher Cu-concentration and regions with higher Sn-concentration are displayed as red-rich and green-rich, respectively. The continuous regions with homogenous crystals have higher Sn-concentrations ( $\text{Cu}_6\text{Sn}_5$ ) and appear in the yellow-green tone. Regions with smaller crystals and increased voiding levels ( $\text{Cu}_3\text{Sn}$ ) appear red.

This verifies the hypothesis that the phase transformation occurs simultaneously with a change of crystal structure.

Multiple phenomena occur during the transformation of  $\text{Cu}_6\text{Sn}_5$  crystals to  $\text{Cu}_3\text{Sn}$  crystals: (1) reduction of the size of crystals from relatively large to small crystals, (2) change of shape from nodule-like to needle-like shape with random direction, and (3) nucleation of sub-micrometer sized voids in the interspaces between the needle-like crystals. In one case the nucleation of voids induced the formation of a gap within a bulk  $\text{Cu}_3\text{Sn}$  IMC matrix, see Figure 5-34. The structure looks similar to a crack, but no sign of fracture could be detected. This indicates that the growth of this gap occurred during the grain transformation process and not during post-aging cooling.

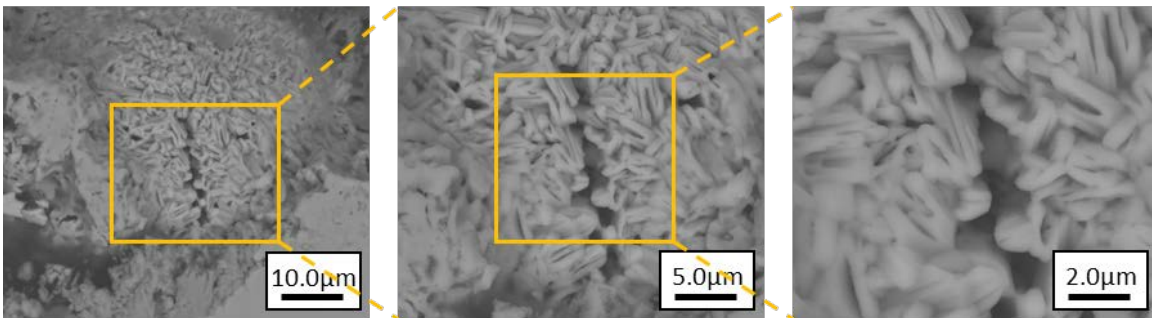


**Figure 5-34: Growth of gap between  $\text{Cu}_3\text{Sn}$  grains. No sign of fracture was detected. This indicates that the growth occurs during grain transformation**

The nucleation of voids can be explained by investigating the density change during the transformation of  $\text{Cu}_6\text{Sn}_5$  to  $\text{Cu}_3\text{Sn}$ . The densities of  $\text{Cu}_6\text{Sn}_5$  and  $\text{Cu}_3\text{Sn}$  have been reported as  $8.28 \text{ g/cm}^3$  and  $8.90 \text{ g/cm}^3$ , respectively. The increase in density can then be computed as 7.49%, which translates into a reduction in volume of 8.05%. The growth of  $\text{Cu}_3\text{Sn}$  from  $\text{Cu}_6\text{Sn}_5$  occurs during the solid state of both IMCs. Consequently, the volume reduction cannot be compensated by rearrangement of the liquid phase, which is the case during the growth of  $\text{Cu}_6\text{Sn}_5$  IMCs, compare section 5.2.1. Only two options remain for the compensation of volume reduction: (1) creation of tensile stresses within the  $\text{Cu}_3\text{Sn}$  IMC

regions or (2) nucleation of voids within the  $\text{Cu}_3\text{Sn}$  IMC regions. The latter phenomenon appears to be the driving force behind the growth of sub-micrometer voids between the  $\text{Cu}_3\text{Sn}$  crystals. This results in the formation of microvoids (sub-micrometer dimensions) within the  $\text{Cu}_3\text{Sn}$  regions, whereas  $\text{Cu}_6\text{Sn}_5$  regions are characterized by macrovoids (with sizes of multiple micrometers).

Two regions with different microvoiding behavior exist. Figure 5-35 shows a cross-section of a TLPS joint near the Cu-coupon. Three areas with different microvoid densities exist in this cross-section: (1) regions free of microvoids near the Co-coupon or Cu-substrates indicated by the white dotted lines, (2) regions with some microvoids in the TLPS bulk IMCs indicated by the yellow dotted lines, and (3) regions with high microvoid density in the proximity of residual Cu-particles and regions of prior Cu-particles indicated by the orange dotted lines.

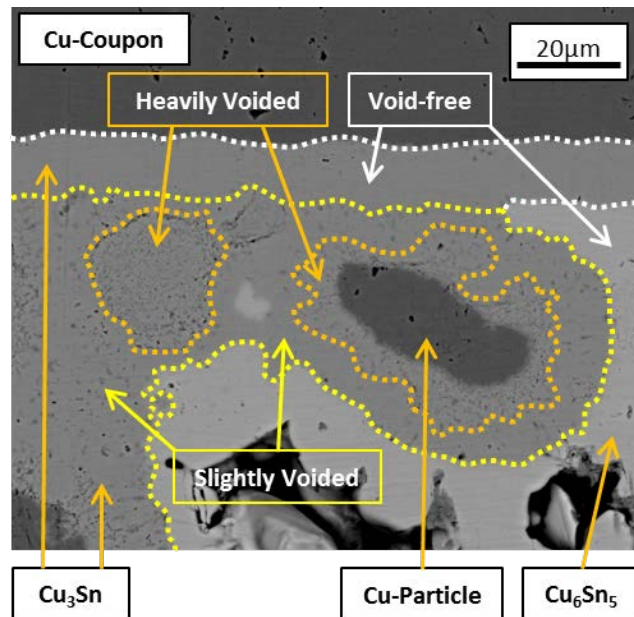


**Figure 5-35: Contrast between the microvoiding behaviors of  $\text{Cu}_3\text{Sn}$  IMCs in the bulk joint (bottom) around Cu-particles and  $\text{Cu}_3\text{Sn}$  IMCs formed at the interface to Cu-coupons and Cu-substrates (top)**

The differences in microvoid density between different joint regions indicates that a correlation exists between the density of microvoids and the proximity of the  $\text{Cu}_3\text{Sn}$  IMCs to Cu-particles. In other words, the formation of microvoids depends on the properties of the type of Cu consumed during the growth of  $\text{Cu}_3\text{Sn}$  IMCs. To analyze the properties of the Cu-particles, cross-sections have been prepared. Figure 5-36 and Figure 5-37 show SEM image of a cross-section of Cu-particles before sintering. Dotted orange lines in Figure 5-36 (bottom) and Figure 5-37 (right) outline regions with different crystal direction. Figure 5-36 (bottom) shows that Cu-grains differ in their direction as well as in their voiding behavior.

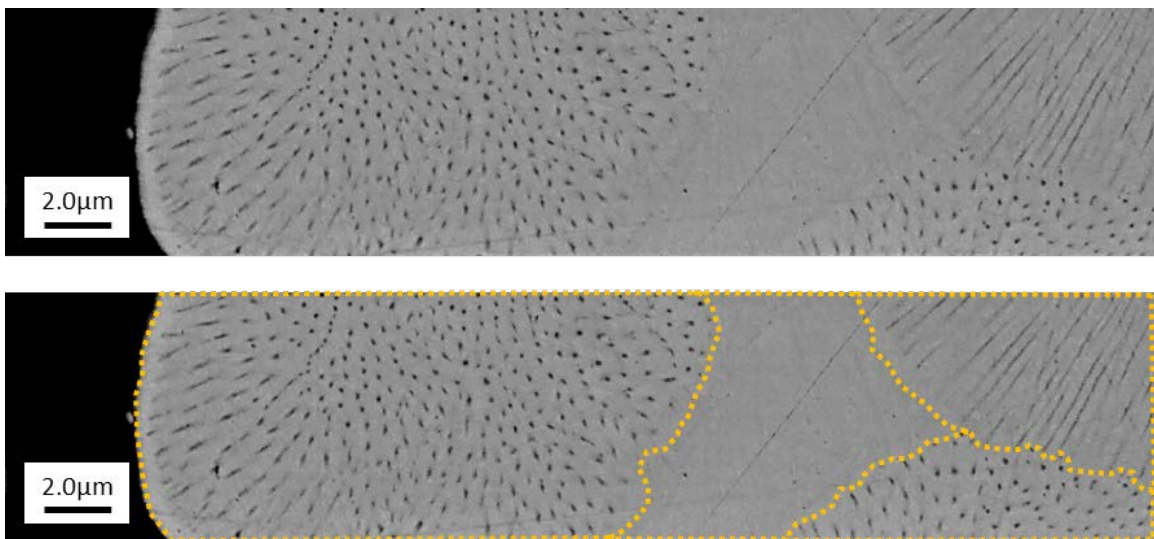


**Figure 5-36: SEM image of a cross-section of a Cu-particle before sintering (top). Regions of different crystal direction can be discerned, indicated by dotted yellow lines (bottom)**

Microvoids are present within some of the Cu-grains, in the example shown in Figure 5-36 these are the two grains on the right and the grain on the left. The center grain appears to be nearly void-free. Different directions become clear comparing the upper right corner grain and the left grain of Figure 5-36 (bottom). The directions of these two grains is approximately perpendicular to one another. The upper right grain seems to have solidified

parallel to the cross-sectional plane, while the left grain appears to have solidified perpendicular to it. The Cu-particle shown in Figure 5-36 consists predominately of nodule-like grains with microvoids embedded in a matrix of unvoided Cu-grains, whereas the Cu-particle shown in Figure 5-37 consists predominately of nodule-like grains without microvoids embedded in a matrix of Cu-grains with microvoids. Considerable presence of microvoids can be seen between the unvoided Cu-grains in Figure 5-37.

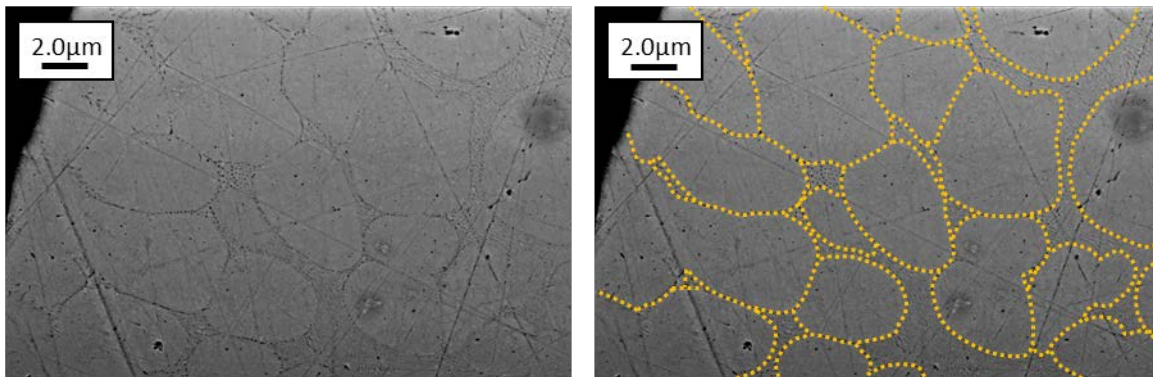


**Figure 5-37: SEM image of a cross-section of a Cu-particle before sintering. Regions of different crystal direction can be discerned, indicated by dotted yellow lines (left)**

No microvoids or discernible micro-grain structure were detected for the material used as Cu-coupons and Cu-substrates. This is in agreement with the expectation from the material (soft annealed 99.9% pure Cu), which should have large grain sizes due to the annealing process. The size of the Cu-grains in the Cu-particles is relatively small ( $< 5 \mu\text{m}$ , see Figure 5-36 and Figure 5-37) compared to that of annealed bulk Cu. This indicates that the susceptibility of microvoid nucleation in the  $\text{Cu}_3\text{Sn}$  IMCs of the TLPS joints depends on the grain size and microvoiding of the consumed Cu. In the following, a comparison to existing literature will be given to verify the feasibility of this hypothesis.

Shang et al. [119] have shown that differences exist between the growth behavior of  $\text{Cu}_3\text{Sn}$  IMCs on single crystalline and polycrystalline Cu. They found that the growth of  $\text{Cu}_3\text{Sn}$  on single crystalline Cu lead to columnar IMC structures with growth predominately

towards the column orientation and highly uniform grain structures. In contrast, the growth of  $\text{Cu}_3\text{Sn}$  on polycrystalline Cu was highly non-uniform and equiaxed. Additionally, the growth of  $\text{Cu}_3\text{Sn}$  was significantly faster on polycrystalline Cu compared to single crystalline Cu. The size of the  $\text{Cu}_3\text{Sn}$  grains on polycrystalline Cu was smaller.

Zhang et al. [120] studied the orientation of  $\text{Cu}_3\text{Sn}$  grains in layer-based Cu-Sn TLPS joints between single crystalline and polycrystalline Cu-substrates. Similarly to Shang et al. they found that the growth of  $\text{Cu}_3\text{Sn}$  IMCs on single crystalline Cu leads to highly uniform columnar  $\text{Cu}_3\text{Sn}$  structures. Additionally, by using single crystalline substrates with different orientations, they showed that the growth direction of the IMCs depends on the orientation of the Cu-substrates crystal. Analogously to Shang et al. the growth of  $\text{Cu}_3\text{Sn}$  IMCs on poly crystalline Cu lead to the formation of less homogeneous grain structures and the formation of smaller grains. The size of the Cu grains was approximately  $10\ \mu\text{m}$ .

Yu et al. [121] studied the relationship between the grain size of Cu-substrates and Kirkendall voiding at the  $\text{Cu}_3\text{Sn}$ -to-Cu interface after aging at  $180\ ^\circ\text{C}$ . They compared three types of Cu substrates: Substrates consisting of a high purity Cu foils that were electroplated with a  $10\ \mu\text{m}$  thick Cu film, substrates consisting of high purity Cu foils that were vacuum sputtered with a  $5\ \mu\text{m}$  thick Cu film, and substrates consisting solely of high purity Cu foils. The size of the grains of the Cu foils, electroplated layer, and the vacuum sputtered layer were  $> 10\ \mu\text{m}$ ,  $< 5\ \mu\text{m}$ , and  $< 1\ \mu\text{m}$ , respectively. After aging, no Kirkendall voids occurred at the  $\text{Cu}_3\text{Sn}$ -to-Cu interface for the unplated and unsputtered Cu foils. In contrast, Kirkendall voids appeared at that interface for both, the electroplated and vacuum sputtered substrates.

This verifies the hypothesis that a correlation exists between the differences in grain size between the Cu-grains in the substrate and coupon (large) and the grain size in the particles (small). Additionally, this could mean that the microvoids found in the bulk of the Cu-Sn TLPS joints are growing by the same mechanism as the Kirkendall voids found in soldering. In that case, the surface morphology of the  $\text{Cu}_3\text{Sn}$  IMCs assessed in this study is the first time the three-dimensional microstructure and surface morphology of Kirkendall-voided Cu-Sn IMCs has been documented. Normally, the presence of  $\text{Cu}_6\text{Sn}_5$  on top of the  $\text{Cu}_3\text{Sn}$  layer, and the presence of Cu at the bottom of the  $\text{Cu}_3\text{Sn}$  layer prevents the assessment of the surface morphology and three-dimensional structure of the  $\text{Cu}_3\text{Sn}$  layer.

### 5.3 High Temperature Stability of Ni-Sn and Ni-Cu-Sn TLPS Joints

The samples used in this study are similar to the Cu-Sn samples described in section 5.1. They were manufactured by sintering Ni-Sn sinter pastes between Ni-substrates and Ni coupons, see Figure 5-38. Sinter and solder pastes were printed and dispensed by the approach introduced in section 4.2.2.1. The dimensions and composition of the materials involved are summarized in Table 5-3. The size of the Ni-coupons and Ni-substrate were 6.35mm x 6.35mm x 1mm and 20mm x 20mm x 1mm and both materials were 99% pure. The sinter paste used in this study consisted of a mix of spherical Ni-particles with diameters between 44  $\mu\text{m}$  and 88  $\mu\text{m}$  and spherical Sn-particles with diameters between 20  $\mu\text{m}$  and 38  $\mu\text{m}$ . Sinter pastes were manufactured by mixing 66 weight-percent (wt.%) Ni-particles, 17wt.% Sn-particles and 17wt% resin-free flux (flux type R0L0) with low post-reflow solid residue. The paste constituents were manually mixed under ambient conditions until homogeneity could be confirmed by optical microscopy inspection. The

Ni-coupons and Ni-substrates were ground with 600 grit SiC grinding paper to remove stains and oxide layers. Afterwards 6.5mm x 6.5mm x 0.2mm layers of sinter paste were stencil printed on top of the center of the Ni-substrates. Ni-coupons were placed on the center of the stencil printed sinter paste layer. Afterwards a ring of Sn solder paste with a diameter of approximately 1mm was dispensed around the stencil printed sinter paste. The solder paste consisted of 85wt.% Sn particles with particle diameters between 20  $\mu\text{m}$  and 38  $\mu\text{m}$  mixed with 15wt.% resin-based flux with high activity.

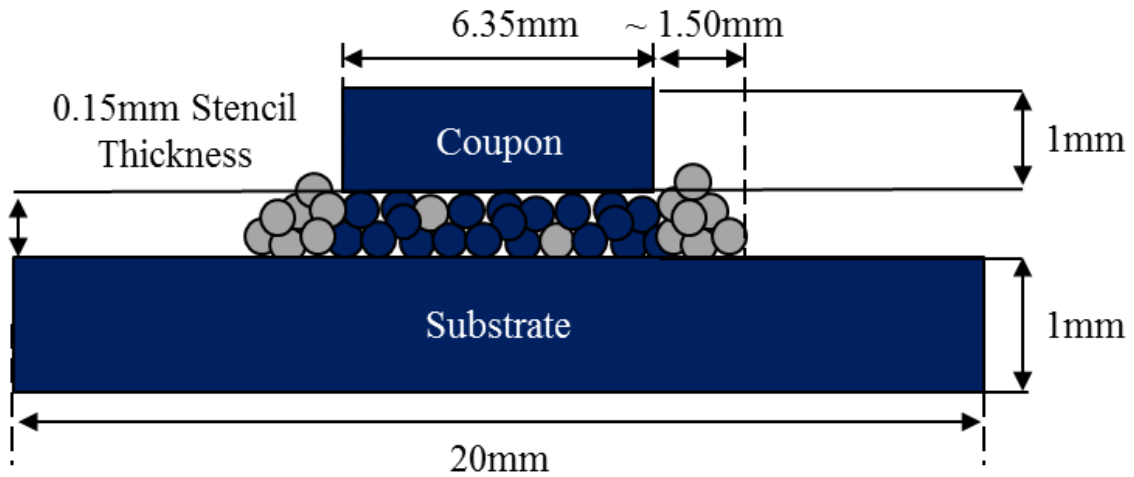


**Figure 5-38: Schematic cross-section of a Ni-Sn TLPS aging study sample before sintering**

**Table 5-3: Composition of substrate, coupon, sinter paste, and solder paste material**

Component	Length [mm]	Width [mm]	Material	Comment
Substrate	20.00	1.00	Ni	
Coupon	6.35	1.00	Ni	
Sinter Paste	6.50	0.15	80 wt.% Ni 20 wt.% Sn	Stencil Thickness
Solder Paste	~ 1.50	~ 0.30	Sn	

The sintering process profiles were identical with those of the Cu-Sn samples, see section 5.1. The samples were placed on the sinter fixture described in section 4.3.1. A pressure of 0.30 MPa was applied homogeneously to the top surfaces of the Ni-coupons. Subsequently

the sinter process was started by initiation of the sinter temperature profile. Two sinter process profiles were applied to samples: (1) a heating ramp from ambient to 300 °C within 5 minutes followed by a dwell time of 2 minutes at 300 °C and subsequent cooling to room temperature within 5 minutes (from here on referred to as 2min@300 °C) and (2) a heating ramp from ambient to 300 °C within 5 minutes followed by a dwell time of 30 minutes at 300 °C and subsequent cooling to room temperature within 5 minutes (from here on referred to as 30min@300 °C). The former sinter profile is similar to conventional high temperature soldering reflow profiles and the latter was chosen because preliminary results with Ni-Sn TLPS indicated high temperature capability. Sintering was performed in ambient atmosphere: no inert or reducing gas was supplied.

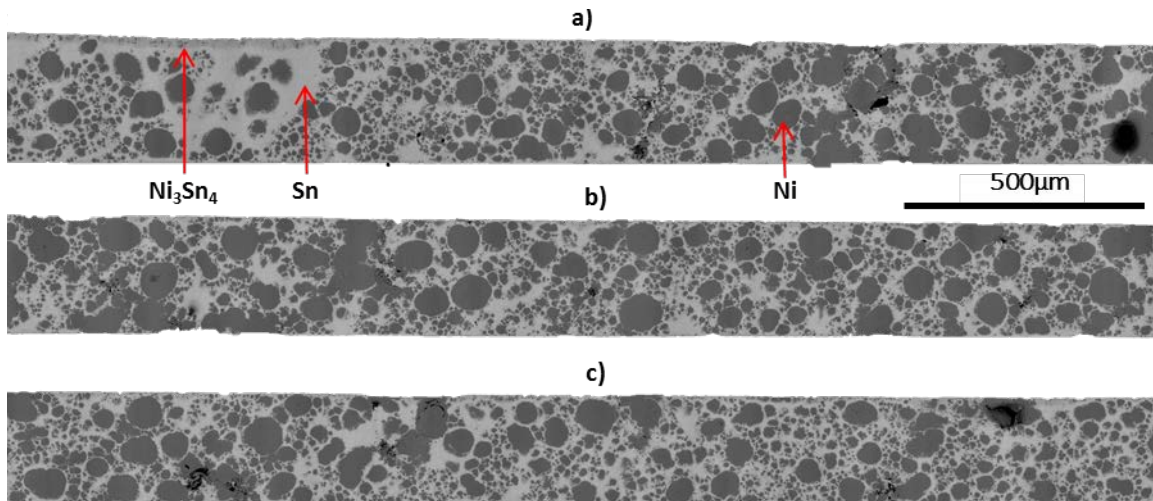
After cooling to ambient temperatures, the pressure applied to the Ni-coupon top surface was relieved. Some randomly selected samples sintered for 30 minutes were subsequently placed in a convection oven, and annealed without application of pressure at 250 °C for 24 hours and 100 hours (from here on referred to as 24h@250 °C and 100h@250 °C respectively). Four samples were manufactured for each sintering and aging condition. They were mounted and cross-sectioned at the centerline of the Ni-coupons parallel to the coupon side. The cross-sectioning procedure was as follows: (1) grinding with a diamond grinding disk until a distance approximately 0.5mm away from the joint center, (2) grinding with SiC grinding papers with grit sizes of 240, 400, 600, 800, and 1200 until the joint center was reached, and (3) polishing with 1 μm diamond suspension until no scratches could be detected by optical microscope inspection. Table 5-4 summarizes the sintering and aging test conditions and related application conditions.

**Table 5-4: Test conditions and related application conditions**

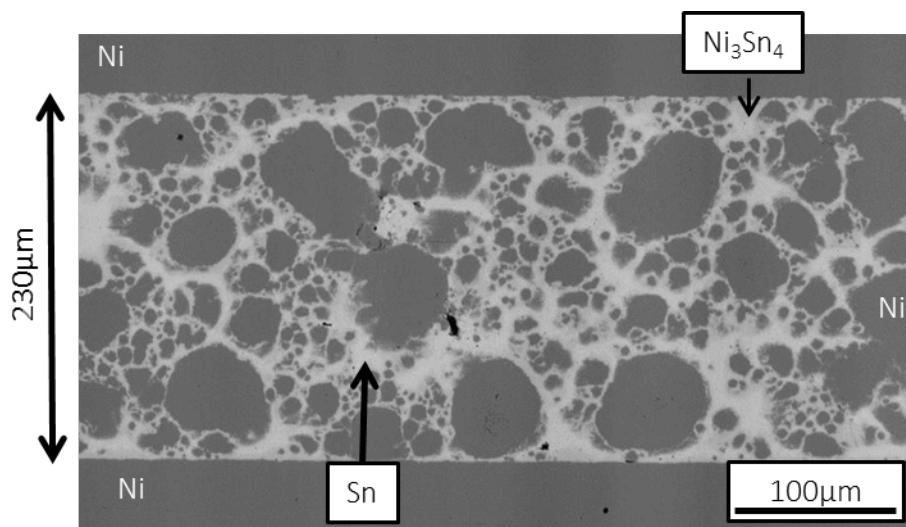
<b>Test Condition</b>	<b>Related Application Condition</b>
2min@300 °C	Typical reflow
30min@300 °C	Expected high-temp. capability
(30min@300 °C) + 24h@250 °C	Few high-temp. excursions
(30min@300 °C) + 100h@250 °C	Long-term high-temp operation

Figure 5-39 to Figure 5-46 show cross-sections of joints after the two processing and two aging steps obtained from ESEM. Because of the large joint area, a complete joint image cannot be obtained by a single ESEM picture. The images shown in Figure 5-39 to Figure 5-46 were created by joining multiple individual images taken with 500x magnification for each joint. To provide a higher magnification and more detailed view, the resulting full joint images were then separated into three sections of equal size (indicated in the figures by a) and c) for the left and right sides of the cross-section, respectively, and b) for the center third of the joint).

Figure 5-39 and Figure 5-40 show cross-sections of joints sintered for 2 minutes at 300 °C. A considerable amount of unconsumed Sn is present throughout the joint. Thin layers of Ni<sub>3</sub>Sn<sub>4</sub> have started to grow at the interfaces between the Ni-particles and Sn as well as at the interfaces between the Ni-substrate and Ni-coupon and Sn. Spherical Ni-particles with a wide range of diameters can be detected. The actual average particle size can be higher than the apparent particle diameter because the cross-section does not intersect the majority of the particles close to their center. Few voids are present in the joint, which are distributed homogeneously throughout the joint. The lack of a continuous presence of high T<sub>m</sub> phases (Ni<sub>3</sub>Sn<sub>4</sub> and Ni-particles) between the top and the bottom of the joint shows that the joint as a whole does not possess high temperature capability.



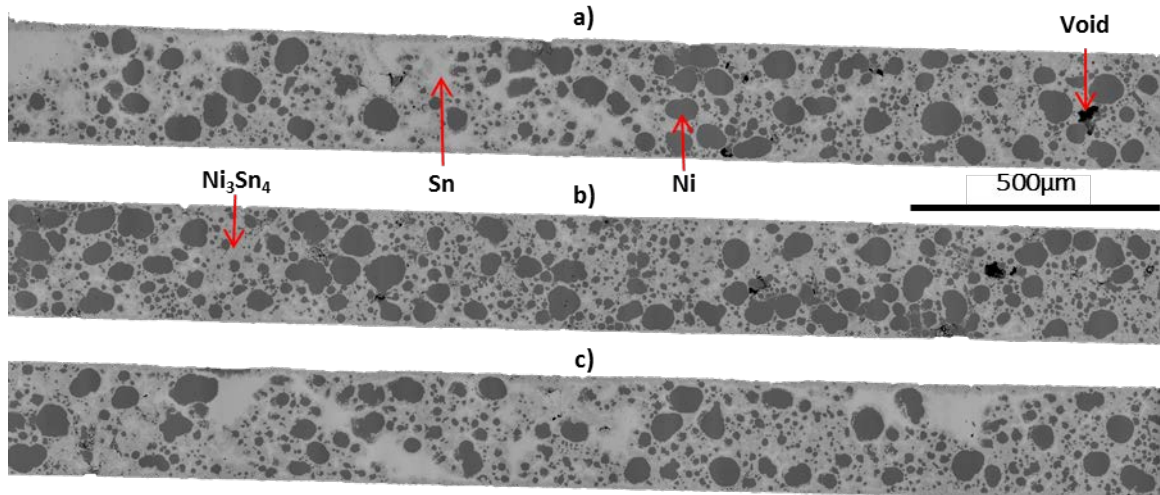
**Figure 5-39: Cross-section of a Ni-Sn joint sintered for 2min at 300 °C. Joint edges a) and c) and joint center b) shown separately. Considerable amounts of unconsumed Sn are still present at the joint edges. Limited  $\text{Ni}_3\text{Sn}_4$  IMCs have started growing around the spherical Ni-particles. Few voids are present**



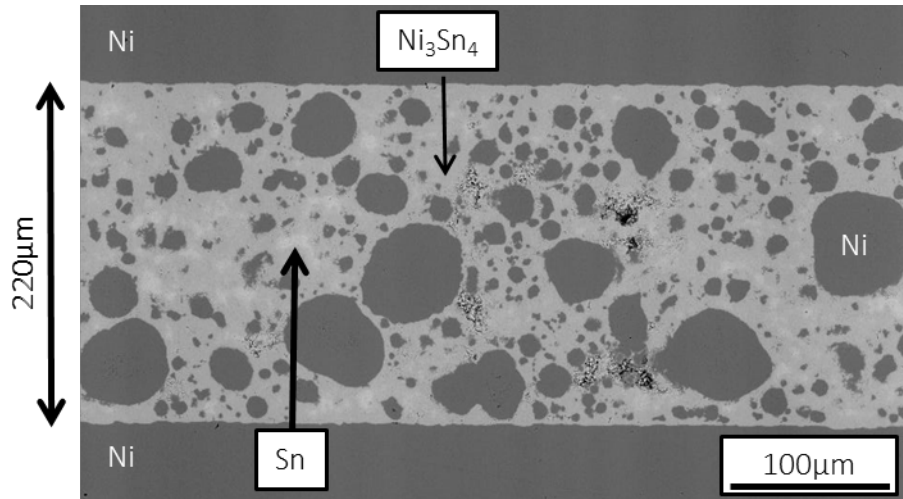
**Figure 5-40: Cross-section of the center region of a Ni-Sn joint sintered for 2min at 300 °C. No continuous high- $T_m$  phases ( $\text{Ni}_3\text{Sn}_4$  and Ni) are present between the Ni-substrate and Ni-coupon**

Figure 5-41 and Figure 5-42 show cross-sections of a Ni-Sn joints sintered for 30 minutes at 300 °C. Considerable amounts of unconsumed Sn are still present at the joint edges, predominately in regions with low Ni-particle density. The center region of the joint is dominated by high- $T_m$  phases (Ni and  $\text{Ni}_3\text{Sn}_4$ ). This indicates that the joint should possess

high temperature capability under this process condition. Similar to the shorter sintering time, voids are distributed homogeneously throughout the joint.



**Figure 5-41: Cross-section of a Ni-Sn joint aged for 30min at 300 °C. Joint edges a) and c) and joint center b) shown separately. Unconsumed Sn remains at the joint edges. The joint center consists predominately of Ni and Ni<sub>3</sub>Sn<sub>4</sub>**



**Figure 5-42: Cross-section of the center region of a Ni-Sn joint sintered for 30min at 300 °C. The joint consists predominately of continuous high-T<sub>m</sub> phases (Ni<sub>3</sub>Sn<sub>4</sub> and Ni)**

Figure 5-43 and Figure 5-44 show cross-sections of Ni-Sn joints sintered for 30 minutes at 300 °C and subsequently aged for 24 hours at 250 °C. Two layers of unconsumed Sn are present in the joint region. They are located between the Ni-coupon/Ni-substrate and the bulk of the TLPS joint characterized by Ni-particles embedded in a Ni<sub>3</sub>Sn<sub>4</sub> matrix. This

bulk of the TLPS joint is similar to the microstructure of the joint center region of Ni-Sn TLPS joints after sintering for 30 minutes at 300 °C. This indicates that the joints did not possess high temperature capability after 30 minutes of sintering, even though all joints showed considerable amount of continuous high temperature phases between the Ni-coupon and Ni-substrate, which should provide high temperature stability. The reason for spreading not occurring during processing is the application of pressure during the process. During aging, no pressure is applied to the Ni-coupons, which no longer prohibits the spreading of the joint and enables the increasing of joint thickness.

No residual Sn is present within the bulk of the TLPS joint between the Sn-layers. Few voids are present in the joint and distributed homogeneously. The thickness of the aged joint has increased compared to the unaged joints. This indicates that the bulk TLPS joint delaminated from the Ni-coupon and Ni-substrate as Sn filled the gaps opened by delamination. Except for one joint, all joints showed almost continuous layers of Sn along the entire joint. The joint that did not possess a continuous layer of Sn, showed the presence of a small chain of unconnected pockets of residual Sn in similar locations, see Figure 5-44 (right). This indicates that a Sn layer was present before, but was mostly consumed during the aging process.

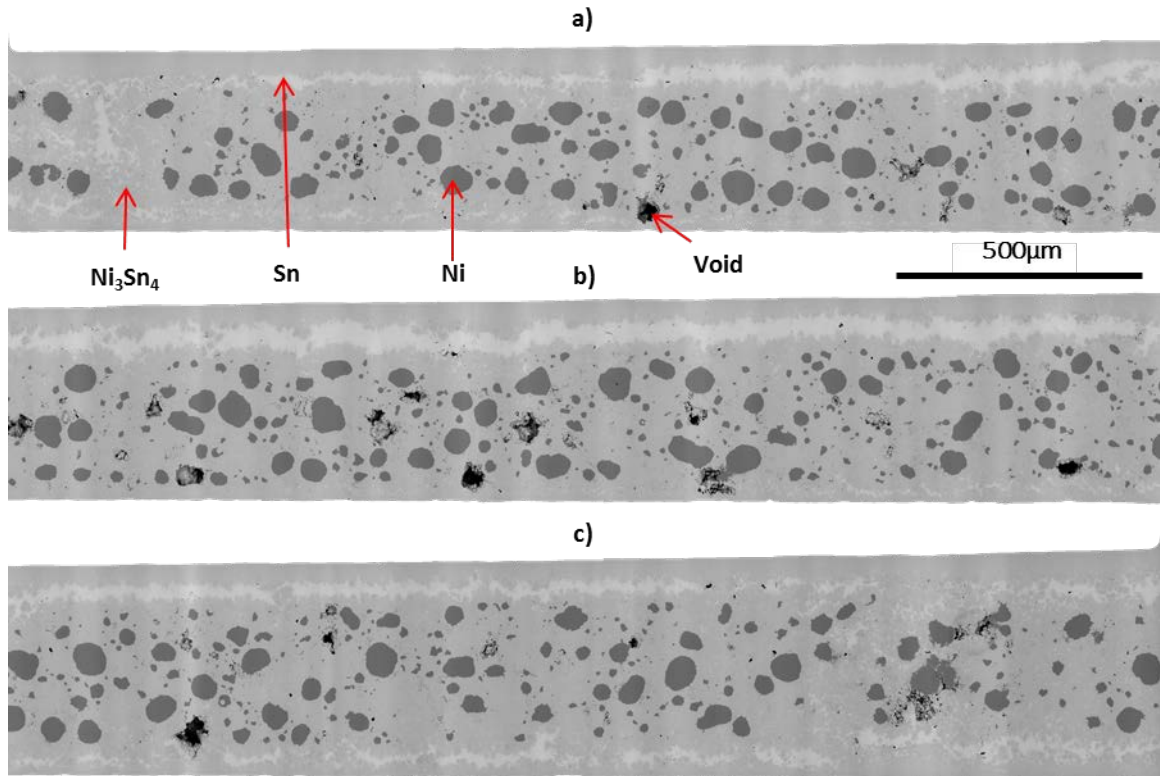


**Figure 5-43: Cross-section of a Ni-Sn joint aged for 24h at 250 °C. Joint edges a) and c) and joint center b) shown separately. Two layers of unreacted Sn are present between the bulk joint and the Ni-coupons and Ni-substrates**

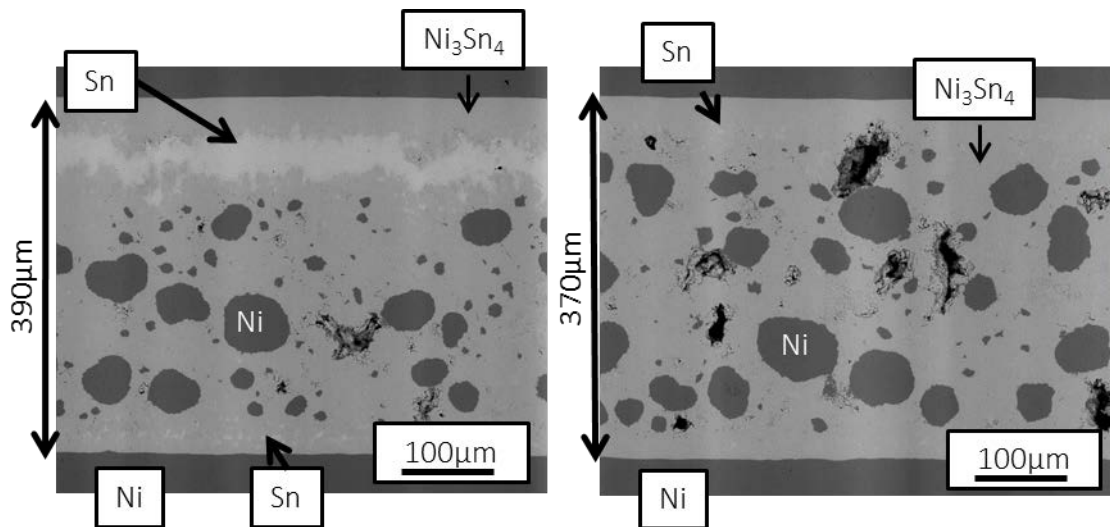


**Figure 5-44: Cross-section of the center regions of two Ni-Sn joints aged for 24h at 250 °C. Most joints showed a delamination of the Ni-coupon and/or Ni-substrate from the bulk of the TLPS joint with layers of Sn in between (left). One joint did not show a continuous Sn-layer, but a chain regions of residual Sn (right)**

Figure 5-45 and Figure 5-46 show cross-sections of Ni-Sn joints sintered for 30 minutes at 300 °C and subsequently aged for 100 hours at 250 °C. After this aging duration, no significant quantities of unconsumed residual Sn are present within the joint region. The regions occupied by layers of Sn after 24 hours of aging are now characterized by considerable quantities of large voids. Almost complete delamination between the bulk of the TLPS joint and the Ni-coupon has occurred. The thickness of the joint after 100 hours of aging has further increased compared to 24 hours of aging.

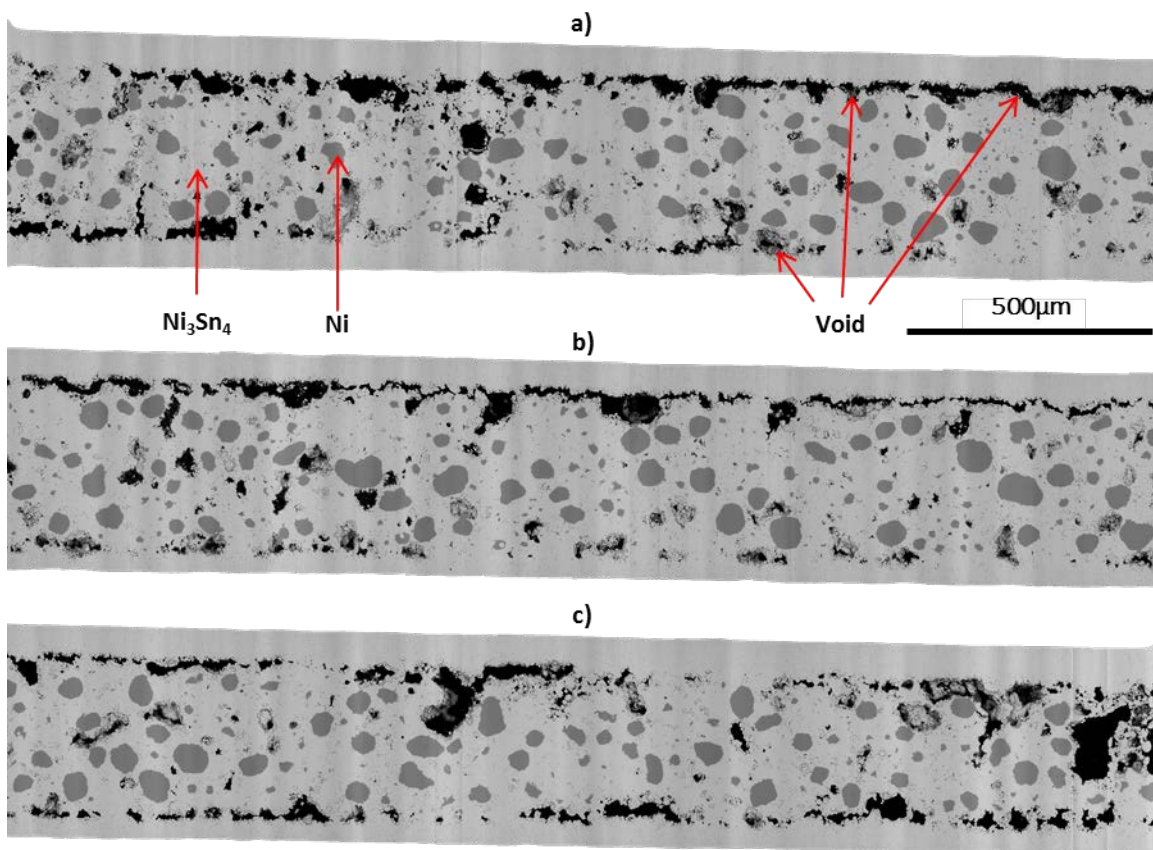


**Figure 5-45: Cross-section of a Ni-Sn joint sintered for 100h at 250 °C. Joint edges a) and c) and joint center b) shown separately. Regions of prior Sn concentrations (between the Ni-coupons and Ni-substrates and the bulk TLPS joint, see Figure 5-43) are now characterized by void formation**

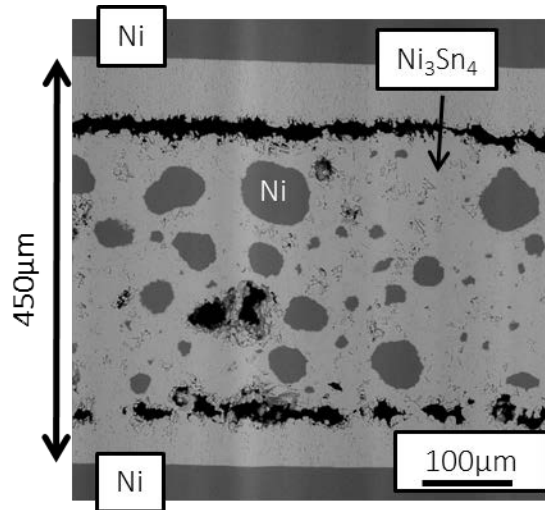


**Figure 5-46: Cross-section of the center region of a Ni-Sn joint aged for 100h at 250 °C. A continuous void layer is present between the Ni-coupon (topside) and the bulk TLPS joint (center)**

The joint volume increases with the joint thickness. This influx of volume into the joint region is provided from the Sn-rich meniscus regions located around the joints. Figure 5-47 shows the evolution of the meniscus volume during the sintering and aging of Ni-Sn TLPS samples. During early process stages, the Sn-particles dispensed in the meniscus region (compare section 4.2.2) melt, wet the surface of the Ni-substrate, and partially infiltrate the joint region. The excess Sn that is not drawn into the joint region remains as a meniscus at the edges between the Ni-coupon and the surfaces of the Ni-substrate.

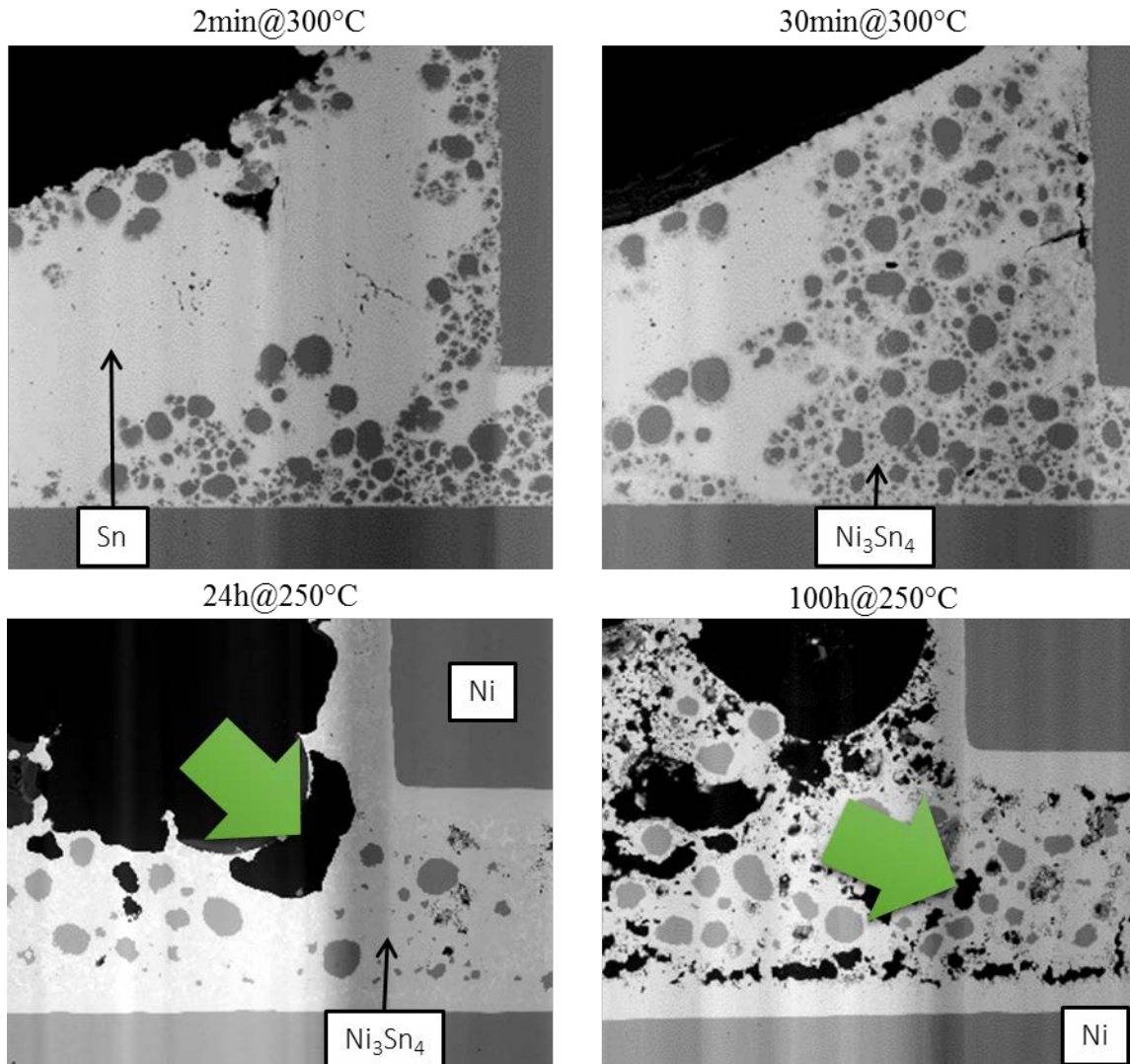


**Figure 5-47: Reduction of Sn meniscus volume during aging. Infiltration of the joint region by Sn during aging is indicated by the green arrows**

Figure 5-47 (top left) shows a cross-section of the meniscus of a Ni-Sn TLPS joint sintered for 2 minutes at 300 °C. The majority of the meniscus consists of Sn. Some Ni-particles have been expelled from the joint region into the meniscus region. Thin  $\text{Ni}_3\text{Sn}_4$  IMCs have grown around these expelled Ni-particles. Figure 5-47 (top right) shows a cross-section of the meniscus of a Ni-Sn TLPS joint sintered for 30 minutes at 300 °C. It is similar to the meniscus of the prior process step. More Ni-particles have been expelled into the meniscus region and the thickness of the  $\text{Ni}_3\text{Sn}_4$  IMCs has increased.

Figure 5-47 (bottom left) shows a cross-section of a Ni-Sn TLPS joint sintered for 30 minutes at 300 °C and subsequently aged for 24 hours at 250 °C. The structure of this meniscus has changed significantly compared to the unaged condition. The volume of the meniscus has decreased. The meniscus now consists of a mix of residual Ni-particles, Sn-regions, and regions dominated by Ni<sub>3</sub>Sn<sub>4</sub> IMCs. The majority of the meniscus volume has disappeared from the meniscus region and was drawn into the joint region. The direction of the volume flow is indicated by the green arrow in Figure 5-47. Figure 5-47 (bottom right) shows a cross-section of a Ni-Sn TLPS joint sintered for 30 minutes at 300 °C and subsequently aged for 100 hours at 250 °C. After this aging duration, no Sn is present in the meniscus region. The meniscus consists of Ni-particles surrounded by Ni<sub>3</sub>Sn<sub>4</sub> IMCs. High levels of voiding are present throughout the entire meniscus region.

Figure 5-48 shows the change of thickness during sintering and aging of Ni-Sn joints with residual Sn in the meniscus region. Blue '+' signs indicate individual thicknesses measured at the left and right edges of the Ni-Sn TLPS joints. Grey squares with blue edges indicate the median joint thickness. The difference in median joint thickness between sintering for 2 minutes at 300 °C and sintering for 30 minutes at 300 °C is small. After 2 minutes of sintering, the median joint thickness is 227 μm, and after 30 minutes of sintering, the median joint thickness is 238 μm. The variation in joint thickness is similar for both sintering conditions with minimum thicknesses of 219 μm and 210 μm, and maximum thicknesses of 271 μm and 281 μm for 2 minutes and 30 minutes of sintering, respectively.

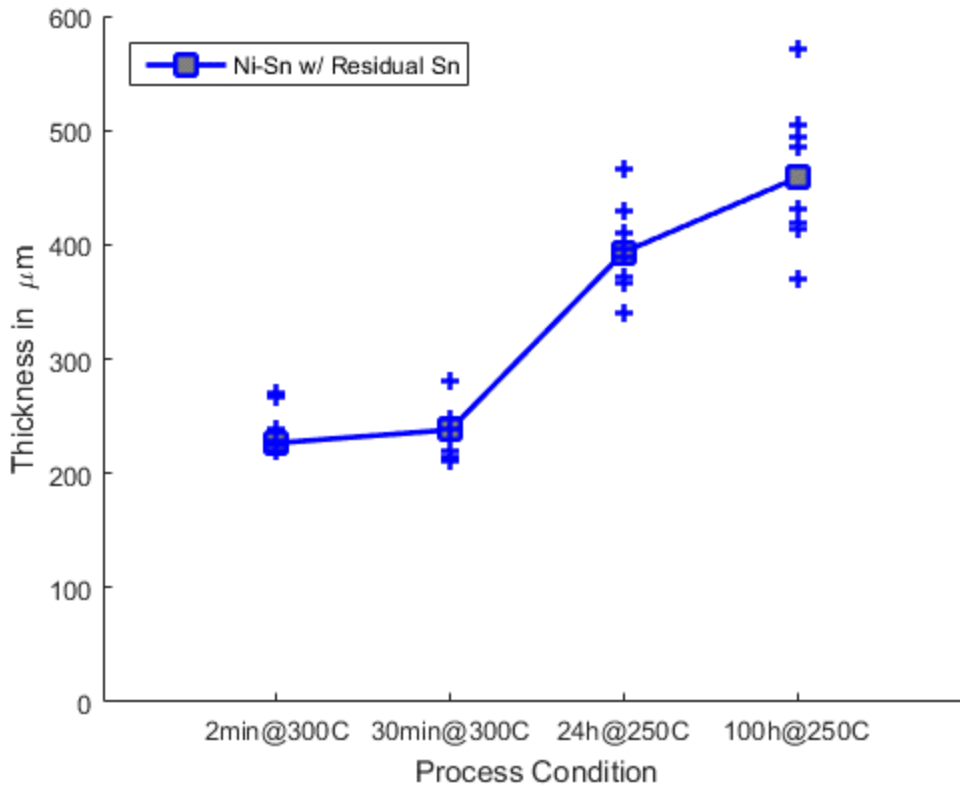


**Figure 5-48: Thickness evolution of Ni-Sn TLPS joints during processing and aging**

Considerable joint spreading occurs during initial aging. After 24 hours of aging at 250 °C, the median joint thickness increases to 394 μm. Additionally, the variation of joint thickness increases compared to unaged joints, with a minimum thickness of 340 μm and a maximum thickness of 467 μm. Further joint spreading occurs during extended aging. After 100 hours of aging at 250 °C, the median joint thickness increases to 459 μm with a minimum thickness of 370 μm and a maximum thickness of 571 μm.

The joint spreading occurs even though considerable amount of high temperature phases are bridging the Ni-coupon and the Ni-substrate after sintering. Shear test studies with multiple high melting temperature attach materials were performed to assess their softening temperatures. Shear specimens of Ni-Sn and Cu-Ni-Sn TLPS sinter joints and Pb5.0Sn2.5Ag solder between Ni-coupons and Ni-substrates were manufactured. The

shear tests were performed in an adapted Tinius Olsen H25K-T benchtop universal testing machine with an integrated miniature oven designed specifically to house the shear test samples and a clamping mechanism. Images of the test setup can be seen in Figure 5-49.

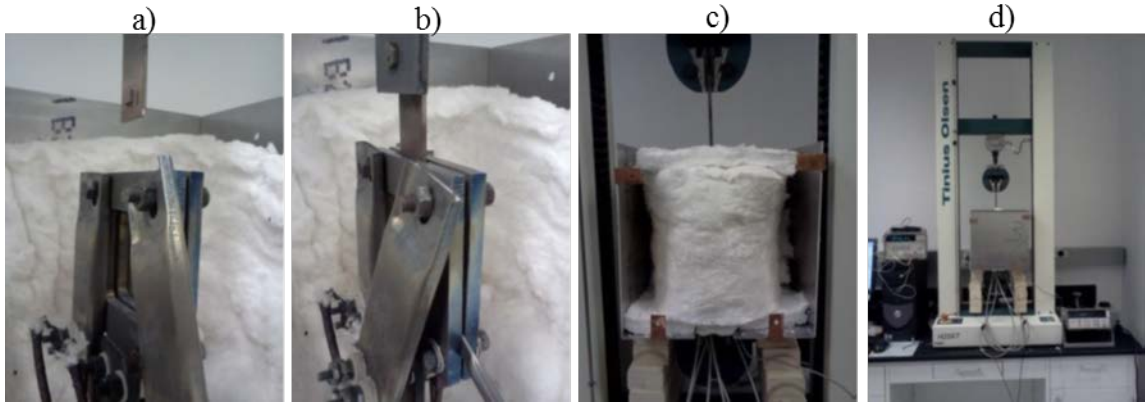


**Figure 5-49: Setup for the assessment of the joint softening temperature: (a) shear fixture and sample, (b) locating the sample in the shear fixture, (c) thermal insulation material, and (d) setup overview**

Initially, the shear sample is attached to a fixture connected to the load cell, see Figure 5-49 (a). Afterwards, the load cell is lowered until the shear sample coupon is located within the shear fixture, see Figure 5-49 (b). Multiple layers of insulation material are used to thermally insulate the tension testing machine from the shear fixture, see Figure 5-49 (c). The full system encompasses automated temperature measuring devices, a power supply to provide heating power to resistive heaters, the shear fixture, high-temperature insulated thermocouples, and the benchtop tension testing machine, see Figure 5-49 (d).

A shear load of 10 MPa is applied to the joints. Heating power is activated and the temperature increased continuously. The temperature when the shear strength drops below 10 MPa is recorded. This temperature is from here on referred to as softening temperature. The softening temperature for the three different materials is shown in Figure 5-50. The measured softening temperature for Pb5.0Sn2.5Ag is 282 °C, which is close to the solidus temperature of 287 °C for this alloy. The softening temperatures of Cu-Ni-Sn and Ni-Sn

joints were 435 °C and >600 °C, respectively. The Ni-Sn joints possessed high shear strength up to the temperature limit of the setup, 600 °C.

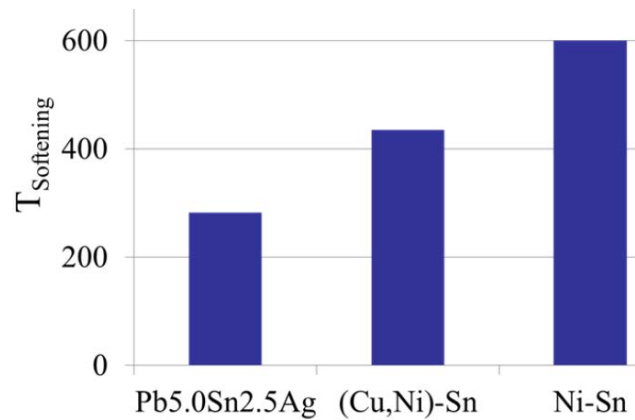


**Figure 5-50: Softening temperature of Pb5.0Sn2.5Ag, Cu-Ni-Sn, and Ni-Sn joints**

The softening tests demonstrate that the Ni-Sn TLPS joints possess high strength at high temperatures. Yet the aging tests show that they are losing this high temperature capability over time. This indicates that a delamination phenomenon occurs during extended storage at high temperature levels. A literature review was performed to explain the fundamentals behind this failure mode. Gur et al. [45] found that above the melting temperature of Sn, Ni<sub>3</sub>Sn<sub>4</sub> in contact with liquid Sn can decouple from underlying Ni<sub>3</sub>Sn<sub>4</sub> grains. In an initial step, mass is transferred from smaller grains towards larger grains, which occurs because of curvature induced gradients in the chemical potential of the liquid-to-Ni<sub>3</sub>Sn<sub>4</sub> grains. Consequently, grain interfaces move, with the grain boundary groove rotating around the triple point between the grains and the liquid towards the grain with the smaller grain size, see Figure 5-51.

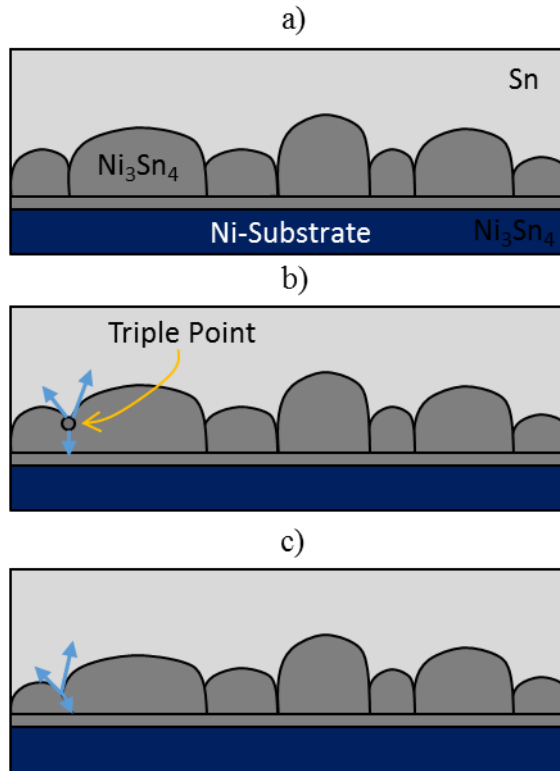


**Figure 5-51: Illustration of the lateral growth process of large  $\text{Ni}_3\text{Sn}_4$  grains, redrawn from [45]. A rotation of the triple point towards the small grain occurs and the large grain grows at the expense of the small grain**

The combination of the rotation of the triple point and the growth of the larger grain at the expense of the smaller grain leads to a consumption of the entire grain boundary, see Figure 5-52. The curvature and location of the grain boundaries change, and the triple point moves closer to the Ni-substrate, see Figure 5-52 (b). Subsequently, the grain boundaries between the small and large grain disconnect, see Figure 5-52 (c). Delamination of the grain boundary between the large grain and the underlying fine-grained  $\text{Ni}_3\text{Sn}_4$  IMC layer is initiated. Eventually, the large grain completely delaminates from the underlying layer, see Figure 5-52 (d). This mechanism is referred to as “crumbling mechanism” [45].

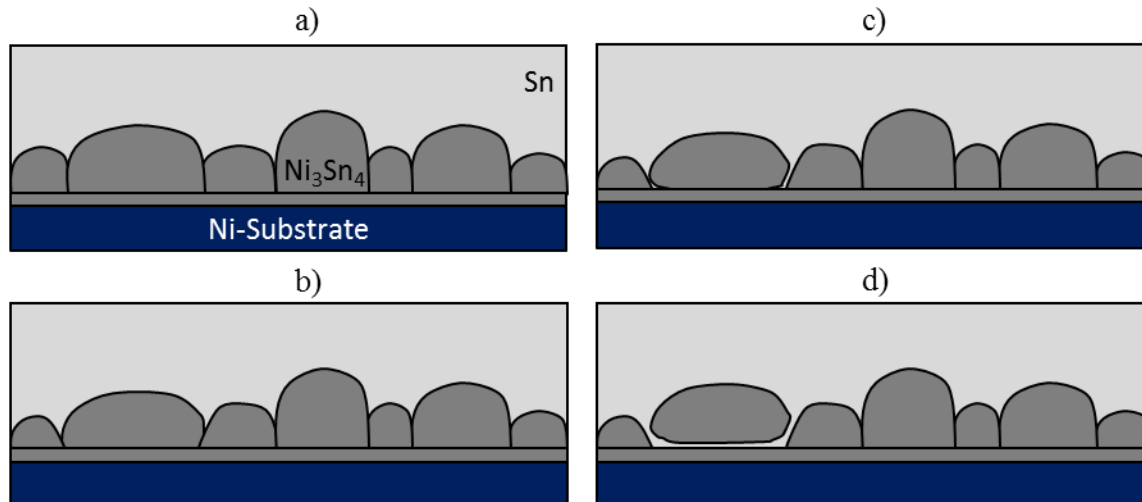


**Figure 5-52: Delamination of  $\text{Ni}_3\text{Sn}_4$  grains, compare [45]**

Figure 5-53 shows the delamination process for the case of the paste-based Ni-Sn TLPS joints studied in this work. Figure 5-53 (a) shows a schematic of the initial microstructure after sintering.  $\text{Ni}_3\text{Sn}_4$  grains have grown laterally from the Ni-coupon towards the joint center. Simultaneously,  $\text{Ni}_3\text{Sn}_4$  grains have grown radially from the spherical Ni-particles in the bulk region of the TLPS joint. Residual Sn from the meniscus regions is visible at the upper left edge of Figure 5-53 (a). During aging, the Sn melts, and grain boundary delamination occurs at the triple point between the liquid Sn and the grain boundaries of IMCs grown from the Ni-coupon and IMCs grown from Ni-particles. This leads to delamination of these grain boundaries and infiltration of the former grain boundary region with liquid Sn, see Figure 5-53 (b). As aging continues, grain boundaries continue to crumble horizontally towards the center of the joint, see Figure 5-53 (c). This process continues until all interfaces have delaminated or all Sn is consumed. If all interfaces delaminated and additional liquid Sn is available, the remaining Sn from the meniscus regions is drawn into the joint region by capillary forces. Joint spreading occurs and the joint thickness increases. For complete delamination and loss of high-temperature stability, the entire joint region must be infiltrated with Sn and complete delamination occur.

Because the dissolution and delamination are diffusion-controlled, this process requires significant time to complete. This explains why the Ni-Sn joints possess high melting temperatures after sintering, compare Figure 5-50, but lose their high temperature capability after extended aging durations.

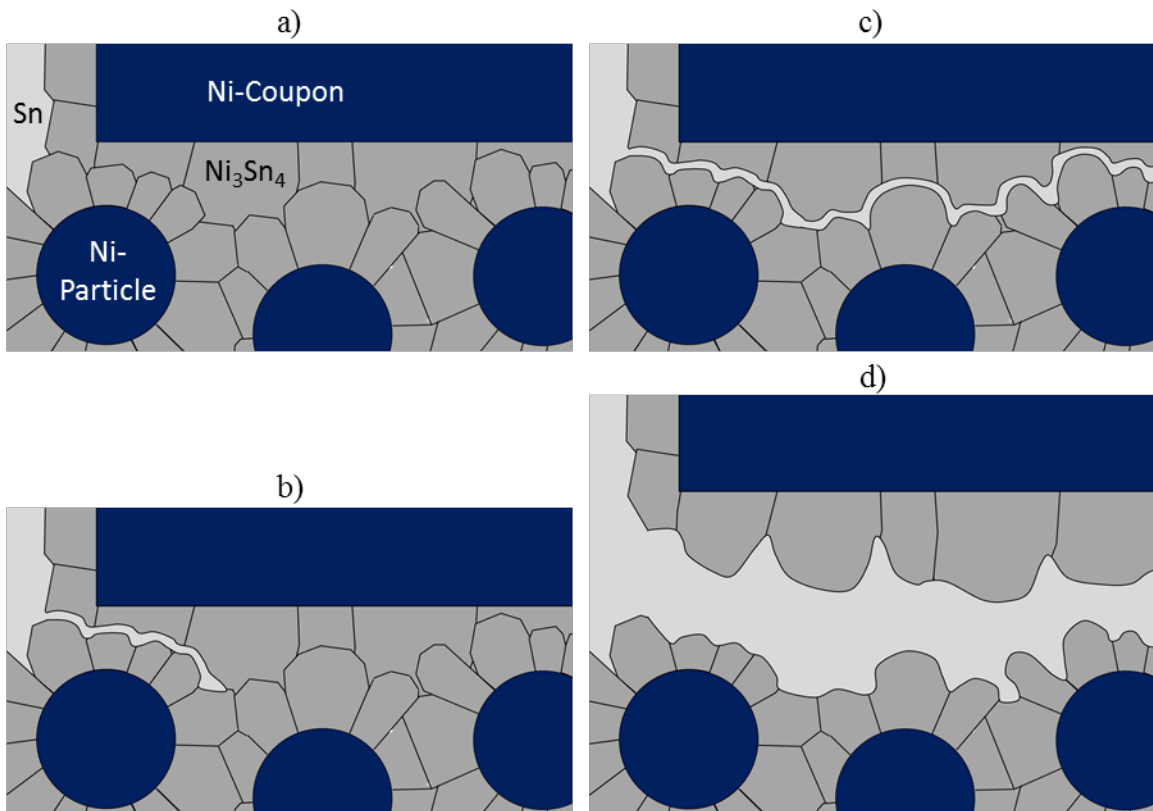
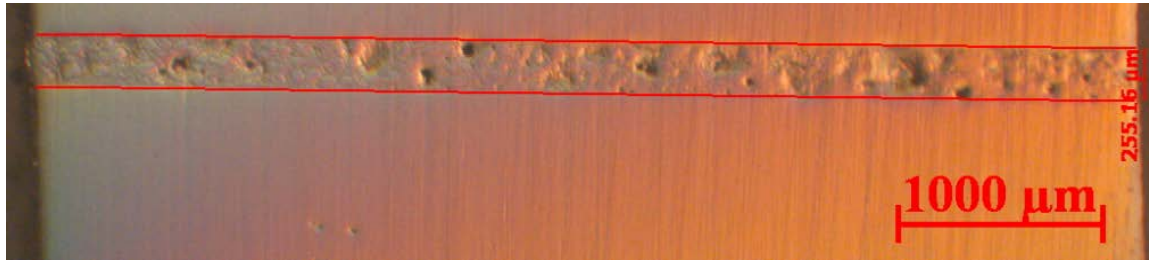


**Figure 5-53: Delamination of the Ni-coupon from the bulk of the Ni-Sn TLPS joint**

To verify the “crumbling effect” hypothesis, Ni-Sn TLPS samples without Sn-menisci were manufactured. The initial parts of the manufacturing process were identical with that of Ni-Sn TLPS joints with Sn-meniscus. In contrast, additional processes to remove the Sn-menisci were added subsequently. This ensured consistency of the microstructure of unaged samples with and without menisci.

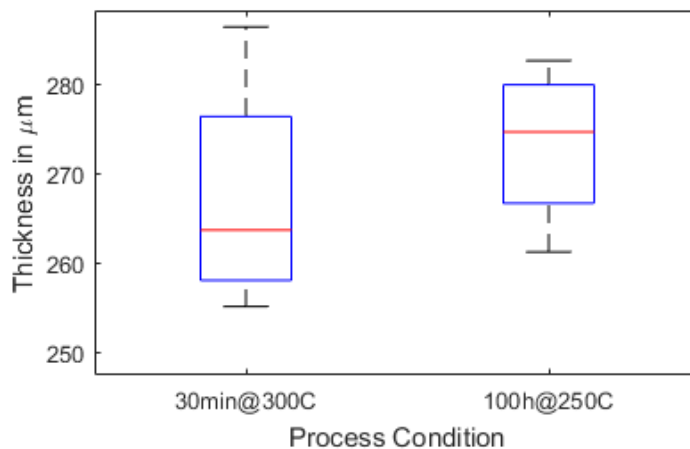
Samples were manufactured by stencil printing and deposition of the sinter pastes as described above and subsequent sintering for 30 minutes at 300 °C. Afterwards the menisci were ground off: In a first mounting step, unaged samples were mounted in an acrylic

mounting material. Subsequently, the samples were ground from two opposite sides to the edges of the Ni-die. Afterwards, the mounting material was dissolved in acetone. The same process was repeated to remove the remaining two opposing edges of the Ni-die. Figure 5-54 shows an optical microscope image side view of a Ni-Sn joint sintered for 30 minutes at 300 °C after removal of its menisci.



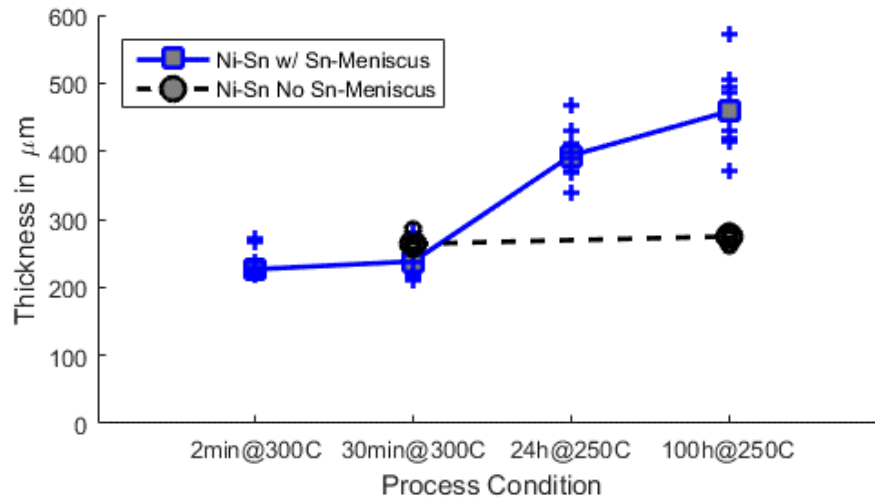
**Figure 5-54: Optical microscope image of a side view of a Ni-Sn joint sintered for 30 minutes at 300 °C**

Eight samples were manufactured for the aging tests without menisci. Four samples were selected randomly and aged at 250 °C for 100 hours. Figure 5-54 compares the thicknesses of joints sintered for 30 minutes at 300 °C and joints sintered for the same duration and subsequently aged for 100 hours at 250 °C. The median thickness increased slightly, but the variation of thickness reduced. Overall, the thickness of the Ni-Sn sinter joints without menisci does not change considerably during aging.



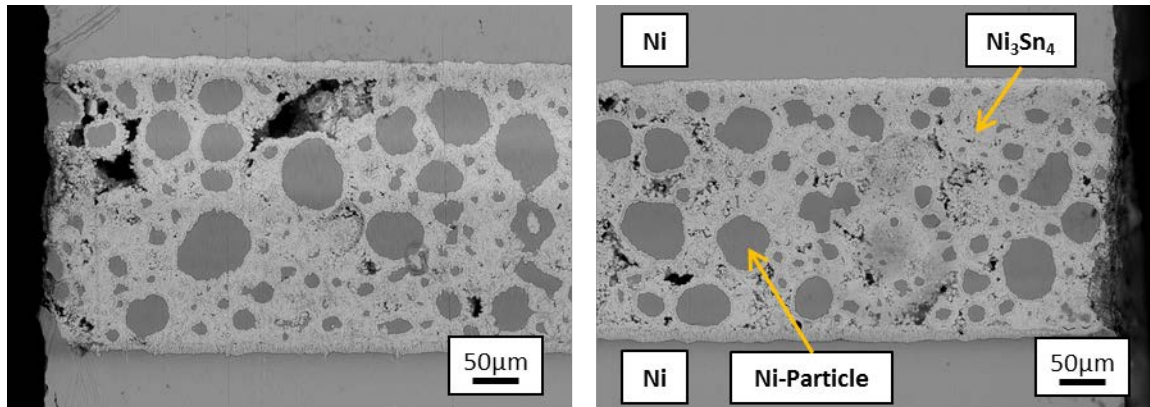
**Figure 5-55: Thickness of unaged (30min@300 °C) and aged (100h@250 °C) samples**

Figure 5-56 compares the thickness evolution of Ni-Sn TLPS joints with and without menisci. Blue crosses indicate individual thicknesses of samples with menisci, black circles indicate individual thicknesses of samples without menisci. The solid blue lines show the median thicknesses of samples with menisci, the dashed black line shows the median thickness of samples without menisci. Low thickness variation exists for the unaged joints, independent of the presence of menisci. A difference exists between the aging behavior of samples with and without menisci. The samples with menisci widen during aging whereas the samples without menisci show almost constant thickness levels as before aging.



**Figure 5-56: Thickness evolution of Ni-Sn TLPS joints with and without menisci**

Figure 5-57 shows ESEM images of Ni-Sn TLPS joints after sintering at 300 °C for 30 minutes and subsequent aging for 100 hours at 250 °C. No crack initiation or joint delamination could be detected anywhere in any of the joints. This shows that the delamination found in Ni-Sn joints with menisci does not originate from thermo-mechanical crack initiation. The only control variable that was changed in the tests was the presence of the Sn-meniscus. This proves that the presence of the meniscus is the driving force behind the delamination and that the failure mechanism is crumbling of  $\text{Ni}_3\text{Sn}_4$  grains.



**Figure 5-57: ESEM images of Ni-Sn TLPS joints after aging for 100 hours at 250 °C. No crack initiation or joint delamination occurred**

Figure 5-58 shows optical microscopy cross-sections of joints formed from Cu-Ni-Sn sinter pastes between a Cu-substrate and a Cu-coupon. Figure 5-58 (a) shows a joint sintered for 2 minutes at 300 °C, Figure 5-58 (b) shows a joint sintered for 30 minutes at 300 °C, Figure 5-58 (c) shows a joint sintered for 30 minutes at 300 °C and subsequently aged at 250 °C for 24 hours. The Cu-Ni-Sn sinter pastes consisted of 40% spherical Cu-particles with diameters between 53 - 88 µm, 40% spherical Ni-particles with diameters between 44 - 88 µm, and 20% spherical Sn particles with diameters between 10 - 25 µm. The solder paste in the meniscus regions was identical with that used for the Ni-Sn aging study samples. The Cu-substrates and Cu-coupons were identical with those from the Cu-Sn aging study samples. Processing and aging conditions were analogous to the Cu-Sn and Ni-Sn aging studies.

Even after short process durations, a limited number of residual Cu-particles is present in the joints region compared to the volume of the residual Ni-particles, see Figure 5-58 (a) and (b). This agrees with the predictions from section 2.4. After 30 minutes of sintering, the joint microstructure is characterized by many residual Ni-particles and few residual Cu-particles embedded in a matrix of (Cu,Ni)<sub>6</sub>Sn<sub>5</sub> IMCs. This verifies the hypothesis that in

the main source of IMC growth in paste-based Cu-Ni-Sn TLPS joints are the Cu-particles of the sinter paste, compare section 2.4. No significant amount of Sn is present in the joint region after this process duration. All phases have high melting temperatures. Yet, after aging for 24 hours at 250 °C without application of pressure, the joint has widened and the voiding levels have increased. This demonstrates that, similar to Ni-Sn joints, the Cu-Ni-Sn joints suffer from delamination with the presence of Sn-menisci.

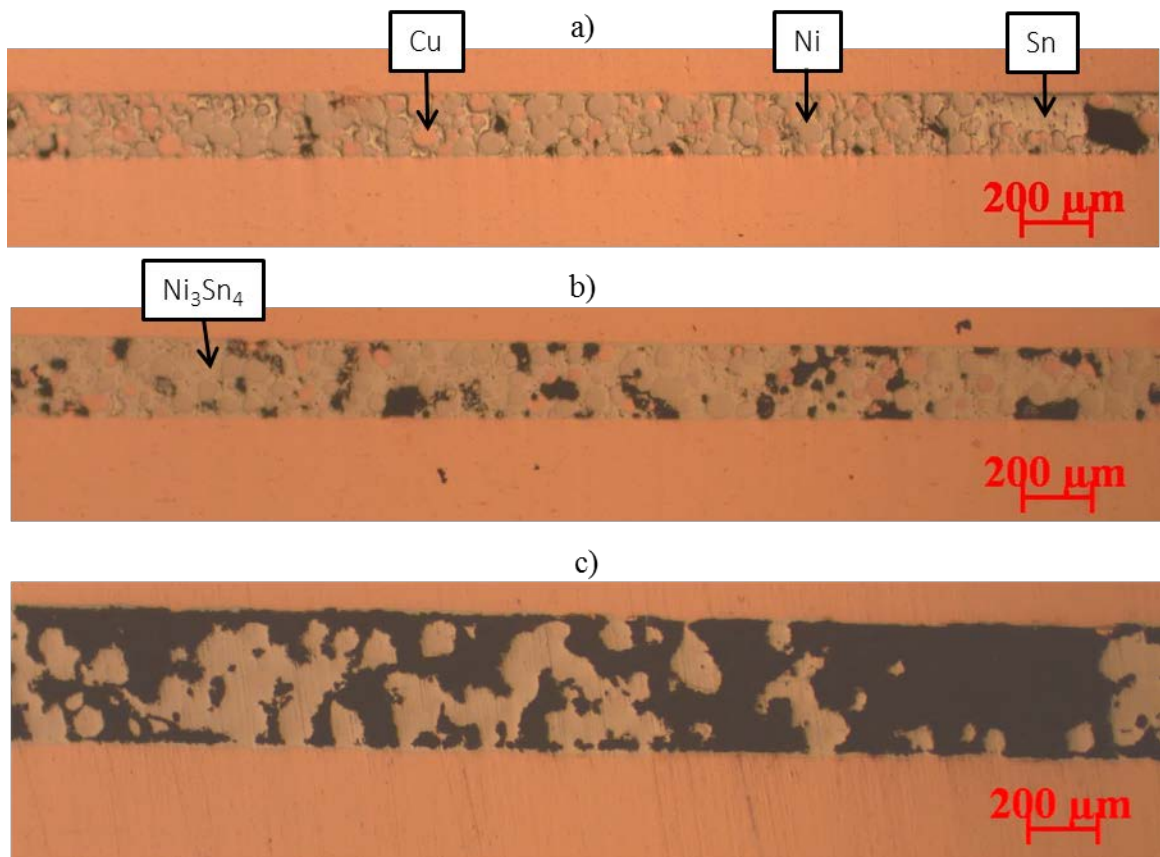


**Figure 5-58: Optical microscope images of cross-sections of Cu-Ni-Sn TLPS joints after (a) 2 minutes of sintering at 300 °C, (b) 30 minutes of sintering at 300 °C, and (c) 30 minutes of sintering at 300 °C followed by 24 hours of aging at 250 °C**

## 6 Assessment of TLPS Interconnect Properties

### 6.1 Simulation Approach

An overview of the process flow for the simulation of the properties of TLPS sinter joints is given in Figure 6-1. The approach consists of the following three steps:

1. Determining the location of *Objects* in the *Joint Space*. The *Joint Space* in this context describes the entirety of the volume occupied by the TLPS interconnect. Within the *Joint Space* are multiple objects, as is the case for real interconnects. These *Objects* include metal particles, voids, and IMC regions filling the space not occupied by metal particles and voids.
2. Creation of a 3D-model of the TLPS joint. The geometry information generated in (1) is used to build a model of the sinter joint in a 3D-CAD environment. Voids are represented by “empty space” *Objects*, and metal particles by non-intersecting “solid” *Objects*, while IMCs comprise the rest of the *Joint Space*.
3. Simulation Computation. The 3D-model from (2) is imported into a simulation environment. Material properties are assigned to the *Objects*, boundary conditions applied, and solutions computed.

This simulation approach has been used to assess the thermal, mechanical, thermo-mechanical, and electrical properties of TLPS interconnects with different microstructures under multiple load conditions.

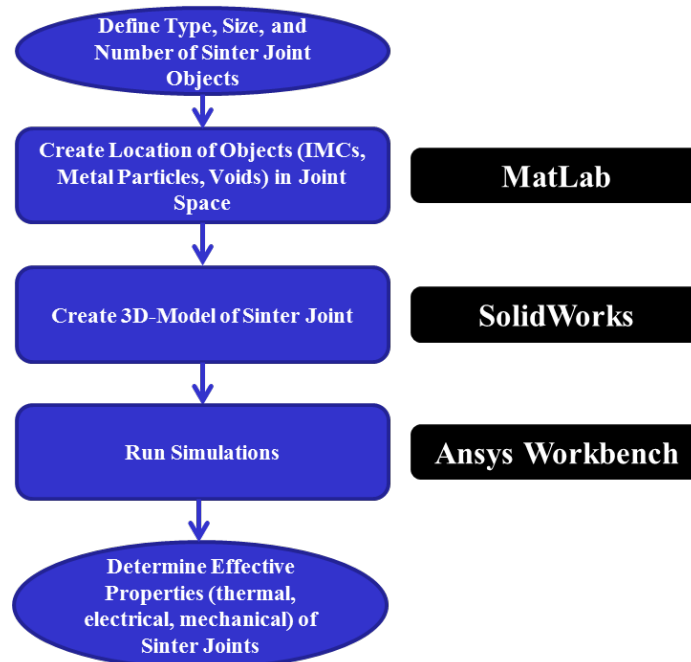


**Figure 6-1: Process flow of the TLPS joints properties simulation approach**

Figure 6-2 shows the process flow for the software algorithm used to determine the location of *Objects* in the *Joint Space*. The program was written in MatLab and will from here on be referred to as the *Particles Distribution Generator*. Required input parameters for the program are the size of the *Joint Space* in x-, y-, and z-direction, the radii of the *Objects*, the desired number of particles of each size, and the minimum distance between *Objects* in the sinter joint (*Minimum Spacing*).

Initially the software generates one combination of random x-, y-, and z-locations that is located within the *Joint Space* at a distance from the boundaries that exceeds the *Minimum Spacing*. Afterwards it is checked whether the distance between this *Object* and all other *Objects* already present in the joint exceeds the *Minimum Spacing*. If that is the case, the location of the *Object* is feasible, and it is added to the list of placed *Objects*. The process is repeated until all *Object* locations have been determined successfully. If the current *Object* intersects with other *Objects*, the space boundaries or *Minimum Spacing* conditions,

the location is invalid. Without storing the current location information, new x-, y-, and z- locations are generated randomly, and the process is repeated.

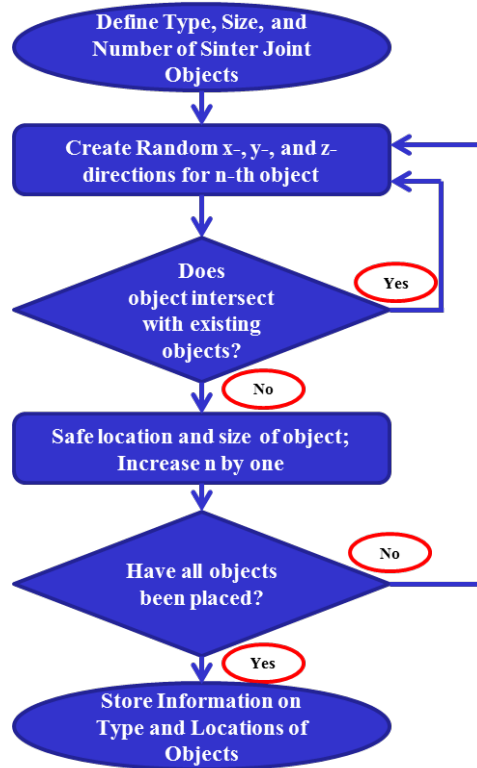


**Figure 6-2: Process flow of the Particle Distribution Generator**

This process is repeated either until the desired number of *Objects* of each radius have been placed or until a sufficient number of placing attempts has been performed (e.g. 10,000 times the number of desired particle placements), at which point the joint is assumed to be saturated with nearly the maximum amount of *Objects* that can be placed. A .zip file containing .txt files with information on *Joint Space*, radii and locations of *Objects* is created.

Figure 6-3 shows an example of input parameters and a resulting 3-dimensional *Object* distribution as geometry output. The *Object* distribution was plotted in MatLab. It is generated automatically as a visual confirmation and check that the program has completed properly. In this example, there was an attempt to place 1000 *Objects* with radii of 50, 20,

10  $\mu\text{m}$  (white, blue, and red spheres respectively) in a *Joint Space* spreading 500 x 500 x 150  $\mu\text{m}^3$ . No *Minimum Spacing* was specified in this example. The total number of *Objects* in this case was below 1000 and not all desired *Objects* could be placed. The total volume-percentage of spheres was approximately 47%. The regions between the particles that appear empty in the image are in later steps modeled as IMC regions.

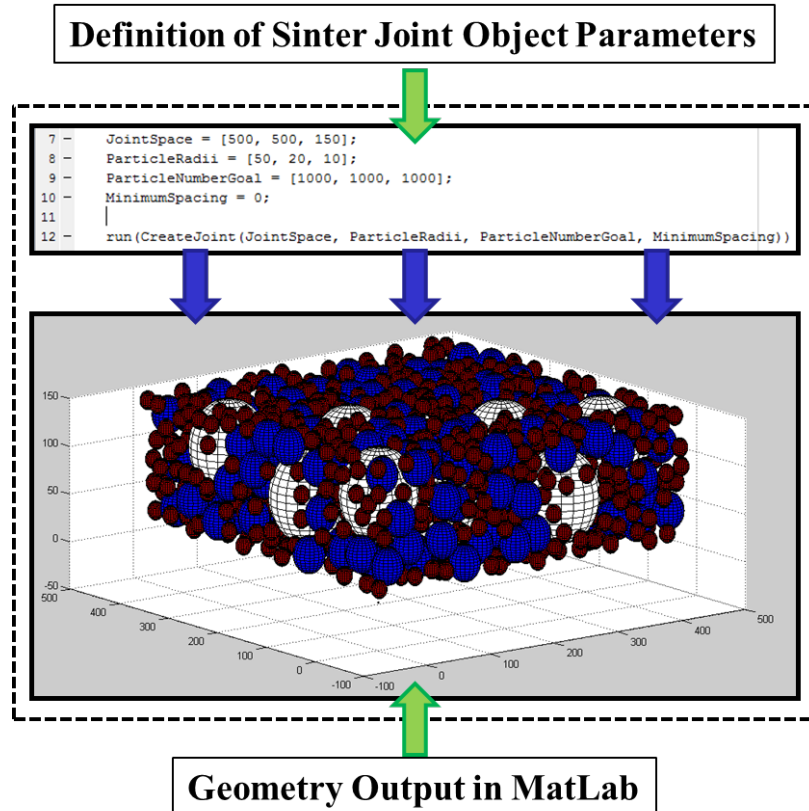


**Figure 6-3: Input parameters and example arrangement of Objects within a Joint Space after completing a Particle Distribution Generator run**

The next step in the simulation process is the generation of the 3D model in a CAD system, see Figure 6-4. A semi-automated macro was written for SolidWorks which opens the .txt files created in MatLab, reads the information and creates the spherical geometries. The user determines which *Objects* should be treated as metal particles and which as voids. The volume of the *Joint Space* that is occupied by neither of these is modeled as IMC regions.

The final joint geometry is generated by logically adding metal particles, voids, and IMC regions. A .step file of the model is created that will be used in subsequent simulation steps.

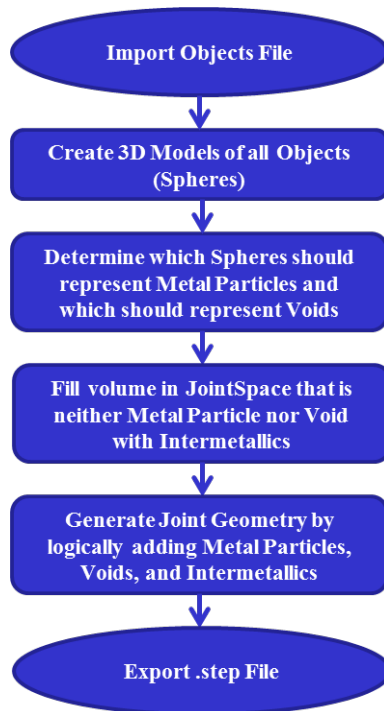


**Figure 6-4: Process flow of the 3D CAD model creation**

Figure 6-5 shows an example of a 3D-model created in SolidWorks. The large *Objects* with a radius of 50  $\mu\text{m}$  (see white spheres in Figure 6-3) are modeled as voids in this case and shown shaded with gray. The 25  $\mu\text{m}$  and 10  $\mu\text{m}$  *Objects* are modeled as metal particles and shown in blue. The IMC regions between the voids and the metal particles are not shown in Figure 6-5.

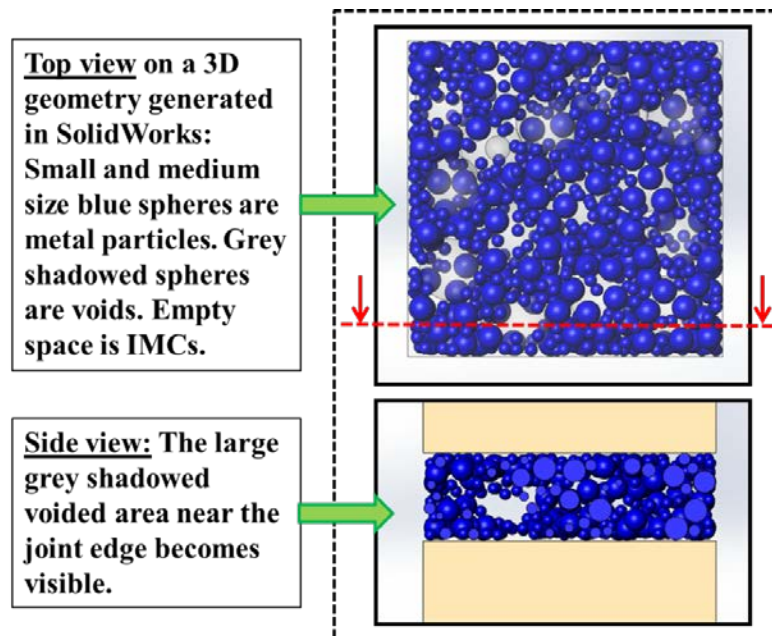


**Figure 6-5: 3D model in SolidWorks. The geometry information from Figure 6-3 was used. White spheres in Figure 6-3 are here shown as grey-shaded voided regions. IMC regions are not shown.**

The final steps of the simulation approach are importing the .step file from SolidWorks into a simulation environment, allocating material properties, defining boundary conditions, and running simulations. The process flow for the case of a thermal simulation is shown in Figure 6-6. The process for structural simulations is performed analogously with different boundary conditions and solvers. Figure 6-7 shows a cross-sectional view of a meshed TLPS interconnect containing Ni-particles with radii of 25  $\mu\text{m}$  and 10  $\mu\text{m}$  and voids with radii of 50  $\mu\text{m}$ . The IMC regions are  $\text{Ni}_3\text{Sn}_4$ . In this case, the thermal resistance of the interconnect was assessed. Voids and metal particles appear to have different sizes even though they do not (e.g., all voids have radii of 50  $\mu\text{m}$ ), because the location where the cross-section intersects the *Object* varies between different *Objects*. Heat is generated in the Si-die on top of the joint, and the temperature at the bottom of the Cu layer is held constant at 20  $^\circ\text{C}$ . The bottom image in Figure 6-7 shows the joint temperature distribution for this case. It can be seen that the heat is not conducted homogeneously in the joint and

that higher temperature gradients exist along the voided volumes where paths with higher resistances exist. Figure 6-8 shows the resulting heat flow distribution under the same boundary conditions. The metal particles have a higher thermal conductivity than the IMCs. Percolation occurs and the heat flow is concentrated to regions with high metal particle density.

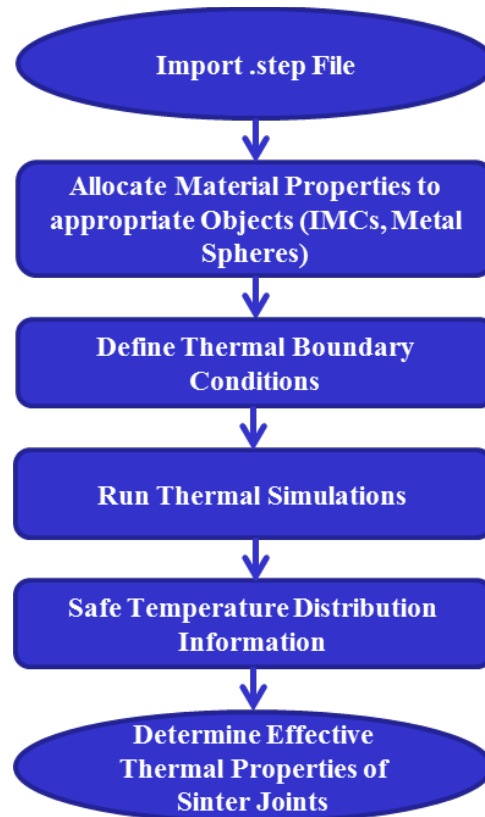


**Figure 6-6: Process flow of a thermal simulation in ANSYS Workbench**

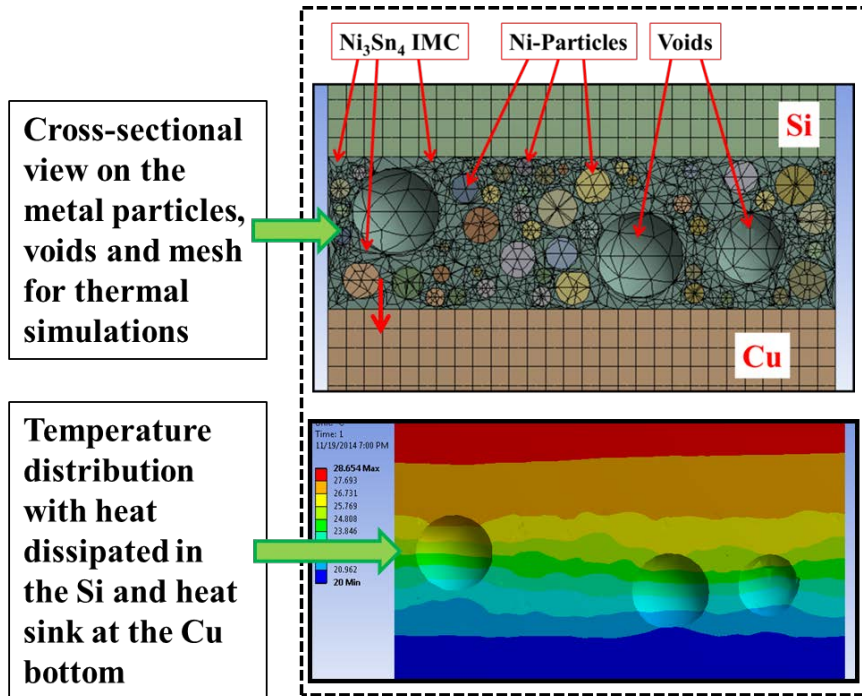


Figure 6-7: Cross-sectional view of a meshed TLPS interconnect in ANSYS Workbench and resulting thermal simulation

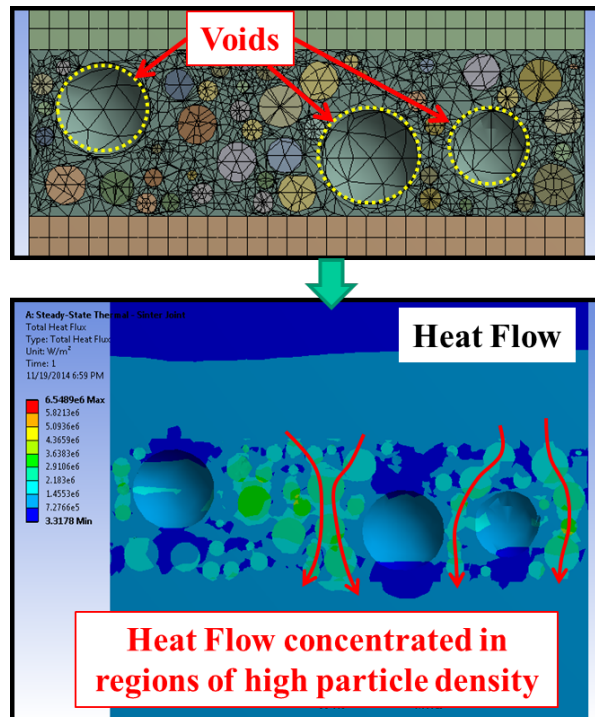


Figure 6-8: Cross-sectional view of a meshed TLPS interconnect in ANSYS Workbench and resulting heat flow distribution

## 6.2 Thermal Conductivity

The thermal properties of paste-based TLPS joints will be studied in this section. Initially the simulation approach detailed in section 6.1 will be used to assess the influence of the material system, voiding, particle size, and metal percentage on the thermal conductivity of the TLPS joints, see section 6.2.1. Subsequently the thermal conductivities of Cu-Sn TLPS joints will be determined experimentally, see section 6.2.2.

### 6.2.1 Prediction

The computation of the thermal conductivity was performed according to the following steps:

1. A model of a sinter joint between a layer of Si and a layer of Cu is generated
2. A model of direct contact between the Si layer and the Cu layer is generated
3. A thermal load condition  $P$  is applied to the top of the Si layer and a constant temperature condition to the bottom of the Cu layer. The temperature difference for this “jointless” structure is recorded ( $\Delta T_{jointless}$ ).
4. Identical boundary conditions are applied to the model with the sinter joint and the temperature difference for this structure recorded ( $\Delta T_{with\ joint}$ ).
5. The contribution of the sinter joint to the system is calculated by subtracting the temperature difference of the “jointless” structure from that with the joint:  $\Delta T_{joint} = \Delta T_{with\ joint} - \Delta T_{jointless}$
6. The effective thermal conductivity of the TLPS joint material is then computed by  $\kappa_{TLPS} = P \cdot l/A \cdot \Delta T$ , where  $l$  and  $A$  are the joint thickness and joint area respectively

Five different simulation conditions have been studied. They are detailed below. The results of the individual study conditions will be discussed in individual sections below.

- A. TLPS joints with a metal loading of 20 vol.-% and one particle size per condition. The particle radii for each condition were 70, 60, 50, 40, 30, 20, and 10  $\mu\text{m}$
- B. TLPS joints with metal particles of one particle size per condition. The particle radii for each condition were 70, 60, 50, 40, 30, 20, and 10  $\mu\text{m}$ . The joint was filled with the maximum amount of particles.
- C. TLPS joints filled with equal volumes of three types of particles per condition (50, 25, and 12.5  $\mu\text{m}$ ). The volumes were 14%/14%/14%, 12.5%/12.5%/12.5%, and 11%/11%/11% for each condition.
- D. As in (3), but for all conditions one sphere type was voids instead of metal particles. This simulated voids with different radii of 50, 25, and 12.5  $\mu\text{m}$  with 14%, 12.5%, and 11% of voids for each size (A total of nine test conditions)
- E. A joint that was filled maximally with particles of three radii (50, 30, and 10  $\mu\text{m}$ )

All test conditions were performed for the three types of microstructures found in past-based TLPS interconnects: ( $\text{Ni}_3\text{Sn}_4 + \text{Ni}$ ), ( $\text{Cu}_6\text{Sn}_5 + \text{Cu}$ ), and ( $\text{Cu}_3\text{Sn} + \text{Cu}$ ). Table 6-1 summarizes the thermal conductivities of all materials used in this study. The interconnect space spanned a volume of  $500 \times 500 \times 150 \mu\text{m}^3$  for all study conditions.

**Table 6-1: Thermal conductivities of materials used in the simulations [122]**

Material	Cu	Ni	SiC	$\text{Ni}_3\text{Sn}_4$	$\text{Cu}_6\text{Sn}_5$	$\text{Cu}_3\text{Sn}$
$\kappa$ [W/mK]	400	90.9	120	19.6	34.2	69.8

### A. Constant Metal Loading (20%), Variation of Particle Size

Under this condition the joints were filled with a total metal loading as close to 20 vol.-% as possible. As particles are discrete and possess a defined volume, minor deviation from the ideal 20 vol.-% exist. Figure 6-9 and Table 6-2 show the thermal conductivities for this test condition.

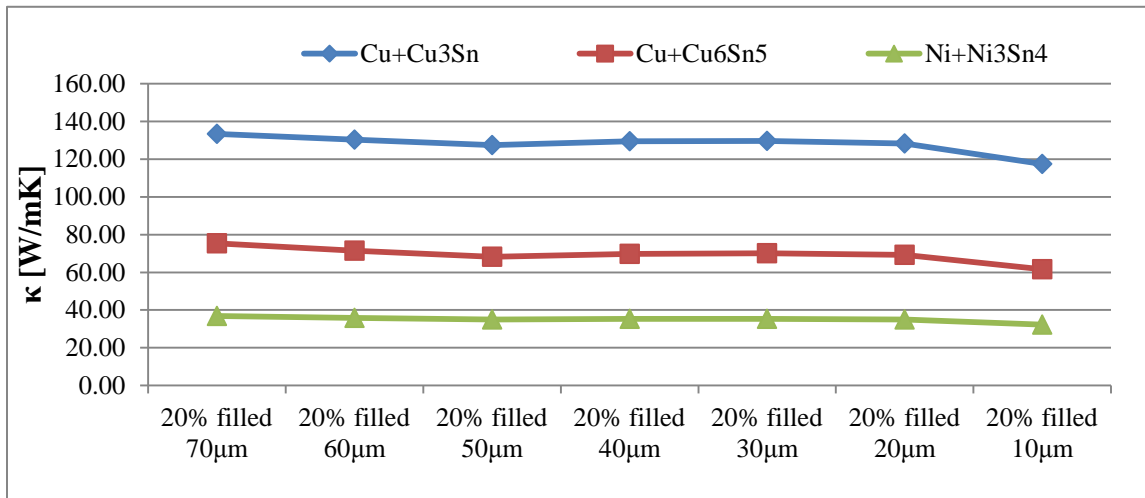


**Figure 6-9: Thermal conductivities for a 20 vol.-% metal particle loading.**

The 70 μm and 60 μm radii particle provide the best thermal conductivity even though their vol.-% is the lowest in the entire test group (19.15 and 19.29 vol.-% respectively). Joints with particle sizes between 50 μm and 20 μm possess almost constant thermal conductivities: the variation within this size range is most pronounced for the Cu+Cu<sub>6</sub>Sn<sub>5</sub> system within a range of 2.7%. In contrast, the thermal conductivity of joints with particles with 10 μm radius is significantly smaller than that of joints with larger particles. The reduction of thermal conductivity of changing the particle size from 20 μm to 10 μm is 8.5%, 11.0%, and 8.0% for the Cu+Cu<sub>3</sub>Sn, Cu+Cu<sub>6</sub>Sn<sub>5</sub>, and Ni+Ni<sub>3</sub>Sn<sub>4</sub> systems, respectively.

**Table 6-2: Thermal conductivities for 20 vol.-% metal particle loading.**

Particle Size [ $\mu\text{m}$ ]	Thermal conductivity [W/mK]		
	Cu <sub>3</sub> Sn+Cu	Cu <sub>6</sub> Sn <sub>5</sub> +Cu	Ni <sub>3</sub> Sn <sub>4</sub> +Ni
70	133.42	75.33	36.87
60	130.29	71.45	35.87
50	127.47	68.31	35.03
40	129.53	69.78	35.41
30	129.62	70.18	35.34
20	128.21	69.18	35.00
10	117.37	61.60	32.21

The thermal conductivity is highest for particles with a size of 70  $\mu\text{m}$  for all material systems. When the thermal conductivities are plotted relative to the highest value within each material system, the reduction of thermal conductivity compared to the 70  $\mu\text{m}$  condition is most pronounced for the (Cu+Cu<sub>6</sub>Sn<sub>5</sub>) joints, see Figure 6-10.

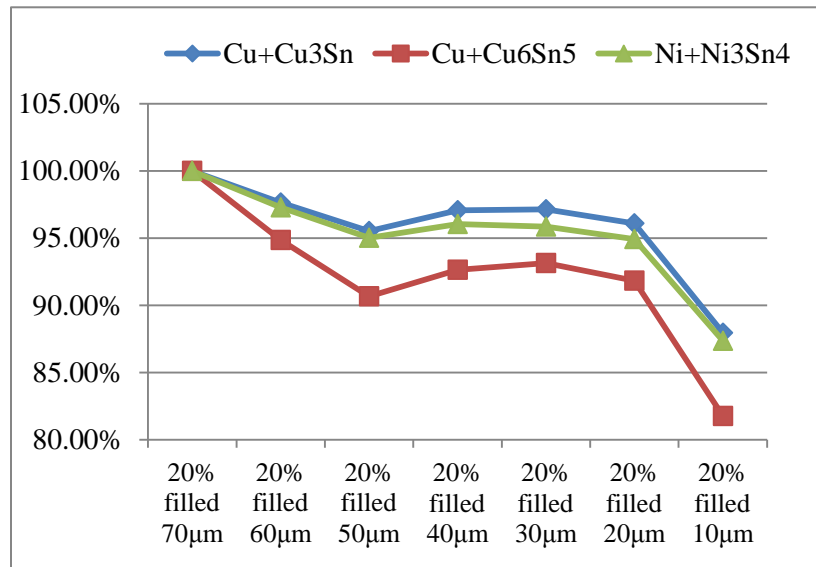


**Figure 6-10: Thermal conductivity relative to that of joints with 70  $\mu\text{m}$  radius particles.**

An explanation for this can be given by comparing the relative thermal conductivities of the respective metal particles and corresponding IMC. The ratio of thermal conductivity is an important factor for the spreading efficiency between particles. This parameter is given

for the three material systems in Table 6-3. For the (Cu+Cu<sub>6</sub>Sn<sub>5</sub>) system, it is considerably lower than for the other systems. The lower the value, the higher is the tendency of the heat to cross the intermetallic region between two neighboring metal particles by the shortest intermetallic path available, see Figure 6-11. In consequence, more spreading and conduction length is required for IMCs with low thermal conductivity, which increases the length of the conduction path within the metal particles and in their proximity. When the radii of the particles are large, the spreading distances are small, as few intermetallic regions must be crossed. For smaller radii, more spreading distances result in reduced effective thermal conductivity. This explains both, the reduced thermal conductivity for very small particle sizes (10 μm) and the higher sensitivity of the Cu+Cu<sub>6</sub>Sn<sub>5</sub> system to particle size variation compared to the other material systems.

**Table 6-3: Ratio of the thermal conductivities of the IMCs to the metal particles for the assessed material systems.**

Thermal conductivity [W/mK]		
Ni <sub>3</sub> Sn <sub>4</sub>	Ni	Ni <sub>3</sub> Sn <sub>4</sub> /Ni
19.6	90.9	0.216
Cu <sub>6</sub> Sn <sub>5</sub>	Cu	Cu <sub>6</sub> Sn <sub>5</sub> /Cu
34.2	400	0.086
Cu <sub>3</sub> Sn	Cu	Cu <sub>3</sub> Sn/Cu
69.8	400	0.175

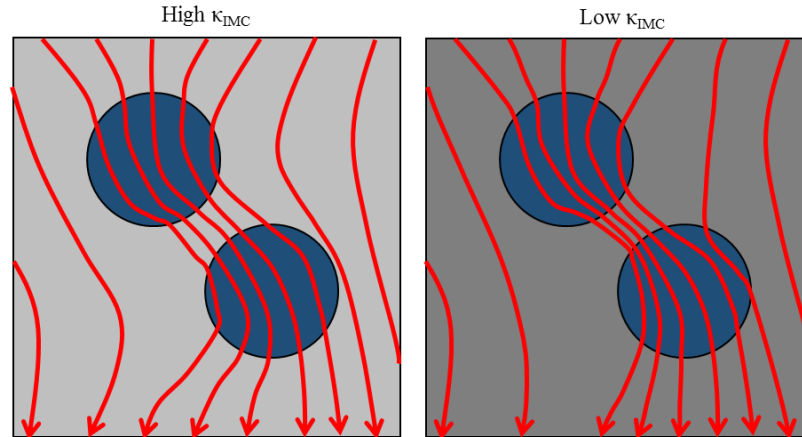


**Figure 6-11: Heat flow paths for a joint with high  $\kappa_{IMC}$  (left) and low  $\kappa_{IMC}$  (right) and identical  $\kappa_{Particle}$ . In joints with a lower ratio of  $\kappa_{IMC}/\kappa_{Particle}$ , heat flow paths are more concentrated in and between metal particles.**

A local minimum for the thermal conductivity exist for joints with 50  $\mu\text{m}$  particles, which is present for all three material systems. This can be explained by the ratio of the particle size to the joint thickness. The joint thickness for all cases is 150  $\mu\text{m}$ . Particles with radii of 70  $\mu\text{m}$  and 60  $\mu\text{m}$  provide highly conductive heat paths consisting predominately of metal between the top and the bottom of the joint. Limited conduction through IMC regions is required. With reducing particle size, more vertical conduction through IMC regions or spreading through IMC contact regions between multiple particles is required. This increases the thermal resistance and reduces the effective thermal conductivity. On the other hand reduced particle sizes enable the vertical stacking of particles between the heat source and the heat sink. Figure 6-12 shows a two-dimensional schematic of heat flow lines for possible particle arrangements depending on particle size. The joint thickness and particle dimensions were chosen to represent the simulations performed above. The joint thickness is 150  $\mu\text{m}$  and the particle radii are 70  $\mu\text{m}$ , 50  $\mu\text{m}$ , and 40  $\mu\text{m}$  respectively. Particles and IMC regions are represented in blue and grey, respectively. Red arrows represents heat flowing through regions of high thermal resistance (predominately IMC regions), and green arrows represent heat flow through regions of high thermal resistance

(metal particles). Orange arrows indicate heat flow through regions of average thermal resistance. The heat is assumed to be dissipated homogeneously at the top of the joint region.

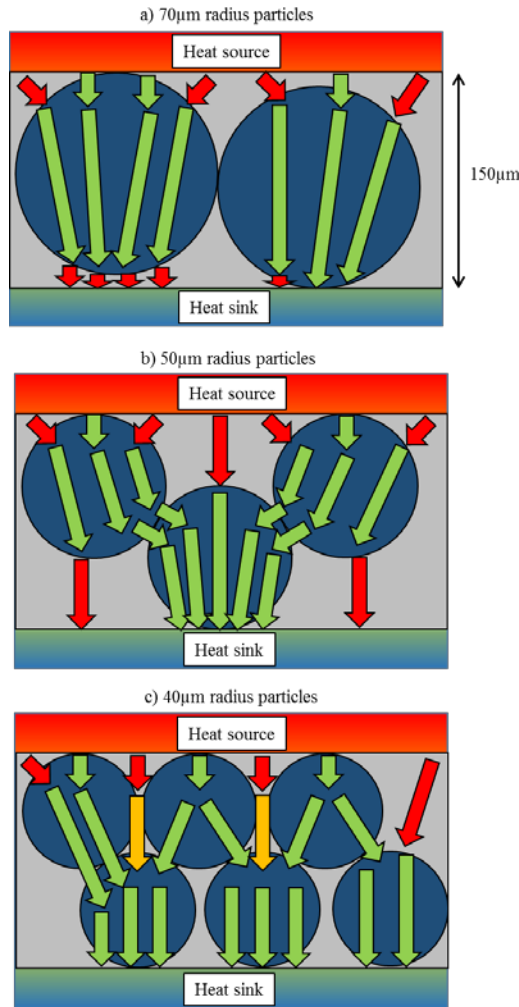


**Figure 6-12: Influence of particle size on the heat flow paths within the TLPS joints. Large metal particles (a) provide uninterrupted vertical heat flow between the heat source and the heat sink. Within a critical size range (b) particles do neither bridge the entire joint thickness nor provide vertically stacked heat paths. At smaller sizes (c) low resistance heat conduction paths are provided by vertically stacked particles**

Particles with radii of 70  $\mu\text{m}$  provide a high ratio of high thermal conductivity paths and only short low conductivity paths are required. As a consequence, the thermal conductivity of these joints is high. Particles with a radius of 50  $\mu\text{m}$  cannot be stacked vertically, and considerable regions with high thermal resistance must be passed. Heat can bridge the joint

predominately through metal particles, but considerable lateral spreading with associated thermal resistance is required. Particles with radii of 40  $\mu\text{m}$ , can be stacked almost vertically, which limits the required lateral spreading and provides heat flow paths of low thermal resistance. The resulting (qualitative) thermal conductivity behavior resembles the simulation results shown in Figure 6-10: Highest thermal conductivity for the 70  $\mu\text{m}$ , a local minimum of thermal conductivity for 50  $\mu\text{m}$  radii particles, and intermediate conductivity for particles with radii of 40  $\mu\text{m}$ . For the 10  $\mu\text{m}$  particles the spreading distances become significant compared to larger particle sizes, which requires significant lateral spreading within and between metal particles, which reduces the thermal conductivity of the TLPS joints under this condition.

Particles with diameters close to the sinter joint thickness are difficult to work with from a manufacturability standpoint. The sinter pastes are stencil printed and particles close to the stencil thickness render the printing process challenging if not impossible. Experience has shown that particles with ratios of particle diameter to stencil thickness below 0.7 are required for adequate printability. Particles with a ratio below 0.4 show good printability. Under these aspects joints formed from particles with radii of 40  $\mu\text{m}$  and below show good manufacturability for sinter joint thicknesses of 150  $\mu\text{m}$ .

### **B. Maximum Metal Load, Variation of Particle Size**

Under this condition the joints were filled with a maximum number of particles of specific radii. Figure 6-13 shows the dependence of the highest achievable metal load in vol.-%. The loading is highest for the 70  $\mu\text{m}$  metal particles followed by the 10  $\mu\text{m}$  particles. Figure 6-14 and Table 6-4: show the thermal conductivities for this test condition. It can be seen that, as with the 20 vol.-% metal loaded sinter joints, the 70  $\mu\text{m}$  radius particles possess the

highest thermal conductivity. Particles with radii of 40, 30, and 20  $\mu\text{m}$  show considerable increase in thermal conductivity because of the increased vol.-%, as well. This effect is less pronounced for the 10  $\mu\text{m}$  particles, even though they have the second highest metal load ratio in this test condition. The 50  $\mu\text{m}$  radius particles have the same fill rate of around 20 vol.-% and do not show an improved thermal conductivity

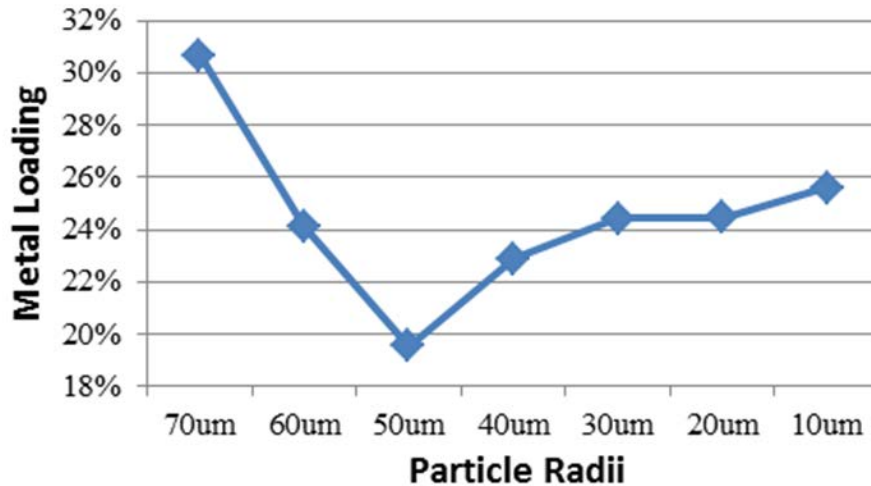


Figure 6-13: Percentage of metal particles in the joint in vol.-%

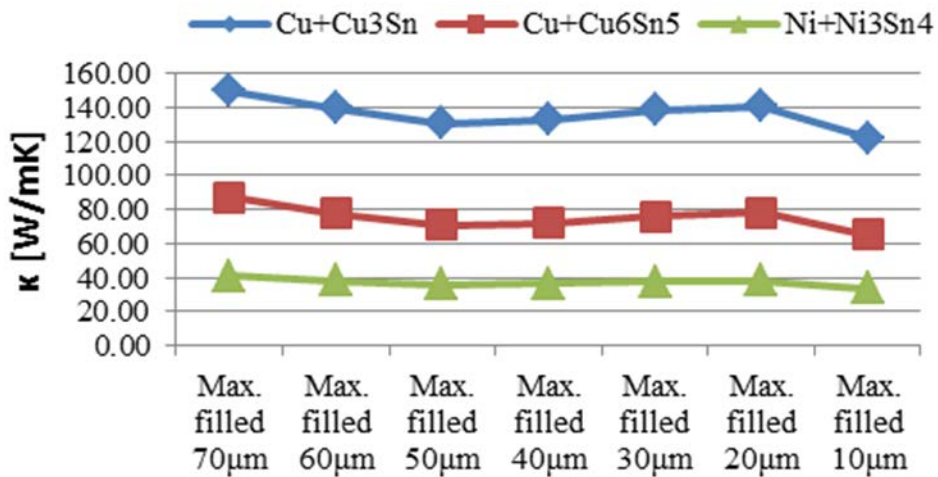
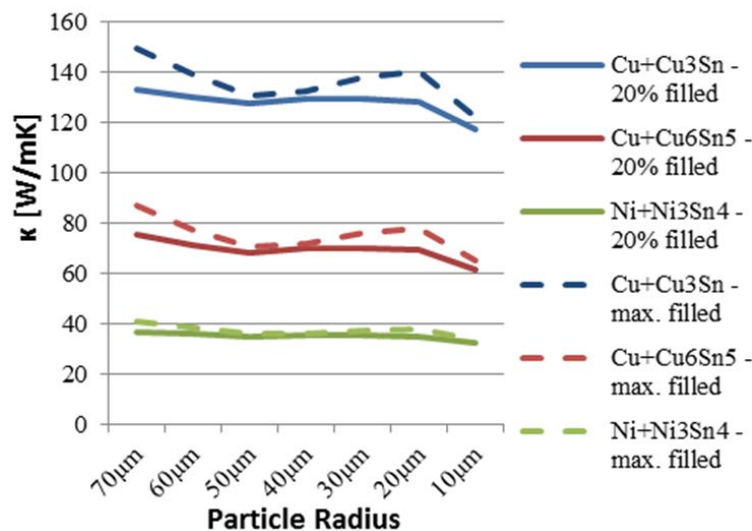


Figure 6-14: Thermal conductivities for the maximally metal particle loaded sinter joints

**Table 6-4: Thermal conductivities for maximally metal particle loaded sinter joints**

Particle Size [ $\mu\text{m}$ ]	Thermal conductivity [W/mK]		
	Cu <sub>3</sub> Sn+Cu	Cu <sub>6</sub> Sn <sub>5</sub> +Cu	Ni <sub>3</sub> Sn <sub>4</sub> +Ni
70	149.37	87.18	41.08
60	139.47	77.61	38.20
50	130.72	70.65	35.84
40	132.63	71.94	36.15
30	138.12	75.93	37.49
20	140.75	77.88	38.02
10	122.25	64.96	33.41



**Figure 6-15: Comparison of the thermal conductivity of joints filled with 20 vol.-% (solid lines) and max. vol.-% (dashed lines) metal particles**

**C. Mixed Particle Sizes, Variation of Metal Loading, No Voids**

Under this condition the joints were filled with a mix of three particle radii (50, 25, and 12.5  $\mu\text{m}$ ) with total metal load vol.-% of 42%, 37.5%, and 33%. Equal volumes of particles of different radii were used (e.g. 11 vol.-% of each 50, 25, and 12.5  $\mu\text{m}$  radius particles for the 33 vol.-% metal load condition). Table 6-5 shows the vol.-% of the particles with the different radii.

**Table 6-5: Vol.-% of the mixed particles for the void-free test condition**

Total vol.-%	50 $\mu\text{m}$ vol.-%	25 $\mu\text{m}$ vol.-%	12.5 $\mu\text{m}$ vol.-%
42	14	14	14
37.5	12.5	12.5	12.5
33	11	11	11

Figure 6-16 and Table 6-6 show the thermal conductivities of void-free sinter joints with mixed metal particles. The thermal conductivity decreases with decreasing metal load. Figure 6-17 shows the decrease in thermal conductivity relative to that of the 42 vol.-% metal load condition. The (Cu+Cu<sub>6</sub>Sn<sub>5</sub>) condition is most sensitive to a reduction of metal load. This can again be explained with the higher tendency in this composite for heat spreading within the Cu particles to minimize the conductive path length through the low conductivity Cu<sub>6</sub>Sn<sub>5</sub> IMC regions caused by the ratio of thermal conductivities of IMC matrix and metal particles, see Table 6-3. It is interesting to note the degree to which this occurs in the (Cu+Cu<sub>6</sub>Sn<sub>5</sub>) system. A reduction from 42 vol.-% to 33 vol.-% equals a reduction of metal load of 21.4%. The thermal conductivity of (Cu+Cu<sub>6</sub>Sn<sub>5</sub>) is reduced by 18.95%, whereas those of (Cu+Cu<sub>3</sub>Sn) and (Ni+Ni<sub>3</sub>Sn<sub>4</sub>) are only reduced by 12.96% and 11.82% respectively. Still, the absolute thermal conductivity of (Cu+Cu<sub>6</sub>Sn<sub>5</sub>) under all test conditions is still more than twice as high as that of the (Ni+Ni<sub>3</sub>Sn<sub>4</sub>) system.

**Table 6-6: Vol.-% of the mixed particles for the void-free test condition**

Metal Loading [vol.-%]	Thermal conductivity [W/mK]		
	Cu <sub>3</sub> Sn+Cu	Cu <sub>6</sub> Sn <sub>5</sub> +Cu	Ni <sub>3</sub> Sn <sub>4</sub> +Ni
42	185.01	112.93	48.67
37.5	172.27	102.46	45.63
33	161.03	92.68	42.92

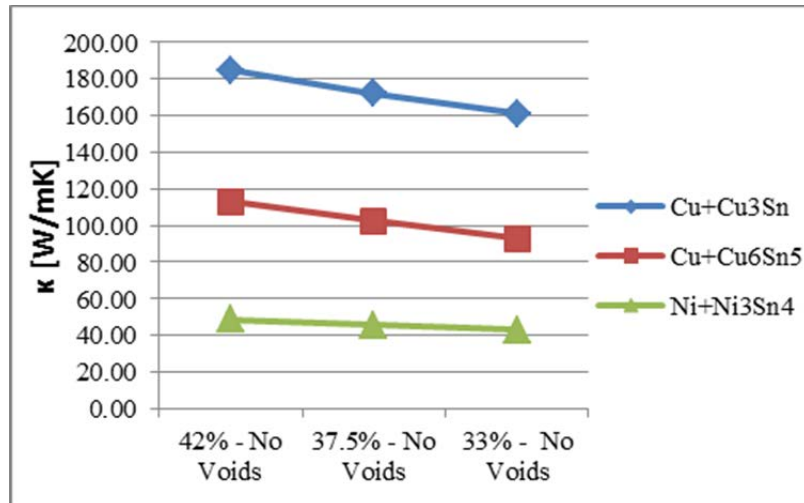


**Figure 6-16: Thermal conductivities of the void-free sinter joints loaded with particles of mixed size**

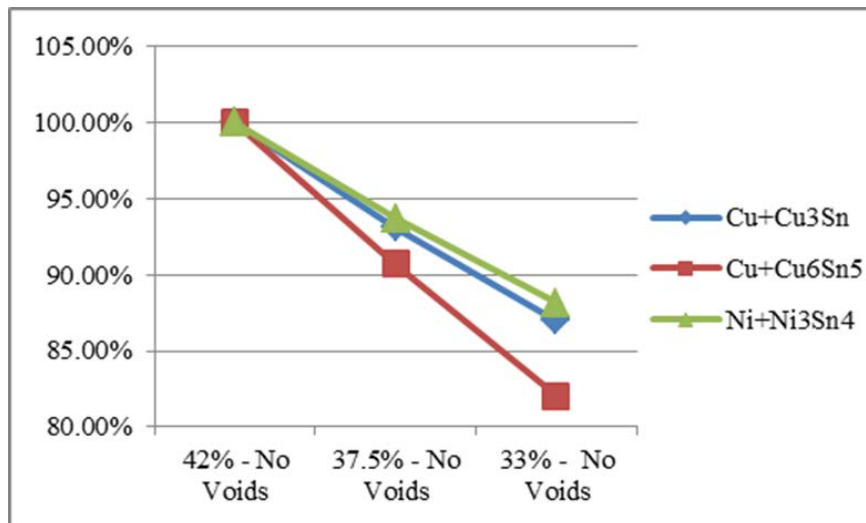


**Figure 6-17: Thermal conductivities relative to that of joints with 42 vol.-% metal loading**

**D. Mixed Particle Sizes, Variation of Metal Loading, Partially Voided**

This condition is similar to that of condition in section 2.3. Yet here, one type of metal particle was replaced with voided regions. For example, the test condition “42% - 50 μm Voids” means that the joint is loaded with 14 vol.-% of particles with radii of 25 and 12.5 μm each, but contains 14 vol.-% of voids with radii of 50 μm.

The introduction of voids into the sinter joint system reduces the thermal conductivity considerably, see Figure 6-18, Figure 6-19, and Figure 6-20, for the (Cu<sub>3</sub>Sn+Cu),

(Cu<sub>6</sub>Sn<sub>5</sub>+Cu), and (Ni<sub>3</sub>Sn<sub>4</sub>+Ni) systems respectively. It should be noted that for the condition assessed here, the introduction of voids reduces the vol.-% of metal particles by 33.3% (e.g. from 42% to 28%). On average the thermal conductivity of the (Cu<sub>3</sub>Sn+Cu), (Cu<sub>6</sub>Sn<sub>5</sub>+Cu), and (Ni<sub>3</sub>Sn<sub>4</sub>+Ni) systems are reduced by 29.04%, 31.89%, and 27.28%. The highest reduction for the (Cu<sub>3</sub>Sn+Cu) systems is 32.44% for the 42% condition with 50 μm voids. For the (Ni<sub>3</sub>Sn<sub>4</sub>+Ni) system, it occurs under the same condition with a reduction of 30.73%. In contrast, for the (Cu<sub>6</sub>Sn<sub>5</sub>+Cu) system, the highest reduction of 36.13% occurs for the 42% condition with 10 μm voids. The difference in behavior occurs even though identical geometries were used. This means that the choice of material system not only influences the relative and absolute reduction of thermal conductivity under voiding, but also which void size has the most significant influence on the reduction.

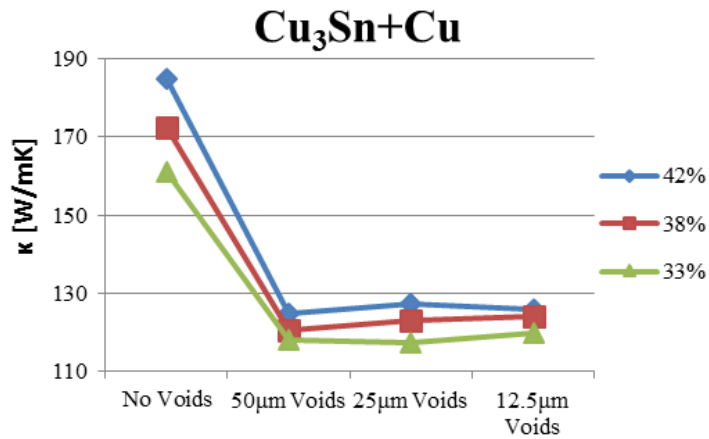


**Figure 6-18: Thermal conductivity of partially voided joints for the (Cu<sub>3</sub>Sn+Cu) system**

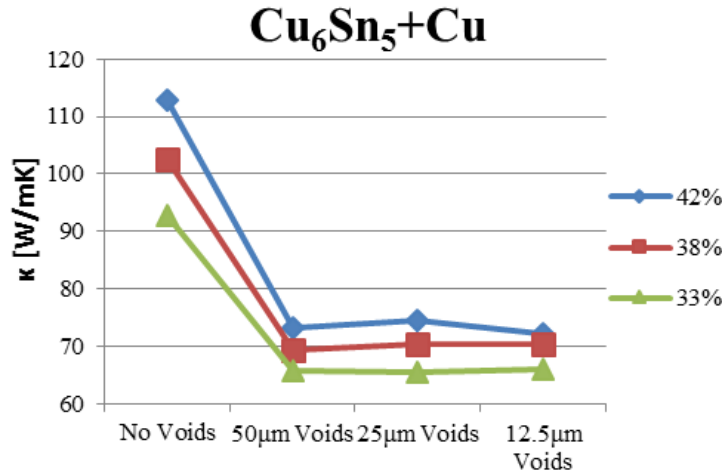


**Figure 6-19: Thermal conductivity of partially voided joints for the (Cu<sub>6</sub>Sn<sub>5</sub>+Cu) system**

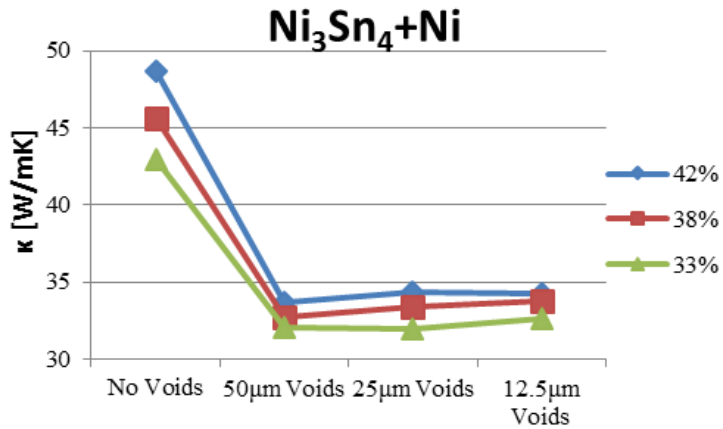


**Figure 6-20: Thermal conductivity of partially voided joints for the (Ni<sub>3</sub>Sn<sub>4</sub>+Ni) system**

**E. Joint Maximally Filled with 50, 30, and 10 µm Radius Metal Particles**

In this condition the joint was maximally filled with metal particles with radii of 50, 30, and 10 µm. The vol.-% of these particles were 20.94%, 12.97%, and 14.58% respectively. This adds up to a total metal loading of 48.49%, which corresponds to an IMC vol.-% of 51.51%. This sinter joint was modelled as void-free. A side view on the arrangement of the metal particles in the sinter joint can be seen in Figure 6-21. Figure 6-22 and Table 6-7 show the thermal conductivity of the three material systems. (Cu<sub>3</sub>Sn+Cu), (Cu<sub>6</sub>Sn<sub>5</sub>+Cu),

and (Ni<sub>3</sub>Sn<sub>4</sub>+Ni) possess thermal conductivities of 200.20 W/mK, 125.47 W/mK, and 59.07 W/mK respectively.

**Table 6-7: Thermal conductivities of the void-free sinter joints loaded with particles of mixed size**

Material System	Cu <sub>3</sub> Sn+Cu	Cu <sub>6</sub> Sn <sub>5</sub> +Cu	Ni <sub>3</sub> Sn <sub>4</sub> +Ni
$\kappa$ [W/mK]	200.20	125.47	59.07

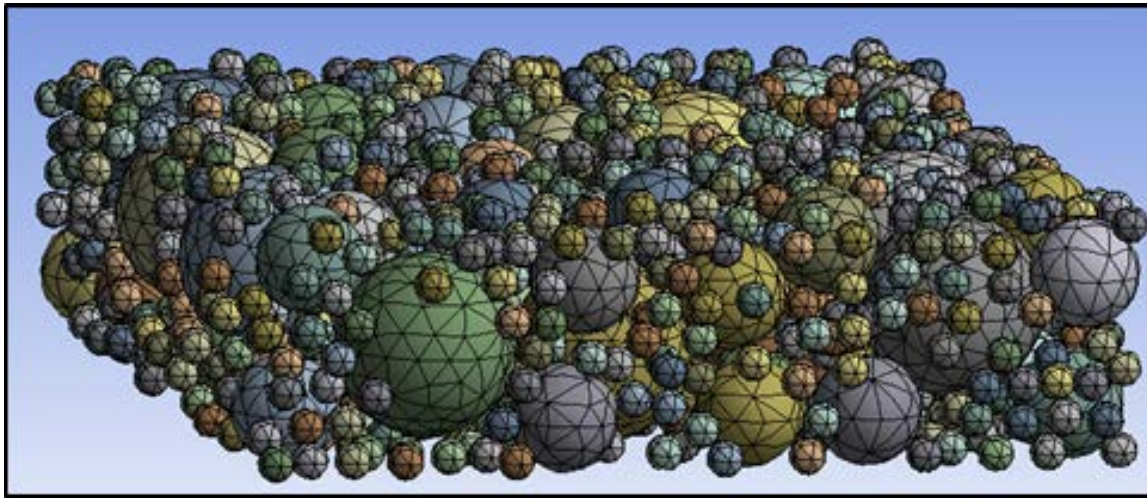


**Figure 6-21: Side view on structure formed by metal particles with radii of 50, 30, and 10  $\mu$ m**

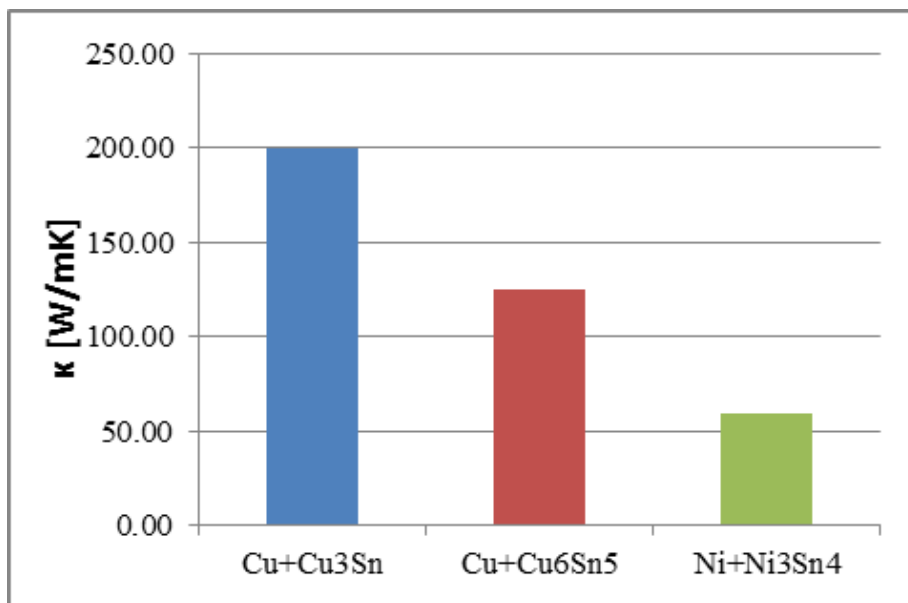


**Figure 6-22: Thermal conductivity of the joint with a metal loading as shown in Figure 6-21**

## Summary

The thermal conductivity of three material systems has been analyzed: (Cu<sub>3</sub>Sn+Cu), (Cu<sub>6</sub>Sn<sub>5</sub>+Cu), and (Ni<sub>3</sub>Sn<sub>4</sub>+Ni). (Cu<sub>3</sub>Sn+Cu) possesses the highest thermal conductivity, followed by (Cu<sub>6</sub>Sn<sub>5</sub>+Cu). The (Ni<sub>3</sub>Sn<sub>4</sub>+Ni) system showed the lowest thermal conductivity. This correlates with the thermal conductivity of the metal particles and the IMC phases ( $\kappa_{Cu} > \kappa_{Ni}$  and  $\kappa_{Cu_3Sn} > \kappa_{Cu_6Sn_5} > \kappa_{Ni_3Sn_4}$ ). Depending on metal particle size, metal content, percentage voiding and void size, their thermal conductivities were found to lie in the range of 117 – 200 W/mK, 64 – 125 W/mK and 32 – 59 W/mK for (Cu<sub>6</sub>Sn<sub>5</sub>+Cu), and (Ni<sub>3</sub>Sn<sub>4</sub>+Ni). (Cu<sub>3</sub>Sn+Cu), respectively. Sinter joints formed by mixes of particles with different radii have the highest metal loading and thus show the highest thermal conductivity.

The thermal conductivity is highest for particle sizes close to the joint thickness. Yet sinter joints with particles of this size are hard to manufacture due to limitations with processability (e.g. stencil printability). Particles within a diameter range of approximately ½ to ¼ the joint thickness show almost constant thermal conductivity under similar particle content conditions and are easy to process. The thermal conductivity of sinter joints formed by particles below that size is significantly reduced.

The dependence of thermal conductivity on the particle size is most pronounced for the (Cu<sub>6</sub>Sn<sub>5</sub>+Cu) system. This can be explained by the ratio of the thermal conductivity of the IMC to that of the metal particles. This ratio is lowest for this system, which leads to considerably higher heat flow crowding in the Cu particles to minimize the high thermal resistance path through the Cu<sub>6</sub>Sn<sub>5</sub> IMC compared to the other systems. The same is true

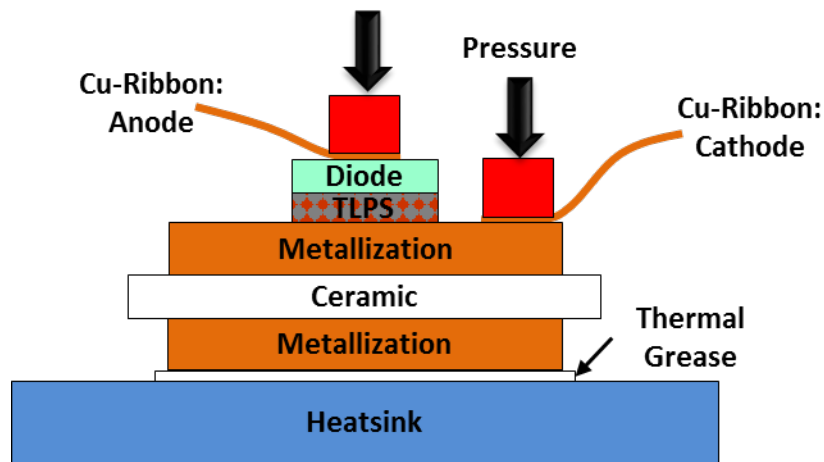
for the influence of voiding on the thermal conductivity of sinter joints. The (Cu<sub>6</sub>Sn<sub>5</sub>+Cu) system has the highest sensitivity towards voiding when compared to the other systems.

### 6.2.2 Verification

The T3Ster test platform from Mentor Graphics was used to determine the thermal conductivity of Cu-Sn TLPS joints experimentally. The platform is a thermal analysis suite used to characterize the transient thermal response of a thermal management stack. It consists of the hardware required to calibrate and measure the thermal response (T3Ster), an analysis tool that transforms the characteristics of the transient response into a time-independent, characteristic structure function (T3Ster Master), and a simulation environment to simulate a structure function. Material properties are determined iteratively by fitting the simulated and experimentally determined structure functions (FloTherm).

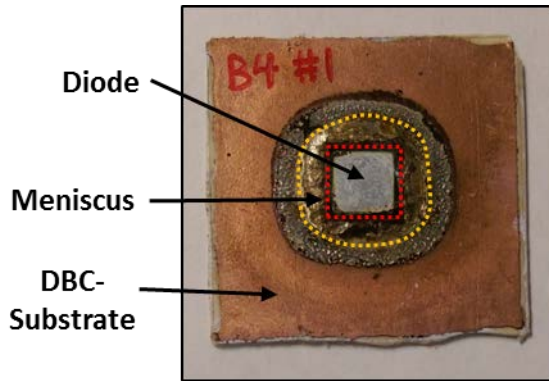
The measurements require an active device with a temperature-dependent correlation between voltage and current. The temperature-dependence of a device voltage drop under a specific measurement current is characterized. The device is electrically heated during the initial test stage. Afterwards the heating current is turned off and the small, thermally insignificant, measurement current applied. During cooling, the voltage changes temperature-dependently. The voltage-current relationship determined during calibration is then used to compute the transient thermal behavior from the voltage response. The transient thermal behavior depends on the thermal properties of all layers in the thermal stack. Therefore, an analysis of the transient thermal response yields insight into the thermal properties of all layers in the thermal stack. In consequence, the thermal conductivity of the TLPS layer can be determined as part of the thermal response of the thermal stack.

Figure 6-23 shows a schematic of a cross-section of the thermal stack used to analyze the thermal properties of the Cu-Sn TLPS joints. A power diode is attached to a Direct Bond Copper (DBC) substrate with a Cu-Sn TLPS joint. The DBC consists of an  $\text{Al}_2\text{O}_3$  ceramic layer sandwiched between two layers of Cu-metallization. The interface between the sample and the heatsink is filled with a thermal grease layer. Cu-ribbons on the top of the diode and the top of the DBC are used to electrically connect the anode and cathode side of the diode. Pressure is exerted on the Cu-ribbons via polyimide spacers to ensure continuous electrical contact between the Cu-ribbons and the diode and to minimize the thermal resistance between the sample and the heatsink.



**Figure 6-23: Schematic of a cross-section through the thermal stack used to analyze the thermal properties of the TLPS joint**

Figure 6-24 shows a top view on one of the samples used for the transient thermal analyses. The sample consists of a diode sintered to the top side of the DBC. A solder meniscus exists around the diode. The diode and the meniscus regions are indicated by dotted red and orange lines, respectively. The grey region located around the meniscus region is the maximum area that was wetted by the solder paste right after melting. The meniscus region is smaller than this region because some solder is infiltrating the joint region and some solder is concentrating in the meniscus region.



**Figure 6-24: Top view on a sample used for the transient thermal analyses. The diode is indicated by the dotted red line and the meniscus region is indicated by the dotted orange line**

Figure 6-25 shows a top view of the test structure used to analyze the transient thermal behavior of the thermal stack. A sample of the structure shown in Figure 6-24 is placed on a heatsink on which a layer of thermal grease has been applied. Four screws are tightened to exert pressure the DBC. As the sample is pressed down, the thermal grease rearranges to a thin layer. Excess grease is squeezed out of the contact region and is subsequently removed. Two of the screws are used to ensure good contact between the Cu-ribbons and the top of the diode and the top of the DBC, compare Figure 6-23.

After preparing the thermal stack, every sample was calibrated individually. The structure shown in Figure 6-25 was placed in a convection oven and the Cu-ribbons connected to the T3Ster setup. A forced convection air stream was applied to the 10 heatsink fans by funneling the air flow of a 120mm x 120mm fan through an air duct. The temperature of the convection oven was increased from 30 °C and 60 °C by increments of 10 °C. After the oven temperature had stabilized, additional 15 minutes of temperature dwell ensured that the thermal stack had a continuous, homogeneous temperature. The temperatures of the oven and the heatsink were verified by thermocouples. 15 calibration measurements at a measurement current of 10mA were taken at every temperature level and their median

computed for each sample. Figure 6-26 shows the temperature-dependence of the voltage of one sample for the calibration current of 10mA.

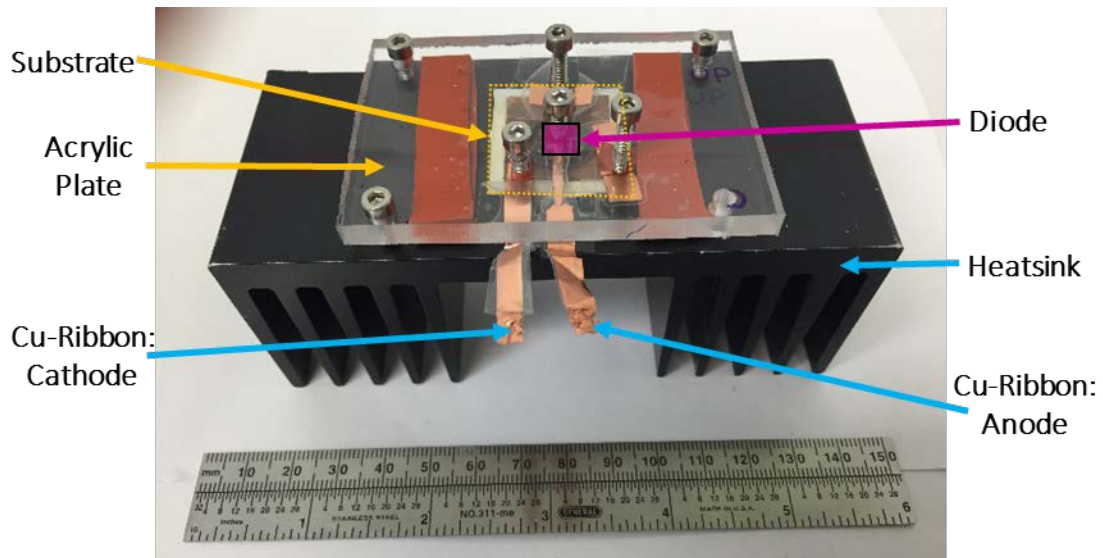


**Figure 6-25: Top view on the test structure. The sample with the diode sintered on the DBC is placed on top of the heatsink with a grease layer sandwiched in between. Four screws are exerting pressure on the DBC. Two of these are ensuring contact between the Cu-ribbons and the diode**

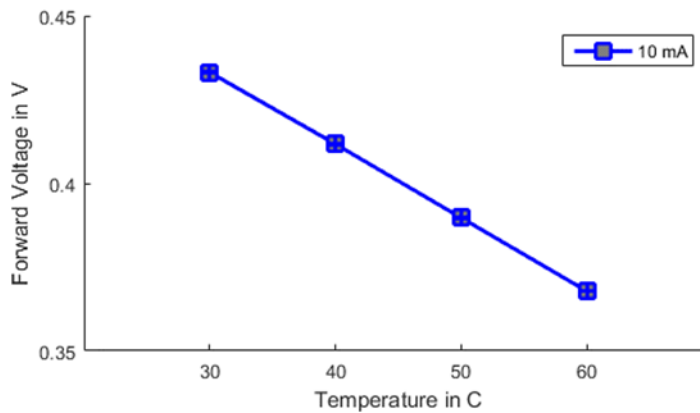


**Figure 6-26: Calibration curve of one sample used in the test**

Figure 6-27 shows two examples of transient thermal response curves derived from transient heating and cooling tests and calibration data. The blue and red curve show the temperature response of an unaged Cu-Sn TLPS sample and a sample aged for 100 hours at 250 °C, respectively. The scale on the time axis (x-axis) is logarithmic. The sampling time during the initial measurements is 1µs and increases exponentially over time.

The period during which the heating current is still active is indicated by the red shading and is approximately  $15\mu\text{s}$ . During this period a heating current is active, which is much higher than the measurement current. Because the temperature response is calibrated to the measuring current, the temperatures recorded during the heating period are not actual device temperatures.

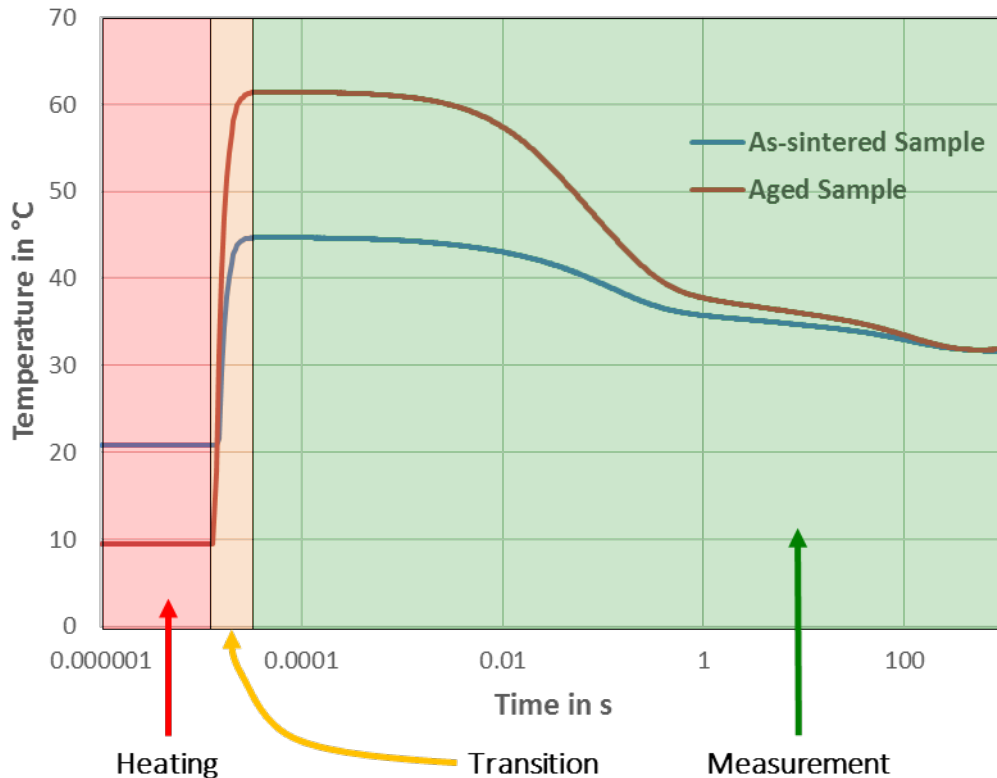


**Figure 6-27: Thermal impedance curve: Transient thermal response curves of a Cu-Sn TLPS sample after sintering (blue line) and after aging for 100 hours at  $250\text{ }^\circ\text{C}$  (red line)**

A transition period exists during which the heating current is deactivated and the measuring current is activated. This change of load does not occur instantaneously, and a transition period of approximately  $20\mu\text{s}$  is required to stabilize the diode in the new steady-state condition. The transition period is indicated by the orange shaded area in Figure 6-27. The stable post-transition region of the transient temperature response is indicated by the green shaded area in Figure 6-27. The calculation of structure functions will be performed with

data acquired from this region. The aged sample shows initial temperatures significantly higher than those of the unaged sample. At the end of the transient analysis the temperature of the aged and unaged samples converge to the ambient temperature of the convection oven. Even though some degradation has occurred in the aged sample, the location and characteristic of that degradation is undiscernible from Figure 6-27.

The process of deriving structure function is explained in detail in [123] and will here be summarized briefly. The temperature response depends on the structure of the thermal stack. Each layer in the thermal stack is characterized by a thermal resistance,  $R$ , and a thermal capacity,  $C$ , and, in combination a time constant,  $\tau$ , as the product of  $R$  and  $C$ . The thermal response curves shown in Figure 6-27 are plotted on a logarithmic scale with temperature  $T$  as a function of time with the relationship

$$T = T(z) \quad \text{Equation 6-1}$$

with

$$z = \ln t$$

It can be proven that for the logarithmic time  $z$

$$\frac{d}{dz}T(z) = \int_0^{\infty} R(\zeta)[\exp(z - \zeta - \exp(z - \zeta))]d\zeta \quad \text{Equation 6-2}$$

which is in the form of a convolution integral [123]. Substituting

$$w_z(z) = \exp(z - \exp(z)) \quad \text{Equation 6-3}$$

yields

$$\frac{d}{dz}T(z) = \int_0^{\infty} R(\zeta)w_z(z - \zeta)d\zeta \quad \text{Equation 6-4}$$

, or

$$\frac{d}{dz}T(z) = R(z) \otimes w_z(z) \quad \text{Equation 6-5}$$

From this  $R$  can be computed in dependence of the logarithmic time as:

$$R(z) = \left[ \frac{d}{dz} T(z) \right] \otimes^{-1} w_z(z) \quad \text{Equation 6-6}$$

$R(z)$  in this form is represented as a continuous function of  $R$  over the  $z$  space [123]. This spectrum can then be discretized into a RC network model with a series of thermal resistances and capacitances by the NID (network identification by deconvolution) method by discretizing the continuous function over multiple time steps  $\tau_i$  with

$$\tau_i = \exp(z_i) \quad \text{Equation 6-7}$$

which yields an equivalent thermal resistance  $R_i$  with

$$R_i = R(\tau_i) \quad \text{Equation 6-8}$$

The thermal network derived this way is of the Foster canonic form represented by the series connection of multiple elements of parallel  $R_i$ s and  $C_i$ s with

$$C_i = \tau_i / R_i \quad \text{Equation 6-9}$$

Because the foster network model does not represent the physical structure of the thermal system it has to be converted into the Cauer canonic form [123]. The Foster and Cauer canonic forms of the thermal networks are shown in Figure 6-28 (top) and Figure 6-28 (bottom), respectively. In the Cauer canonic form each combination of capacity and resistance beginning from the load side (left side of Figure 6-28 (bottom)) represents one thermal mass. Figure 6-29 shows a Cauer canonic form network and elements representing individual elements in the thermal stack. One pair of thermal resistances  $R_i$  and thermal capacities  $C_i$  represent one element of the thermal stack. As a simplified example of a TLPS sample, the elements close to the load,  $R_1$  and  $C_1$ , could represent die region, the elements to the right of them,  $R_2$  and  $C_2$ , the die attach region, etc. Every step for the computation of the Cauer canonic for thermal network is performed automatically by the software tool T3Ster Master.

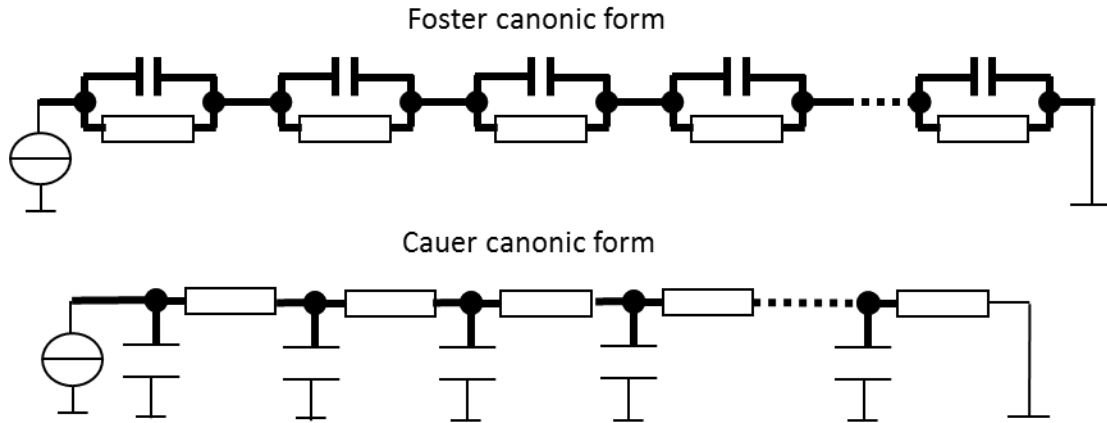


**Figure 6-28: The Foster (top) and Cauer (bottom) canonic forms of thermal networks**

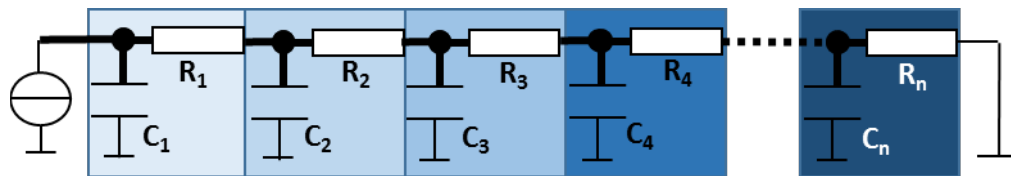


**Figure 6-29: Physical equivalent of the Cauer canonic form: Every  $R_i$ - $C_i$  pair corresponds one element of thermal resistance and thermal capacities in the thermal stack**

Plotting the total capacity of the Cauer network shown in Figure 6-29 over resistance yields the system structure function. The structure function is generated automatically by the T3Ster Master software tool. An example of a structure function of a Cu-Sn TLPS sample on a power electronic substrate is shown in Figure 6-30. The structure function is represented by the red line and red dots. The structure function starts at the origin at zero resistance and zero capacity. It ends at a finite resistance and an infinite capacity. Resistance and capacitance are both monotonously increasing. This corresponds to the continuously increasing heat path that is passed as heat flows from the source to the sink. The heat capacity at the maximum resistance is practically infinite because of the infinite thermal mass of the ambient air. Indicated in green are specific regions in the thermal stack corresponding to the structure function. Example elements include the die, the die attach, the power electronic substrate, and the heatsink. The shaded green regions of the thermal

stack elements are not part of the structure function and have been added after further analysis had been performed to facilitate the interpretation of the structure function.

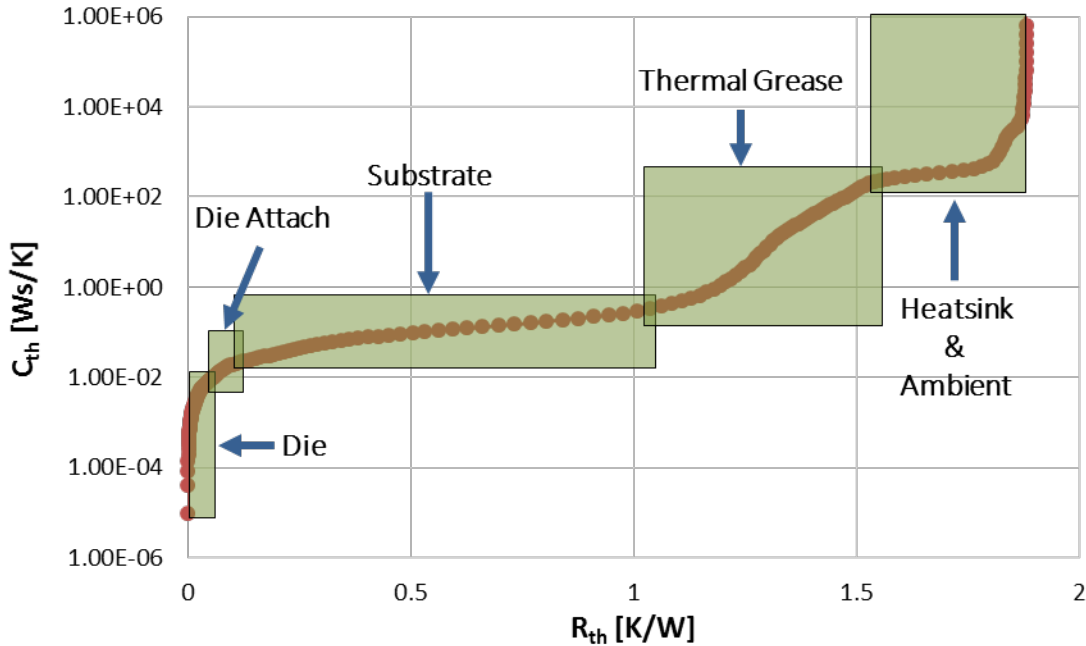


**Figure 6-30: Example structure function of a Cu-Sn TLPS sample**

To establish a correlation between the structure function and elements in the thermal stack, quantifying analyses must be performed. The determination of the thermal properties of the TLPS joints requires a quantification of all layers in the thermal stack. The calibration and quantification of the experimental structure functions is achieved by comparison to structure functions simulated in the FloTherm simulation environment. An overview of the simulated geometry of an example temperature distribution of a transient simulation run are shown in Figure 6-31 and Figure 6-32. Dimensions of all elements were determined by measurements (e.g. heat sink size, substrate side length, meniscus side length) or cross-sections of samples (e.g. joint thickness, meniscus thickness). Thermal properties of known elements (everything besides TLPS joint properties) were taken from literature. Predicted properties (compare section 6.2.1) of the Cu-Sn joints were used for initial simulation runs.

The experimentally determined properties of Cu-Sn joints were found by iterative adaptation and fitting of simulated structure curves to experimental structure curves.

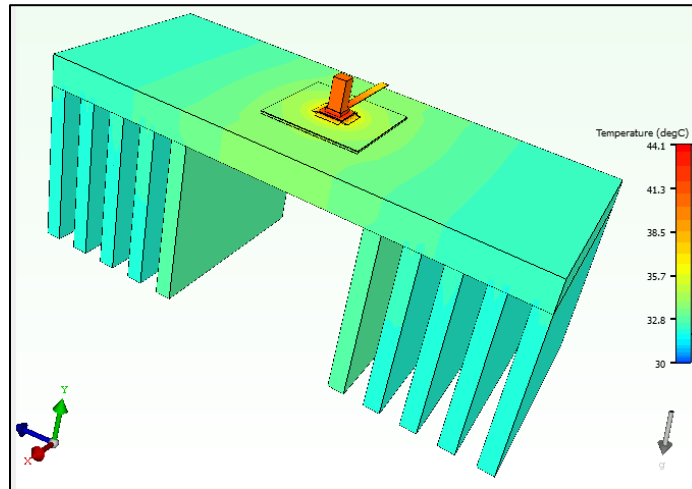


**Figure 6-31: Temperature distribution in a simulated Cu-Sn TLPS sample in FloTherm. The geometry shows high resemblance with the test samples, compare Figure 6-25**

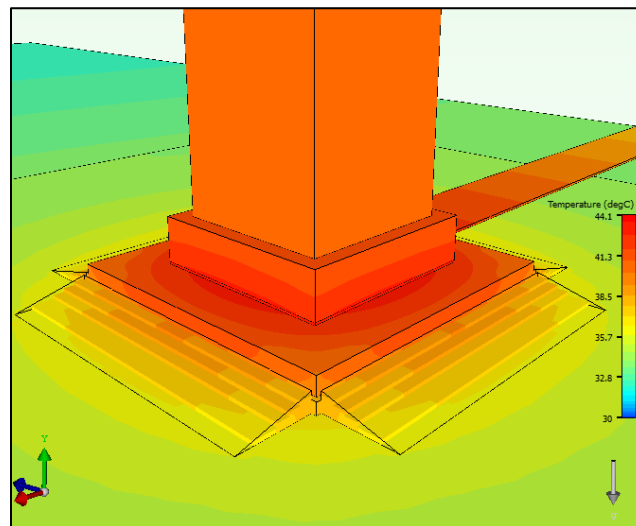


**Figure 6-32: View on the die region of the simulation shown in Figure 6-31. The geometry includes menisci, Cu-ribbon, polyimide-spacers and tightening screw elements**

Figure 6-33 shows a comparison of a structure function obtained by experiments (solid blue line) and a corresponding simulated structure function (solid red lines) as well as the corresponding 1<sup>st</sup> derivatives of the structure functions (dashed blue and dashed red lines, respectively). Fitting of the simulated curve to the experimental curve was performed by

iteratively adjusting the thermal conductivity and capacitance of the TLPS joint material and the contact resistances between elements of the thermal stack.

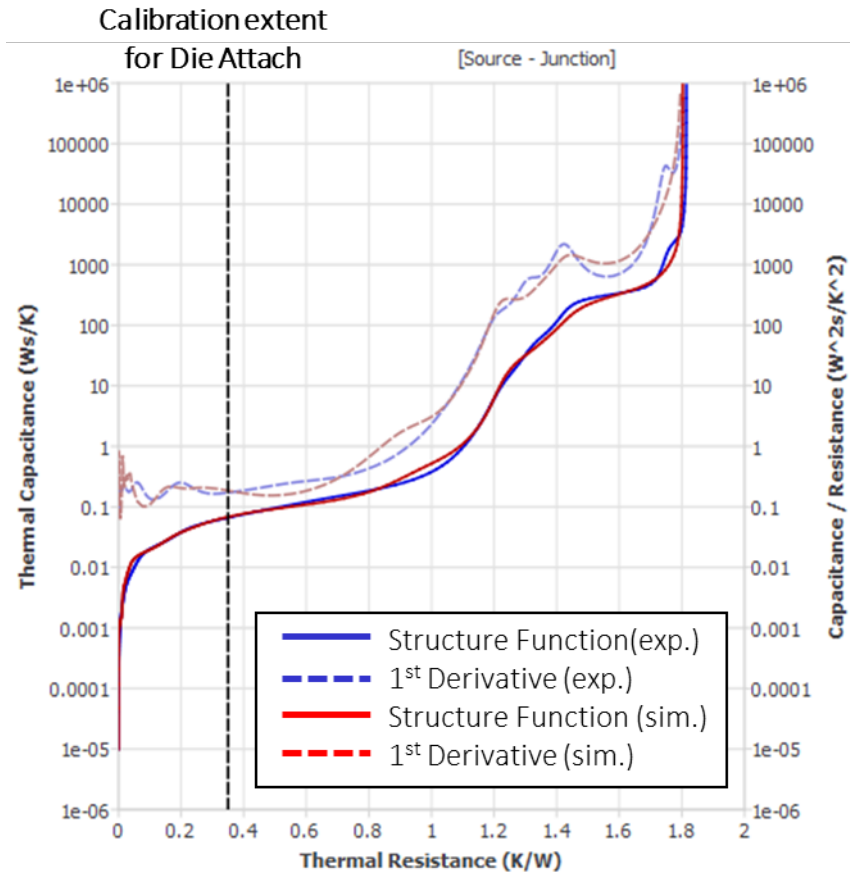


**Figure 6-33: Fitting of the simulated structure function (red line) to the structure function from T3Ster experiments (blue line)**

The geometric constraints (e.g. side length and height of meniscus, sinter joint thicknesses) were adapted in the simulation models to measured sample dimensions for every simulation case to ensure consistency between the experimental samples and the simulations. Table 6-8 summarizes the joint thicknesses, thermal conductivities, and resulting joint resistances for the unaged samples. The thermal conductivity of the Cu-Sn TLPS joints sintered for 30 minutes at 300 °C was found to vary between 95.7 and 189.0 W/mK. No significant correlation between the joint thickness and the thermal conductivity was found. The average thermal conductivity of the Cu-Sn joints was determined as 140.2

W/mK. The microstructure of Cu-Sn joints after this sintering conditions is characterized predominately by  $\text{Cu}_6\text{Sn}_5$  IMCs and Cu, compare section 5.1.1. The thermal conductivity of Cu-Sn joints consisting of  $\text{Cu}_6\text{Sn}_5$  IMCs and Cu-particles for high Cu-density has been predicted as 125.5 W/mK, compare Table 6-7, which is in good agreement with the experimental results.

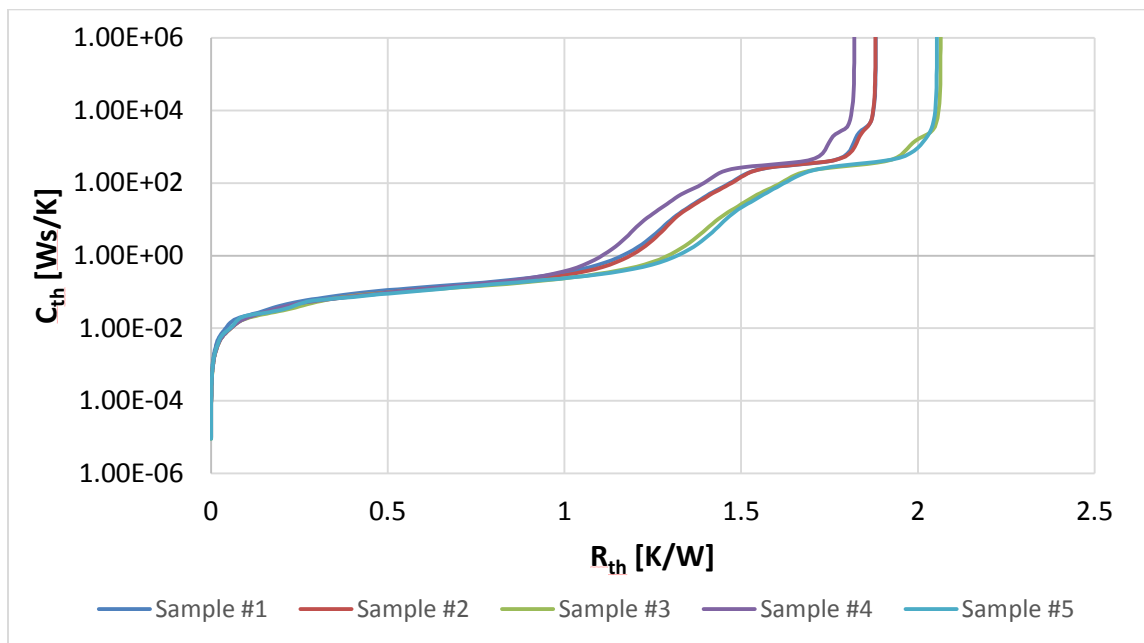
**Table 6-8: Joint thickness, best-fit thermal conductivity, and computed joint resistance of the unaged Cu-Sn TLPS sinter joints.**

Sample #	Joint thickness [ $\mu\text{m}$ ]	TLPS Conductivity [W/mK]	Joint Resistance [K/W]
1	220	95.7	5.79E-02
2	263	136.4	4.86E-02
3	221	189.0	2.95E-02
4	242	124.4	4.90E-02
5	218	155.6	3.53E-02
<b>Average</b>	<b>232.8</b>	<b>140.2</b>	<b>4.41E-02</b>

Besides process variation (e.g. particle rearrangement, void distribution), the variation of the TLPS joint bulk conductivity can be explained high contact resistances at the Die-To-DieAttach-interface and the DieAttach-to-DBC-interface, which were required to achieve good match between the simulated and experimental structure functions. These resistances on average dominated the total thermal resistance of the die attach region. The average contribution of the bulk joint resistance, the Die-To-DieAttach-interface resistance, and the DieAttach-to-DBC-interface resistance were 7.1%, 20.2%, and 72.7%, respectively. Yet, good physical contact was established between the die and the die attach as well as between the die attach and the substrate, because of good wetting behavior during sintering. This should lead to small contact resistances and a joint resistance that is dominated by the thermal conductivity of the bulk of the TLPS joint. The discrepancy between the good interfacial adhesion and the high interface resistances should be explored in future studies

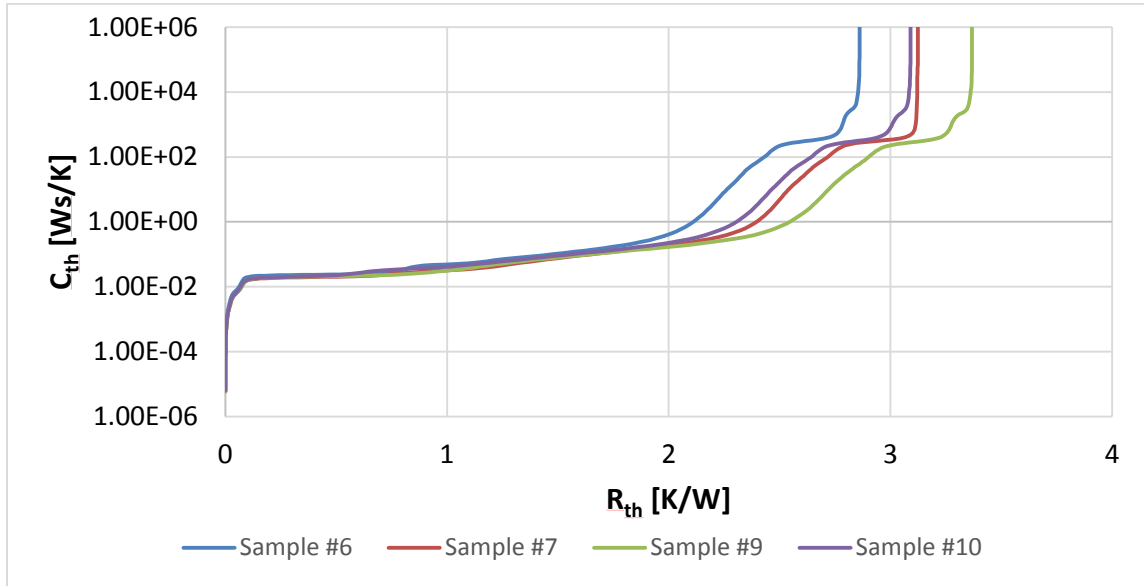
of thermal properties of TLPS joints. One explanation for this discrepancy might be that the thermal networks derived during the derivation of the structure functions assume an ideal 1-D heat flow RC network between the heat source and the heatsink. In contrast, the samples used in this study were highly 3-dimensional and the associated spreading resistances might not be reflected properly in the structure functions.

Figure 6-34 shows the structure functions of unaged Cu-Sn TLPS. The minimum, average, and maximum thermal resistances of the thermal stacks of the unaged samples are 1.82, 1.94, and 2.06 K/W, respectively. Variations in total thermal resistance are predominately related to variations of the contact resistance in the thermal grease region between the DBC substrate and the heatsink. The results in the low thermal resistance regions related to the die, die attach, and substrate layers ( $< 0.5\text{K/W}$ ) are highly consistent. The small variations in the die attach regions relate to variations in the thickness of the TLPS joints, variations of joint conductivity, size and height of the menisci, which are properties related to variation of sintering process variation.



**Figure 6-34: Structure functions of the unaged Cu-Sn TLPS samples**

Figure 6-35 shows the structure functions of aged Cu-Sn TLPS. The minimum, average, and maximum thermal resistances of the thermal stacks of the aged samples are 2.86, 3.11, and 3.37 K/W, respectively.

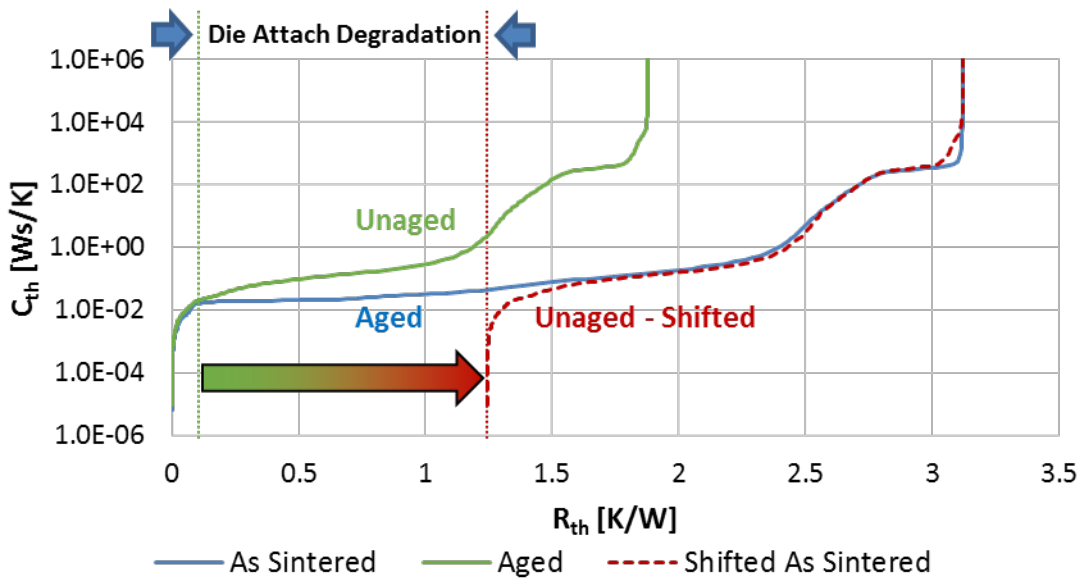


**Figure 6-35: Structure functions of the Cu-Sn TLPS samples aged for 100 hours at 250 °C**

The source of the biggest difference between the structure functions of unaged and aged samples is the thermal behavior of the die attach layer. This is illustrated in Figure 6-36. The solid green curve is the structure function of an unaged Cu-Sn TLPS sample after sintering. The solid blue curve is the structure function of an aged Cu-Sn TLPS sample after sintering and subsequent aging. The dashed red line shows the structure function of the unaged Cu-Sn sample (compare solid green line) shifted by 1.24 K/W. The maximum thermal resistances of the shifted unaged and the aged samples are identical.

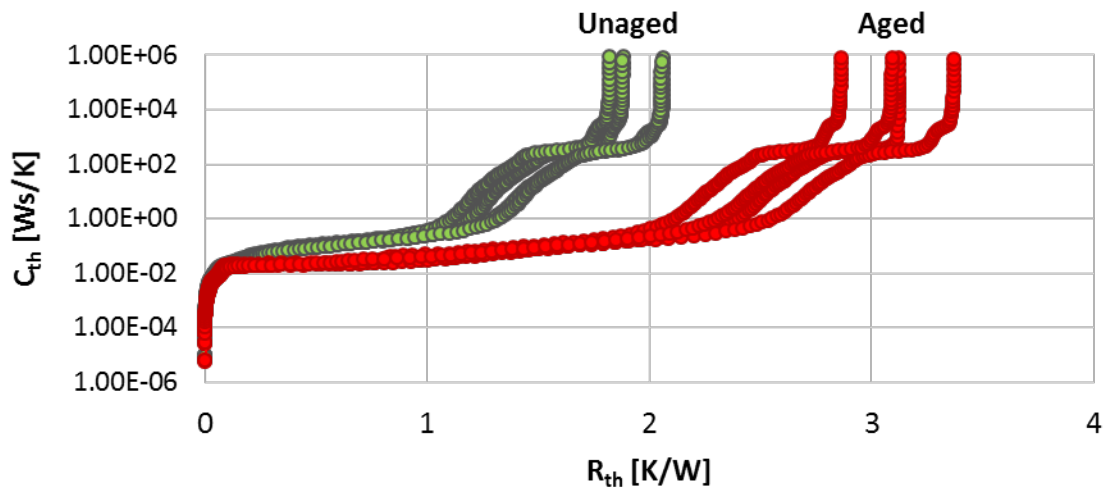
Two things can be concluded from Figure 6-36: (1) the low thermal resistance regions of the unaged and aged structure functions are almost identical. This shows that the degradation did not occur in the die region. (2) The high thermal resistance regions of the shifted unaged and aged structure functions are almost identical. This shows that the

degradation did not occur in the substrate, thermal grease, or heatsink regions. It can therefore be concluded that the degradation occurred in the die attach region.



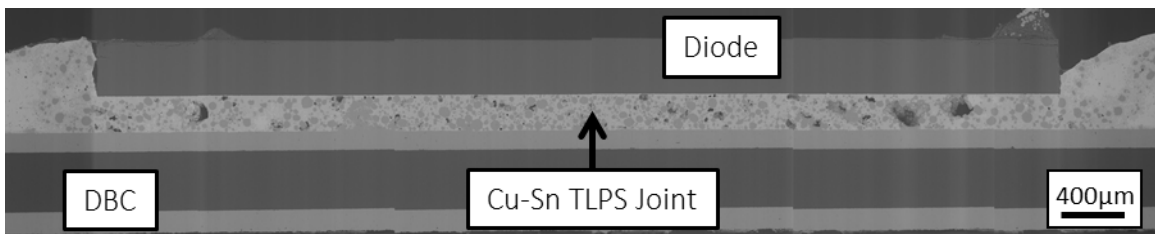
**Figure 6-36: Degradation of the die attach layer is the main source of difference between the structure functions of aged and unaged samples**

Figure 6-37 shows the structure functions of the Cu-Sn TLPS samples assessed in this study. High consistency exists within their assessment group for both, the unaged and the aged samples. Variation of thermal resistance within the unaged and aged groups is predominately caused by variations of the thermal grease layer. The average thermal resistance of the die attach layer before aging was approximately 0.044 K/W. It increased on average by 1.17K/W during aging, an increase by more than 26 times. This indicates that the TLPS layer has degraded to the point of practical delamination.



**Figure 6-37: Structure functions of unaged (green) and aged (red) Cu-Sn TLPS samples**

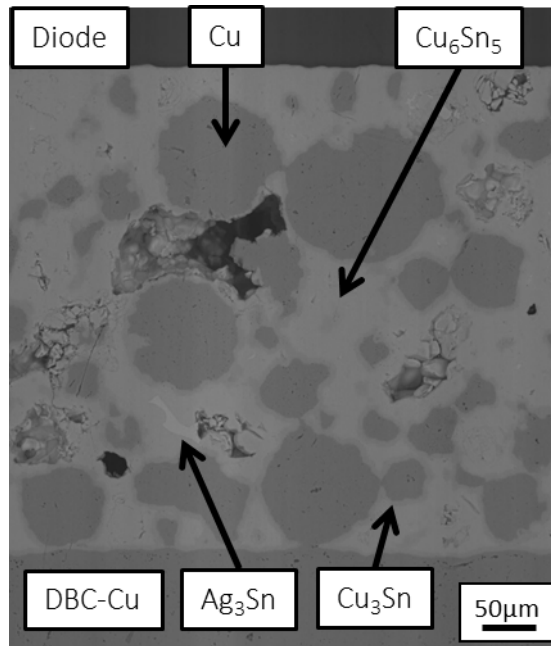
Figure 6-38 shows a cross-section of an unaged sample used for the transient thermal analyses. The image was created by merging six individual SEM microscopy images. The thickness of the joint is approximately 230  $\mu\text{m}$ . The diode backside metallization and the Cu-layer of the DBC have been wetted complete. Good contact exists between the diode and the joint as well as between the joint and the DBC. Small gaps exist between the diode body and the menisci.



**Figure 6-38: Cross-section of an unaged Cu-Sn TLPS sample**

Figure 6-39 shows a high magnification cross-section of a part of the joint shown in Figure 6-38. The microstructure consists predominately of residual Cu-particles embedded in a matrix of  $\text{Cu}_6\text{Sn}_5$ . Thin layers of  $\text{Cu}_3\text{Sn}$  with a layer thicknesses smaller than 10  $\mu\text{m}$  have grown between the Cu-particles and  $\text{Cu}_6\text{Sn}_5$ . Few regions of  $\text{Ag}_3\text{Sn}$  IMCs existed throughout the joint. No Ag is present in the sinter pastes or the DBC substrates. The only

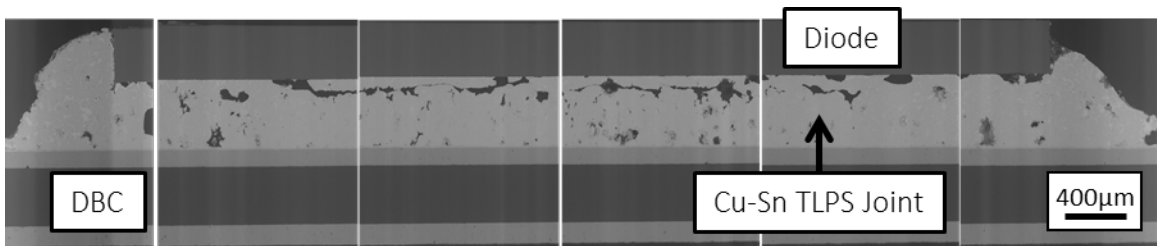
source of Ag during sintering is the diode backside metallization layer. Small regions with  $\text{Ag}_3\text{Sn}$  were present throughout the joint region after sintering and no layer of residual Ag was present at the diode interface after processing. This indicates that during processing, the Ag from the diode backside metallization dissolves completely into the liquid Sn and distributes homogeneously throughout the joint region. Some voids are present in the joint. The voiding levels are below 5%.



**Figure 6-39: Cross-section of a Cu-Sn TLPS sample without aging**

Figure 6-40 shows a cross-section of an unaged sample used for the transient thermal analyses. The image was created by merging six individual SEM microscopy images. The thickness of the joint is approximately  $470\ \mu\text{m}$ , twice as thick compared to unaged samples. No residual Cu-particles are present in the joint region. The microstructure consists of small regions of  $\text{Cu}_6\text{Sn}_5$  embedded in a  $\text{Cu}_3\text{Sn}$  matrix. The number and size of voids has increased compared to the unaged condition. A network of large horizontal voids is located within the interconnect close to the diode. Similar to the results of the aging test performed on Ni-Sn joints, see section 5.3, the increase in joint thickness correlates with an influx of

Sn from the meniscus region and a reduction of the meniscus width. Yet, for aging test performed on Cu-Sn joints with an identical sinter paste system, no joint thickness increase or meniscus consumption occurred, see section 5.1.1. This indicates that the small amounts of dissolved Ag and Ni from the diode backside metallization change the long-term aging stability of the Cu-Sn joints and enable a detachment mechanism similar to that of Ni-Sn joints. This is also in agreement with the IMC growing behavior found in the kinetics analyses for the Cu-Ni-Sn system, compare section 2.4.



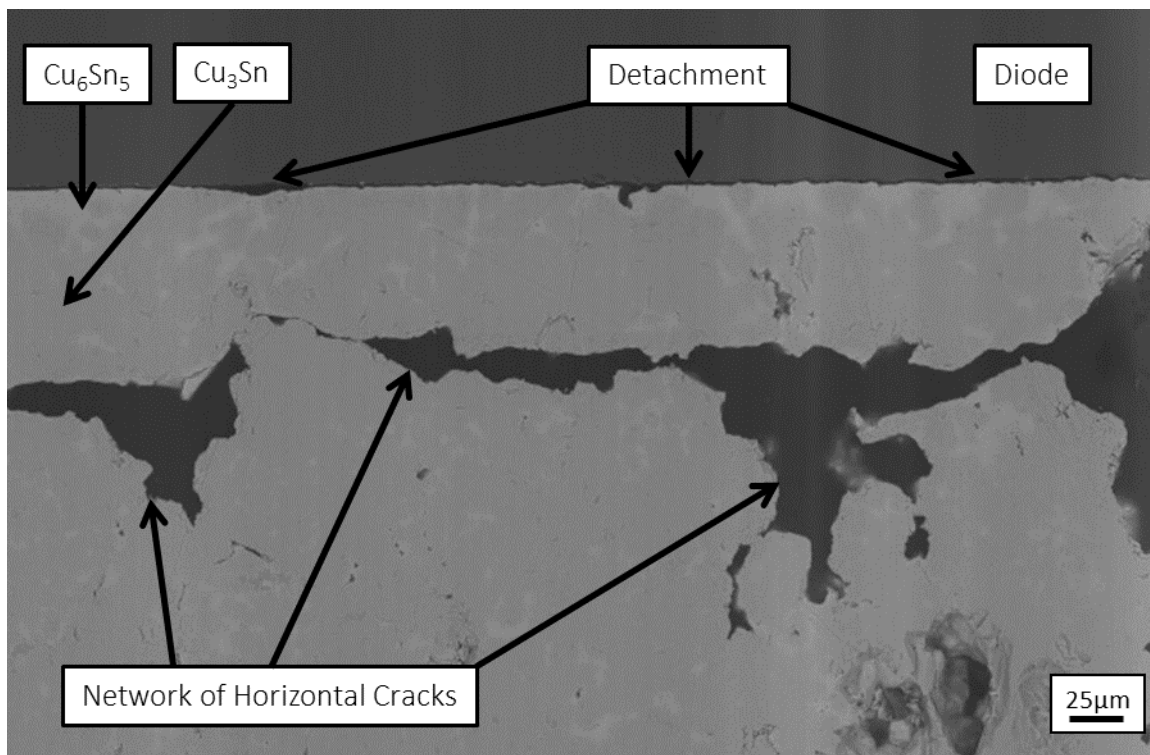
**Figure 6-40: Cross-section of a Cu-Sn TLPS sample after aging**

Figure 6-41 and Figure 6-42 show high magnification cross-sections of Cu-Sn TLPS joint samples after aging. Two failure modes can be identified. The first is the growth of a network of horizontal cracks within the joint within a distance of 100  $\mu\text{m}$  below the diode backside. The second type of failure mode is the detachment of the diode body from the bulk of the TLPS joint. The detachment occurred throughout the joint region and was most pronounced in regions with voids at the diode interface. Some samples showed almost complete detachment of the TLPS joint from the diode backside.

Multiple factors contribute to the increase in thermal resistance of the aged joints compared to the unaged joint. (1) The increase in joint thickness increases the heat path length, which is directly proportional to the thermal resistance. Aged joints were approximately twice as thick as unaged joints. (2) The change of the joint microstructure from a matrix of  $\text{Cu}_6\text{Sn}_5$  with embedded residual Cu-particles for unaged samples to a  $\text{Cu}_3\text{Sn}$  matrix with regions

of  $\text{Cu}_6\text{Sn}_5$  reduces the thermal conductivity of the TLPS material. As shown above, the average thermal conductivity of the unaged samples is 140.2 W/mK. The thermal conductivities of  $\text{Cu}_3\text{Sn}$  and  $\text{Cu}_6\text{Sn}_5$  are 69.8 and 34.2 W/mK, respectively, see Table 6-1. This leads to a lower limit estimate of the thermal conductivity of the aged joint material of 34.2 W/mK. This is approximately one quarter of the thermal conductivity of the unaged joints. Excluding voids and cracks, the joint shown in Figure 6-40 consists to approximately 85% of  $\text{Cu}_3\text{Sn}$  and 15%  $\text{Cu}_6\text{Sn}_5$ . Estimating the resulting thermal conductivity by the rule of mixture yields a thermal conductivity of 64.5 W/mK.

(3) Formation of a network of horizontal voids. The samples showed networks of voids that spanned approximately 75% of the length of the die attach region with some void free-regions within the network, compare Figure 6-40 and Figure 6-41. (4) The detachment of the diode die from the TLPS joint over long ranges.



**Figure 6-41: Cross-section of a Cu-Sn TLPS sample after aging, two failure modes can be identified: (1) horizontal crack formation and (2) die detachment**

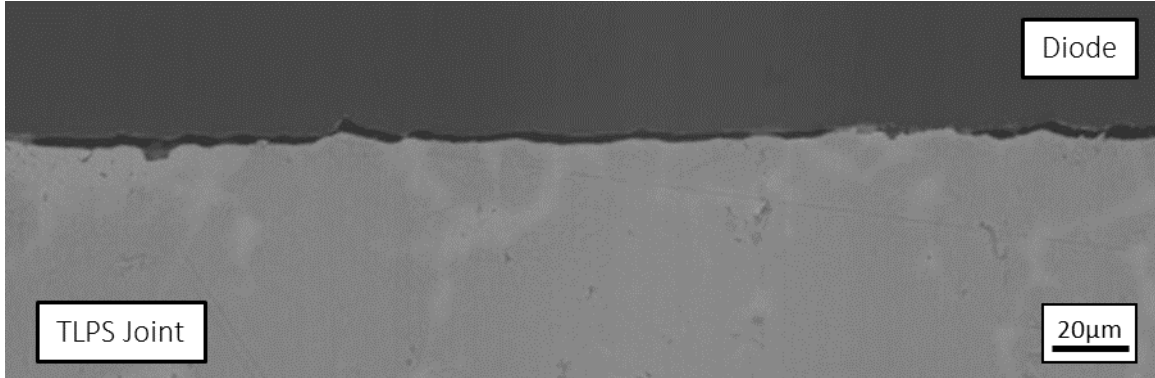


**Figure 6-42: Detachment of the Cu-Sn TLPS joint from the diode die after aging**

The effective reduction of heat path area by void formation and die detachment can be computed by comparing the measured thermal resistance  $R_{th}$ , thermal conductivity  $\kappa$ , and joint thickness  $l$  of unaged and aged samples. The relationship between these parameters is given by

$$R_{th} = \frac{l}{A \kappa} \quad \text{Equation 6-10}$$

with  $R_{th}$ : Thermal Resistance [K/W]  
 $l$ : Joint Thickness [m]  
 $A$ : Effective Cross-sectional Area [m<sup>2</sup>]  
 $\kappa$ : Thermal Conductivity [W/(mK)]

Comparing the experimental results of unaged and aged samples (in the following indicated by index “u” and “a”, respectively) yields:

$$R_{th,u} = \frac{l_u}{A_u \kappa_u} \quad \text{Equation 6-11}$$

and

$$R_{th,a} = \frac{l_a}{A_a \kappa_a} \quad \text{Equation 6-12}$$

Combining Equation 6-11 and Equation 6-12 by dividing the two thermal resistances yields

$$\frac{R_{th,u}}{R_{th,a}} = \frac{l_u A_a \kappa_a}{l_a A_u \kappa_u} \quad \text{Equation 6-13}$$

which can be rewritten as

$$\frac{A_a}{A_u} = \frac{R_{th,u} l_a \kappa_u}{R_{th,a} l_u \kappa_a} \quad \text{Equation 6-14}$$

With  $A_a/A_u$  as the ratio of the effective cross-sectional areas after and before aging.

Computing the ratio for the values determined above yields

$$\frac{A_a}{A_u} = \frac{0.044 \frac{K}{W} 470 \mu m}{1.17 \frac{K}{W}} \frac{140.2 \frac{W}{mK}}{230 \mu m 64.5 \frac{W}{mK}} = 0.167 \quad \text{Equation 6-15}$$

which means that only approximately 16.7% of the original effective area is available for heat conduction after aging. In other words, approximately 5/6 of the joint cross-section is effectively obstructed by horizontal voids and detachment.

### 6.3 Elastic-Plastic Constitutive Behavior

In this section the constitutive properties of TLPS joints are predicted by simulation with the approach outlined in section 6.1 and assessed experimentally with Iosipescu shear test samples.

#### 6.3.1 Simulation

The experimental testing of constitutive properties (elastic, elastic-plastic, creep) is performed with Iosipescu shear samples. Details on the constitutive properties experiments can be found in section 6.3.2. Figure 6-43 shows a top view on a conventional Iosipescu sample with a solder joint sandwiched between two Cu-coupons. The width, length, and thickness of a typical Iosipescu joint are approximately 3mm, 1mm, and 200  $\mu$ m respectively, but limited variation between different batches may occur due to process variability. Ideally, a TLPS joint simulation should include a maximum level of detail

including all metal particles, all voids, and all representative particle and void sizes. Furthermore the entire joint geometry should be modeled. Yet the computational effort for running simulations increases rapidly with complexity and joint models become extremely computationally intense.

The computation of a transient stress-strain curve for a joint with less than 500 metal particles meshed with the fine mesh standard settings of the Ansys Workbench Structural meshing tool, with a total number of approximately 900,000 nodes and 700,000 elements, takes approximately 4 hours on a current generation desktop computer (if computation of creep deformation is not included). A transient structural solution for one stress state in the stress-strain curve requires the computation of at least two stress conditions, more if creep models are included, and at least 20 datapoints should be computed during the transients between the stress conditions. The time to compute this one transient stress state therefore increases to  $4 \times 20 = 80$  hours. This would then have to be performed for three different material systems (Cu-Sn, Ni-Sn, Cu-Ni-Sn) for each geometry and at different temperature levels, with different metal loads contents and void distributions.

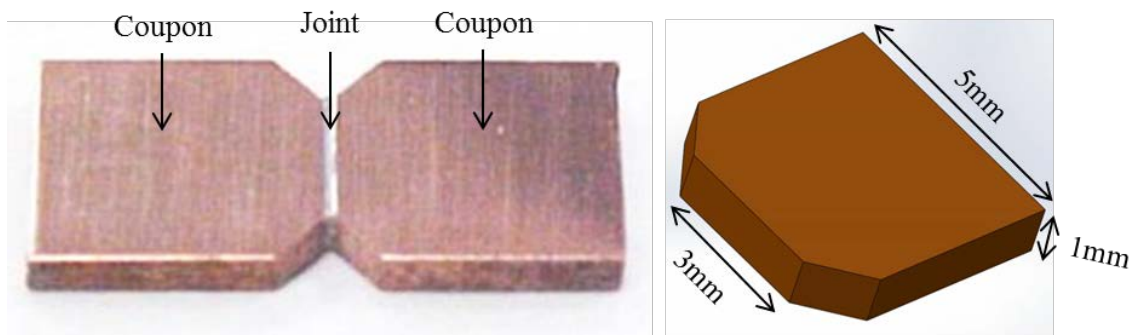


**Figure 6-43: Standard Iosipescu shear test sample: Solder joint between Cu-coupons (left) and coupon dimensions (right)**

If a full Iosipescu joint is modeled as a TLPS interconnect with the above mentioned sizes without voids with comparably large metal particles with a particle radius of  $20 \mu\text{m}$  and a

small metal content of 20 vol.%, the total resulting number of particles is 3581. The mesh of this structure would be approximately one order of magnitude more complex compared to the above example with less than 500 particles. Because the computational effort increases exponentially with mesh complexity, a simulation of a full TLPS joint Iosipescu model is not feasible.

The computational effort furthermore increases as the particle size decreases. The particle volume for spherical particles  $V_{sp}$  is inversely proportional to the third power of the particle radius  $r$ :  $V_{sp} \sim r^3$ . If compared to the above example the particle radius was reduced to 10  $\mu\text{m}$ , the number of metal particles would increase by a factor of 8, increasing computation hardware requirements exponentially.

For the above reasons it is impractical to model and simulate the constitutive properties of Iosipescu samples in full detail. A different approach is followed in this work. An overview of the constitutive properties modeling approach is shown in Figure 6-44. Instead of modeling the entire TLPS interconnect volume as a heterogeneous structure in full detail (all discrete particles, voids, etc.), compound properties are derived for smaller volumes. Heterogeneous material properties are associated to the corresponding elements of this model, load boundary conditions applied, and the corresponding system behavior is recorded. The constitutive behavior of the system is the relationship between the load condition and the corresponding system response.

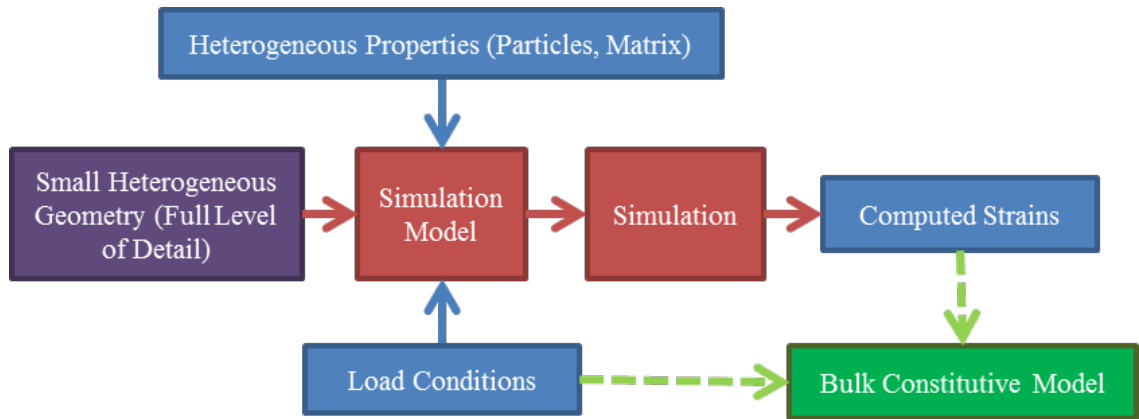


**Figure 6-44: Flow chart of the constitutive properties modeling process**

The heterogeneous microstructure of TLPS samples leads to heterogeneous system behavior to load conditions. As an example, in Cu-Sn TLPS joints, the ductile Cu particles will undergo elastic deformation under stress levels below the yield stress and plastic deformation above it, whereas the brittle Cu-Sn IMCs do not show considerable plastic deformation and deform elastically up to fracture. A Cu-Sn TLPS sample, to which a homogeneous stress above the yield stress of Cu is applied, will undergo purely elastic deformation of its IMCs, but partially elastic, partially plastic deformation in regions with Cu particles. As a consequence, the system reaction to a homogeneous load is heterogeneous. To yield bulk constitutive properties, the heterogeneous material response must be homogenized (i.e. averaged). This does not necessarily mean that a material response must be isotropic, but the anisotropic response to stress conditions must be independent of geometric parameters like scale and must not fluctuate.

In the following, an exemplary set of two shear and tensile stress-strain constitutive properties are derived for a Cu-Sn TLPS, to illustrate the process. Figure 6-45 shows the sample geometry and the distribution of metal particles. The block has a width and height of 200  $\mu\text{m}$ , approximately the thickness of the joint for Iosipescu samples. Its length is 2000  $\mu\text{m}$ . A total of 405 Cu particles with a radius of 20  $\mu\text{m}$  are distributed randomly in

the volume. The rest of the volume is occupied by  $\text{Cu}_6\text{Sn}_5$  IMCs. Two types of load conditions were applied to this sample structure: (1) Shear stress: A uniform force load is applied in x-direction on the top surface of the bar. The top side is free for displacement in x-direction but no displacement in y- and z-direction is allowed. The bottom side is fixed. All other surfaces have no displacement limitations. (2) Tensile/Compressive stress: A uniform force load is applied in x-direction to one end of the bar, which is not restricted from displacement in any direction. The opposite side is restricted from displacement in all directions. All other sides have no displacement restrictions.

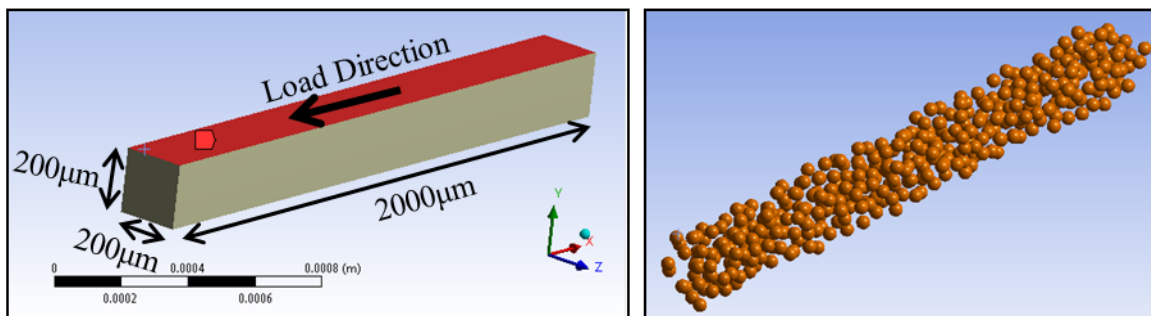


**Figure 6-45: Example geometry for the analysis of constitutive properties: Sample dimension and shear force application (left) and metal particle distribution (right)**

The displacement in x-direction was recorded as output parameter for both load conditions. Figure 6-46 shows the associated contour plots and the absolute values. The relevant areas are indicated by dotted yellow lines in the figure (top side and right side for the shear and tensile load respectively). The minimum, maximum, and average values of displacement in x-direction are displayed in Figure 6-46, bottom ( $\Delta x$  min,  $\Delta x$  max, and  $\Delta x$  avg respectively). The variance is much higher for the shear load compared to the tensile load. As a consequence of this variation of the model response, minimum or maximum values cannot be used as model response parameter. Instead, the deformation values are averaged over all the nodes of the associated surfaces. Figure 6-47 and Figure 6-48 show the applied

load and the resulting strain computed by the averaging method for the shear and tensile load respectively.

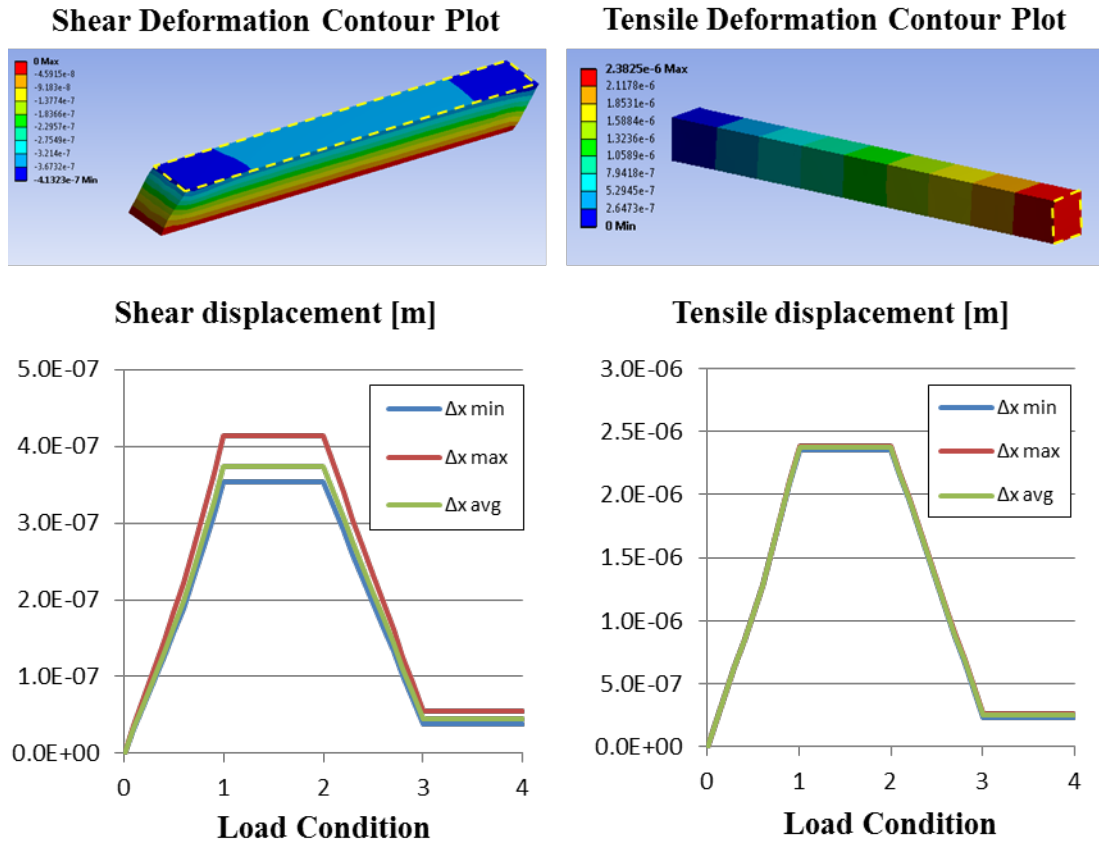


**Figure 6-46: Displacement contour (top) plots in x-direction for shear (left) and tensile (right) load and associated absolute displacements at the load locations (bottom). The tensile load has lower variance**

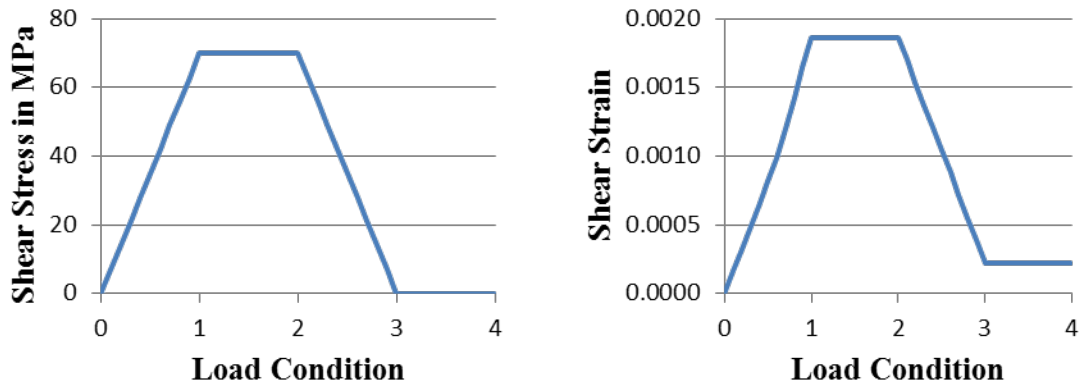


**Figure 6-47: Applied stress and corresponding average strain for the shear strain condition**

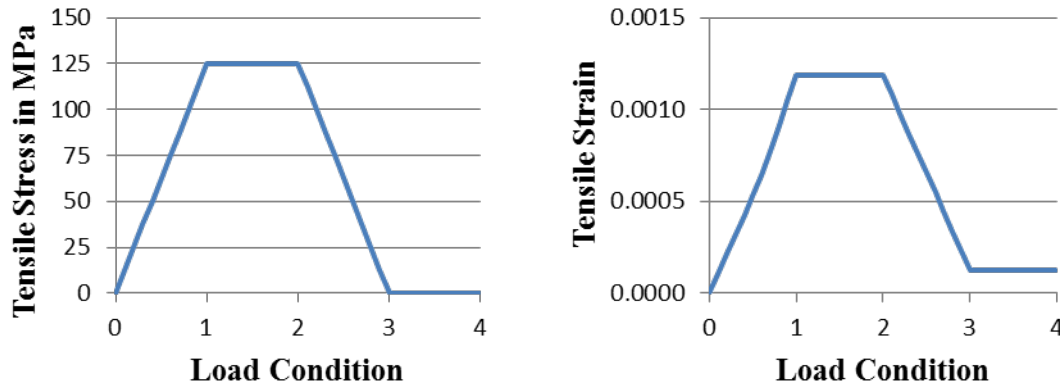


**Figure 6-48: Applied stress and corresponding average strain for the tensile strain condition**

The constitutive properties for the material are the transfer function between the strain behavior and the stress condition that induced it. The bulk constitutive properties are derived by the averaged (homogenized) strains and stresses. Figure 6-49 and Figure 6-50 show the computed stress strain curves for the shear and tensile load condition respectively. Qualitatively these curves show the same bilinear hardening behavior: Initially the strain increases linearly with an increase in stress up to approximately the yield stress of the Cu particles (i.e. the tensile yield stress of 74 MPa), see Figure 6-48. Up to this point the stiffness of the IMC matrix and the stiffness of the metal particles contribute to the total stiffness of the compound. As the stress level increases, more and more metal particles transition from elastic deformation to plastic deformation as their individual stress levels exceed their yield stress. The stress field inside the volume is non-homogeneous. Consequently plastic deformation is not induced at the exact same time in all metal particles, but within a small transition range around 74 MPa.

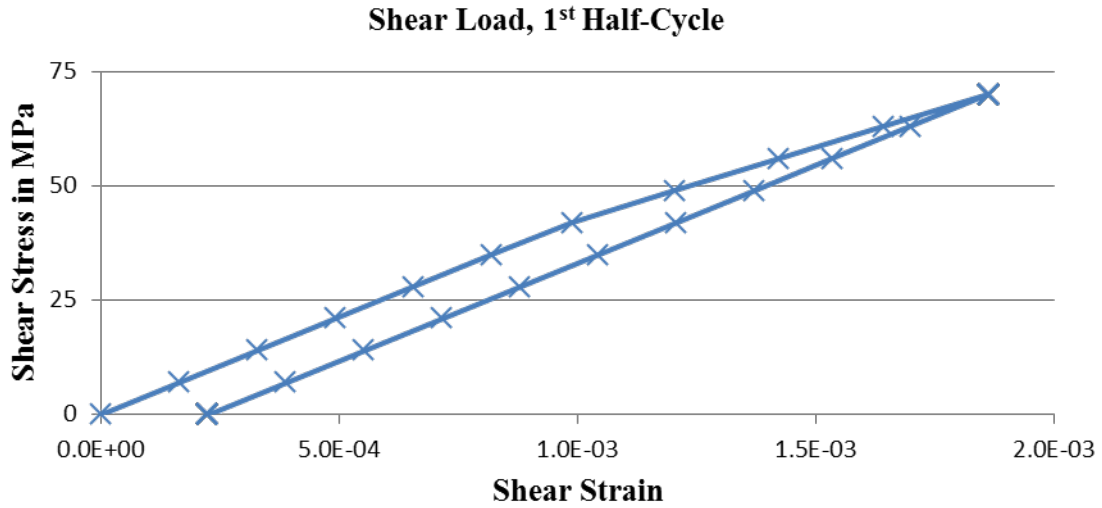


**Figure 6-49: Stress-strain curve computed from the stress and strain curves for the shear load condition, see Figure 6-47**

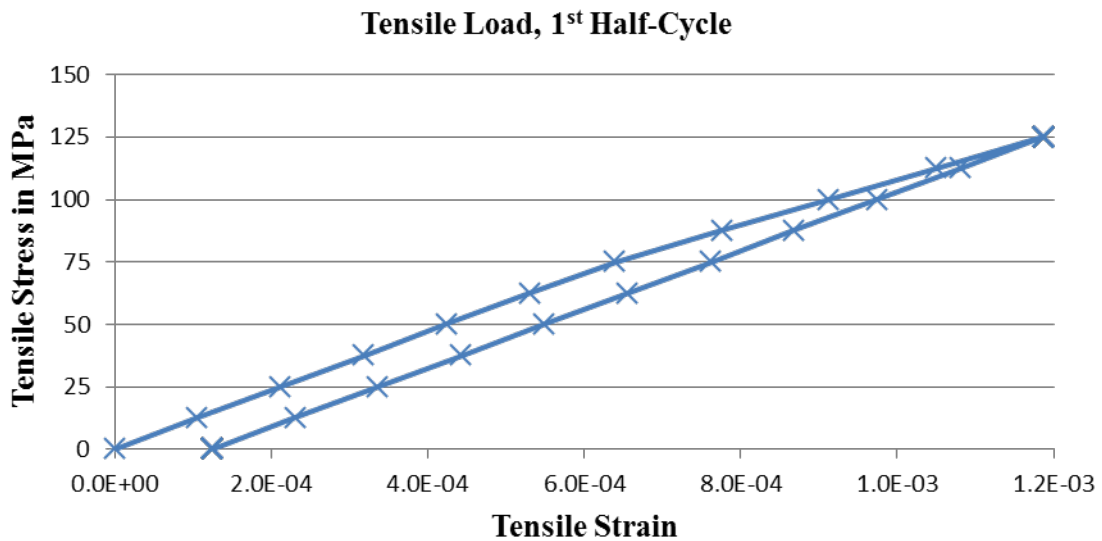


**Figure 6-50: Stress-strain curve computed from the stress and strain curves for the tensile load condition, see Figure 6-48**

As the metal particles transition from elastic deformation behavior to plastic deformation behavior, their contribution to the total stiffness of the compound reduces. After all metal particles undergo yielding, the stiffness of the compound is dominated by the stiffness of the IMC matrix. The incremental increase of strain per incremental increase of stress during this phase is larger than during the phase of purely elastic deformation: the slope of the stress-strain curve after yielding is smaller than before yielding, see Figure 6-51. When the

load is reduced, the strain reduces with the combined stiffness of the elastic moduli of the IMC matrix and the metal particles. The slope of the unloading curve is antiparallel to the slope of the loading curve before yielding. The difference between the strain at the end of the load cycle and the beginning of the load cycle (the two intercepts at the stress level of zero) is the residual plastic strain.

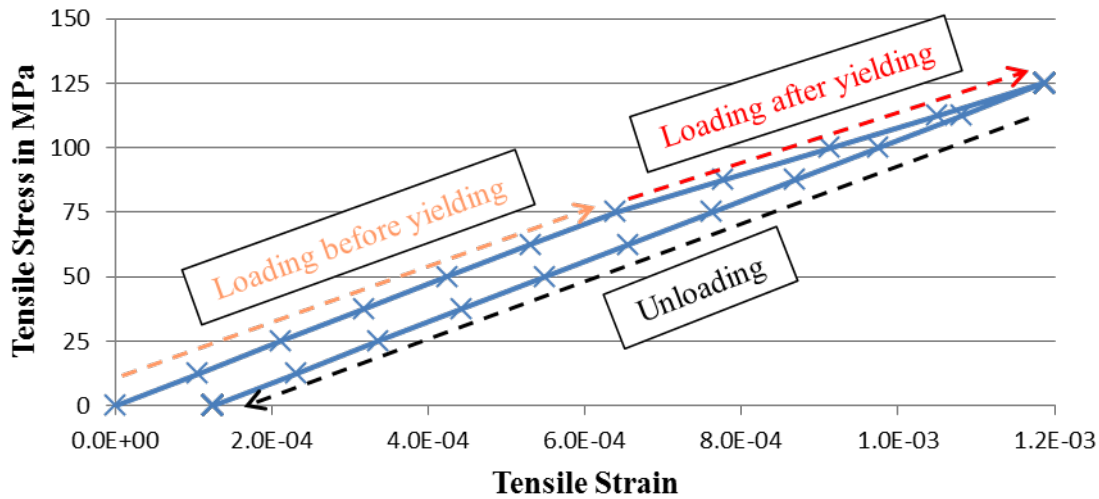


**Figure 6-51: Deformation behavior of a Cu-Cu<sub>6</sub>Sn<sub>5</sub> TLPS compound: Bilinear hardening behavior with high stiffness below yielding and low stiffness after yielding**

In the discussion above, the load condition was as follows: (1) Loading to a maximum load followed by (2) unloading to a zero stress level. This will from now on be referred to as a half load cycle. A full load cycle will in the following be defined as: (1) Loading to a (positive) maximum load, (2) Unloading to a zero stress level, (3) loading to a (negative) minimum load (with the same amplitude as the maximum load), and (4) unloading to a zero stress level. An example for two full tensile stress load cycles is shown in Figure 6-52.

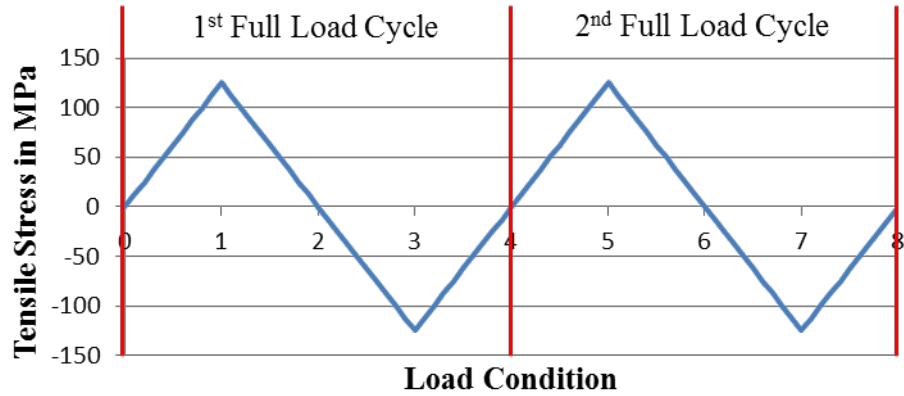


**Figure 6-52: Example for two full tensile load cycle: (1) Loading to a maximum load, (2) Unloading to zero stress level, (3) loading to a minimum load, and (4) Unloading to zero stress level. The second cycle is identical with the first cycle and includes time steps 5 - 8**

Kinematic hardening was assumed as primary hardening mechanism. Figure 6-53 (left) shows the strain response to the 1<sup>st</sup> full load cycle. The upper right quadrant of the left part of Figure 6-53 is identical with the stress-strain curve shown in Figure 6-50. The difference is that after Unloading to zero from 125 MPa, the load continues to reduce to a minimum stress level of -125 MPa. It can be seen that a change of gradient occurs at a load level of approximately 25 MPa from a steeper slope to a more gradual slope. This can be explained by the hardening of the material. The radius of the yield surface remains constant for kinematic hardening, but the location of its center point is shifting. This is illustrated in Figure 6-54.

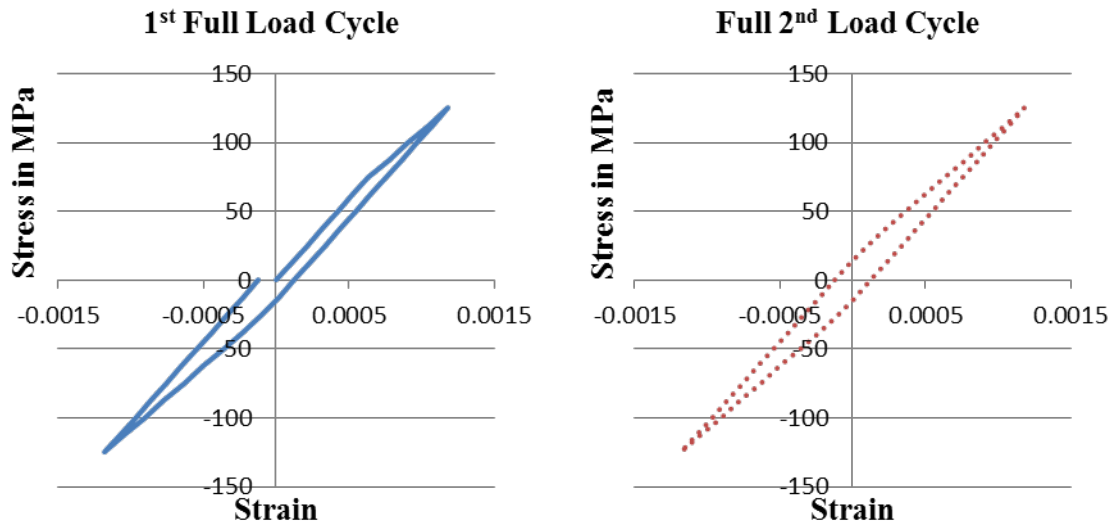


Figure 6-53: Stress-strain curves for the 1<sup>st</sup> (left) and 2<sup>nd</sup> (right) load cycles shown in Figure 6-52. Kinematic hardening behavior was followed

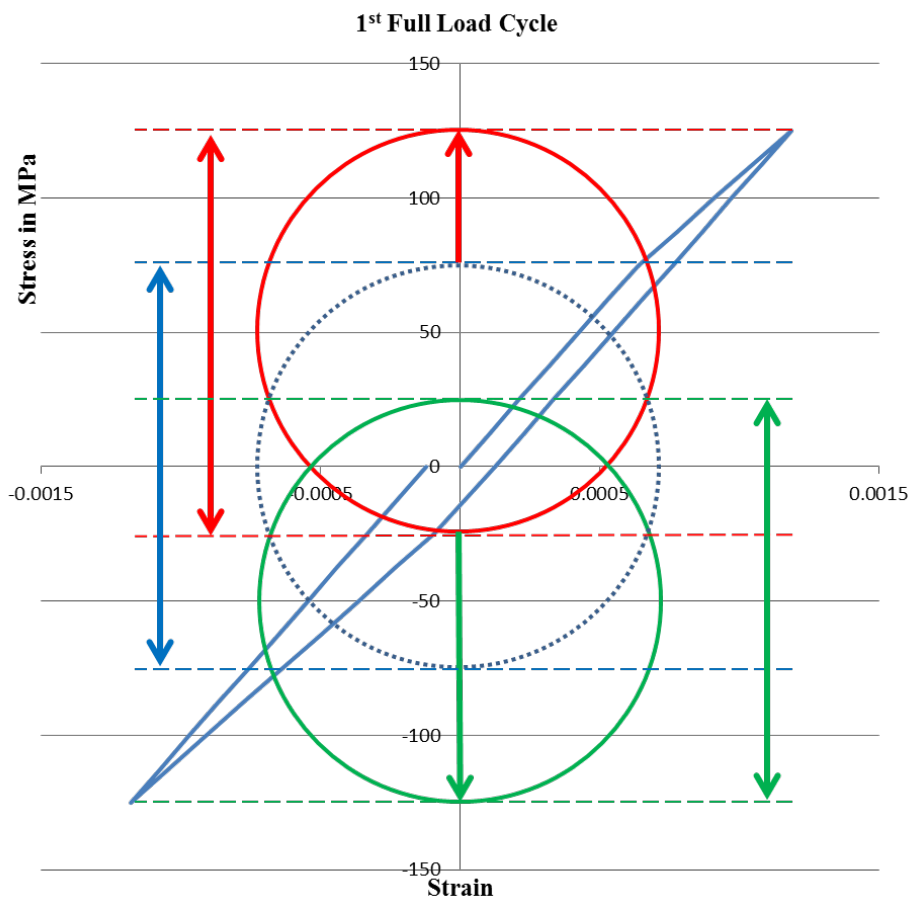


Figure 6-54: Kinematic hardening during the 1<sup>st</sup> full load cycle: Original yield surface (dotted blue), yield surface after increasing the load to +125 MPa (red), and after decreasing the load to -125 MPa (green). Note that the load is uniaxial along the vertical direction of this figure

It is assumed that initially the center point for the yield surface is at a stress level of zero. For uniaxial load (which is the case under ideal tension), the yield stress levels are initially  $\pm 74$  MPa, compare the dotted red circle of Figure 6-54. As the stress level increases beyond 74 MPa, the yield surface shifts with the maximum load, the Cu is deforming plastically and the slope of the stress-strain curve decreases. At the final load level of 125 MPa, the yield surface has shifted 51 MPa into the load direction (red single-ended arrow in Figure 6-54). The new uniaxial yield stress levels are 125 MPa and -23 MPa (red circle in Figure 6-54). As the load is reduced, the material deforms with a steep slope until the stress level hits the new yield stress level of -23 MPa. The yield surface starts shifting towards lower stress levels. The slope of the stress-strain curve becomes less steep. This continues until the minimum load of -125 MPa is reached. At this point the new yield stresses are -125 MPa and 23 MPa, see green circle in Figure 6-54. As the unloading towards zero stress occurs, the stress level does not intersect with these yield stress limits. The material unstrains elastically with a steep slope.

If another load cycle is initiated, the load increases again as the yield circle moves towards the location of the red circle. For the negative load it moves to the location of the green circle again. The material has reached a hysteresis condition. The resulting stress-strain curve is shown in Figure 6-53 (right). For an isotropic hardening condition the radius of the yield surface would increase and the center point remains constant. After the hardening of the first loading step, the yield stresses would be  $\pm 125$  MPa. Real metals deform with a combination of isotropic and kinematic hardening. Generally, pure kinematic hardening is better suited to describe the deformation behavior of Cu and Ni than pure isotropic hardening.

### 6.3.2 Experiments

The samples used for assessing the constitutive behavior of TLPS joints are Iosipescu shear samples, see Figure 6-55. They provide multiple advantages compared to other material analysis sample geometries. (1) The thickness of the Iosepescu joint region is similar to the length scales of interconnects used in electronic products. Material properties can vary with length scales. Similarity in size ensure that the properties determined experimentally are in agreement with the properties of real interconnects. (2) The arrangement of notched samples with limited meniscus regions around the joint provides almost ideal shear stress throughout the entire joint region. (3) Manufacturing of bulk TLPS samples (> few mm of length in multiple directions) by the two-step approach introduced in chapter 4.2 can lead to different results from the conventional TLPS joining process for electronic interconnects because of extensive particle rearrangement, variations in flux activation and evaporation behavior because of increased thermal mass, etc.

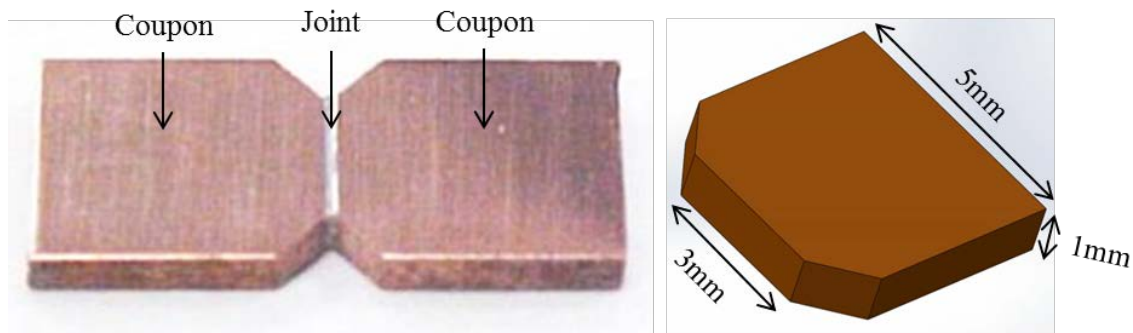


**Figure 6-55: Standard Iosipescu shear test sample: Solder joint between Cu-coupons (left) and coupon dimensions (right)**

The standard Iosipescu samples used for electronic interconnect analyses at CALCE consist of two Cu-coupons with the joint material sandwiched between a necked geometry, compare Figure 6-55 (right). During testing, displacement is applied between the Cu-coupons in the direction of the long dimension of the joint, creating almost ideal shear

stresses in the sample. Conventional solder interconnect technologies such as Sn3.5Ag, Pb3Sn, or Sn37Pb alloys have lower elastic moduli and yield strengths than Cu, see Table 6-9, Figure 6-56 and Figure 6-57. As a consequence, for these samples the Iosepescu joint material absorbs the majority of the displacement that is applied during testing.

**Table 6-9: Mechanical properties of select electronic materials [122] [124] [125] [126] [127] [128]**

	Cu	Ni	Cu <sub>6</sub> Sn <sub>5</sub>	Cu <sub>3</sub> Sn	Ni <sub>3</sub> Sn <sub>4</sub>	Mo	W	Sn3.5Ag	Pb3Sn	Sn37Pb
Elastic Modulus [GPa]	127.7	210	85.56	108.3	133.3	340	340	26.2	19	15.7
Yield Strength [MPa]	74	86	n/a	n/a	n/a	415	550	22.5	7.8	27.2

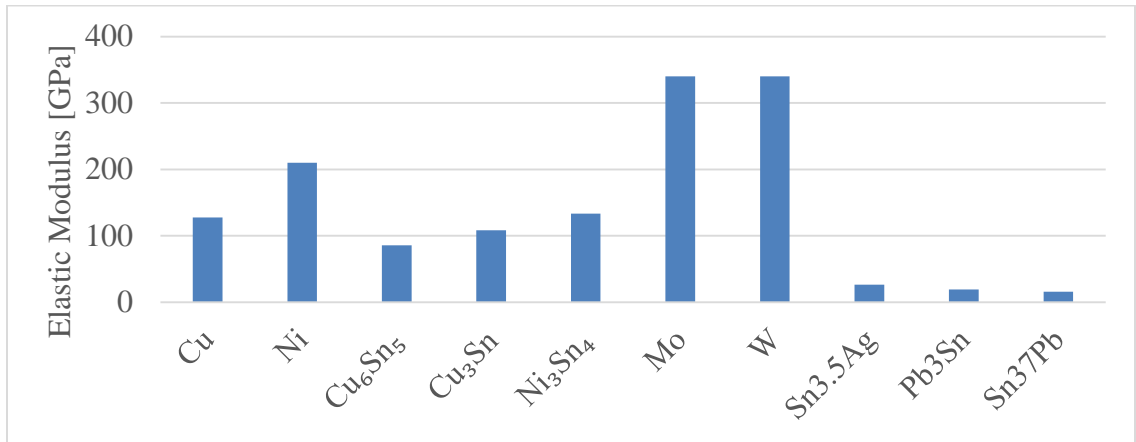


**Figure 6-56: Elastic modulus of select electronic materials**

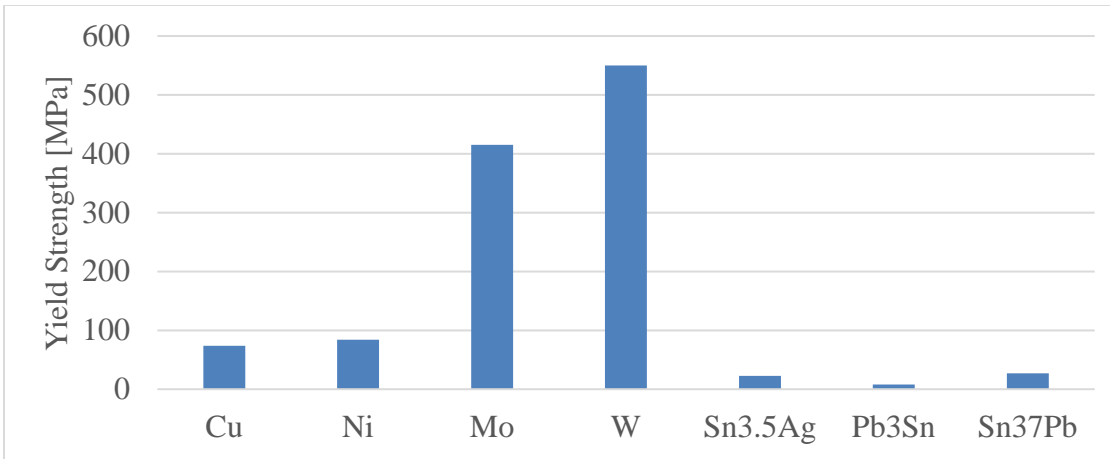


**Figure 6-57: Yield strength of select electronic materials**

In contrast, the TLPS joints consist of materials with similar or higher elastic moduli than Cu (Cu, Ni, IMCs) and equally high or higher yield strengths<sup>3</sup>. In this case, when a displacement is applied to the Iosipescu sample, most of the deformation occurs in the coupons, not in the joint. In consequence, Iosipescu samples with Cu-coupons cannot be used to record and document the constitutive behavior of TLPS joints. Alternative coupons consisting of materials with high elastic modulus and high yield strength are required to study the constitutive behavior of TLPS interconnects. Mo and W have the potential to be used as substitute materials for Cu in these test, compare Table 6-9, Figure 6-56 and Figure 6-57.

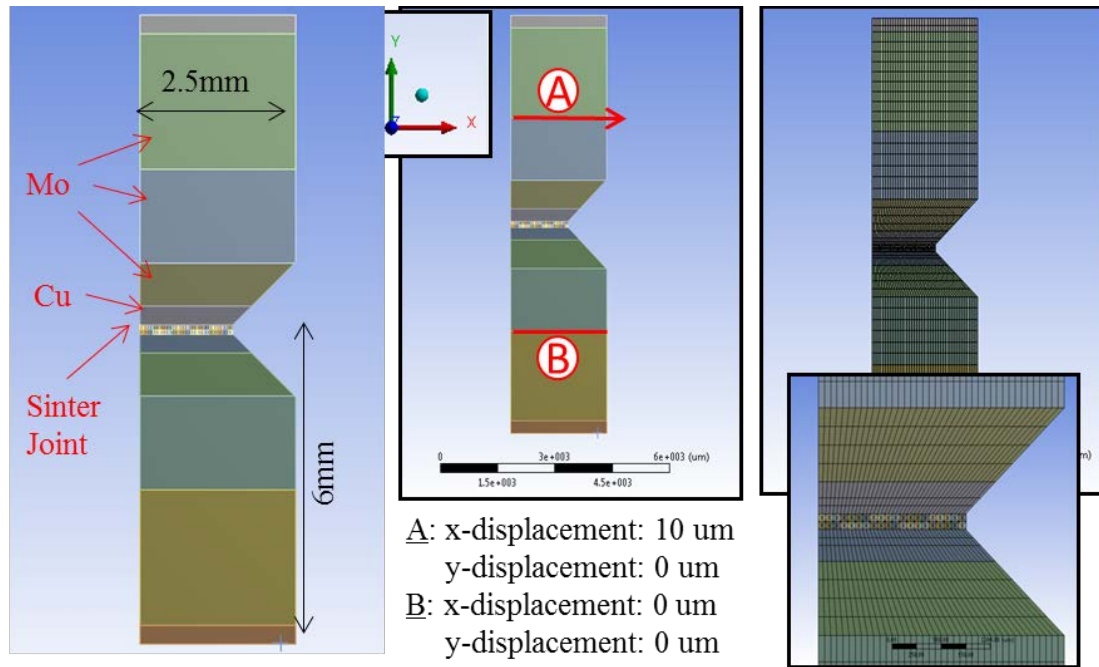
Detrimental to their use as coupon materials is their low wettability by Sn, which renders them practically unsolderable. Two options to manufacture solderable Mo and W coupons exist: (1) procuring Ni-Mo-Ni, Cu-W-Cu and Cu-W-Cu laminate structures or (2) plate Mo/W coupons with Ni/Cu layers. The total coupon length is 5 mm. Commercially available laminate structures are generally only available in specific thickness ratios (e.g.

---

<sup>3</sup> IMCs show predominantly brittle behavior without significant plastic deformation before fracture

1:3:1 or 1:5:1), which leads to thick (relative to the TLPS joint thickness, e.g. 300  $\mu\text{m}$ ) Cu- or Ni-layers at the joint interfaces. Structural simulations were performed to assess the influence of these layers on the stress-strain response of Iosipescu samples.

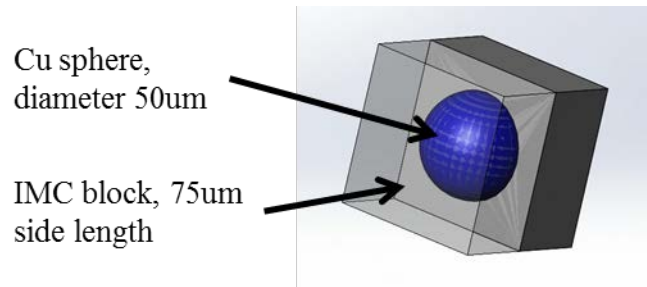
Figure 6-58 shows the half-model of an Iosipescu sample used to predict the stress-strain behavior of the sample. The coupons consist of Cu-Mo-Cu laminates with Cu-layer thicknesses of 300  $\mu\text{m}$ , see Figure 6-58 (left). The center of the bottom coupon is restricted from displacement in x- and y-direction. The center of the top coupon is restricted in y-direction, but has a fixed replacement in x-direction of 10  $\mu\text{m}$ , see Figure 6-58 (center). Figure 6-58 (right) provides an overview and details on the mesh of the coupons and the joint region.



**Figure 6-58: Half-model of a Iosepescu sample with TLPS joint and Mo-coupons with laminated Cu metallization. Overall structure (left), load condition (center), and mesh (right)**

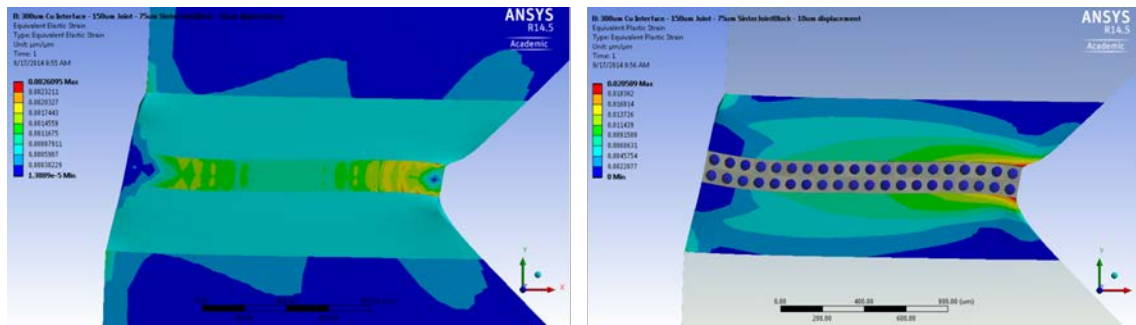
Figure 6-59 shows a detailed view on a unit cell of the simplified TLPS joint. It consists of a Cu sphere with a diameter of 50  $\mu\text{m}$  embedded in the center of a  $\text{Cu}_6\text{Sn}_5$  IMC cube with

side lengths of 75  $\mu\text{m}$ . An additional simulation model in which the Cu-Mo-Cu laminate structure was replaced with a Mo-only structure of identical geometry was designed to contrast the influence of Cu-metallization layer thickness on the stress-strain response of Iosipescu samples.



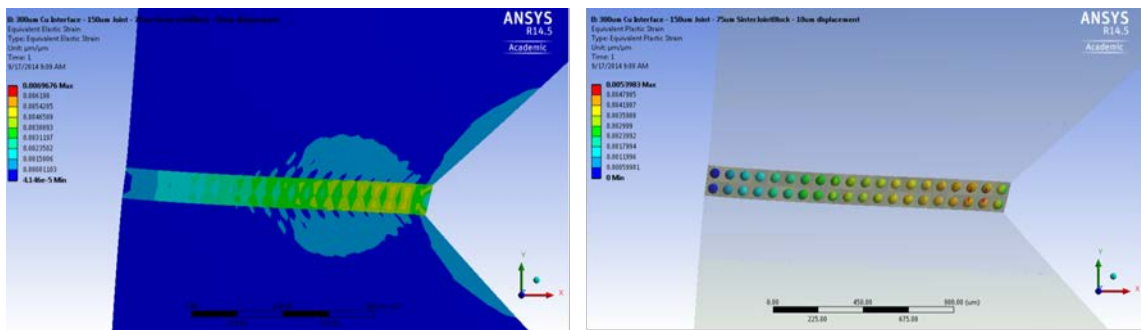
**Figure 6-59: Semi-transparent view on a Cu-Cu<sub>6</sub>Sn<sub>5</sub> unit cell**

Figure 6-60 shows the elastic (left) and plastic (right) strains near the joint region of the Cu-Mo-Cu coupon geometry upon loading. The maximum strains are 0.0026 and 0.0206, respectively. The highest elastic strain occurs in the IMC regions. Plastic strain occurs predominately in the Cu-layer of the Cu-Mo-Cu laminate close to the TLPS joint. No plastic deformation occurs in the Cu-particles of the TLPS joint. Additionally, the maximum strain in the Cu-layers is approximately 8 times that of the maximum strain in the TLPS joint. This proves that Iosipescu samples with laminated structures, like Cu-coupons, cannot be used to assess the constitutive behavior of the TLPS materials.



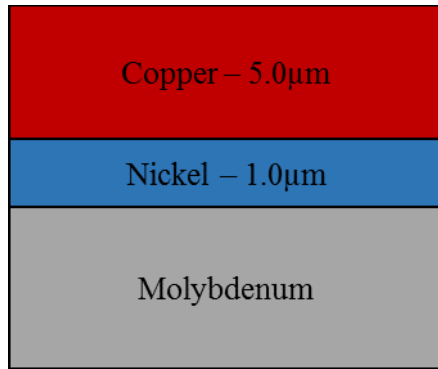
**Figure 6-60: Elastic (left) and plastic (right) strain near the joint region for the laminated Cu-Mo-Cu coupon shown in Figure 6-58**

Figure 6-61 shows the elastic (left) and plastic (right) strains near the joint region of the Mo-only coupon geometry upon loading. The maximum strains are 0.0070 and 0.0054, respectively. Similar to the Cu-Mo-Cu case, the highest elastic strain occurs in the IMC regions, yet the elastic strains in the Mo-coupon are significantly lower than the elastic strains in the Cu-layer of the Cu-Mo-Cu case. Additionally, for the Mo-coupon simulation, the highest plastic strain occurs within the Cu-particles in the TLPS joint. In combination, the majority of the sample displacement occurs in the joint region. This shows that Mo-coupons with thin or completely consumed metallization layers can be used to characterize the stress-strain behavior of TLPS sinter joints.



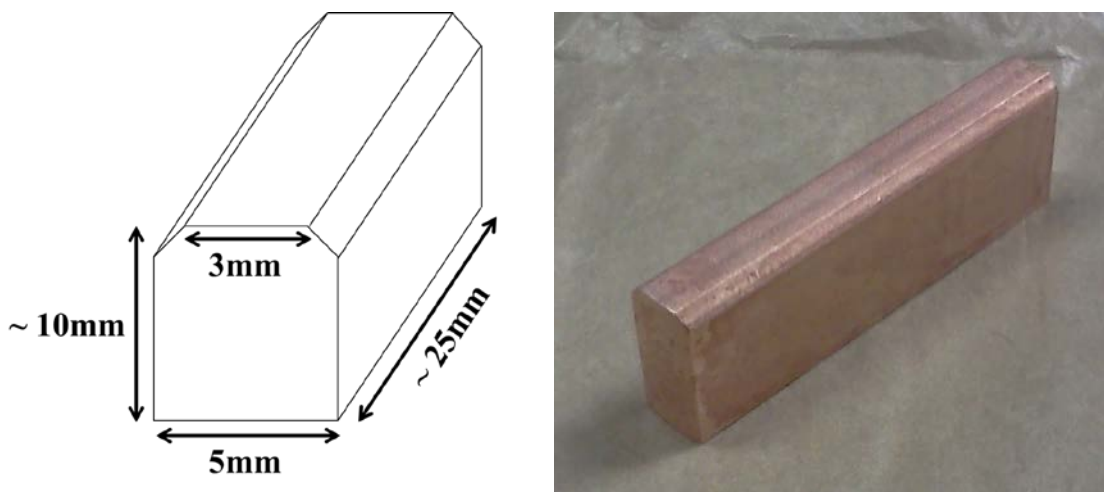
**Figure 6-61: Elastic (left) and plastic (right) strain near the joint region for a sample with Mo-only coupons**

Figure 6-62 shows the metallization layers applied to the surface of the Mo-coupons for Cu-Sn TLPS joint assessment. The thickness of the Cu-layer is 5.0  $\mu\text{m}$ . During sintering, this layer will be mostly consumed and the residual low yield strength metal layer reduces to a minimum. A Ni-layer with a thickness of 5.0  $\mu\text{m}$  is used as a buffer and adhesion layer between the Mo and the Cu metallization. The purpose of this layer is twofold: (1) Ni has better adhesion to Mo than Cu or Cu-Sn IMCs, which helps prevent the delamination of the TLPS joint from the Mo-coupon, and (2) during processing, Cu is converted to Cu-Sn IMCs. These IMCs have limited adhesion capability from the Mo-surface which could lead to loss of adhesion for the joint from the Mo-surface during sintering.



**Figure 6-62: Metallization layers of the Mo-coupons for the Cu-Sn Iosipescu samples**

An unplated Mo-bar was cut out of a Mo-rod by Wire Electrical Discharge Machining (Wire EDM). A sketch and the dimensions of the bar are shown in Figure 6-63 (left). Figure 6-63 (right) shows a photograph of the metallized Mo-bar (right) after electroplating with Ni and Cu.



**Figure 6-63: Sketch of the EDM-cut Mo-bar with dimensions (left) and picture of the Cu-plated bar (right)**

After electroplating, the bar was sliced to coupons with a thickness of 1mm. Figure 6-64 shows a low magnification cross-section image of a sliced Mo-coupon. Considerable roughness is present at the top surface, which will be used as joint surface for the TLPS joint. Besides long-distance (>1mm scale) roughness, the coupon also showed smaller, local roughness, see Figure 6-65. The roughness originates from the Mo-bar, not from the

plating. The metallization is continuous, but follows the surface morphology of the Mo. Some voids are visible at regions of extensive roughness, see Figure 6-65 (left). EDS-analyses of the metallization showed that the Mo, Ni, and Cu, are easily discernible and that the thickness of the Ni and Cu layer are close to the expected values of 1 and 5  $\mu\text{m}$ , see Figure 6-66.

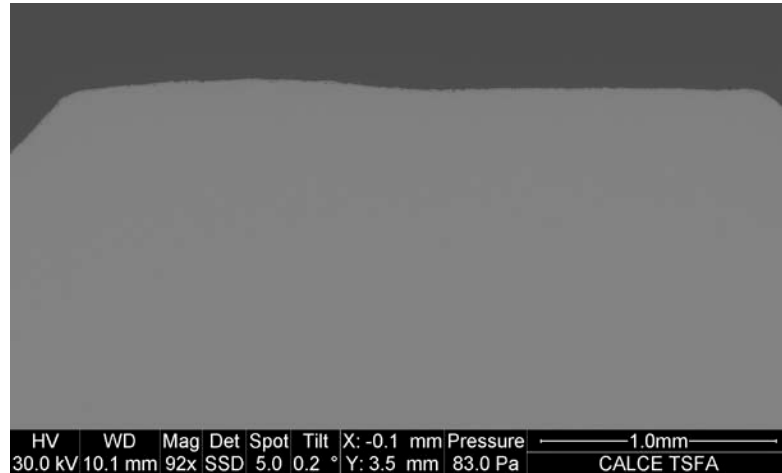


**Figure 6-64: Cross-section of a plated Mo-Coupon. Considerable roughness is visible on the top surface**

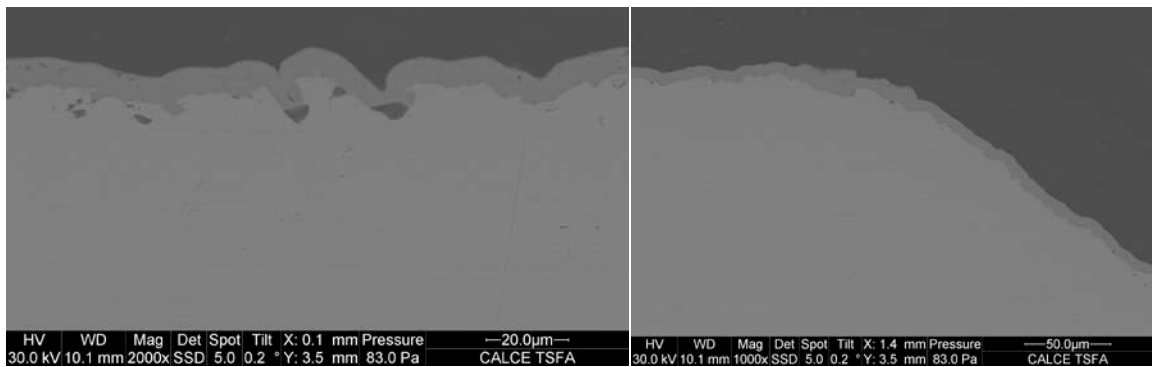


**Figure 6-65: Surface morphology of the plated Mo-coupons**

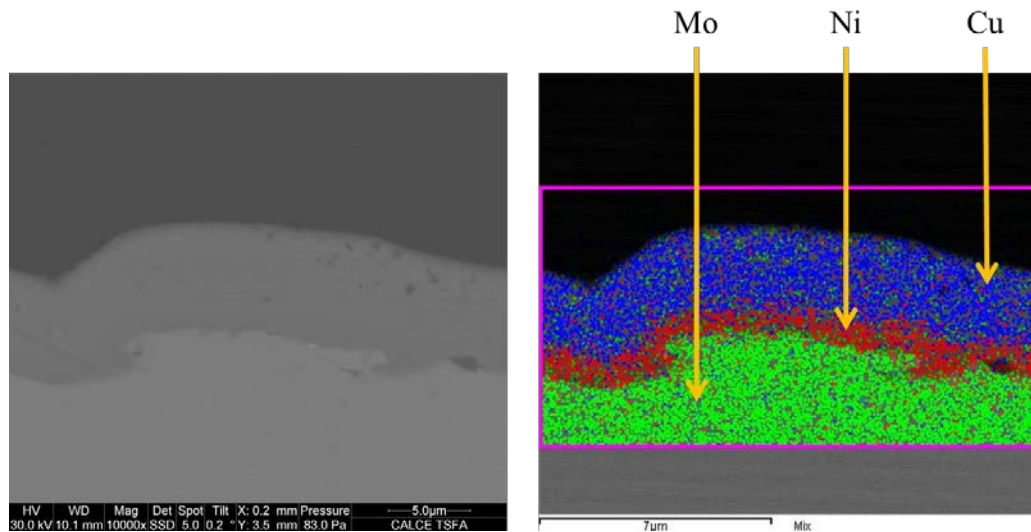


**Figure 6-66: EDS analysis of the coupon metallization**

A sinter fixture for TLPS Iosipescu samples was designed, see Figure 6-67. A top view of the Iosipescu sinter fixture can be seen in Figure 6-68. The process flow of the sintering process is as follows (compare Figure 6-69): (1) sinter paste is deposited on the joint surface of the 1<sup>st</sup> Iosipescu coupon, (2) the 1<sup>st</sup> Iosipescu coupon is placed in position by pushing it towards the positioning wedge at the thermocouple holding clip side of the fixture, (3) the set screw for the 1<sup>st</sup> Iosipescu coupon is tightened to fix it in its position, (4) the 2<sup>nd</sup> Iosipescu coupons is pushed towards the positioning wedge, (5) the positioning bar is inserted, (6) the set screw for the 2<sup>nd</sup> Iosipescu coupon is tightened to fix it in its position, and (7), the set screw for the position bar is tightened to fix it in its position. Afterwards, solder paste is deposited on the top if the sinter paste within the joint region. The Iosipescu fixture is placed on the sinter fixture, and the sinter process initiated. The fixture wedge and the alignment rod ensure consistency of the joint thickness between different samples.

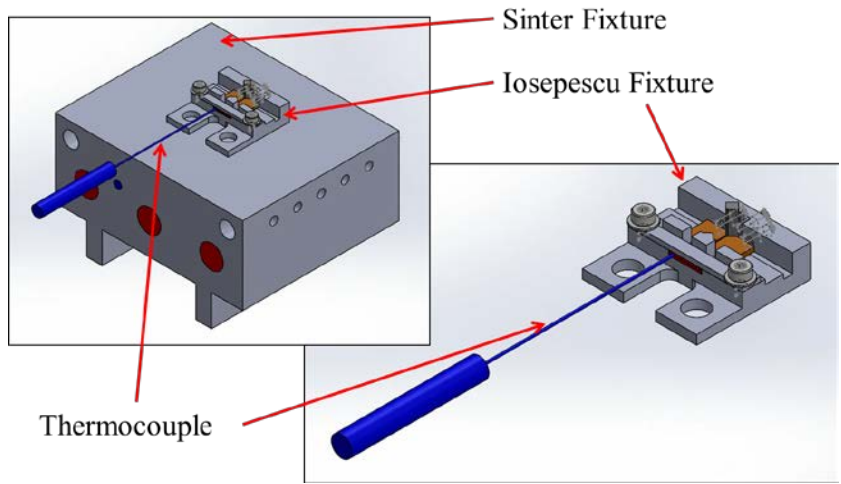


**Figure 6-67: Isometric view on the Iosipescu sinter fixture individually (right) and on the sinter fixture (left)**

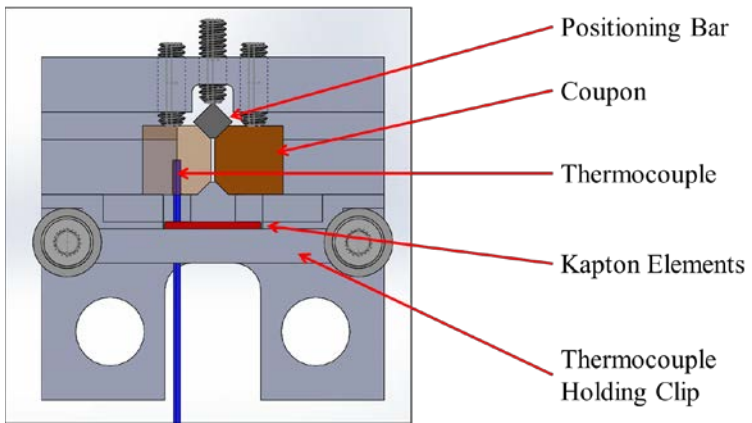


**Figure 6-68: Top view on the Iosipescu sinter fixture**

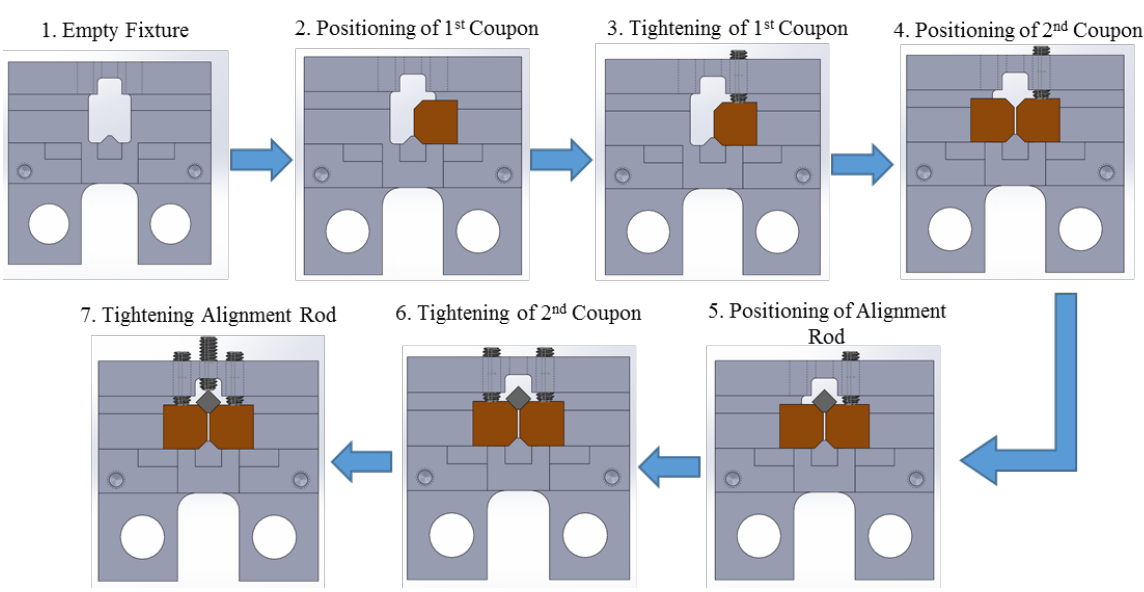


**Figure 6-69: Process flow for the positioning of the Iosipescu coupons in the fixture**

Figure 6-70 and Figure 6-71 show top-views and side-views of a Cu-Sn Iosipescu sample after sintering, respectively. The two coupons (indicated by orange dashed lines) are joined by a solid TLPS joint. After melting, the solder spreads, wets the surfaces of the Cu-particle and the coupon metallization, and infiltrates the sinter paste region. Rearrangement of sinter paste and spreading of the solder along the coupon flanks are prevented by the presence of the fixture wedge and the alignment rod. After spreading, sintering and growth of IMCs occurs. Small regions of unconsumed solder remain on the top and bottom sides of the sinter joint (indicated by dashed green lines) after process completion. These regions need to be carefully ground off after removing the sample from the Iosipescu sinter fixture. If they were present during the shear tests, the stress boundary conditions at the joint edges would become non-homogeneous.

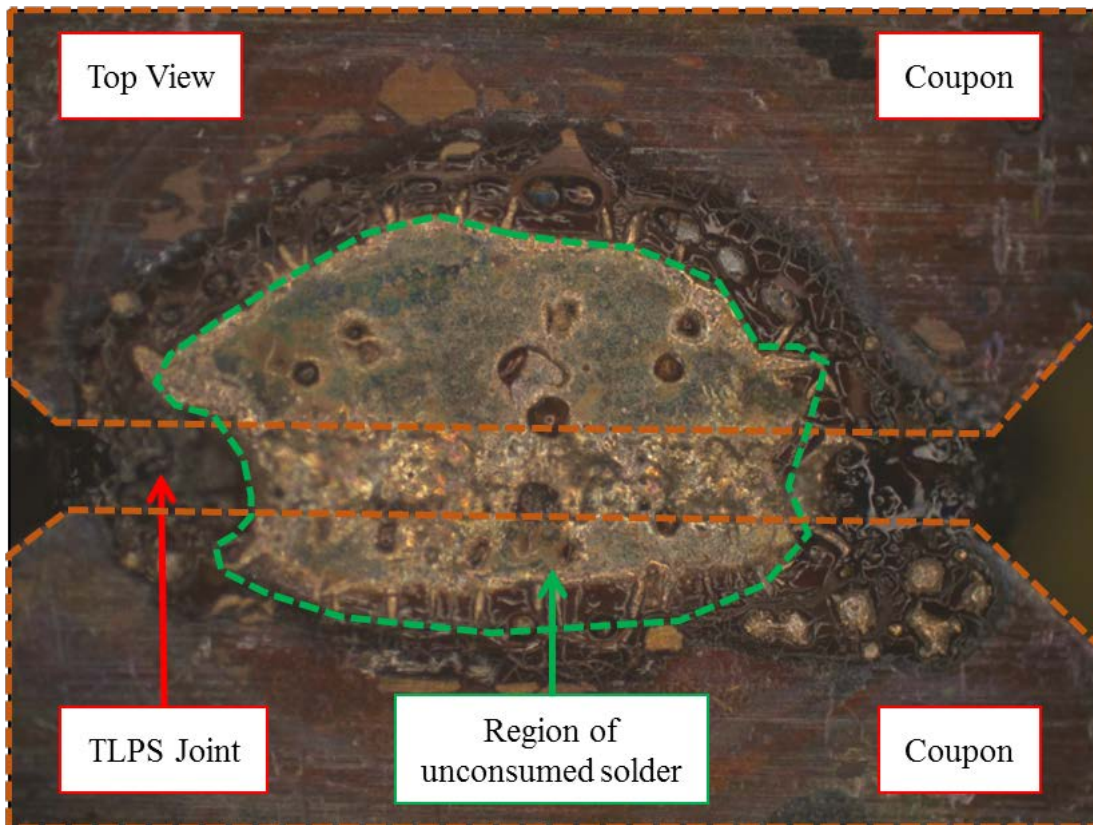


**Figure 6-70: Top view on a Cu-Sn TLPS Iosipescu sample**

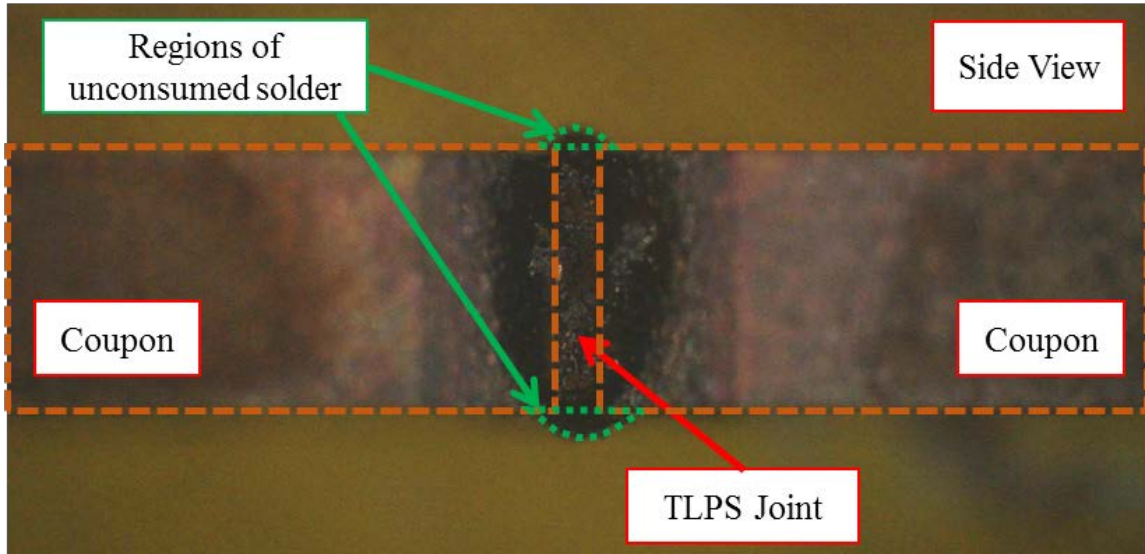


**Figure 6-71: Side view on the Cu-Sn TLPS Iosipescu sample show in Figure 6-70**

Figure 6-72 shows an SEM cross-sectional image of a Cu-Sn TLPS joint between two Mo-coupons with Ni/Cu metallization layers after sintering and removal of the regions of unconsumed solder. The extent of meniscus formation is small, see Figure 6-72. Figure 6-73 shows an optical microscopy image of a different Cu-Sn joint with Mo-coupons. Figure 6-73 (top) and Figure 6-73 (bottom) show the front-side and back-side of the sample. A large void is present in the center of the front-side of the TLPS joint. Voids of this size can alter the mechanical properties of the joint significantly compared to unvoided joints. Inspection of Iosipescu samples is necessary, to sort out joint outliers with unusual characteristics (i.e. unusual wetting behavior, particle distribution, or extensive voiding). Such joints were not assessed in the constitutive studies detailed below. In most regions, the Ni-layer is perfectly wetted after sintering, but some locations show a broken Ni-layer with void formation at the interface between the Mo-coupon and the TLPS joint, see Figure 6-74.

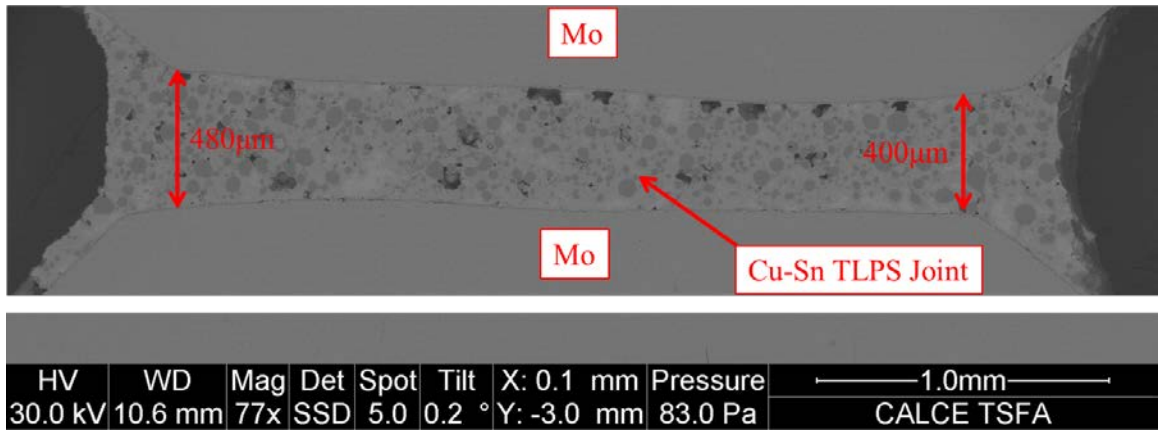


Figure 6-72: SEM view of a Cu-Sn Iosipescu shear test sample

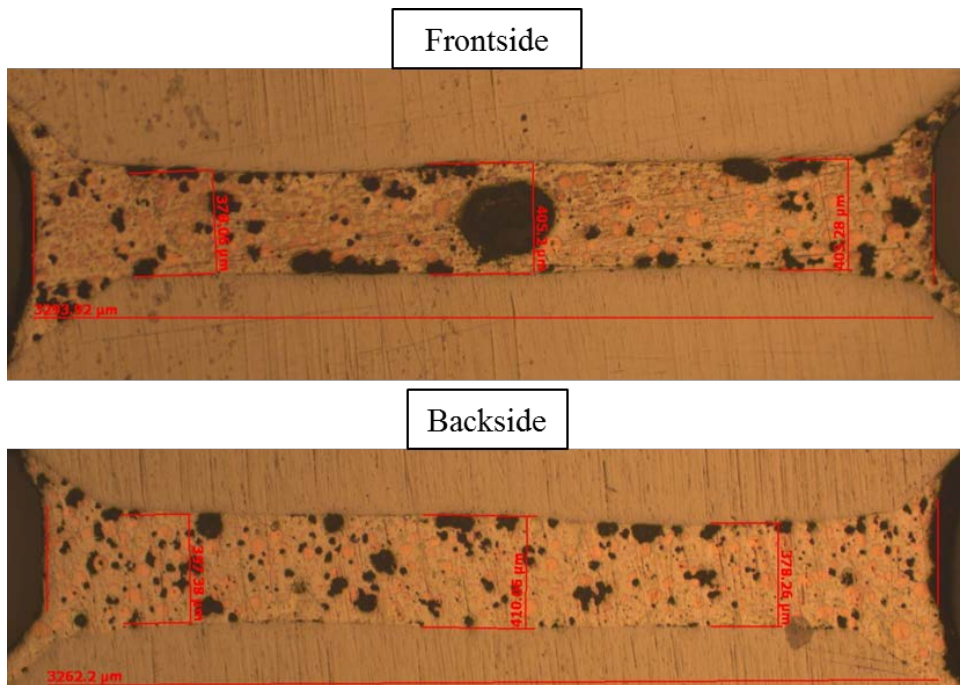
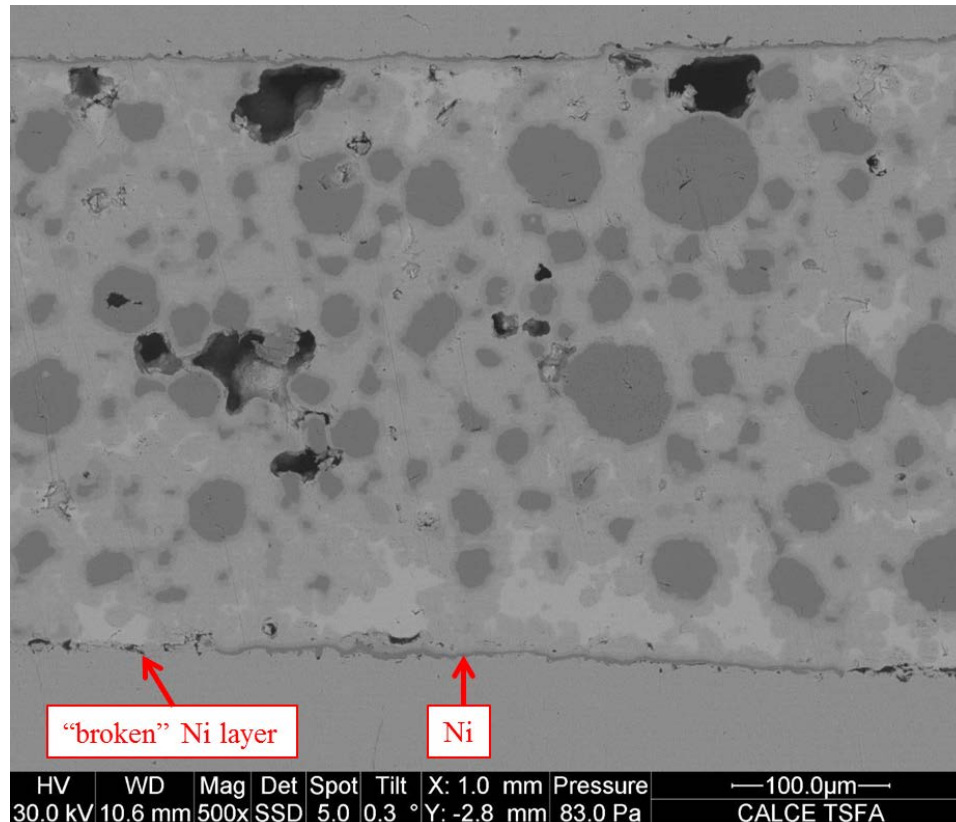


Figure 6-73: Optical microscopy image of a Cu-Sn Iosipescu shear test sample. Considerable voiding is visible on the sample frontside



**Figure 6-74: Adhesion of the TLPS joint to the metallization: Locally broken Ni layer indicates flaws in the metallization layer due to coupon roughness**

Shear tests were performed with the Iosipescu samples on the CALCE thermo-mechanical-microstructural (TMM) test apparatus. The TMM can provide a sub-micrometer displacement in shear direction on one coupon while the other coupon is fixed in position. Displacement is used as control parameter and the load level at the load cell recorded simultaneously. The displacement, load, and joint geometry information are subsequently used to compute the constitutive behavior (e.g. stress-strain curves) for the specific test condition<sup>4</sup>.

Figure 6-75 shows the stress-strain curve of a Cu-Sn TLPS joint between two Ni/Cu-plated Mo-coupons. To ensure consistency with the simulations, compare section 6.3.1, a cyclic

---

<sup>4</sup> The width, height, and length of the TLPS joints were measured by optical microscopy

displacement of  $\pm 10 \mu\text{m}$  was applied to the center of the Mo-coupons. The dark blue curves show the stress-strain correlation during multiple cycles. Red and bright blue curves indicate the simplified joint behavior.

During the first cycle, the sample is displaced from its original zero stress and zero displacement state. During the initial displacement in negative direction, the slope of the stress-strain curve is steep (high stiffness). During later stages of the displacement in negative direction, the slope of the stress-strain curve is less steep (low stiffness). As the displacement direction is reversed, the curve is, again, initially steep, and later becomes less steep. After the first load cycle, the stresses and strains stabilize on a hysteresis loop.

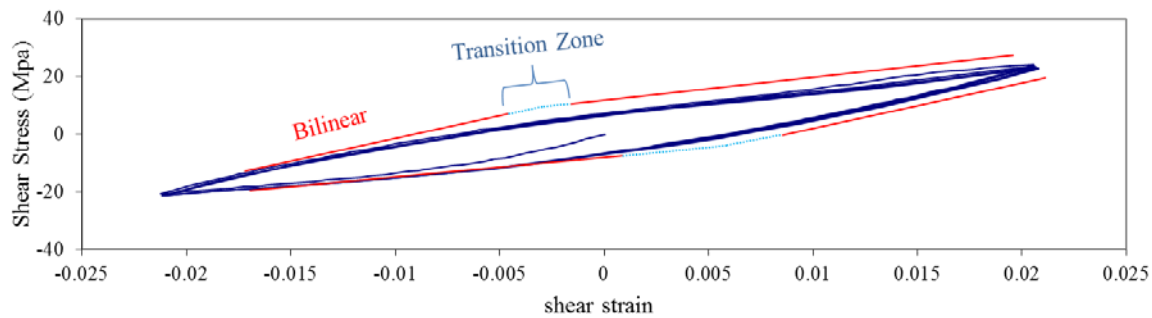


**Figure 6-75: Shear stress-strain curve for a Cu-Sn TLPS sample cyclically displaced by  $\pm 10 \mu\text{m}$**

The constitutive behavior is quantitatively identical with the behavior predicted by the simulations in section 6.3.1. The stress-strain hysteresis loop shows a bilinear behavior (illustrated by the four red lines framing the hysteresis loops in Figure 6-75) with a transition zone (bright blue). The simulations predicted this behavior, too, compare section 6.3.1.

This shows that qualitatively, the developed TLPS joint modeling approach predicts the constitutive properties very well. Considering the dispersed voids in the joint the stress level at which the Cu begins yielding is close to the predicted values. Yet one significant difference exists compared to the results from the simulations: the strain levels in the

experiments are approximately one order of magnitude higher than those predicted (compare Figure 6-53 and Figure 6-75). Upon further investigation, it was found that this discrepancy also exists for tests performed by other researchers on different types of materials (e.g. SAC solders between Cu coupons) tested on the TMM.

Considering the relatively large voids in the joint, the stress level at which the Cu begins yielding is approximately where predicted. But one significant difference exists compared to the results from the simulations: the strain levels in the experiments are approximately one order of magnitude higher than those predicted (compare Figure 6-51 and Figure 6-75). This discrepancy also exists for research performed by other researchers on different types of materials (e.g. SAC solders between Cu coupons) tested on the TMM. Multiple interacting influences were identified as sources for this behavior, and the TMM currently undergoes major revision. For that reason, a quantitative verification of the simulated TLPS joint constitutive behavior cannot be given at this point. Yet, it has been proven with this work, that qualitatively, the experimentally determined constitutive behavior follows the bilinear behavior predicted by simulation.

Another interesting aspect is the failure analysis of TLPS samples cycled to failure on the TMM. Figure 6-76 shows one edge of an Iosipescu Cu-Sn TLPS joint after cycling to a load drop level of 80% with a cyclic displacement cyclic  $\pm 10 \mu\text{m}$ . The dominant failure mode is the delamination of the metallization from the Mo-coupon. Even in heavily voided regions (see lower part of Figure 6-76), the voids delaminate with the metallization from the Mo-coupon. Limited crack propagation within the TLPS joint occurs predominately at the meniscus. Crack propagation through the TLPS material occurred by a mixed failure

mode through the Cu-particles and through the IMC. Predominately the metallization peels from the Mo-coupon.

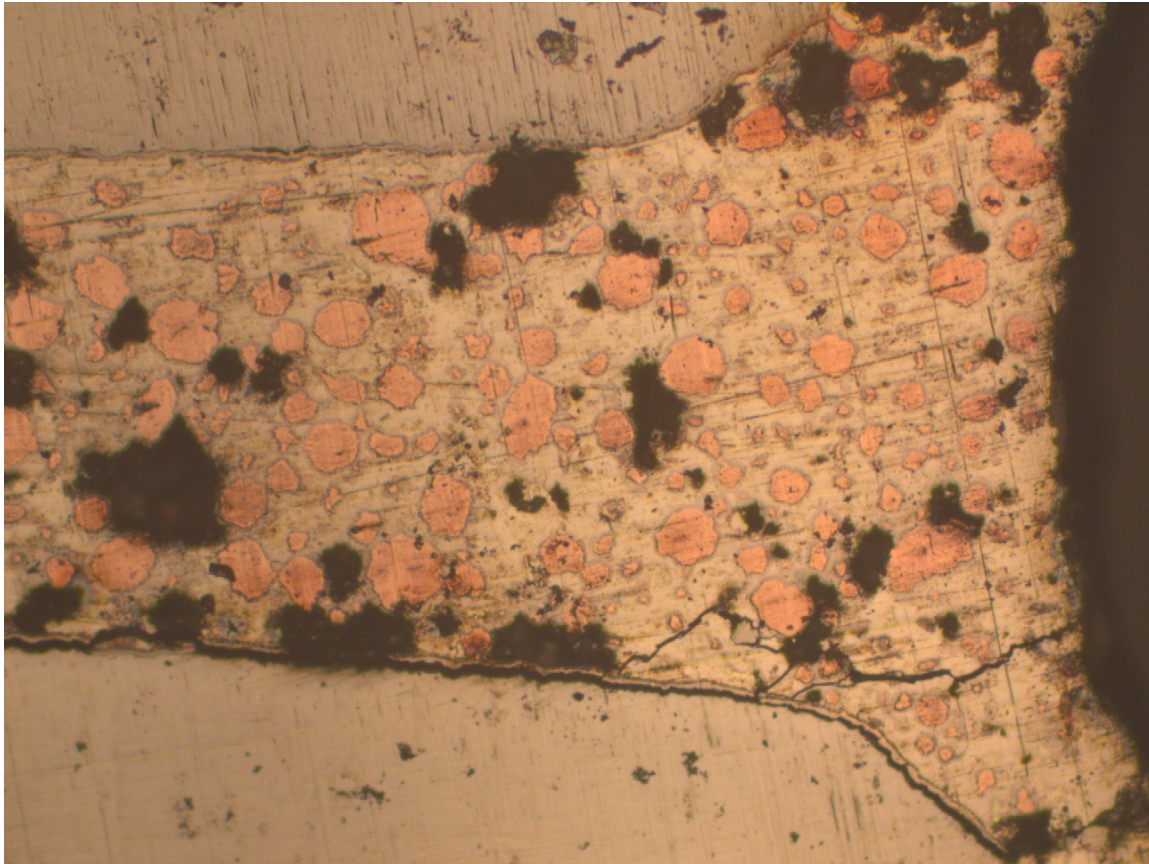


**Figure 6-76: Delamination of the metallization after cycling of a Cu-Sn TLPS sample to 80% load drop**

Figure 6-77 shows the load drop plotted against the number of cycles. After an initial phase of approximately 20 cycles the load drop levels (blue) remain constant up to approximately 70 cycles. The constitutive properties of the material are derived by using data from hysteresis loops in the constant load drop regime. The delamination after multiple dozens of cycles after the constant load regime is not an issue for the assessment of the constitutive properties of the joints in this study. Nevertheless, for future iterations of these test, performed on an overhauled TMM system, this failure mode should be mitigated to enable the determination of joint cyclic fatigue. One option to improve joint adhesion could be the

implementation of buffer and adhesion layers between the Mo-coupon and the Ni-metallization.

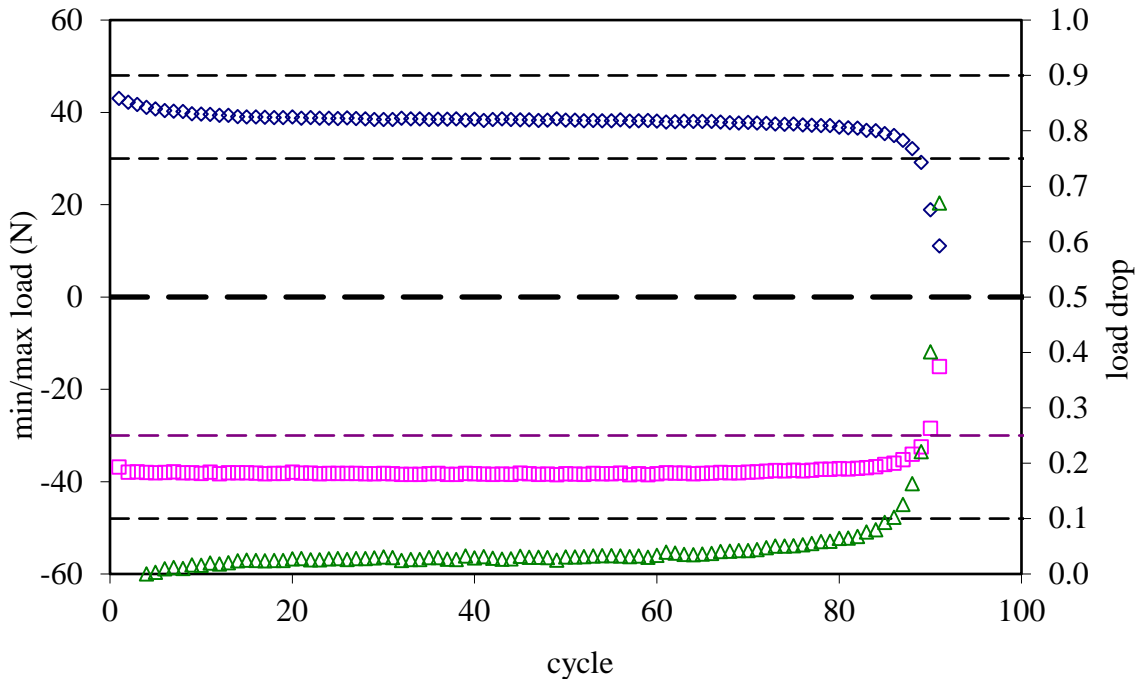


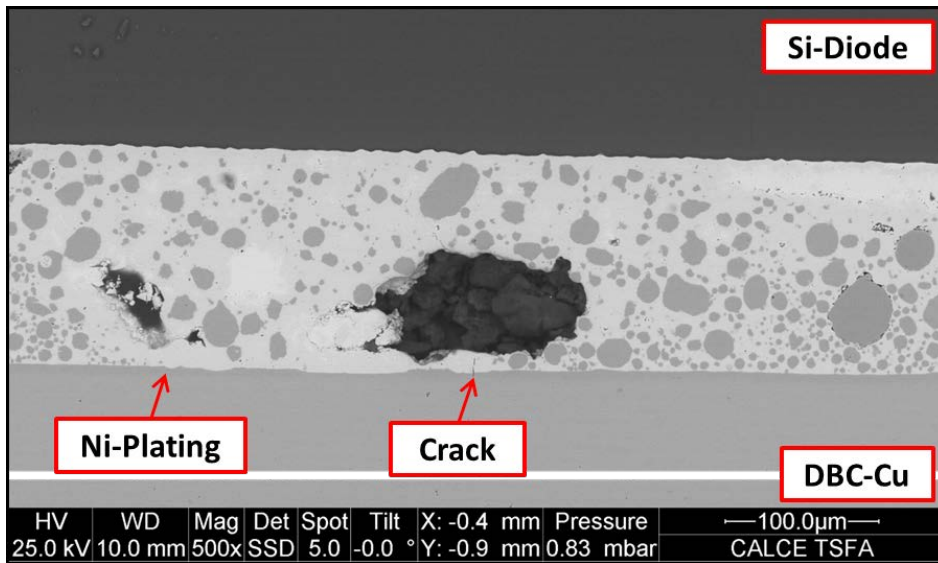
**Figure 6-77: Development of the load drop vs. number of cycles**

#### 6.4 Cooling-induced Crack Formation

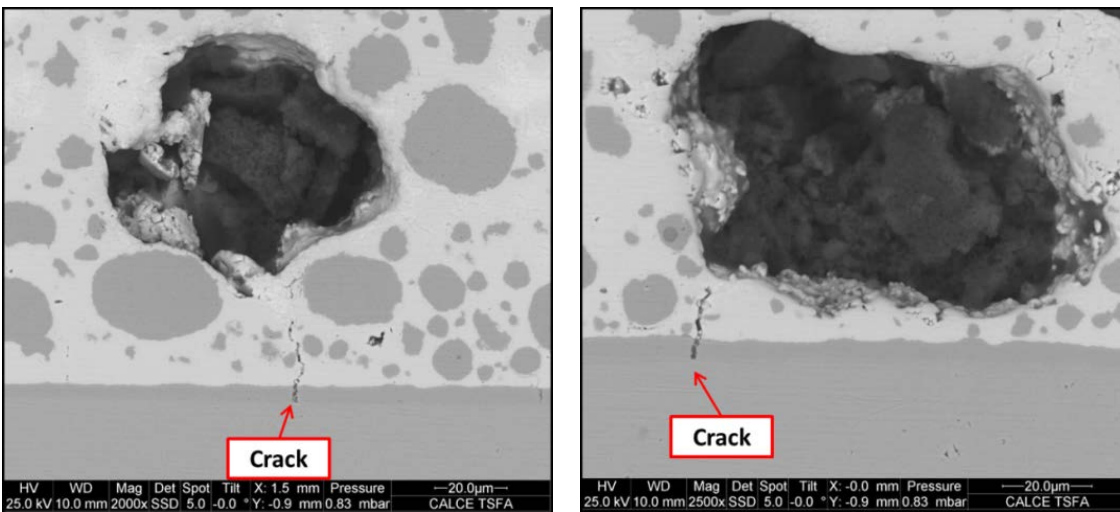
During processing, the temperature is increased to temperatures above  $T_{m,Sn}$ , 232 °C. The temperature is held at process temperature levels (e.g. 300 °C) until the Sn in the joint has been converted to IMCs and the process is completed. Still at high temperature levels, the joint solidifies completely and afterwards consists completely of high strength and stiffness materials. During subsequent cooling, thermo-mechanical stresses are induced by CTE mismatches within the package structure.

Figure 6-78 shows a cross-section of a TLPS joint formed between a Si-diode and a Ni-plated DBC substrate. In this specific joint, a large void is present near the IMC-to-DBC interface, and a crack formed between the void and the DBC substrate. Figure 6-79 shows two more examples of this type of crack formation at higher magnification. This failure

mode occurs in die-to-DBC systems attached with TLPS joints. In other samples, crack formation was found to occur for non-plated DBC substrates in die-to-DBC assemblies. Here the cracks propagate from the void through the IMCs and DBC Cu layer and are arrested at the DBC AlN layer.



**Figure 6-78: Crack formation in a diode-on-DBC assembly after processing**



**Figure 6-79: Examples of crack formation in die-on-DBC systems: The crack propagates between the void, through the IMC region and Ni plating, and stops at the DBC Cu layer**

This phenomenon has so far only been detected for TLPS joints that have been sandwiched between low-CTE layers (e.g. Si/SiC and AlN) and it only occurs when large voids are

present in the joint near the joint-to-DBC interface. The cracks propagate in vertical direction. No such cracks were detected in aging study samples manufactured with identical process parameters because of their small CTE mismatches.

The simulation model used to assess the failure mechanism underlying this failure mode is shown in Figure 6-80. It is a quarter-model of a power diode attached to a Direct Bond Copper (DBC) substrate with a TLPS joint layer with symmetry boundary conditions applied in the y and z directions and no displacement allowed at the bottom of the DBC. The thermal boundary conditions were set as homogeneous cooling from a process temperature of 300 °C to 25 °C.

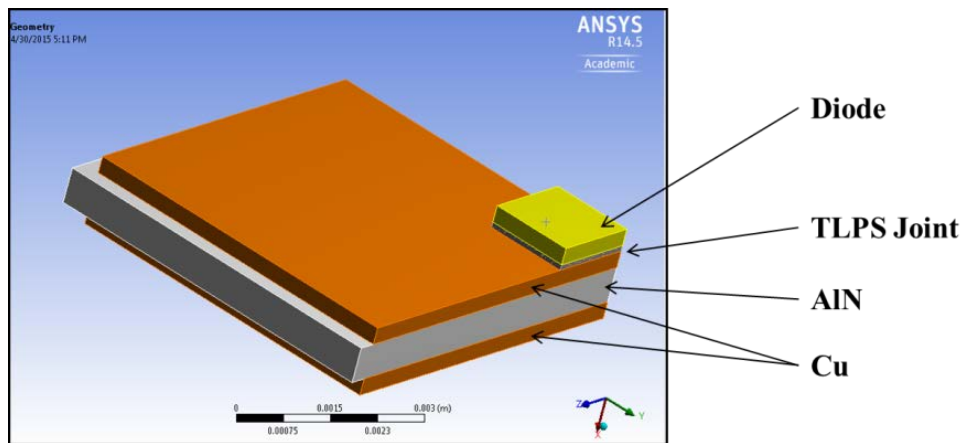


**Figure 6-80: Structure for the assessment of the thermo-mechanical assembly behavior**

A TLPS joint model consisting of 20 vol.-% metal particles with a radius of 20  $\mu\text{m}$ , and 10 vol.-% voids with radii of 30  $\mu\text{m}$  and 12  $\mu\text{m}$ , was used. Figure 6-81 (left) shows the mesh of the quarter-model of the assessed assembly. A detailed view of the mesh of the TLPS joint including the metal particles (blue), IMC regions (grey), and voids can be seen in Figure 6-81 (right). The constitutive properties of the materials are listed in Table 6-10 and Figure 6-82.

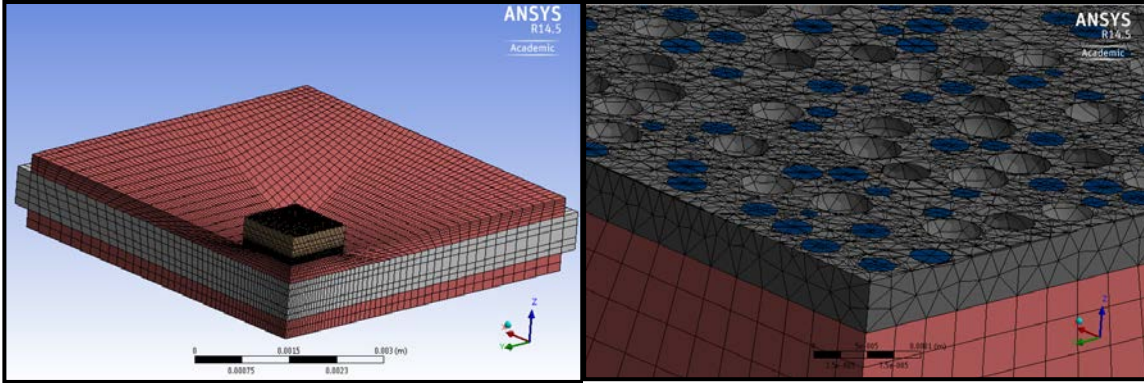


**Figure 6-81: Simulation model mesh for the cooling-induced cracking study**

Table 6-11 summarizes the maximum stresses in the assembly after cooling from 300 °C to 25 °C. The void size has a limited influence on the von Mises stress in the metal particles. The metal particle stresses for the large voided samples are 1.6%, 1.7%, and 2.8% higher for the Cu+Cu<sub>6</sub>Sn<sub>5</sub>, Cu+Cu<sub>3</sub>Sn, and Ni+Ni<sub>3</sub>Sn<sub>4</sub> system compared to the small voided samples, respectively. Similarly, the principal stresses in the die are only slightly influenced by the size of the voids. The die stresses for the large voided samples are 1.0% higher for Cu+Cu<sub>6</sub>Sn<sub>5</sub>, 3.4% smaller for Cu+Cu<sub>3</sub>Sn, and 3.0% smaller for the Ni+Ni<sub>3</sub>Sn<sub>4</sub> system than those for the small voided samples.

**Table 6-10: Elastic modulus, coefficient of thermal expansion (CTE), and thermal conductivity of the materials used in this study**

Material	AlN	Cu	Cu <sub>3</sub> Sn	Cu <sub>6</sub> Sn <sub>5</sub>	Ni	Ni <sub>3</sub> Sn <sub>4</sub>	SiC
E-Modulus [GPa]	330	119	133	117	250	144	410
CTE [ppm/K]	4.5	17	19	19	13.4	13.7	4
κ [W/mK]	160	400	69.8	34.2	90.9	19.6	120

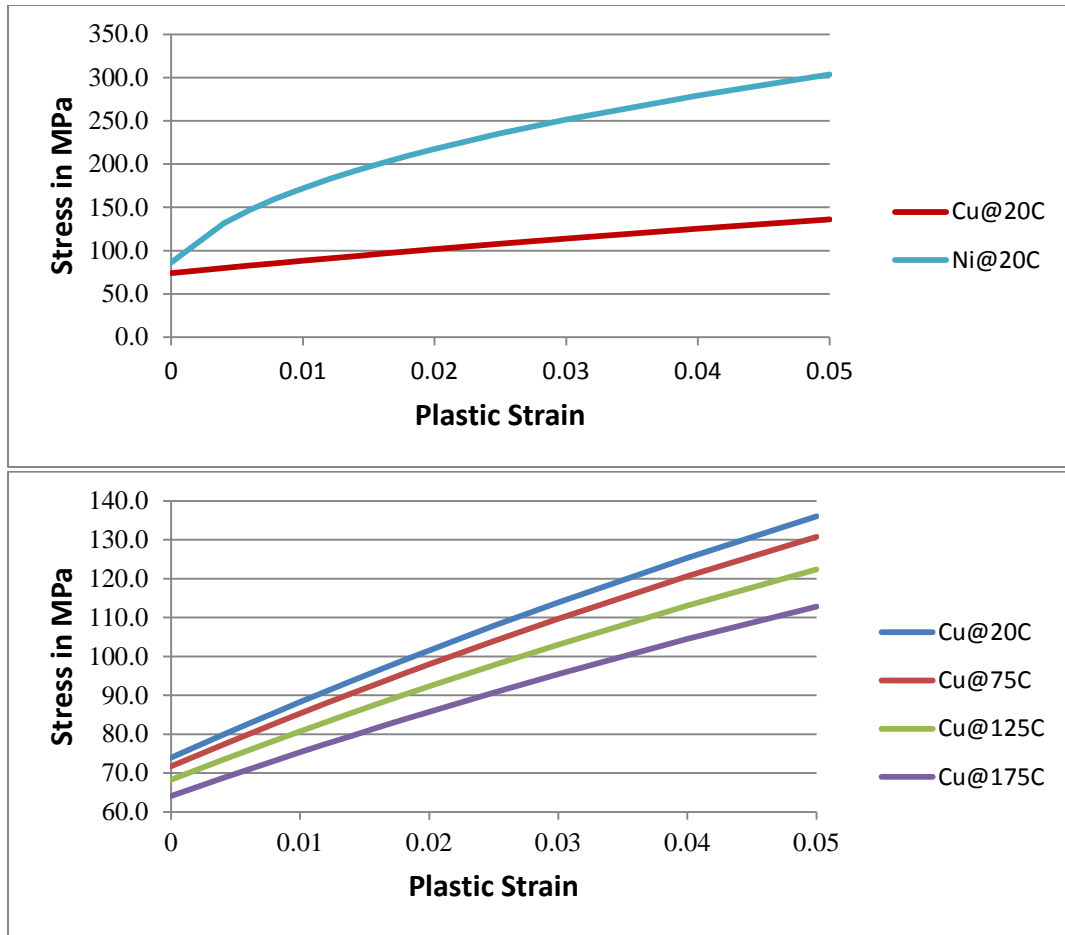


**Figure 6-82: Stress vs. plastic strain for Ni and Cu at 20 °C (above) and Cu at multiple temperatures**

In contrast, the principal stresses of the IMCs show a considerable dependence on the size of the voids, see Figure 6-83. The stresses for the large voided samples are 14.9%, 11.4% and 11.4% smaller for the Cu+Cu<sub>6</sub>Sn<sub>5</sub>, Cu+Cu<sub>3</sub>Sn, and Ni+Ni<sub>3</sub>Sn<sub>4</sub> system, respectively, compared to the small voided samples.

**Table 6-11: Maximum stresses in the assembly after cooling for large and small voids (30 μm and 12 μm respectively)**

	Cu+Cu <sub>6</sub> Sn <sub>5</sub>		Cu+Cu <sub>3</sub> Sn		Ni+Ni <sub>3</sub> Sn <sub>4</sub>	
Void radius [ μm]	30	12	30	12	30	12
von Mises stress, Particle [MPa]	87.4	86.0	87.4	85.9	143.9	139.9
Principal Stress Die [MPa]	698	691	721	746	485	500
Principal Stress IMC [MPa]	1491	1752	1736	1959	1201	1355

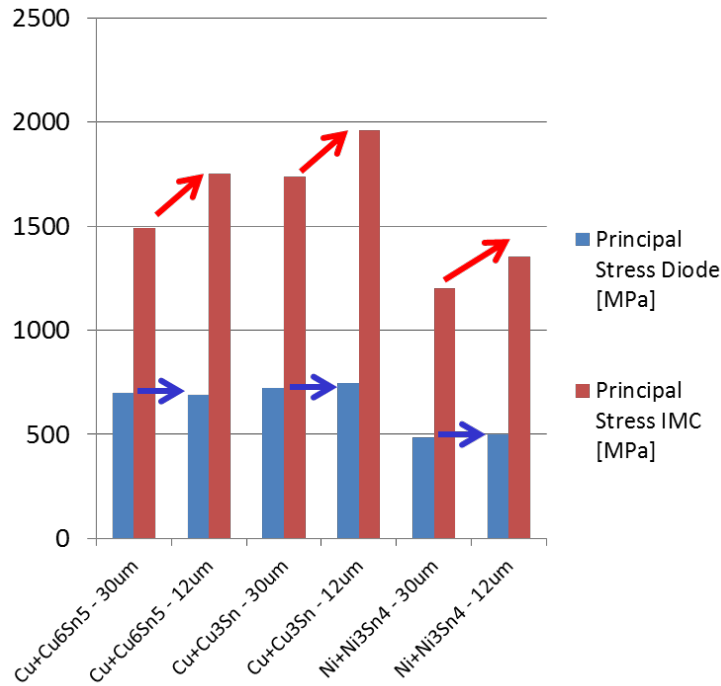
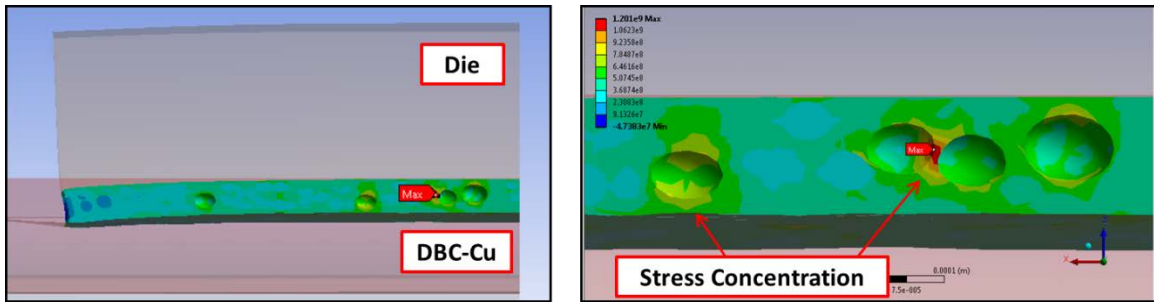


**Figure 6-83: Dependence of the maximum principal stresses of die and IMCs on the void size. In contrast to the die maximum principal stress, the IMC shows a strong dependence on void size**

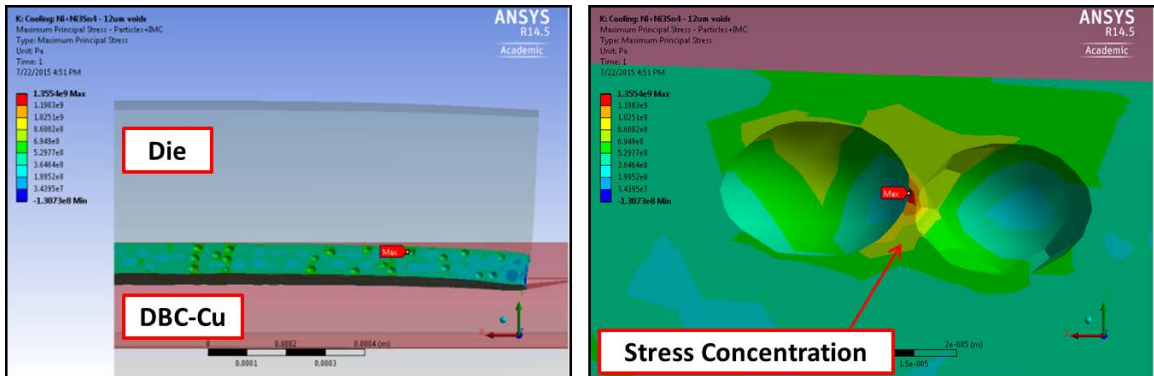
This is counter-intuitive to conventional engineering judgment (i.e., larger voids should lead to locally more concentrated stress fields and higher stress levels). Additionally, the constant stress levels in the die indicate that the influence of void size is confined to the TLPS joint region.

Figure 6-84 shows a cross-section through an assembly with a TLPS joint with large (30 μm) voids after cooling from 300 °C to 25 °C. Figure 6-85 shows an analogous cross-section of a TLPS joint with small (12 μm) voids. The locations of the cross-sections were chosen to show the maximum principal stress in the IMC. Two distinct types of stress concentration regions exist: The first are (Type I) stress concentrations between voids located at the edge of the joint close to the DBC Cu or the Si die. The second (Type II) are stress concentrations located at regions between adjacent voids in close proximity. The

stress concentrations are tensile, which can induce initiation of cracks and fracture during the cooling process.



**Figure 6-84: Cross-section through a TLPS joint with large (30  $\mu\text{m}$  radius) voids. Two distinct types of stress concentration exist: (1) between voids and Cu or Si, and (2) between adjacent voids in close proximity**



**Figure 6-85: Cross-section through a TLPS joint with small (12  $\mu\text{m}$  radius) voids. The higher number of voids in the joint increases the probability of voids in close proximity**

The maximum principal stresses in the TLPS joints are located between voids in close proximity (Type II). In real TLPS joints, two voids in very close proximity are unlikely to form because during processing, these voids typically coalesce to a single bigger void. The thin bridges connecting these voids in the simulations will then not be present in real joints. If they should exist after processing, the Type II stress regions will crack and effectively form areas characterized by the presence of individual large voids.

The failure mode found in real joints, as shown in Figure 6-78 and Figure 6-79, is of Type I stress concentrations. Figure 6-86 and Figure 6-87 show the stress distribution at the DBC

Cu-to-TLPS joint interfaces for samples with large (30  $\mu\text{m}$  radius) and small (12  $\mu\text{m}$  radius) voids, respectively. Local stress maxima (yellow regions) are distributed along the interface. The density of these regions increases with proximity to the joint center. The maxima correlate to regions with voids close to the Cu-to-TLPS joint interface (Type I). The average stress level at this interface is higher at the joint center (upper right corner and lower right corner in the quarter-model in the left images of Figure 6-86 and Figure 6-87, respectively) than at the joint edges.

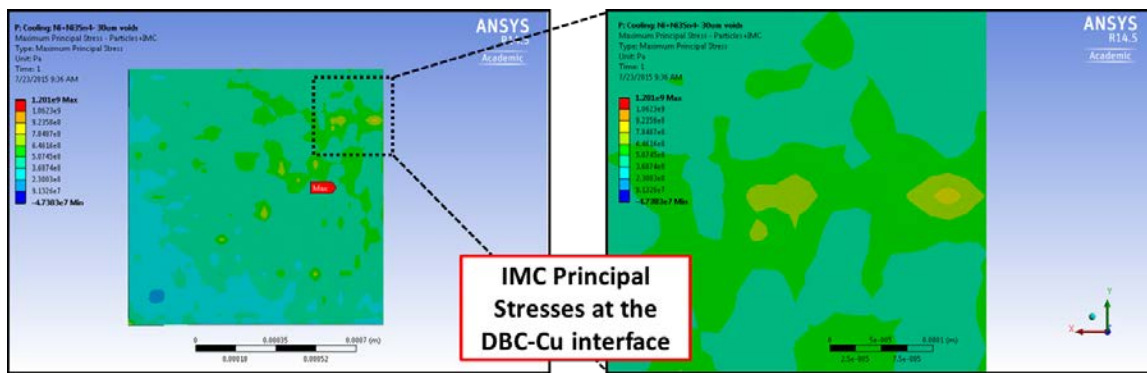


**Figure 6-86: Maximum principal stress distribution at the DBC Cu-to-TLPS joint interfaces for large (30  $\mu\text{m}$  radius) voids**

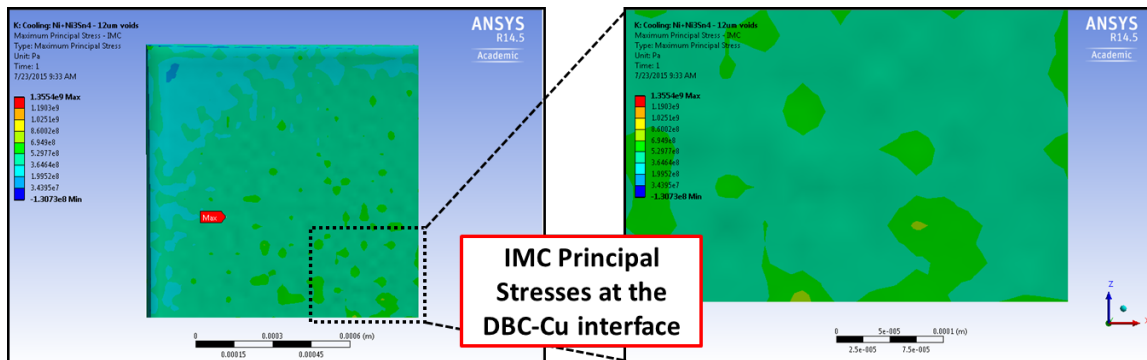
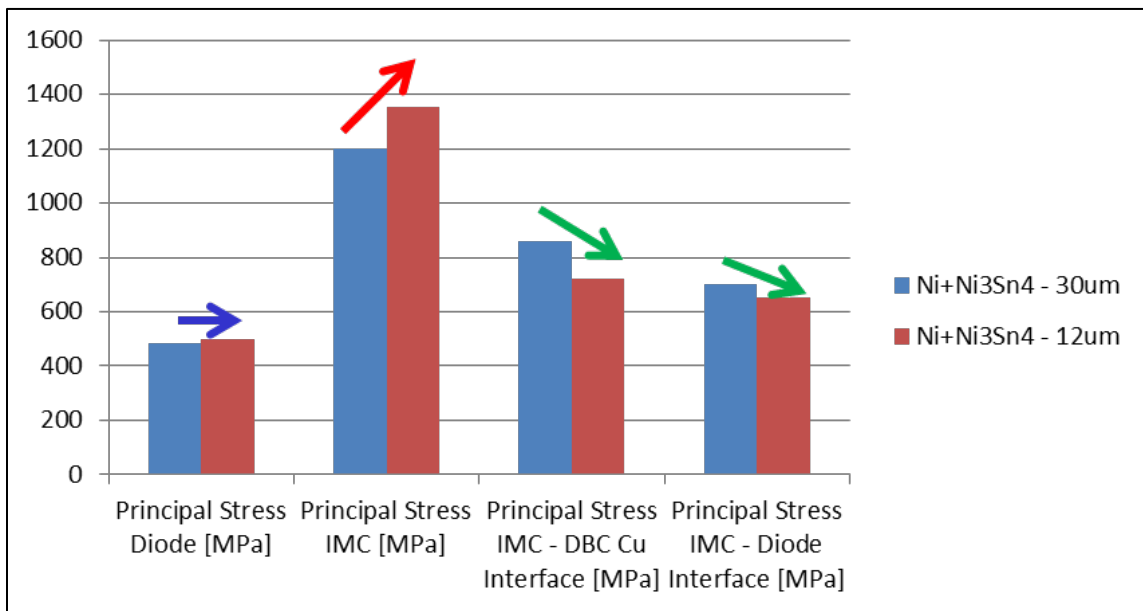


**Figure 6-87: Maximum principal stress distribution at the DBC Cu-to-TLPS joint interfaces for small (12  $\mu\text{m}$  radius) voids**

As one example, for the Ni+Ni<sub>3</sub>Sn<sub>4</sub> system, the highest principal stresses at this interface are 860 MPa and 720 MPa for the large and small voids, respectively. Additionally, the influence zone is larger for large voids than for small voids. When choosing, for example, a threshold criterion of 640 MPa, the zone of influence with stresses above this level has a

radius of approximately 25  $\mu\text{m}$  for the joint with large voids in contrast to an influence radius of approximately 7.5  $\mu\text{m}$  for the small voids.

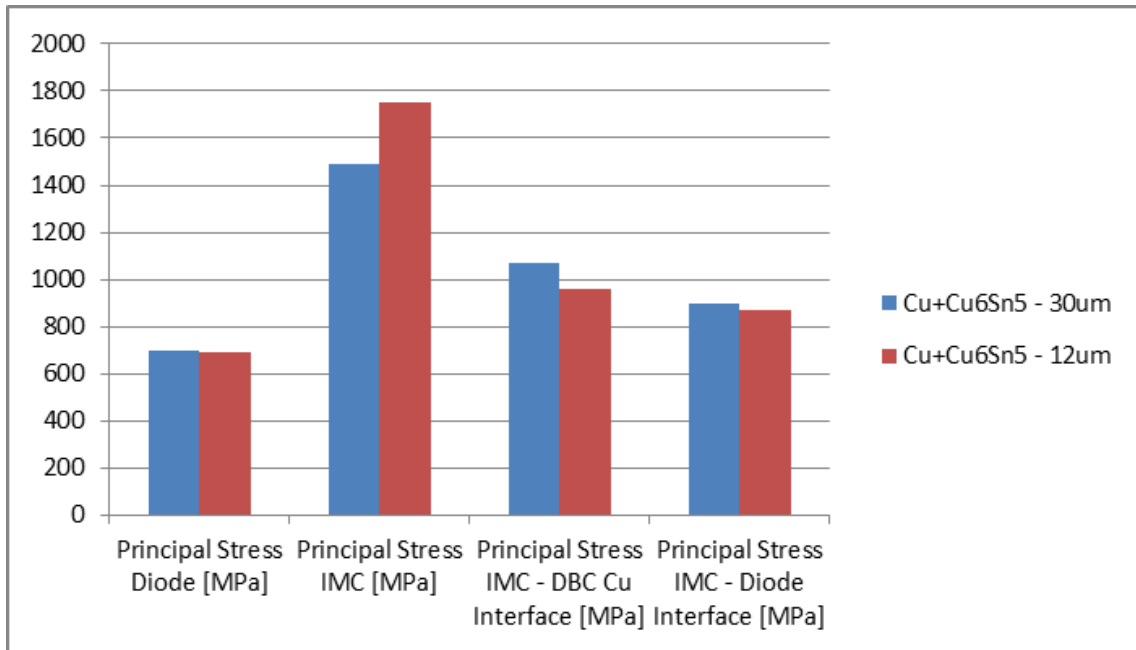
Figure 6-88 shows the principal stresses in the assembly for the Ni+Ni<sub>3</sub>Sn<sub>4</sub> system for the TLPS joints with large (30  $\mu\text{m}$  radius) and small (12  $\mu\text{m}$  radius) voids. The maximum principal stress in the diode is almost independent of the void size (indicated by the blue arrow). The maximum principal stress in the IMC is increasing considerably with decreasing void size (red arrow). The maximum principal stresses at the IMC-to-DBC Cu and IMC-to-Diode interfaces decreases considerably with void size. These stress locations correspond to Type I stress regions and the associated vertical cracking failure modes described above.



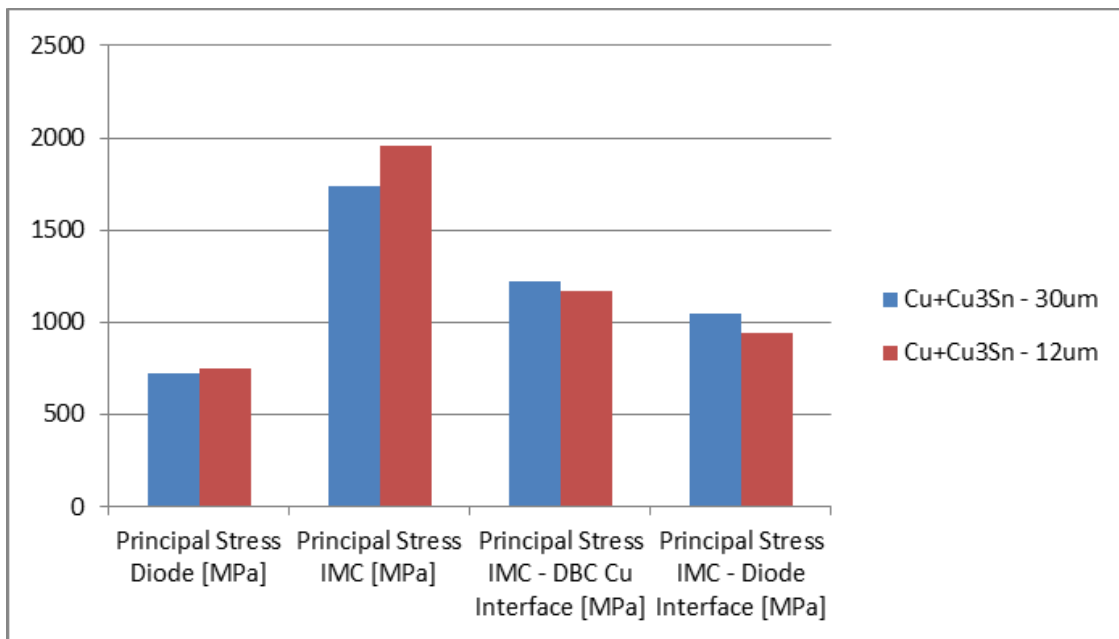
**Figure 6-88: Maximum principal stresses in the IMC, diode, IMC-to-Diode and IMC-to-DBC Cu interfaces for the Ni+Ni<sub>3</sub>Sn<sub>4</sub> system with large and small voids**

Figure 6-89 and Figure 6-90 show comparable principal stress trends for the Cu+Cu<sub>6</sub>Sn<sub>5</sub> and Cu+Cu<sub>3</sub>Sn systems, respectively. Qualitatively the behavior is identical to that of the Ni+Ni<sub>3</sub>Sn<sub>4</sub>, but the principal stress amplitudes are different. The Ni+Ni<sub>3</sub>Sn<sub>4</sub> system has the

lowest stress levels, followed by the Cu+Cu<sub>6</sub>Sn<sub>5</sub> system, and the cooling induced stresses are highest in the Cu+Cu<sub>3</sub>Sn system.



**Figure 6-89: Maximum principal stresses in the IMC, diode, IMC-to-Diode and IMC-to-DBC Cu interfaces for the Cu+Cu<sub>6</sub>Sn<sub>5</sub> system with large and small voids**



**Figure 6-90: Maximum principal stresses in the IMC, diode, IMC-to-Diode and IMC-to-DBC Cu interfaces for the Cu+Cu<sub>3</sub>Sn system with large and small voids**

Very limited data is available in literature on the ultimate tensile strength of the IMCs found in these systems. The fracture stress of  $\text{Cu}_6\text{Sn}_5$  IMCs under compressive load has been analyzed by micropillar testing in [129]. The stress-strain curves of pillars until first strain burst show that fracture begins at stress levels of approximately 1200 MPa, see Figure 6-91. Considering that  $\text{Cu}_6\text{Sn}_5$  is a brittle material, the fracture stress for compression will be significantly higher than the fracture stress under tension. In consequence, the required stress levels for fracture would then be exceeded by the results yielded in the above simulations.

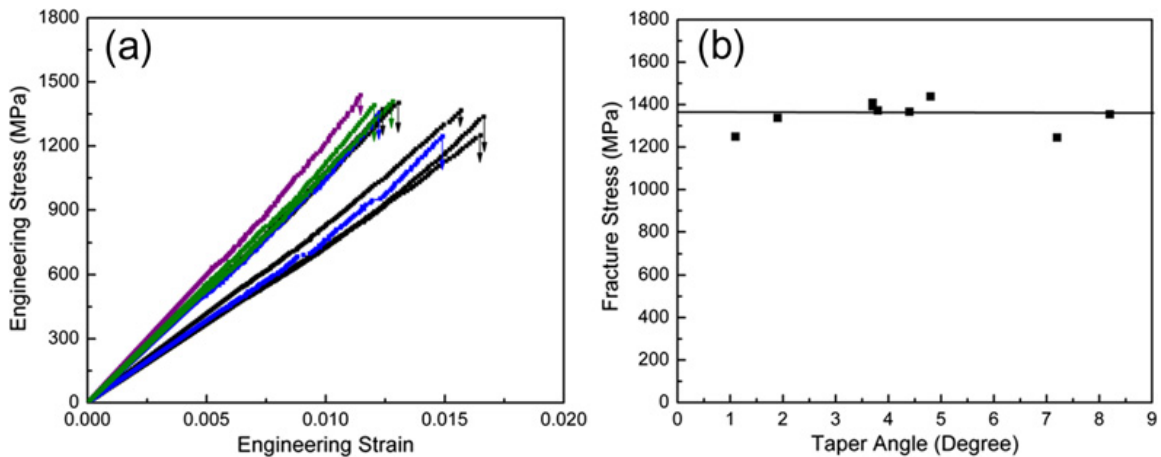


**Figure 6-91: (a) The stress-strain curves of pillars until the onset of first strain bursts and (b) a plot showing the relation between top fracture stress and taper angle of pillars [129]**

In the following, the consequences of vertical crack formation by Type I stresses on reliability and performance of the TLPS joint and the assembly will be discussed. Figure 6-92 shows a cross-section of a TLPS joint with a large void at the TLPS-to-DBC Cu interface and formation of a vertical crack by Type I stress concentration. During application, heat is generated in the diode on top of the interconnect and conducted through the joint towards the DBC Cu layer. Similarly a current is conducted in the vertical direction from the diode to the joint or vice versa. Crowding of the flow of heat and

electricity will occur around the edges of the void (compare red arrows in Figure 6-92). The contribution of the crack to the thermal or electrical resistance of the system will be small; the crack is not interfering with the flow of heat or current (the crack orientation is parallel to the flow fields). In contrast, the formation of horizontal cracks within the bulk interconnect (see Type II stress concentration in Figure 6-84 and Figure 6-85) can interfere with the heat and electron flow path and be detrimental to the thermal and electrical properties. Vertical cracking might pose a reliability risk for voids near the TLPS-to-Diode interfaces if the voids are large enough to concentrate stresses to levels high enough for crack initiation and propagation into the die, which could deteriorate device functionality.

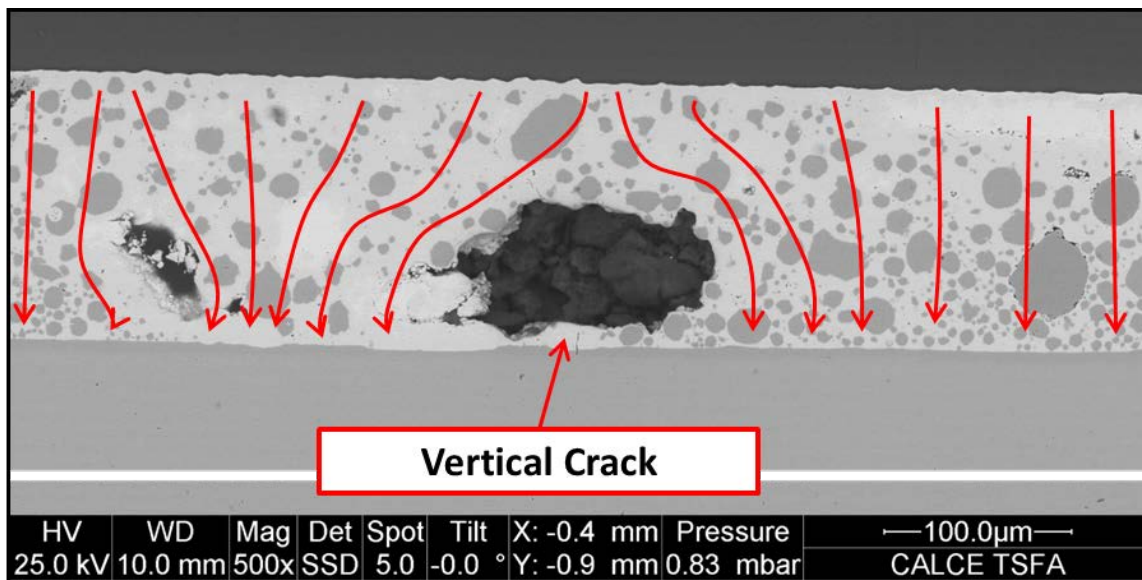


**Figure 6-92: Concentration of current and heat flux by vertical cracking: The introduction of vertical cracks at the TLPS-to-DBC Cu interface should not decrease the thermal or electrical conductivity of the assembly significantly.**

In the following, the conclusion from the cooling-induced crack formation studied are summarized:

- During the post-sintering cooling stage, tensile stresses are introduced in the TLPS joint system

- A novel failure mechanism has been identified that can cause vertical cracking in the IMCs between voids at the TLPS-to-DBC Cu interface
- The failure does not directly correlate with the maximum principal stress in the joint (Type II stress concentrations). Instead, good predictors for the failure location are the maximum principal stresses at the TLPS-to-DBC Cu interface (Type I stress concentrations)
- Smaller voids increase Type II stress concentrations, but reduce the crucial Type I stress concentration levels
- The stress levels predicted by thermo-mechanical simulations correlate well with fracture stress information for  $\text{Cu}_6\text{Sn}_5$  IMCs in literature. No such information is available for  $\text{Cu}_3\text{Sn}$  or  $\text{Ni}_3\text{Sn}_4$  as of the writing of this report
- The novel failure mode was successfully predicted by the simulation approach introduced here

## **7 Summary and Conclusions**

In this work a paste-based transient liquid phase sintering (TLPS) interconnect technology was developed and assessed. Chapter 1 summarizes the background of electronic packaging interconnect technology and that novel high temperature, low cost, lead-free attach technologies are required. Chapter 2 introduces TLPS as a potential substitute technology for high temperature attach materials. The fundamental TLPS process requirements are outlined in section 2.1 and potential low cost, high melting temperature TLPS systems introduced in sections 2.2 - 2.4. The advantages of paste-based TLPS approaches compared to layer-based approaches, such as faster process completion and roughness compensation, are explained in section 2.7. Chapter 3 summarizes the objectives and the statement of work.

Chapter 4 describes the processes related to the manufacturing of sinter pastes and the sintering process for the formation of joints from sinter pastes. Sinter pastes based on the binary Cu-Sn and Ni-Sn and the tertiary Cu-Ni-Sn material systems were developed, see section 4.1. Novel paste deposition approaches were developed to optimize the process capability of the technology, see section 4.2. The new two-step sinter paste deposition process reduces voiding, improves joint cohesion, and enables higher process capability and consistency. Yet, presence of significant amount of residual low temperature phases can be present at the menisci forming at the sinter joint edges during processing. Optimized sinter process profile information concerning heating and cooling rates and pressure levels as well as an overview of the fixture built for and used to process the sinter pastes are provided in section 4.3.

Chapter 5 examines the evolution of the microstructure of paste-based TLPS joints during processing and high temperature exposure. The development and growth of phases in Cu-Sn joints during sintering and aging is analyzed qualitatively and quantitatively in section 5.1. The evolution of Cu-Sn joints is characterized by the combination of three mechanisms: (1) void nucleation and coalescence, (2) phase homogenization, and (3) grain evolution. After typical reflow durations (e.g. 2 minutes at 300 °C), Cu-Sn joints do not yet have high temperature capability because of the presence of significant amount of unconsumed Sn in the joint region. They have high temperature capability after 30 minutes of sintering at 300 °C. After this duration their microstructure is characterized predominately by residual unconsumed Cu-particles embedded in a matrix of  $\text{Cu}_6\text{Sn}_5$  IMCs.

An analysis of the growth of voids and grains in Cu-Sn TLPS joints is performed in section 5.2. Large voids (“Macrovoids”) form at locations of prior pockets of liquid Sn as Sn is consumed. The growth of these voids is driven by volume reduction during the formation of Cu-Sn IMCs. With subsequent aging, the Cu-particles continue to be consumed as a growing percentage of  $\text{Cu}_6\text{Sn}_5$  IMCs is transformed to  $\text{Cu}_3\text{Sn}$  IMCs. Microstructural differences exist between the joint composition at the center of the joint and the edges of the joints, which are dominated by  $\text{Cu}_3\text{Sn}$  and  $\text{Cu}_6\text{Sn}_5$  IMCs as matrix materials, respectively. The Macrovoids formed during sintering are stable during aging. Small voids (“Microvoids”) nucleate during aging within the TLPS bulk joint simultaneously with the transformation from  $\text{Cu}_6\text{Sn}_5$  to  $\text{Cu}_3\text{Sn}$ . Yet these voids do not nucleate in interfacial  $\text{Cu}_3\text{Sn}$  IMCs at the interface between the bulk of the Cu-Sn TLPS joint and the Cu-substrates. The nucleation of Microvoids can be explained by the fine grains of the Cu-particles of the

sinter paste.  $\text{Cu}_6\text{Sn}_5$  IMCs grow relatively large grains which, simultaneously with the transformation to  $\text{Cu}_3\text{Sn}$  IMCs, separate into many smaller grains. The  $\text{Cu}_6\text{Sn}_5$  grains consist of large, continuous crystals with well-defined boundaries, whereas the  $\text{Cu}_3\text{Sn}$  grains consist of small, discontinuous crystals with Microvoids dispersed in between.

The high temperature stability of Ni-Sn joints during identical process and aging conditions was assessed in section 5.3. After 30 minutes of sintering at 300 °C, Ni-Sn joints are characterized by the continuous presence of high temperature phases in the joint region, consisting of Ni and  $\text{Ni}_3\text{Sn}_4$  IMCs. It was found that, in contrast to Cu-Sn joints, Ni-Sn joints do not possess high temperature stability during high temperature aging with the presence of Sn-rich menisci. In contrast, Ni-Sn joints without these kinds of menisci showed high temperature stability during aging test. The crumbling mechanism of  $\text{Ni}_3\text{Sn}_4$  IMCs in the presence of liquid Sn was identified as failure mechanism for Ni-Sn TLPS joints. Similarly, Cu-Ni-Sn TLPS joints with menisci did not possess high temperature stability during high temperature aging.

Chapter 6 describes approaches for and results of the assessment of properties of paste-based TLPS joints. The complex microstructure of TLPS interconnects requires that the models for the simulation of constitutive and thermal properties are capable of representing a high level of joint detail concerning features such as particle sizes or particle distribution. Section 6.1 shows the approach for the modeling of realistic joint geometries developed in this work. It is based on development of geometric information in MatLab, modeling of 3D-geometries from the MatLab information in SolidWorks, and running simulation in the Ansys Workbench software suite.

The thermal conductivity of TLPS joints was simulated and determined experimentally in section 6.2. The influence of particle size, metal volume percentage, and voiding on the thermal properties of Cu-Sn (Cu-particles embedded in  $\text{Cu}_6\text{Sn}_5$  matrices and Cu-particles embedded in  $\text{Cu}_3\text{Sn}$  matrices) and of Ni-Sn (Ni-particles embedded in  $\text{Ni}_3\text{Sn}_4$  matrices) was assessed by simulation. The Cu+ $\text{Cu}_3\text{Sn}$  system has the highest thermal conductivity, followed by the Cu+ $\text{Cu}_6\text{Sn}_5$  and the Ni+ $\text{Ni}_3\text{Sn}_4$  system. The thermal conductivity reduces considerably for metal particle sizes below 20  $\mu\text{m}$ . Joints with wide particle size distribution have the highest possible metal load content and, consequently the highest thermal conductivity. The thermal conductivity of Cu-Sn joints formed between diodes and DBC substrates was studied by transient thermal analyses and compared to the simulation results. The thermal conductivity determined experimentally is in good agreement with that of the simulated Cu+ $\text{Cu}_6\text{Sn}_5$  system, which is consistent with the joint phases present after completion of the sintering process. The thermal conductivity of samples aged at high temperatures degraded considerably. This is contradictory to the results found in the aging studies of the Cu-Sn system. One explanation for the degradation during aging could be, that the Ag/Ni-plating on the diode surfaces initiates a delamination mechanism similar to the crumbling mechanism found for Ni-Sn samples during aging.

The constitutive properties of paste-based TLPS interconnects were predicted by simulation in section 6.3. The predicted constitutive models follow a bilinear hardening behavior. Shear tests with Iosipescu samples were used to determine the constitutive properties of Cu-Sn joints. The bilinear stress-strain behavior predicted by simulations was verified, but a transition zone exists between the two linear ranges. Yet the amplitude of the experimental strains deviated from the amplitude predicted by simulations. It was found

that this behavior was not limited to TLPS samples but was also found for other Iosipescu samples. An overhaul of the TMM test machine will be required to establish quantitatively correct material properties models in the future.

Vertical cracking near large interfacial voids was detected as a novel failure mode specific to TLPS joints, compare section 6.4. The cracking was predicted successfully by simulations and mitigation methods for the prevention of this failure mechanism were introduced.

## 7.1 Academic Contributions

- 1) **Processing:** Sinter pastes based on the Cu-Sn, Ni-Sn, and Cu-Ni-Sn TLPS systems were developed. Additionally, a two-step sintering process was developed. This novel process approach makes the formation of sinter joints of good quality possible and ensures process consistency. It is the first process for Cu-Sn, Ni-Sn, and Cu-Ni-Sn sinter pastes that does not require the use of vacuum, inert, or reducing gas atmosphere during processing and can be used as a substitute process for conventional high temperature solders.
- 2) **Microstructural Evolution:** The studies on the microstructural evolution of Cu-Sn, Ni-Sn, and Cu-Ni-Sn joints during high temperature aging were the first that were performed on paste-based TLPS joints. Specific contributions include:
  - A. The void growth mechanisms of Cu-Sn TLPS joints were described for the first time. Two types of distinctly different void growth phenomena were identified. It was found that the growth of Macrovoids is correlated with the simultaneous growth of  $\text{Cu}_6\text{Sn}_5$  IMCs and is driven by solid-liquid rearrangement processes during early sintering stages. In contrast, the

growth of Microvoids occurs simultaneously with the transformation of  $\text{Cu}_6\text{Sn}_5$  crystals to  $\text{Cu}_3\text{Sn}$  crystals in the solid state. Furthermore, the formation of Microvoids is influenced by the size of Cu-grains as is the formation of Kirkendall voids. Additionally, this work is the first to document the three-dimensional growth of Kirkendall voids in contrast to related work on Kirkendall void growth, which is limited to two-dimensional analyses.

B. The Ni-Sn TLPS joints detachment failure mode was detected for the first time. The failure mechanism was explained phenomenologically. The detachment mechanism hypothesis is based on infiltration of  $\text{Ni}_3\text{Sn}_4$  grain boundaries by liquid Sn, grain boundary detachment, and subsequent rapid influx of residual Sn from the meniscus regions into the joint. The correctness of the hypothesis was confirmed experimentally. Furthermore it was shown that the detachment also occurs in Cu-Ni-Sn TLPS joints, but not in Cu-Sn joints. This indicates that presence of Ni is required to make these joint susceptible to this detachment mechanism.

### 3) **Mechanical Properties:**

A. A simulation methodology for the assessment of mechanical properties of paste-based TLPS joints was developed. This new approach made it possible to model the complex microstructure of the joints and assess joint properties with a higher degree of realism. The elastic-plastic behavior of sinter paste joints was predicted. Additionally, shear test with Iosipescu samples were performed and the data compared to the simulation

predictions. This was the first time that an integrated approach with simulations and experiments was used to predict mechanical properties of these types of interconnects and verify the prediction approach experimentally. The insight gained from these results and the developed methodology provides future researchers and engineers with an approach for the development of sinter pastes optimized for specific application conditions.

B. Thermo-mechanical simulations were performed to assess the reliability of paste-based TLPS joints in power module package structures. The results showed that stress concentrations exist near voids within the bulk of the joint and at the joint interfaces after post-process cooling. Post-sintering experiments with power module structures were performed and a novel failure mechanism identified. The failure locations correlate well with the predicted stress concentration locations. This was the first time that this novel failure mechanism was predicted or identified.

4) **Thermal Properties:**

A. A simulation methodology for the assessment of thermal properties of paste-based TLPS joints was developed. This new approach made it possible to model the complex microstructure of the joints and assess joint properties with a higher degree of realism. The thermal properties of Cu-Sn, Ni-Sn, and Cu-Ni-Sn sinter paste joints were predicted by simulation. For the first time the influence of particle size, metal volume percentage, and voiding levels on the thermal properties of these joints was assessed.

The insight gained from these results and the developed methodology provides future researchers and engineers with an approach for the development of sinter pastes optimized for specific application conditions.

- B. The thermal conductivity of Cu-Sn TLPS joints in power module packages was assessed. Good agreement was found between the predictions from simulation and experimental results. This verifies the technical feasibility of the novel simulation methodology and the potential of Cu-Sn TLPS joints as die attach for high power density power modules.

## 7.2 Future Work

Potential fields of future investigations directly related to this research include, arranged by chapter:

A. Chapter 4, “Processing of Paste-based TLPS Interconnects”:

- Develop a meniscus-free process for the sinter pastes. This could, for example, be achieved by fine-tuning the composition of the sinter pastes and solders pastes and the quantities stencil printed and dispensed. This would mitigate the delamination phenomena identified for the Ni-Sn and Cu-Ni-Sn joints
- Build a process chamber for processing of sinter pastes in vacuum and reducing atmospheres. This would enable the use of sinter pastes that do not require fluxes for process activation. The prevention of solid organic residue would minimize voiding level, protect metal particles and substrates from surface re-oxidation and ensure good wetting capability. In

consequence, fluxless sinter pastes might possess lower voiding levels, which could enable the application of 1-step process sinter pastes.

B. Chapter 5, “Microstructural Evolution of TLPS Interconnects in High Temperature Environments”:

- After development of meniscus-free 2-step process sinter pastes or the use of a process chamber to enable meniscus-free 1 step process sinter pastes, process completion and aging studies as performed in this work should be performed with those materials. These would be used to quantify the microstructural evolution behavior of Cu-Ni-Sn sinter pastes.

C. Chapter 6, “Assessment of TLPS Interconnect Properties”:

- To prevent degradation of the Cu-Sn joints during aging of samples used for the transient thermal analyses, a Cu-metallization layer could be applied to the active device. This Cu-layer would be partially consumed during sintering and prevent the consumption of the underlying Ag/Ni layers. This would prevent the formation of  $\text{Ni}_3\text{Sn}_4$  IMCs during sintering, which would prevent the delamination due to the crumbling effect and thereby enable a study of time-dependent thermal properties to add to the study of post-process completion thermal properties of Cu-Sn sinter joints performed in this work.
- Adapt the thermal stack structure of the sample used for the transient thermal analyses. The sample structure used in this work possessed highly three-dimensional characteristics with significant lateral spreading in the substrate layer. In contrast, ideal samples should have a close to one-

dimensional structure, e.g. the side length of the diodes should be identical with the side length of subsequent layer of the thermal stack. A reason for the high contact resistances at the interfaces of the Cu-Sn TLPS joints might be lateral spreading effects, which are abstracted as contact resistances during the computation of the Cauer and Foster thermal networks. Novel sample geometries with less pronounced lateral spreading effects could be used to verify that lateral spreading is the source of the high thermal contact resistances.

- A full experimental DoE on the constitutive properties of paste-based TLPS joints could not be performed in this work because the TMM available for the analyses measured strain levels almost an order of magnitude higher than actual strain levels. The TMM setup is currently undergoing a refit to resolve this issue. After that is completed, a full DoE for at least Cu-Sn TLPS samples should be performed to determine the elastic-plastic and creep constitutive properties of these joints. Subsequently, the same setup can be used to develop energy partitioning reliability models. Initially, cycles to failure statistics for elastic and plastic fatigue as well as creep must be collected. Coupled with simulations by the approach outlined in this work, the simulated stress levels can be calibrated against the failure statistics. The combination of constitutive properties models, simulation approach, and time to failure statistics will enable engineers and researchers to design reliable joints and predict application-condition specific product life cycles for TLPS materials.



## 8 Bibliography

- [1] F. McCluskey, R. Grzybowski and T. Podlesak, *High Temperature Electronics*, Boca Raton, 1997.
- [2] C. Buttay, D. Planson, B. Allard, D. Bergogne, C. Bevilacqua, C. Joubert, M. Lazar, C. Martin, H. Morel, D. Tournier and C. Raynaud, "State of the Art of High Temperature Power Electronics," *Materials Science and Engineering: B*, vol. 176, no. 4, pp. 283-288, 2011.
- [3] C. Raynaud, D. Tournier and H. P. D. Morel, "Comparison of High Voltage and High Temperature Performances of Wide Bandgap Semiconductors for Vertical Power Devices," *Diamond and Related Materials*, vol. 19, no. 1, pp. 1-6, 2010.
- [4] [Online]. Available: <http://www.cree.com/Power>.
- [5] [Online]. Available: <http://www.infineon.com/SiC>.
- [6] [Online]. Available: <http://www.epc-co.com>.
- [7] [Online]. Available: <http://www.microgan.com>.
- [8] M. Chinthavali, L. Tolbert, H. Zhang, J. Han, F. Barlow and B. Ozpineci, "High Power SiC Modules for HECs and PHEVs," *2010 International Power Electronics Conference (IPEC)*, 2010.
- [9] P. Ning, D. Zhang, R. Lai, D. Jiang, F. Wang, D. Boroyevich, R. Burgos, K. Karimi, D. Immanuel and E. Solodovnik, "Development of a 10-kW High-Temperature, High-Power-Density, Three-Phase AC-DC-AC SiC Converter," *IEEE Industrial Electronic Magazine*, vol. 7, no. 1, 2013.

- [10] T. Funaki, J. Balda, J. Hunghans, A. M. H. B. F. Kashyap, T. Kimoto and T. Hikihara, "Power Conversion with SiC Devices at Extremely High Ambient Temperatures," *IEEE Transactions on Power Electronics*, vol. 22, no. 4, 2007.
- [11] H. Chin, K. Cheong and A. Ismail, "A Review on Die Attach materials for SiC-Based High-Temperature Power Devices," *Metallurgical and Materials Transactions B*, vol. 41, no. 4, pp. 824-832, 2010.
- [12] R. Thompson, in *Proceedings of the SMTA/CAVE Workshop Harsh Environment Electronics*, Dearborn, Mi, 2003.
- [13] P. McCluskey, "Reliability of Power Electronics Under Thermal Loading," *7th International Conference on Integrated Power Electronics Systems (CIPS)*, 2012.
- [14] G. Zheng, S. McDonald and K. Nogita, "Development of High-Temperature Solders: Review," *Microelectronics Reliability*, vol. 52, no. 7, pp. 1306-1322, 2012.
- [15] J. Song, H. Chuang and T. Wen, "Thermal and Tensile properties of Bi-Ag Alloys," *Metallurgical and Materials Transactions A*, vol. 38, no. 6, pp. 1371-1375, 2007.
- [16] K. Suganuma, S.-J. Kim and K.-S. Kim, "High-Temperature Lead-free Solders: Properties and Possibilities," *The Journal of The Minerals, Metals & Materials Society (TMS)*, vol. 61, no. 1, pp. 64-71, 2009.
- [17] V. Chidambaram, J. Hattel and J. Hald, "High-Temperature Lead-free Solder Alternatives," *Microelectronic Engineering*, vol. 88, no. 6, pp. 981-989, 2011.
- [18] H. Schwarzbauer and R. Kuhnert, "Novel Large Area Joining Technique for Improved Power Device Performance," *Conference Record of the 1989 IEEE Industry Application Society Annual Meeting*, 1989.

- [19] J. Bai, Z. Zhang, J. Calata and G.-Q. Lu, "Low-Temperature Sintered Nanoscale Silver as a Novel Interconnect Material," *IEEE Transactions on Components and Packaging Technologies*, vol. 29, no. 3, 2006.
- [20] R. German, *Sintering: From Empirical Observations to Scientific Principles*, Oxford: Butterworth-Heinemann, 2014.
- [21] R. German, *Liquid Phase Sintering*, New York: Plenum Press, 1985.
- [22] E. Kirkendall, "Diffusion of Zinc in Alpha Brass," *Trans. AIME*, vol. 147, pp. 104-109, 1942.
- [23] A. Smigelskas and E. Kirkendall, "Zinc Diffusion in Alpha Brass," *Trans. AIME*, vol. 171, pp. 130-142, 1947.
- [24] D. Kim, J. Chang, J. Park and J. Pak, "Formation and Behavior of Kirkendall Voids within Intermetallic Layers of Solder Joints," *Journal of Materials Science: Materials in Electronics*, vol. 22, no. 7, pp. 703-716, 2011.
- [25] R. Labie, W. Ruythooren and J. Van Humbeek, "Solid State Diffusion in Cu-Sn and Ni-Sn Diffusion Couples with Flip-Chip Scale Dimensions," *Intermetallics*, vol. 15, no. 3, pp. 396-403, 2007.
- [26] W.-M. Tang, A.-Q. He, Q. Liu and D. Ivey, "Solid State Interfacial Reactions in Electrodeposited Cu/Sn Couples," *Transactions of Nonferrous Metal Society of China*, vol. 20, no. 1, pp. 90-96, 2010.
- [27] Y. Yang, H. Lu, C. Yu and Y. Li, "Void Formation at the Interface in Sn-Cu Solder Joints," *Microelectronics Reliability*, vol. 51, no. 12, pp. 2314-2318, 2011.

- [28] I. Tuah-Poku, M. Dollar and T. Massalski, "A Study of the Transient Liquid Phase Bonding Process applied to a Ag/Cu/Ag Sandwich Joint," *Metallurgical and Materials Transactions A*, vol. 19, no. 3, pp. 675-686, 1988.
- [29] R. German, P. Suri and S. Park, "Review: Liquid Phase Sintering," *Journal of Materials Science*, vol. 44, no. 1, pp. 1-39, 2009.
- [30] S. Bader, W. Gust and H. Hieber, "Rapid Formation of Intermetallic Compounds by Interdiffusion in the Cu-Sn and Ni-Sn Systems," *Acta Metallurgica et Materialia*, vol. 43, no. 1, pp. 329-337, 1995.
- [31] A. Hayashi, C. Kao and Y. Chang, "Reactions of Solid Copper with pure liquid Tin and liquid Tin saturated with Copper," *Scripta Materialia*, vol. 37, no. 4, pp. 393-398, 1997.
- [32] C. Kao, "Microstructures Developed in Solid-liquid Reactions: Using Cu-Sn Reaction, Ni-Bi Reaction, and Cu-In Reaction as Examples," *Materials Science and Engineering: A*, vol. 238, no. 1, pp. 196-201, 1997.
- [33] J. Li, P. Agyakawa and C. Johnson, "Interfacial Reaction in the Cu/Sn/Cu System during the Transient Liquid Phase Soldering Process," *Acta Materialia*, vol. 59, no. 3, pp. 1198-1211, 2011.
- [34] S. Fuertauer, D. Li, D. Cupid and H. Flandorfer, "The Cu-Sn Phase Diagram, Part I: New Experimental Results," *Intermetallics*, vol. 34, pp. 142-147, 2013.
- [35] T. Laurila, V. Vuorinen and J. Kivilahti, "Interfacial reactions between Lead-free solders and common Base Materials," *Materials Science and Engineering: R: Reports*, vol. 49, no. 1, pp. 1-60, 2005.

- [36] K. Nogita, S. Suenaga, S. McDonald, H. Tsukamoto, J. Read and T. Nishimura, "Inhibition of Crackin in Cu<sub>6</sub>Sn<sub>5</sub> Intermetallic Compounds at Sn-Cu Lead-free Solder and Cu Substrate Interfaces," *Proceedings of the International Conference on Electronics Packaging (ICEP2009)*, 2009.
- [37] R. Gagliano, G. Ghosh and M. Fine, "Nucleation Kinetics of Cu<sub>6</sub>Sn<sub>5</sub> by Reaction of molten Tin with a Copper Substrate," *Journal of Electronic Materials*, vol. 31, no. 11, pp. 1195-1202, 2002.
- [38] P. Vianco, K. Erickson and P. Hopkins, "Solid State Intermetallic Compound Growth between Copper and High Temperature, Tin-rich Solders--Part I: Experimental Analysis," *Journal of Electronic Materials*, vol. 23, no. 8, pp. 721-727, 1994.
- [39] T. Takenaka, S. Kano, M. Kajihara, N. Kurokawa and K. Sakamoto, "Growth Behavior of Compound Layers in Sn-Cu-Sn Diffusion Couples During Annealing at 433-473K," *Materials Science and Engineering: A*, vol. 396, no. 1, pp. 115-123, 2005.
- [40] P. Vianco, P. Hlava and A. Kilgo, "Intermetallic Compound Layer Formation Between Copper and Hot-Dipped 100In, 50In-50Sn, 100Sn, and 63Sn-37Pb Coatings," *Journal of Electronic Materials*, vol. 23, no. 7, pp. 583-594, 1994.
- [41] M. Onishi and H. Fujibuchi, "Reaction-diffusion in the Cu-Sn system," *Transactions of the Japan Institute of Metals*, vol. 16, no. 9, pp. 539-547, 1975.

- [42] A. Paul, C. Ghosh and W. Boettinger, "Diffusion Parameters and Growth Mechanism of Phases in the Cu-Sn System," *Metallurgical and Materials Transactions A*, vol. 42, no. 4, pp. 952-963, 2011.
- [43] R. Gagliano and M. Fine, "Thickening Kinetics of Interfacial Cu<sub>6</sub>Sn<sub>5</sub> and Cu<sub>3</sub>Sn Layers during Reaction of Liquid Tin with Solid Copper," *Journal of Electronic Materials*, vol. 32, no. 12, pp. 1441-1447, 2003.
- [44] C. Schmetterer, H. Flandorfer, K. Richer, U. Saeed, M. Kaufman, R. Roussel and H. Ipsier, "A new Investigation of the System Ni-Sn," *Intermetallics*, vol. 15, no. 7, pp. 869-884, 2007.
- [45] D. Gur and M. Bamberger, "Reactive Isothermal Solidification in the Ni-Sn System," *Acta Materialia*, vol. 46, no. 14, pp. 4917-4923, 1998.
- [46] J. Goerlich, D. Baither and G. Schmitz, "Reaction Kinetics of Ni-Sn Soldering Reaction," *Acta Materialia*, vol. 58, no. 9, pp. 3187-3197, 2010.
- [47] W. Tomlinson and H. Rhodes, "Kinetics of Intermetallic Compound Growth between Nickel, Electroless Ni-P, Electroless Ni-B and Tin at 453 to 493K," *Journal of Materials Science*, vol. 22, no. 5, pp. 1769 - 1772, 1987.
- [48] H. Blair, T. Pan and J. Nicholson, "Intermetallic Compound Growth on Ni, Au/Ni, and Pd/Ni Substrates with Sn/Pb, Sn/Ag, and Sn Solders," *48th IEEE Electronics and Technology Conference (ECTC)*, 1998.
- [49] M. Mita, M. K. N. Kajihara and K. Sakamoto, "Growth Behavior of Ni<sub>3</sub>Sn<sub>4</sub> Layer during Reactive Diffusion between Ni and Sn at Solid-state Temperatures," *Materials Science and Engineering: A*, vol. 403, no. 1, pp. 269-275, 2005.

- [50] M. Islam, Y. Chan, M. Rizvi and W. Jillek, "Investigations of Interfacial reactions of Sn-Zn based and Sn-Ag-Cu Lead-free Solder Alloys as Replacement for Sn-Pb Solder," *Journal of Alloys and Compounds*, vol. 400, no. 1, pp. 136-144, 2005.
- [51] Y. Jee, Y. Ko and J. Yu, "Effect of Zn on the Intermetallics Formation and Reliability of Sn-3.5Ag Solder on a Cu Pad," *Journal of Materials Research*, vol. 22, no. 07, pp. 1879-1887, 2007.
- [52] K. Gupta, "An Expanded Cu-Ni-Sn system (Copper-Nickel-Tin)," *Journal of Phase Equilibria*, vol. 21, no. 5, pp. 479 - 484, 2000.
- [53] C. Lin, S. Chen and C. Wang, "Phase Equilibria and Solidification Properties of Sn-Cu-Ni alloys," *Journal of Electronic Materials*, vol. 31, no. 9, pp. 907 - 915, 2002.
- [54] F. Sadi and C. Servant, "Phase Transformation and Phase Diagram at Equilibrium on the Cu-Ni-Sn System," *Journal of Thermal Analysis and Calorimetry*, vol. 90, no. 2, pp. 319 - 323, 2007.
- [55] S.-W. Chen, S.-H. Wu and S.-W. Lee, "Interfacial Reactions in the Sn-(Cu)/Ni, Sn-(Ni)/Cu, and Sn/(Cu, Ni) Systems," *Journal of Electronic Materials*, vol. 32, no. 11, pp. 1188-1194, 2003.
- [56] J. Tsai, Y. Hu, C. Tsai and C. Kao, "A Study on the Reaction between Cu and Sn<sub>3.5</sub>Ag Solder doped with small Amounts of Ni," *Journal of Electronic Materials*, vol. 32, no. 11, pp. 1203-1208, 2003.
- [57] C. Chuang, P. Shih and K. Lin, "Mechanical Strength of Sn-3.5Ag-based Solders and related Bondings," *Journal of Electronic Materials*, vol. 33, no. 1, pp. 1-6, 2004.

- [58] I. Angerson and J. Haringa, "Suppression of Void Coalescence in Thermal Aging of Tin-Silver-Copper-X Solder Joints," *Journal of Electronics Materials*, vol. 35, no. 1, pp. 94-106, 2006.
- [59] C. Ho, S. Yang and C. Kao, "Interfacial Reaction Issues for Lead-free Electronic Solders," in *Lead-Free Electronic Solders*, Springer US, 2007, pp. 155-174.
- [60] V. Vuorinen, T. Laurila, T. Mattila, E. Heikinheimo and J. K. Kivilahti, "Solid-state Reactions between Cu (Ni) alloys and Sn," *Journal of Electronic Materials*, vol. 36, no. 10, pp. 1355 - 1362, 2007.
- [61] H. Yu, V. Vuorinen and J. Kivilahti, "Solder/substrate Interfacial Reactions in the Sn-Cu-Ni Interconnection System," *Journal of Electronic Materials*, vol. 36, no. 2, pp. 136 - 146, 2007.
- [62] C. Ho, R. Tsai, Y. Lin and C. Kao, "Effect of Cu Concentration on the Reactions between Sn-Ag-Cu Solders and Ni," *Journal of Electronic Materials*, vol. 31, no. 6, pp. 584-590, 2002.
- [63] S.-M. Hong, C.-S. Kange and J.-P. Jung, "Plasma Reflow Bumpin of Sn-3.5Ag Solderfor Flux-free Flip Chip Package Application," *IEEE Transaction on Advanced Packaging*, vol. 27, no. 1, pp. 90-96, 2004.
- [64] D. Yu, C. Wu, D. He, N. Zhao, L. Wang and J. Lai, "Effects of Cu Contents in Sn-Cu Solder on the Composition and Morphology of Intermetallic Compounds at a Solder/Ni Interface," *Journal o Materials Research*, vol. 20, no. 8, pp. 2205-2212, 2005.

- [65] C. Ho, Y. Lin and C. Kao, "Strong Effect of Cu Concentration on the Reaction between Lead-free Microelectronic Solder and Ni," *Chemistry of Materials*, vol. 14, no. 3, pp. 949-951, 2002.
- [66] W.-T. Chen, C. Ho and C. Kao, "Effect of Cu Concentration on the Interfacial Reactions between Ni and Sn-Cu Solders," *Journal of Materials Research*, vol. 17, no. 2, pp. 263-266, 2002.
- [67] W. Luo, C. Ho, J. Tsai, Y. Lin and C. Kao, "Solid-state Reactions between Ni and Sn-Ag-Cu Solders with different Cu Concentrations," *Materials Science and Engineering: A*, vol. 396, no. 1, pp. 385-391, 2005.
- [68] C. Ho, Y. Lin, S. Yang, C. Kao and D. Jiang, "Effects of limited Cu Supply on Soldering Reactions between SnAgCu and Ni," *Journal of Electronic Materials*, vol. 35, no. 5, pp. 1017-1024, 2006.
- [69] J. Ha, T. Oh and K. Tu, "Effect of Supersaturation of Cu on Reaction and Intermetallic Compound Formation between Sn-Cu Solder and Thin Film Metallization," *Journal of Materials Research*, vol. 18, no. 9, pp. 2109-2114, 2003.
- [70] C.-H. Wang and S.-W. Chen, "Sn-0.7 wt.% Cu/Ni interfacial Reaction at 250C," *Acta Materialia*, vol. 54, no. 1, pp. 247-253, 2006.
- [71] K. Nogita, "Stabilisation of Cu<sub>6</sub>Sn<sub>5</sub> by Ni in Sn-0.7Cu-0.05Ni Lead-free Solder Alloys," *Intermetallics*, vol. 18, no. 1, pp. 145-149, 2010.
- [72] G. Ghosh and M. Asta, "Phase Stability, Phase Transformation, and Elastic Properties of Cu<sub>6</sub>Sn<sub>5</sub>: Ab initio Calculations and Experimental Results," *Journal of Materials Research*, vol. 20, no. 11, pp. 3102-3117, 2005.

- [73] C. Yu, J. Liu, H. Lu, P. Li and J. Chen, "First-principles Investigation of the Structural and Electronic Properties of  $\text{Cu}_{6-x}\text{Ni}_x\text{Sn}_5$  ( $x=0, 1, 2$ ) Intermetallic Compounds," *Intermetallics*, vol. 15, no. 11, pp. 1471-1478, 2007.
- [74] K. Hong, J. Ryu, C. Park and J. Huh, "Effect of Cross-Interaction between Ni and Cu on Growth Kinetics of Intermetallic Compounds in Ni/Sn/Cu Diffusion Couples During Aging," *Journal of Electronic Materials*, vol. 37, no. 1, pp. 61-72, 2008.
- [75] S. Wan and C. Liu, "Kinetic Analysis of the Interfacial Reactions in Ni/Sn/Cu Sandwich Structures," *Journal of Electronic Materials*, vol. 35, no. 11, pp. 1955-1960, 2006.
- [76] K. Gupta, S. Rajendraprasad, D. Ramakishna and A. Jena, "The Cu-Ni-Sn (Copper-Nickel-Tin) System," *Journal of Alloy Phase Diagrams*, vol. 4, no. 3, pp. 160-174, 1988.
- [77] C. Lin, S. Chen and C. Wang, "Phase Equilibria and Solidification Properties of Sn-Cu-Ni Alloys," *Journal of Electronic Materials*, vol. 31, no. 9, pp. 907-915, 2002.
- [78] H. Greve, S. Moeini and F. McCluskey, "Reliability of Paste Based Transient Liquid Sintered Interconnects," *64th IEEE Electronics Components and Technology Conference (ECTC)*, pp. 1314-1320, 2014.
- [79] P. Quintero and F. McCluskey, "Temperature Cycling Reliability of High-temperature Lead-free Die-attach Technologies," *IEEE Transactions on Device and Materials Reliability*, pp. 531-539, 2011.

- [80] K. Wang, K. Aasmundtveit and H. Jakobsen, "Surface Evolution and Bonding Properties of electroplated Au/Sn/Au," *2nd IEEE Electronics Systems-Integration Technology Conference (ESTC)*, 2008.
- [81] P. Soto, P. Quintero, M. Mulero and D. Ibitayo, "Microstructural Stability of Au-Sn SLID Joints for Harsh Environments," *ASME 2015 International Technical Conference and Exhibition on Packaging and Integration of Electronic and Photonic Microsystems collocated with the ASME 215 13th International Conference on Nanochannels, Microchannels, and Minichannels*, 2015.
- [82] C. Liu, Y. Lin, M. Huong and Y. Wang, "The Microstructure Investigation of Flip-chip Laser Diode Bonding on Silicon Substrate by using Indium-Gold Solder," *IEEE Transactions on Components and Packaging technologies*, vol. 26, no. 3, pp. 635-641, 2003.
- [83] K. Chu, J. Lee, H. Cho, H. Park and D. Jeon, "A fluxless flip chip bonding for VCSEL arrays using silder coated indium solder bumps," *Proceedings of 2004 International IEEE Conference on the Asian Green Electronics*, pp. 110-116, 2004.
- [84] Y. Sohn, Q. Wang, S. Ham, B. Jeong, K. Jung, M. Choi, W. Kim and C. Moon, "Wafer-level low Temperature Bonding with Au-In System," *Proceedings of the 57th IEEE Electronic Components and Technology Conference*, pp. 633-637, 2007.
- [85] B. Grummel, H. Mustain, Z. Shen and A. Hefner, "Reliability Study of Au-In Transient Liquid Phase Bonding for SiC Power Semoconductor Packaging," *2011 IEEE 23rd International Symposium on Power Semiconductors and ICs (ISPSD)*, pp. 260-263, 2011.

- [86] J. Kim, T. Yokozuka and C. Lee, "Fluxless Bonding of Silicon to Copper with High-temperature Ag-Sn Joint made at low Temperature," *Proceedings of the 56th IEEE Electronic Components and Technology Conference*, 2006.
- [87] N. Nobeen, R. Imade, B. Lee, R. Phua, E. Jian, C. Wong, C. Gan and Z. Chen, "Transient Liquid Phase (TLP) Bonding using Sn/Ag Multilayers for high Temperature Applications," *15th IEEE Electronics Packaging Technology Conference (EPTC 2013)*, pp. 647-652, 2013.
- [88] H. Mustain, W. Brown and S. Ang, "Transient Liquid Phase Die Attach for High-Temperature Silicon Carbide Power Devices," *IEEE Transactions on Components and Packaging Technologies*, vol. 33, no. 3, pp. 563-570, 2010.
- [89] Y. Wu and C. Lee, "High Temperature Ag-In Joints between Si Chips and Aluminum," *2013 IEEE 63rd Electronic Components and Technology Conference (ECTC)*, pp. 1617-1620, 2013.
- [90] R. Chuang and C. Lee, "Silver-Indium Joints produced at low Temperature for high Temperature Devices," *IEEE Transactions on Components and Packaging Technologies*, pp. 453-458, 2002.
- [91] H. Huebner, S. Penska, B. Barchmann, M. Eigner, W. Gruber, M. Nobis, S. Janka, G. Kristen and M. Schneegans, "Microcontacts with sub-30um pitch for 3D Chip-on-chip Integration," *Microelectronic Engineering*, vol. 83, no. 11, pp. 2155-2162, 2006.
- [92] N. Hoivik, K. Wang, K. Aasmundtveit, G. Salomosen, A. Lapadatu, G. Kittilsland and B. Stark, "Fluxless Wafer-level Cu-Sn Bonding for Micro- and Nanosystems

- Packaging," *2010 3rd Electronic Systems-Integration Technology Conference (ESTC)*, 2010.
- [93] K. Guth, N. Oeschler, L. Boewer, R. Speckels, G. Strotmann, N. Heuck, S. Krasel and A. Ciliox, "New Assembly and Interconnect Technologies for Power Modules," *2012 7th International Conference on Integrated Power Electronics Systems (CIPS)*, 2012.
- [94] N. Heuck, K. Guth, M. Thoben, A. Mueller, N. Oeschler, L. Boewer, R. Speckels, S. Krasel and A. Ciliox, "Aging of New Interconnect-technologies of Power-modules during Power-cycling," *2014 8th International Conference on Integrated Power Systems (CIPS)*, 2014.
- [95] X. Zhao, Y. Tian and N. Wang, "Shearing Properties of low Temperature Cu-In Solid-Liquid Interdiffusion in 3D Package," *2013 14th Conference on Electronic Packaging Technology (ICEPT)*, pp. 143-147, 2013.
- [96] S. yoon, K. Shiozaki, S. Yasuda and M. Glover, "Highly reliable Nickel-tin Transient Liquid Phase Bonding technology for High Temperature Operational Power Electronics in Electrified Vehicles," *2012 Twenty-Seventh Annual IEEE Applied Power Electronics Conference and Exposition (APEC)*, pp. 478-482, 2012.
- [97] S. Yoon, M. Glover and K. Shiozaki, "Nickel-tin Transient Liquid Phase Bonding towards high-temperature operational Power Electronics in electrified Vehicles," *IEEE Transactions on Power Electronics*, vol. 28, no. 5, pp. 2448-2456, 2013.
- [98] "<http://www.wolfspeed.com/cpw5-1700-z050b>," [Online].

- [99] A. Sharif, C. Gan and Z. Chen, "Transient Liquid Phase Ag-based Solder Technology for High-temperature Packaging Applications," *Journal of Alloys and Compounds*, vol. 587, pp. 365-368, 2014.
- [100] M. Fujino, H. Narusawa, Y. Kuramochi, E. Higurashi, T. Suga, T. Shiratori and M. Mizukoshi, "Transient Liquid-Phase Sintering Using Silver and Tin Powder Mixture for Die Bonding," *Japanese Journal of Applied Physics*, vol. 55, no. 4S, 2016.
- [101] C. Ehrhardt, M. Hutter, H. Oppermann and K. Lang, "Transient Liquid Phase Soldering for Lead-free Joining of Power Electronic Modules in High Temperature Applications," *Proceedings of the IMAPS International Conference and Exhibition on High Temperature Electronics (HiTEC 2012)*, pp. 25 - 33, 2012.
- [102] C. Ehrhardt, M. Hutter, H. Oppermann and K. Lang, "A Lead Free Joining Technology for High Temperature Interconnects using Transient Liquid Phase Soldering (TLPS)," *64th IEEE Electronic Components and Technology Conference (ECTC)*, pp. 1321-1327, 2014.
- [103] X. Liu and H. Nishikawa, "Microstructure of Transient Liquid Phase Sintering Joint by Sn-Coated Cu Particles for High Temperature Packaging," *Proceedings of the 48th International Symposium on Microelectronics*, pp. 449-452, 2015.
- [104] X. Liu, S. He and H. Nishikawa, "Thermally Stable Cu<sub>3</sub>Sn/Cu Composite Joint for High-temperature Power Device," *Scripta Materialia*, vol. 110, pp. 101-104, 2016.

- [105] T. Hu, H. Chen and M. Li, "Die Attach Materials with High Remelting Temperature Created by Bonding Cu@Sn Microparticles at Lower Temperatures," *Material & Design*, vol. 108, pp. 383-390, 2016.
- [106] S. Corbin, "High-temperature variable Melting Point Sn-Sb Lead-free Solder Pastes using Transien Liquid-Phase Powder Processing," *Journal of Electronic Materials*, vol. 34, no. 7, pp. 1016-1025, 2005.
- [107] O. Mokhtari and H. Nishikawa, "Transient Liquid Phase Bonding of Sn-Bi Solder with added Cu Particles," *Journal of Materials Science: Materials in Electronics*, pp. 1-13, 2016.
- [108] F. Lang, H. Yamaguchi, H. Nakagawa and H. Sato, "Thermally stable Bonding of SiC Devices with Ceramic Substrates: Transient Liquid Phase Sintering Using Cu/Sn Powders," *Journal of the Electrochemical Society*, vol. 160, no. 8, pp. 315-319, 2013.
- [109] R. Dudek, P. Sommer, A. Fix, S. Rzepka and B. Michel, "Reliability Issues for high Temperature Interconnections based on Transient Liquid Phase Soldering," *14th International Conference on Thermal, Mechanical, and Multi-Physics Simulations and Experiments in Microelectronics and Microsystems (EuroSimE)*, pp. 1-8, 2013.
- [110] R. Dudek, P. Sommer, A. Fix, J. Trodler, S. Rzepka and B. Michel, "Reliability Investigations of High Temperature Interconnects," *Soldering & Surface Mount Technology*, vol. 26, no. 1, pp. 27-36, 2014.
- [111] R. Dudek, P. Sommer, R. Doring, T. Herberholz, A. Fix, B. Seiler and S. Rzepka, "Thermo-mechanical behavior and Reliability issues for High Temperature

- Interconnections," *2014 IEEE Intersociety Conference on Thermal and Thermomechanical Phenomena in Electronic Systems (ITherm)*, pp. 912-919, 2014.
- [112] H. Ji, M. Li, S. Ma and M. Li, "Ni<sub>3</sub>Sn<sub>4</sub>-Composed Die Bonded Interface Rapidly Formed by Ultrasonic-assisted Soldering of Sn/Ni Solder Paste for High-temperature Power Device Packaging," *Materials & Design*, vol. 108, pp. 590-596, 2016.
- [113] M. Noguchi, S. Joshi and E. Dede, "Design of Mechanical Properties of Transient Liquid Phase Bonds with Tertiary Metal Particles," *IEEE 66th Electronic Components and Technology Conference (ECTC)*, pp. 1235-1240, 2016.
- [114] "1/32 DIN Ramp/Soak Controllers," Omega, [Online]. Available: <http://www.omega.com/pptst/CN7500.html>. [Accessed 2016].
- [115] "Copper - Element information, properties, and uses," Royal Society of Chemistry, [Online]. Available: <http://www.rsc.org/periodic-table/element/29/copper>.
- [116] "Tin - Element information, properties, and uses," Royal Society of Chemistry, [Online]. Available: <http://www.rsc.org/periodic-table/element/50/tin>.
- [117] B. Alchagirov and A. Chochaeva, "Temperature Dependence of the Density of Liquid Tin," *High Temperature*, vol. 38, no. 1, pp. 44 - 48, 2000.
- [118] H. Frederikse, R. Fields and A. Feldman, "Thermal and Electrical Properties of Copper-Tin and Nickel-Tin Intermetallics," *Journal of Applied Physics*, vol. 72, no. 7, pp. 2879 - 2882, 1992.

- [119] P. Shang, Z. Liu, X. Pang, D. Li and J. Shang, "Growth Mechanisms of Cu<sub>3</sub>Sn on Polycrystalline and Single Crystalline Cu Substrates," *Acta Materialia*, vol. 57, no. 16, pp. 4697-4706, 2009.
- [120] R. Zhang, Y. Tian, C. Hang, B. Liu and C. Wang, "Formation Mechanism and Orientation of Cu<sub>3</sub>Sn Grains in Cu-Sn Intermetallic Compound Joints," *Materials Letters*, vol. 110, pp. 137-140, 2013.
- [121] C. Yu, J. Chen, Y. Huang, J. Chen, J. Xu and H. Lu, "Fine Grained Cu Film Promoting Kirkendall Voiding at Cu<sub>3</sub>Sn/Cu Interface," *Journal of Alloys and Compounds*, vol. 660, pp. 80-84, 2016.
- [122] R. Fields, S. Low and L. G.K., "Physical and Mechanical Properties of Intermetallic Compounds Commonly found in Solder Joints," in *Proceedings of the TMS Symposium*, 1991.
- [123] A. Poppe, "Thermal Measurements and Qualification Using Transient Method - Principles and Applications," *21st Annual IEEE SEMI-THERM Symposium*, 2005.
- [124] R. Sandström, J. Hallgren and G. Burman, Stress Strain Flow Curves for Cu-OFP, Svensk kärnbränslehantering (SBK), 2009.
- [125] H. Boyer, Atlas of Stress-Strain Curves, Metals Park, Ohio, USA: ASM International, 1987.
- [126] T. Siewert, S. Liu, D. Smith and J. Madeni, "Properties of Lead-free Solders, release 4.0," National Institute of Standards and Technology & Colorado School of Mines, 2002.
- [127] [Online]. Available: <http://www.goodfellow.com/E/Molybdenum.html>.

- [128] [Online]. Available: <http://www.goodfellow.com/E/Tungsten.html>.
- [129] L. Jiang and N. Chawla, "Mechanical Properties of Cu<sub>6</sub>Sn<sub>5</sub> Intermetallic by Micropillar Compression Testing," *Scripta Materialia*, no. 63, pp. 480-483, 2010.
- [130] [Online]. Available: <http://www.rohsguide.com>.
- [131] K. Erickson, P. Hopkins and P. Vianco, "Solid State Intermetallic Compound Growth Between Copper between Copper and High Temperature, Tin-rich Solders-Part II: Modeling," *Journal of Electronic Materials*, vol. 23, no. 8, pp. 729-734, 1994.
- [132] Z. Mei, A. Sunwoo and J. Morris, "Analysis of Low-Temperature Intermetallic Growth in Copper-Tin Diffusion Couples," *Metallurgical transactions A*, vol. 23, no. 3, pp. 857-864, 1992.
- [133] K. Santosh, C. Handwerker and M. Dayananda, "Intrinsic and Interdiffusion in Cu-Sn System," *Journal of Phase Equilibria and Diffusion*, vol. 32, no. 4, pp. 309-319, 2011.
- [134] Z. Mei, A. Sunwoo and J. Morris, "Analysis of Low-temperature Intermetallic Growth in Copper-tin Diffusion COuples," *Metallurgical Transactions A*, vol. 23, no. 3, pp. 857-864, 1992.
- [135] S. Cain, J. Wilcox and R. Venkatraman, "A Diffusional Model for Transient Liquid Phase Bonding," *Acta Materialia*, vol. 45, no. 2, pp. 701-707, 1997.
- [136] M. Park and R. Arroyave, "Concurrent Nucleation, Formation and Growth of Two Intermetallic Compounds (Cu<sub>6</sub>Sn<sub>5</sub> and Cu<sub>3</sub>Sn) during the early Stages of Lead-Free Soldering," *Acta Materialia*, vol. 60, no. 3, pp. 923-934, 2012.

- [137] J. Liu, P. Kumar, I. Dutta, R. Raj, R. Sidhu, M. Renavikar and R. Mahajan, "Liquid Phase Sintered Cu-In Composite Solders for Thermal Interface Material and Interconnect Applications," *Journal of Materials Science*, vol. 46, no. 21, pp. 7012-7025, 2011.
- [138] G. Dong and G. Arslanian, "Fluxless Soldering of Flip Chip Assemblies," *Nepcon West*, pp. 96-112, 1996.
- [139] C. Dong, A. Schwarz and D. Roth, "Feasibility of Fluxless Reflow of Lead-free Solders in Hydrogen and Forming Gas," *Nepcon Malaysia 97*, pp. 03-32, 1997.
- [140] W. Lin and Y. Lee, "Study of Fluxless Soldering using Formic Acid Vapor," *IEEE Transaction on Advanced Packaging*, vol. 22, no. 4, pp. 592-601, 1999.
- [141] Y. Lin, C. Shih and W. Chang, "Fluxless Reflow of Eutectic Solder Bump using Formic Acid," *Proceedings of the IEEE 12th International Symposium on Integrated Circuits (ISIC'09)*, pp. 514-517, 2009.
- [142] T. Yagishita, K. Ishikawa and N. Moritaka, "Cleaning of Copper Surface Using Vapor-Phase Organic Acids," *Proceedings of the International Symposium on Plasma Processing for the 100nm Node and Copper Interconnects with Low-k Inter-level Dielectric Films*, vol. 2003, p. 320, 2003.
- [143] X. Liu and H. Nishikawa, "Microstructure of Transient Liquid Phase Sintering Joint by Sn-Coated Cu Particles for High Temperature Packaging," *International Symposium on Microelectronics*, vol. 1, pp. 449-452, 2105.

